Republic of Iraq
Ministry of Higher Education and Scientific Research
University of Babylon / College of Engineering
Civil Engineering Department

Anti-vortex Effect on Triangular Stepped Labyrinth Side Weir Hydraulics

A Thesis
Submitted to the Department of Civil Engineering, College of Engineering, University of Babylon in Partial Fulfilment of the Requirements for the Master Degree in Engineering /Civil Engineering /Water Resources

By:

Riyam Deyaa Mohammed Hassan

Supervised by:

Prof.Dr: Thair Jabbar Mizhir Alfatlawi

2022A.D **1444 A.H**

بِسْمِ اللَّهِ الرَّحْمَنِ الرَّحِيمِ

"يَرْفَعِ اللَّهُ الَّذِينَ آمَنُوا مِنْكُمْ وَالَّذِينَ أُوتُوا الْعِلْمَ دَرَجَاتٍ ۚ

وَاللَّهُ بِمَا تَعْمَلُونَ خَبِيرٌ"

صدق اللّهُ العظيم

سورة المجادلة {من الأية:11 }

Supervisor Certification

I certify that this thesis which is entitled ***(Anti-vortex Effect on Triangular Stepped Labyrinth Side Weir Hydraulics)*** has been prepared by ***(Riyam deyaa mohammed hassan)*** under my supervisionat College of Engineering, Babylon University, in partial fulfilment of the requirements for the Master Degree in Engineering /Civil Engineering /Water Resources

Signature:

Name: ***Prof. Dr. Thair Jabbar Mizhir Alfatlawi***

Date: / / 2023

EXAMINATION COMMITTEE CERTIFICATION

We certify that we have read this thesis entitled ***"Anti-vortex Effect on Triangular Stepped Labyrinth Side Weir Hydraulics"*** presented by ***"Riyam deyaa mohammed hassan "*** and as an examining committee, we examined the student in its content and in what is connected with it, and that in our opinion it meets standard for the Master Degree in Engineering /Civil Engineering /Water Resources

Name: ***Prof. Dr. Thair J.Mizhir Alfatlawi***	Name: ***Asst. Prof. Dr. Riyadh Jasim Mohammed Al-saadi***
(Supervisor and Member)	(Member)
Date: / /	Date: / /
Signature:	Signature:
Name: ***Asst. Prof. Dr. Riyadh H. Mohammed Muttaleb***	Name: ***Prof. Dr. Abdul-Hassan K. Al-Shukur***
(Member)	(Chairman)
Date: / /	Date: / /
Signature:	Signature:

Approved by the Head of the Civil Engineering Department

Signature:

Name: ***Prof. Dr. Thair J.Mizhir Alfatlawi***

Date: / /

Approved by the Dean of college of Engineering

Signature:

Name: ***Prof. Dr.*** **Hatem Hadi Obeid**

Date: / /

Deduction

I would like to dedicate

“To My GOD ALmight who is always there when I am in need ,and for giving me this apportainity to do my master degree which would not have been possible other wish ”

“To the messenger of GOD and prophet of mercy, the prophet Mohammed “my GOD’s prapers and peace be upon him ”

“To my beloved parents ,who have been source of inspiration and gave me strength when i thought of giving up,and containually provide their moral ,spiritual, emotion ,and financial support ”

"To everyone who helped me tomove the rocks on my way,
to everyone who believed on me."

With love and respect
RIYAM

Acknowledgements

In the name of Allah, the Most Gracious, the Most Merciful. Praise be to Allah for the blessing has bestowed upon me, and prayers and peace be upon the one who was sent with mercy, and upon his family, and upon his honourable companions and after.

I would like to express my sincere and cordial thanks to my superviso Prof. Dr. Thair Jabbar Mizhir Alfatlawi for his valuable advices, guidance, constructive, criticism, encouragement, and cooperation throughout all stages of preparing this study.

As I stand here, I can't express enough thanks to my dearest persons ever my mother and father who provide me with all the financial and moral support so that I can reach what I have reached with their prayers.

I would like to thank Mr. Thair Hashim Rasheed and Mr. Firas Habeeb for their guidance and help with this study.

I am very grateful to all my teachers, starting from primary school and ending with higher studying of college, thanks very much for all of them.

My thanks and appreciation to the staff of the Department of civil engineering, Fluid Laboratory of Civil Engineering, College of Engineering, Babylon University, Iraq, for their support and assistance.

Abstract

Side weirs are essential structural elements that are commonly used to control water levels in rivers and canals. Labyrinth side weirs can be preferred for the weirs with the same opening instead of the other conventional side weirs. However, the vortex occurring in the cycles of the labyrinth side weir usually obstructs overflow in the side weirs.

The present study suggested four types of antivortex structures installed in stepped labyrinth side weir with different hydraulic conditions. This study investigates the vortex formation at upstream of the labyrinth side weir by experimental and numerical modelling. Also, it studied the influence of installing an antivortex structure in these side weirs on discharge capacity, and evaluated the performance of proposed models. Using data from 168 experimental runs without antivortex to allow comparison and 672 experimental runs to determine the best performance of antivortex structures that improved discharge capacity, and 528 runs of velocity measurements to investigate the intensity of secondary currents generated by lateral flow and other hydraulic conditions, including water surface profiles. The experiments are performed for two widths of the stepped labyrinth side weir ($L = 0.3m$ and $0.45m$), heights of the weir ($P = 0.08m$ and $0.14m$), and three numbers of steps ($N = 4, 8$, and 10) and angles ($\theta^o = 45, 60$). Physical models are simulated numerically using the FLOW 3D 11.2.2.01 software program to investigate vortex formation for different water levels and expand the application of software to include the cases not studied experimentally. The volume of fluid (VOF) technique, turbulence, and the free flow surface are all simulated using the (LES) model in the Flow 3D software. Visual simulations and analysis results of numerical models prepared and analyzed in Flow 3D are examined in Flow Sight. The first numerical models examine the vortices and their exact location in the stepped labyrinth side weir based on experimental visualizations, while the later numerical models examine the structures that prevent the vortices and their dimensions in these weirs.

The results indicated that the discharge coefficient values increased by installing antivortex structures to reach the maximum values with increased steps number, decreased head angle, and weir length ratio. Models that included ten steps, head angle (θ^{o} =45), and weir length ratio (weir length (L) /main flume width (B) = 1), produces greater discharge coefficient values. Thus, installing antivortices regulated the flow, significantly improved the efficiency of the single-cycle stepped labyrinth side weir, and lowered secondary flows caused by interaction with the vertical axis. After analyzing the best type of antivortex, considering shape and height type1 outperforms other types by increasing discharge coefficient to 18%, and decreasing the amount of secondary flows by about 9%.

The numerical results show that the most significant relative error in validating the numerical model with the experimental data is 3.07 percent, confirming that the model predicts the flow requirements over the labyrinth weir. The simulations are run to determine the dimensions of antivortex structures by installing the antivortex in the location of the vortex and varying the location and dimensions of the antivortex structures with the crest height (p), length (L), and step number. The software also calculates the hydraulic characteristics such as flow surface levels, Froude number, velocity, and vortex formation in the stepped labyrinth weir.

List of Content

List of Symbols

Symbol	Description	Dimension
a_s	Step height	L
B	Width of the main flume	L
b_s	Step width	L
C_d	Coefficient of discharge	L
d	Side weir depth	L
F_1	Froude number at the upstream end of side weir	dimensionless
F	volume flow function	-
g	Gravitational acceleration	LT^{-2}
h_1	Water head above side weir crest at the upstream of the side weir	L
h_2	Water head above side weir crest at the center of the side weir	L
h_3	Water head above side weir crest at the downstream of the side weir	L
Δh_s	Friction loss	dimensionless
H_s	Water depth above side flume rectangular weir	L
h_a	Average nappe height	L
L	Weir opening length	L
l	Total weir crest length of labyrinth side weir	L
N	Number of steps	dimensionless
P	Weir crest height	L
Q_d	Downstream discharge	$L^3.T^{-1}$
Q_{sw}	Lateral side weir discharge	$L^3.T^{-1}$

Q_u	Upstream discharge	$L^3.T^{-1}$
V_1	Main flume upstream flow velocity	$L\ T^{-1}$
V_2	Main flume downstream flow velocity	$L\ T^{-1}$
V_F	open volume ratio to flow	-
v_s	Velocity of flow near the flow surface	$L\ T^{-1}$
v_b	Velocity of flow near the flow bottom	$L\ T^{-1}$
y_1	Flow depth at the upstream end of the side weir	L
y_2	Flow depth at the downstream end of the side weir	L
θ°	The internal angle between two tangents of internal steps connection points.	degree
α_1, α_2	Experimental constant	dimensionless
A_x, A_y, A_z	Fractional areas	-
u, v, w	Velocity in the x, y, z direction, respectively	$L\ T^{-1}$
x_i, x_j	Cartesian coordinates	-
u_i, u_j	Cartesian components of the velocity vector	-
$\bar{P}$	Pressure	ML
μ	Dynamic viscosity of water	$M\ L^{-1}\ T^{-1}$
ρ	The mass density of water	$M\ L^{-3}$
Φ	varied flow function of De Marchi	dimensionless
ξ	Correction coefficient for Schmidt approach	dimensionless

List of Abbreviations

Abbreviations	Description
CFD	Computational Fluid Dynamics
FAVOR	Fractional Area / Volume Obstacle Representation
LSW	Labyrinth Side Weir
LES	Large Eddy Simulation
MAPE	Mean Absolute Percentage Error
PKSW	Piano Key Side Weir
R^2	Coefficient of Regression
RANS	Reynolds Average Navier Stocks
RMSE	Root Mean Square Error
RNG	Renormalized Group
SLSW	Stepped Labyrinth Side Weir
STL	Stereolithgraph
TruVOF	True Volume Of Fluid
TLSW	Triangular Labyrinth Side Weir
VOF	Volume Of Fluid

List of Figures

List of Tables

Chapter One

Introduction

1.1 Overview

Hydraulic engineers have been encouraged to seek creative solutions to engineering problems to ensure that hydraulic structure projects are practical and economical. Side weirs can either take in the required water or hold it at the desired level. The flooding in this structure is gravitational, and it is commonly employed since the transferred flow is continuous, and no additional energy is spent in the water transfer (such as in pumping stations).

Side weirs have a variety of cross-sections, and their performance has been studied recently (for example, trapezoidal, triangular, rectangular, and circular). The labyrinth side weir is a relatively new weir style that was first introduced by (Emiroglu et al., 2010). Labyrinth weirs consist of a row of straight weirs folded in a zigzag pattern to provide a longer weir crest length for a given weir site than a straight (linear) weir and improve discharge coefficient. As a result, discharge coefficients for this type of weir can be up to (1.5-5.0) times higher than for linear side weirs (Emiroglu & Kaya, 2011). Many studies have employed labyrinth weir specifications with different configurations to improve the hydraulic performance of traditional structures, such as (Crookston & Tullis, (2012); Maatooq & Ojaimi, (2014); Sangsefidi et al., (2018);Ghaderi, Abbasi, et al., (2020); Alfatlawi & Shlaash, (2021)). Side weirs of various shapes and sizes are shown in Figure 1.1.

A free surface vortex is a typical hydraulic phenomenon in hydraulic engineering structures its extending into the side weir might cause significant problems, such as decreasing the discharge capacity of the weir, decreasing hydraulic unit performance and drainage capacity, increasing the flow fluctuation, and causing scouring (Abbasi et al., 2020). The importance of preventing the effects of the free surface vortex is necessary because it is important to realize that the flow through the labyrinth side weirs is related to vortex generation, which is more effective in labyrinth side weirs (for different Froude numbers), hence decreasing the performance of the labyrinth weir (Emiroglu et al. (2017); Abbasi et al. (2020)). The installation of antivortex structures and increasing the hydraulic performance of the stepped weir can be considered basic techniques for vortex prevention.

The flow direction changes from the main flume and enters the labyrinth weir. This change causes vortex formation and water surface level to fluctuate along the opening length of the stepped labyrinth side weir. At the end of the labyrinth weir, there is a sudden height increase along the folding length (weir crest). The collision at the weir crest height causes the returning flow created by lateral flow (Emiroglu & Kaya, 2011) or a slight jump in the flow, leading to the formation of a separation zone and reversing flow area, which takes place along the labyrinth weir as shown in Figure 1.2. The present study investigates the effect of the geometric and hydraulic parameters of antivortex structures installed in the stepped labyrinth side weir on discharge capacity considering four different shapes and weir heights. The study is organized as follows: First, the stepped weir models are investigated experimentally, corresponding to discharge capacity and hydraulic characteristics of the main flume and the weir cross-section with subcritical and steady state flow conditions for free overfall to allow comparison. Second, the antivortex structures are installed in stepped weirs to investigate the efficiency of the weir in different hydraulic and geometric characteristics of the models studied. Computational fluid dynamics (CFD) is a subject of fluid mechanics that solves and analyses fluid flow issues using numerical analysis and algorithms. Consequently, Flow 3D version 11.2 is an advanced numerical simulation software used to simulate the experimental models and ensure that the results matched to ensure the examined phenomena' validity. With this powerful instrument, experimental data can be broadened to enable subsequent investigations that would otherwise be impossible to conduct experimentally.

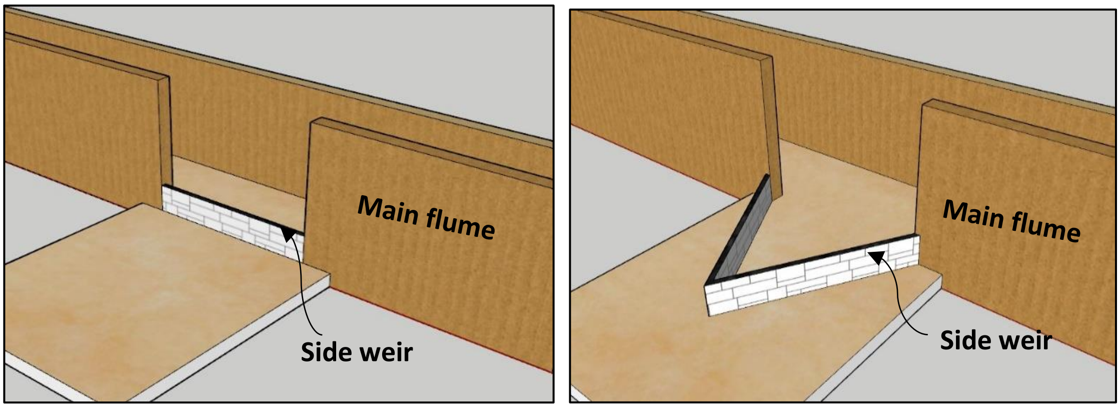

A-Rectangular linear side B-Triangular LSW

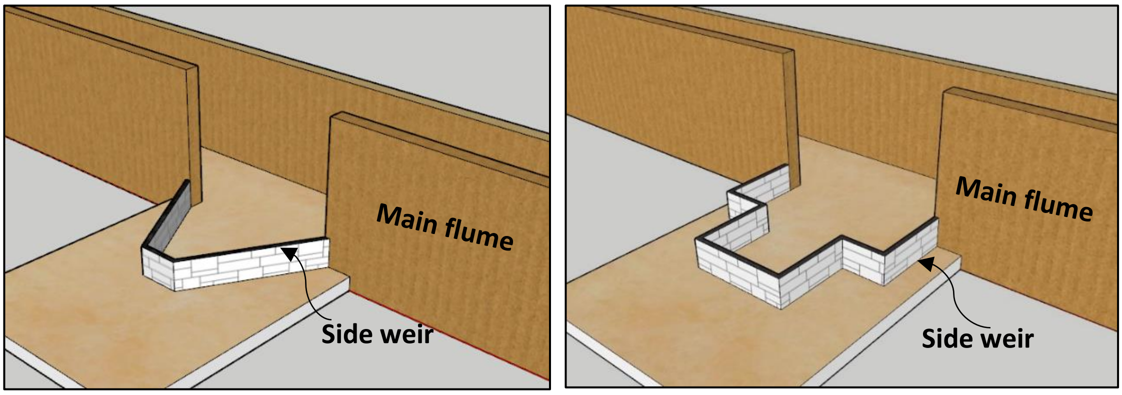

C-Trapezoidal LSW D-Stepped LSW

Figure 1.1: Samples of linear and labyrinth side weirs cross-section.

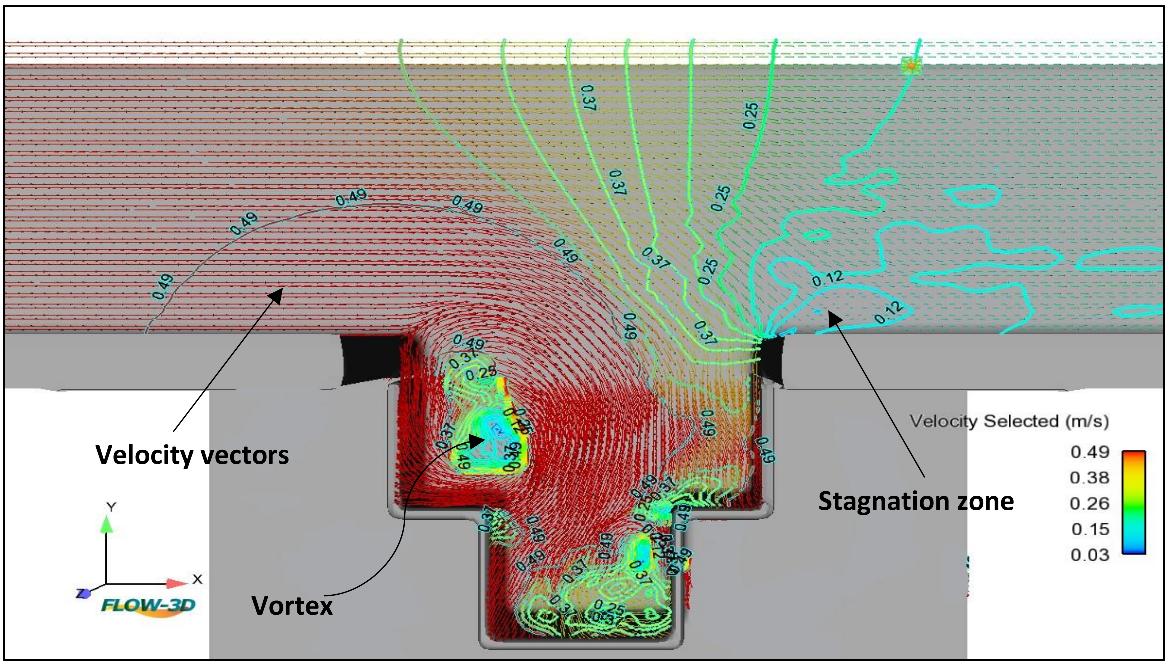

Figure 1.2: Velocity distribution represented by contour lines and flow velocity vectors through the main flume and SLSW (present study).

1.2 Aim of the Study

This study aims to increase the discharge capacity of SLSW. The objectives required to attain the aim can be summarized as follow:

1- Investigating the hydraulic characteristics at which vortices would form at the side weir cross-section.

2- Comparing the hydraulic performance of the stepped labyrinth weir with and without antivortex structures to determine the efficiency of the anti-vortex models in improving the performance of the stepped weir.

3-Studying the hydraulic characteristics in SLSW cross-section using Flow 3D software to inform the user about the software efficiency when employed as a solver for analyzing the hydraulic conditions that cause vortices.

4- Predicting the most efficient shape and dimensions of the antivortex structure by using Flow 3D software.

1.3 Assumptions and Limitations of the Study

1. The longitudinal slope of the laboratory flume is zero (horizontal) and is assumed to be neglected.
2. Subcritical flow along the side weir opening and free flow conditions over the side weir with a sharp edge and proper nappe aeration.
3. Viscosity and surface tension effect are neglected due to the free surface open channel flow situation where gravity is predominated.
4. The number of steps (N) are 4, 8 and 10.
5. Head angle $\theta^{\circ}=45$, $\theta^{\circ}=60$.
6. Four types of antivortex.
7. Weir length ratio L/B=1 and 1.5.

1.4 Methodology

The current study plan has been arranged in Figures 1.3a and 1.3b.

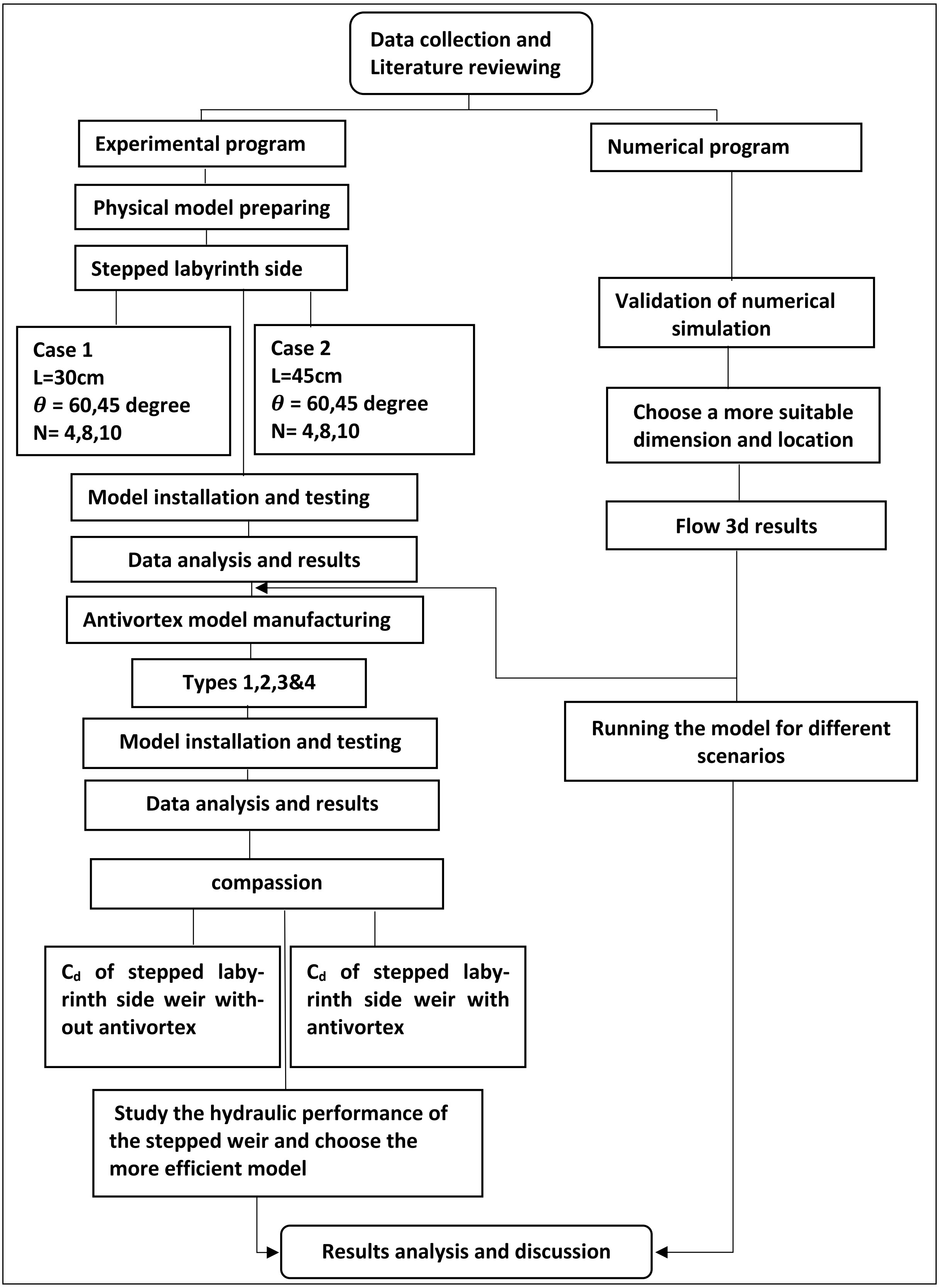

Figure 1.3a: Experimental study methodology.

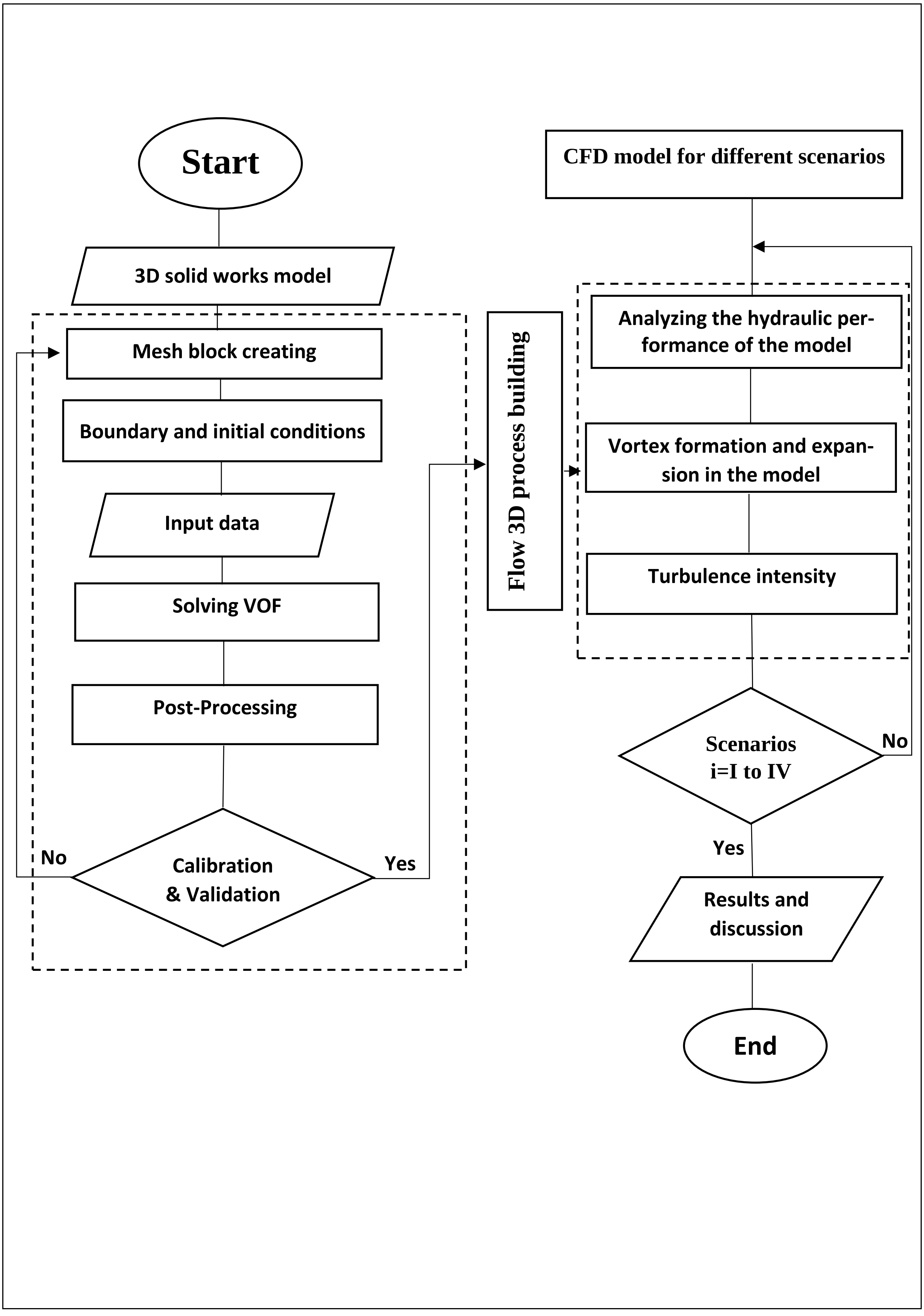

Figure 1.3b: Numerical study methodology.

Chapter Two

Basic Concepts and Literature Review

2.1 General Overview

The first technical experimental studies on concentrated vortex flows are conducted in 1938 (Binnie, 1938). Swirling flows have been observed to be problematic in a wide range of hydraulic structures with various geometrical designs. Therefore, to prevent the effects of vortex formation and turbulence flow, investigations are conducted on installing antivortex structures in different types and hydraulic characteristics in the labyrinth weir. The results indicated basic properties of the parameters that influence the hydraulic behaviour and discharge coefficient of side weirs and the effect of vortex formation. This chapter collects and presents an investigation of these previous experimental investigations, highlighting essential conclusions on the effect of a vortex approach flow on the performance of the side weir.

2.2 The Hydraulic Behaviour of Side Weirs

Weirs are often installed perpendicular to the main channel's flow direction. The essential elements in defining a weir's capacity are its height compared to the upstream depth, crest shape, and crest length. In this context, capacity refers to the flow rate or discharge for a particular depth of flow over the weir's crest. Among these parameters, the crest length has the most significant effect on the discharge capacity. By folding the weir's crest into many parts, the crest length can be extended while keeping the downstream dimension minimal. The duckbill spillway is one example of this concept in action (Falvey, 2003). A Labyrinth weir is an overflow weir that has been folded in plan view to produce a longer total effective length for a given weir width. The entire length of a labyrinth weir is usually three to five times the width of the weir. As a result, using these labyrinth side weirs, there is more open space in front of the side weir for water flow and possibly more lateral movement of water over the weir. The 'useful length' of the weir (d) for water flowing over it rises without increasing the flume's width. Thus, the flow conditions differ from traditional weirs, where the flow is three-dimensional and more complex. Its capacity varies with head, but it is often twice that of a regular weir or overflow crest of the same width (Borghei et al. (1999); Tullis et al. (1995)). See Figure 2.1.

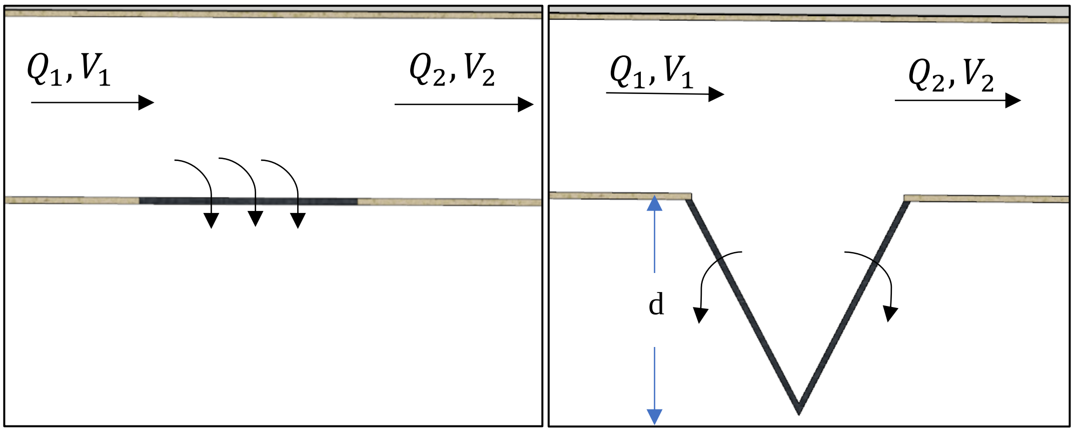

a-linear weir b-triangular LSW (Emiroglu et al., 2011).

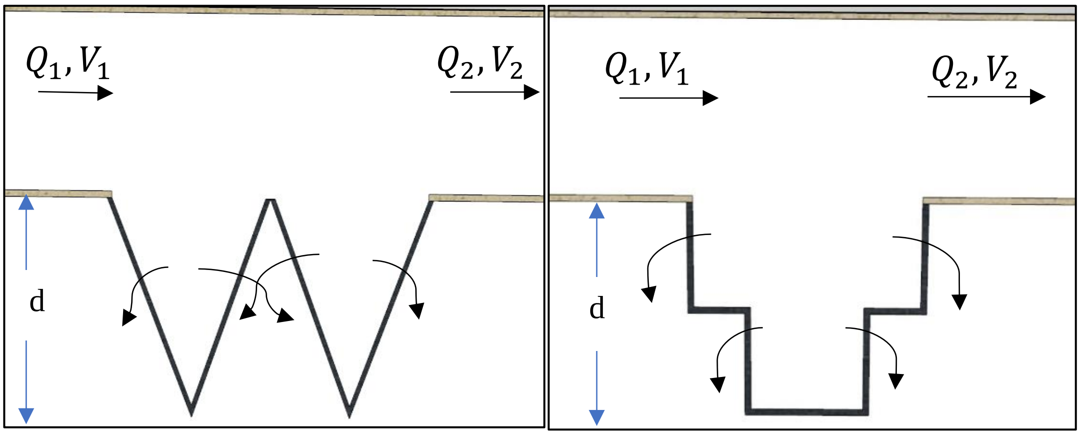

c-LSW with2 cycles (Khameneh et al., 2014). d-SLSW (Alfatlawi & Shlaash, 2021).

Figure2.1: Cross sections of linear and labyrinth side weir.

2.2 Side Weir Discharge Capacity

As previously stated, flow over side weirs is complicated and differs from traditional weirs. Many assumptions are made to use one-dimensional solutions for spatially variable flow, and One-dimensional flow solutions have two variations depending on the method: energy or momentum in the main channel (May, 2003).

The flow over the side weir is classified as a spatially varied flow. Existing studies of side weir flow are primarily concerned with applying the energy concept (De Marchi, 1934). The energy principle means that the longitudinal component of the velocity vector of spill flow at any point in the channel equals the average flow velocity. As a result, apart from frictional losses, the total energy per unit mass of water remaining in the channel is unaffected by the spill flow.

The flow's total energy in the main channel is constant. When investigating the flow characteristics of these weirs, the idea of constant specific energy is frequently used for example (Ranga Raju et al. (1979); Hager (1987); Singh et al. (1994);Borghei et al. (1999)). Table 2.1 displays the rectangular side weir equations found in the literature. Emiroglu et al. (2011) revealed enough coherence among all these equations, basing the differences on experimental data and the methodologies employed to determine the discharge coefficient.

De Marchi's approach has frequently been used in the literature to estimate discharge coefficients, although Schmidt, (1954) provided a more practical approach to computing discharge coefficients. Emiroglu & Ikinciogullari, (2016) and Ikinciogullari & Emiroglu (2019) conducted that the Schmidt method was found to be a dependable approach for estimating discharge capacity, and hydraulic designers can use it confidently for this purpose. There are several methods for determining the discharge capacity of side weirs, including the De Marchi method, the Schmidt method, and the Dominguez method. These approaches are described below:

Table2.1: Available rectangular side weir discharge coefficient equations in the literature for straight channels.

NO.	Discharge equation	Reference
1	$C_d = 0.432\left(\frac{2-\mathrm{F}_1^2}{2+2\mathrm{F}_1^2}\right)^{0.5}$	(Nadesamoorthy& Thomson, 1972)
2	$C_d = 0.8641\left(\frac{1-\mathrm{F}_1^2}{2+\mathrm{F}_1^2}\right)^{0.5}$	(Subramanya & Awasthy, 1972)
3	$C_d = 0.623 - 0.222\mathrm{F}_1$	(Yu-Tek, 1972)
4	$C_d = 0.81 - 0.6\mathrm{F}_1$	(Ranga Raju et al., 1979)
5	$C_d = 0.485\left(\frac{2+\mathrm{F}_1^2}{2+3\mathrm{F}_1^2}\right)^{0.5}$	(Hager, 1987)
6	$C_d = 0.45 - 0.221\mathrm{F}_1^2$	(Cheong, 1991)
7	$C_d = 0.33 - 0.18F_1 + 0.49\left(\frac{p}{h_1}\right)$	(Singh et al., 1994)
8	$C_d = 0.71 - 0.41F_1 - 0.22\left(\frac{p}{h_1}\right)$	(Jalili & Borghei, 1996)
9	$C_d = 0.7 - 0.48\mathrm{F}_1 - 0.3\left(\frac{p}{h_1}\right) + 0.06\frac{L}{B}$	(Borghei et al., 1999)
10	$C_d = 1.06\left[\left(\frac{14.14p}{8.15p+h_1}\right)^{10} + \left(\frac{h_1}{h_1+p}\right)^{15}\right]^{-0.1}$	(Swamee et al., 1994)
11	$C_d = \left[0.836\left(\begin{matrix}-0.035 + 0.39\left(\frac{p}{h_1}\right)^{12.69} + 0.158\left(\frac{L}{B}\right)^{0.59} \\ +0.049\left(\frac{L}{h_1}\right)^{0.42} + 0.244\mathrm{F}_1^{2.125}\end{matrix}\right]^{3.018}\right]^{5.36}$	(Emiroglu et al., 2011)
12	$C_d = 0.265(F_1)^{-0.404}(h_1/L)^{-0.115}(h_1/p)^{0.134}(L/B)^{-0.086}$	(Bagheri et al., 2014)

2.2.1 De Marchi Approach

De Marchi is the first scientist who give an analytical solution for predicting the water surface profile along a rectangular side weir with rectangular cross-sections in an open canal and show how to solve the water surface differential equation for side weirs. This solution made a significant contribution to the problem. The basis for this solution is the constant weir coefficient, velocity distribution coefficient, and specific energy along the side weir. De Marchi (1934) presented a method to resolve water surface differential equation for side weirs.

The following equation is assumed for the discharge over the side weir per unit length, q:

$$q = -\frac{dQ}{ds} = \frac{2}{3} C_d \sqrt{2g} [y - p]^{3/2} \qquad 2.1$$

De Marchi solve the partial differential equation of the side weir's spatially variable flow analytically under the assumption that the specific energy of the flow in the main channel is constant over the length of the side weir. The following equation is the outcome:

$$C_d = \frac{3}{2} \frac{B}{L} (\Phi_2 - \Phi_1) \qquad 2.2$$

In which, L is the side weir opening, B is the channel width, and C_d is the discharge coefficient. Based on Eq. (2.2), De Marchi investigated a correlation between C_d, canal width, side weir length, and Φ. Here, Φ_1 and Φ_2 reflect immediate side weir upstream and downstream (varied flow function), respectively. C_d must be found experimentally. Eq. (2.3) could be utilized to calculate Φi, and Eq. (2.4) could be used to determine the flow rate.

$$\Phi_i = \frac{2E_i - 3p}{E_i - p} \sqrt{\frac{E_i - y_i}{y_i - p}} - 3 sin^{-1} \left(\sqrt{\frac{E_i - y_i}{E_i - p}} \right) \qquad 2.3$$

$$Q_w = \frac{2}{3} C_d \sqrt{2g}\, L [y_1 - p]^{3/2} \qquad 2.4$$

In which Q_w is the side weir discharge (m^3/s), E is the specific energy, y is the main flow depth, L is the opening length of the side weir, B is the width of the canal, p is the crest height and g is the acceleration of gravity.

Thus, the discharge within the main channel at the downstream end of the side weir can be written as:

$$Q_2 = Q_1 - Q_w$$

Where Q_2 is the discharge within the main channel at the downstream end of the side weir and Q_1 is the total discharge within the main channel at the upstream end of the side weir.

2.2.2 Schmidt Approach

Schmidt, (1954) calculates the side weir's discharge capacity in a subcritical flow regime. Figure 2.2, displays the specific energy variation. Schematic representation of the specific energy equation along the side weir is determined using Figure 2.2, as given in equations:

$$\mathrm{S_0L} + y_1 + \alpha_1 \frac{\mathrm{V_1^2}}{\mathrm{2g}} = y_2 + \alpha_2 \frac{\mathrm{V_2^2}}{\mathrm{2g}} + \Delta\mathrm{h_s} \qquad 2.4$$

$$\mathrm{S_0L} + \mathrm{p} + \mathrm{h_1} + \alpha_1 \frac{\mathrm{V_1^2}}{\mathrm{2g}} = \mathrm{h_3} + \mathrm{p} + \alpha_2 \frac{\mathrm{V_2^2}}{\mathrm{2g}} + \Delta\mathrm{h_s} \qquad 2.5$$

$$\mathrm{h_1} = \mathrm{h_3} + \alpha_2 \frac{\mathrm{V_2^2}}{\mathrm{2g}} - S_0L - \alpha_1 \frac{V_1^2}{2g} + \Delta\mathrm{h_s} \qquad 2.6$$

where, S_0 is the slope of the canal, h_1 and h_3 are the nappe heights upstream and downstream of the side weir, Δhs is the friction loss, and V_1 and V_2 are the mean velocities upstream and downstream of the side weir, respectively. The Manning-Strickler formula could be used to determine $\Delta\mathrm{h_s}$ as $\Delta\mathrm{h_s} = S_EL$. Schmidt recognizes that the energy grade line and channel slope are nearly equivalent in this approach ($S_EL \cong S_0L$). The channel slope is extremely small ($\sin\theta \cong \tan\theta = S_0$). As a result, it is acceptable that the specific energy is constant along the side weir, as in other approaches. According to Emiroglu & Ikinciogullari, (2016), considering nappe heights at two points, as Schmidt suggests, is sufficient to produce correct results. The Schmidt method can be used to approximate discharge coefficients without having to compute ξ.

According to Emiroglu et al. (2011), for the De Marchi equation used, the specific energy variation between the upstream and downstream ends should be negligible (<4%). Emiroglu et al., (2017) estimated the mean difference between E_1 and E_2 of a 0.8% value for subcritical flow. Thus, Checking the subcritical flow assumption of constant energy is necessary to apply the Schmidt equation. Nearly all values are found to converge to the trend line (Figure 2.3). Between E_1 and E_2, there is an average difference (<4%). Thus, the concept of constant energy is accepted for more analysis, and the discharge coefficient is calculated using the Schmidt method without energy losses.

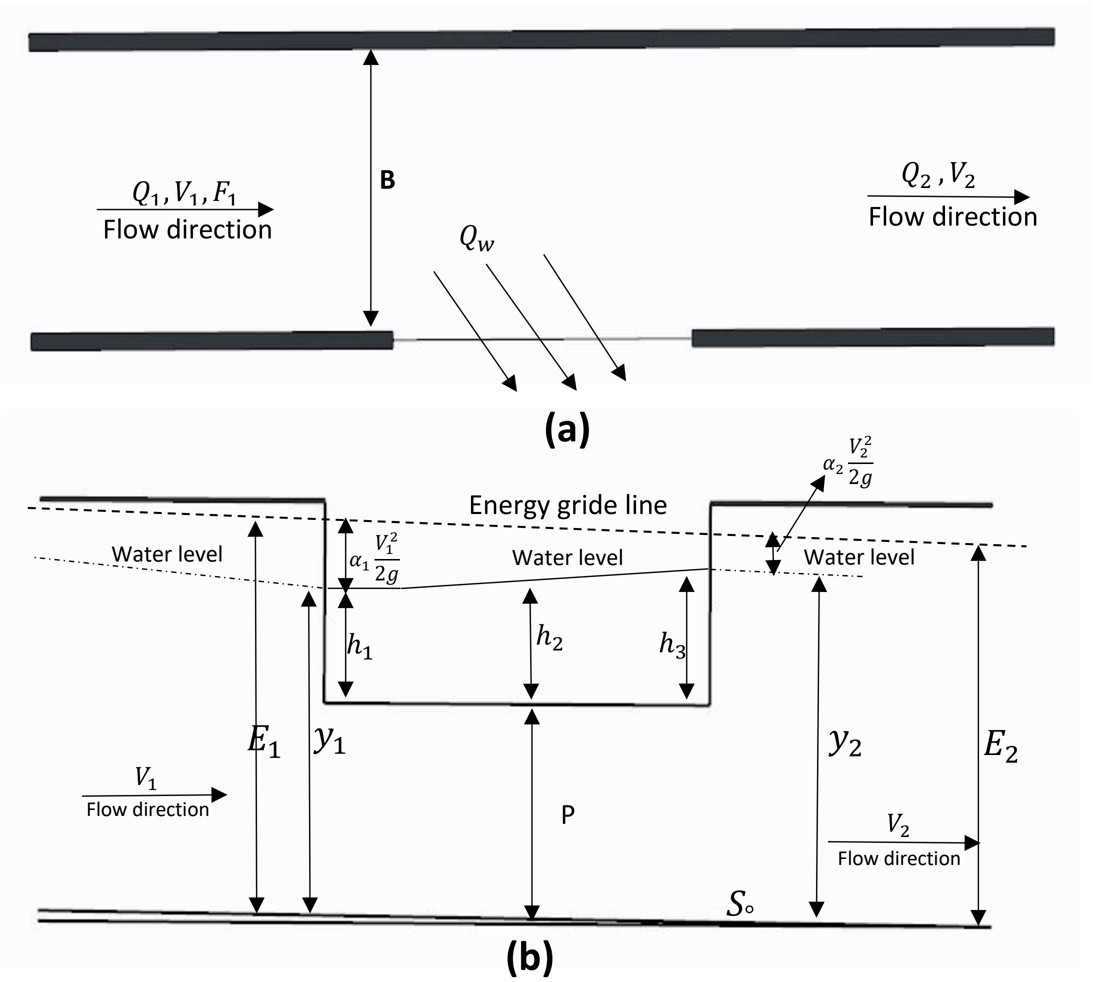

Figure2.2: (a) Definition of a classical side weir in plan;(b)Variation of specific energy and water surface profile along a side weir (Emiroglu & Ikinciogullari, 2016).

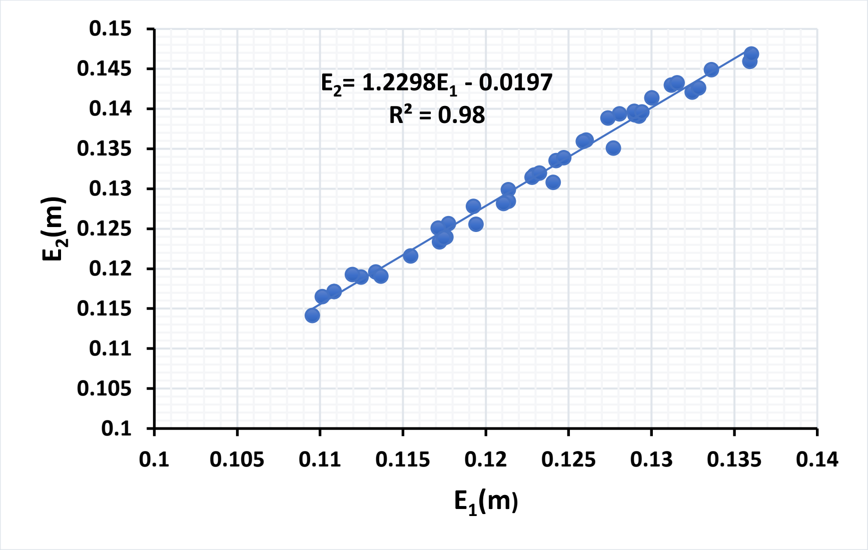

Figure 2.3: Variation in specific energy of the flow at the upstream and downstream ends of the side weir.

2.3 Formation of Vortices in Weirs

The flow over a side weir gradually changes with a reducing discharge. The hydraulic behaviour over a side weir is entirely different from that over a weir normal to the approach channel due to the flow profile and velocity distribution transverse variations. Thus, the main channel's separation zone, the dividing streamline, and the stagnation point at the downstream end of the side weir are all flow components. Many researchers, including (Subramanya & Awasthy, (1972); Fares & Herbertson, (1993); Coşar & Agaccioglu, (2004);Aǵaçcioǵlu & Önen, (2005)), additionally noticed a separating zone and the reverse flow at the side weir's downstream end. These researchers noted that the Froude number at the upstream side of the weir and the length of the side weir affect the location and dimensions of the separation zone and reverse flow area; as the upstream Froude number rises, the separation zone and reverse flow area shift toward the side weirs downstream end (Coşar & Agaccioglu, 2004). As a result, the flow entering the side weir causes vortices. The influence of secondary flow caused by lateral flow close to the downstream end of the side weir has been used to explain the water surface level. Despite subcritical flow conditions in the latter third of the weir section, the secondary flow generated by the lateral flow significantly disturbs the water's surface and causes vortices. Numerical models are currently practical tools for engineers. It can circumvent the time-consuming and expensive experimental experiments based on physical models using a fully validated numerical model to determine the characteristics of flows formed in hydraulic structures, as shown in Figure 2.4.

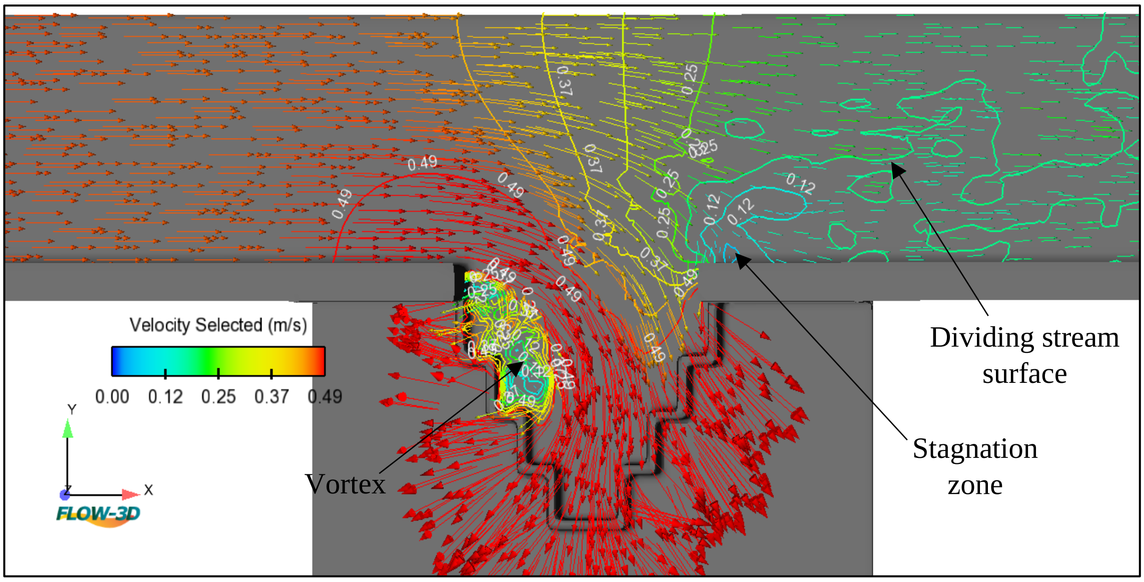

Figure 2.4: Flow over an SLSW in subcritical conditions represented by contour lines and velocity vectors.

2.4 Computational Fluid Dynamic (CFD)

CFD is an acronym for Computational Fluid Dynamics, a mathematical tool that simulates fluid flow problems. The simulation results are then used to investigate the kinematics and thermodynamics of flow particles inside a specific geometry. This would be helpful in recommendations for upgrading the current study and facilities. Appropriate partial differential equations can characterize all flow fields, referred to as government equations. CFD is a method of solving these equations numerically and getting flow variables.

The number of unknown variables, such as pressure, velocity, and temperature, must be defined for each flow field variable (Vyzikas et al., (2017); Yamini et al.,(2022)). For a long time, researchers have been conducting physical model experiments and establishing empirical equations to understand the mechanism of hydraulic features better. With the advancement in computer capacity, numerical models have recently gained popularity in this field. Researchers combined theory and data to create an accurate description of the model.

2.6 Literature Review

Rectangular sharp-crested side weirs have been extensively studied, according to a review of previous studies, involving works by (Subramanya & Awasthy, (1972); Singh et al., (1994); Borghei et al., (1999); Venutelli, (2008)) investigated the sharp-crested side weir discharge coefficient in subcritical flow and created an equation for the sharp-crested rectangular side weir discharge coefficient. Additionally, in order to study how the discharge coefficient changes along side weirs, Aghayari et al., (2009) experimentally studied the influence of side weir height, width, and crest slope on the spatial discharge coefficient across broad-crested inclined side weirs in a rectangular channel with the subcritical flow. Parvaneh & Borghei, (2009) made specific adjustments to raise the effectiveness of the oblique side weir. Their research on an oblique side weir with a changeable geometry showed that obliqueness is a significant element in maximizing its effectiveness and should be considered during design. As a result, a greater effective length improved the weir's orthogonal influence. Emiroglu et al., (2011) conducted an extensive laboratory investigation to study the hydraulic effect of triangular labyrinth side weirs, and they concluded that the discharge coefficient of labyrinth side weirs is considerably greater than that of conventional weirs. The discharge coefficient of such side weirs depends on the upstream

Froude number, main channel slope, weir height, and length. Furthermore, as the Froude Number rises, the water surface profile along the side weir section has a lower elevation at the upstream end of the side weir, then rises toward the downstream end of the side weir to achieve maximum elevation.

Labyrinth weirs have recently been favored over traditional weirs or spillways to improve discharge efficiency. Many attempts are made to increase the efficiency of side weirs. Such as, Emiroglu & Kaya, (2011) studied the discharge characteristics of a trapezoidal labyrinth side weir using a series of tests and providing a nonlinear equation that considers all effective dimensionless parameters with one and two cycles. According to their results, the discharge coefficient of labyrinth side weirs is (1.5–5.0) times greater than that of conventional rectangular side weirs. Khameneh et al., (2014) investigated the effect of increasing the cycle number on the discharge coefficient by folding the crest length into one, two, and four cycles. Their findings can be summarized as the reverse relationship between the cycle number and the discharge coefficient. Gebhardt et al., (2018) conducted an experimental study on the (PKW) to investigate sedimentation at labyrinth weirs. They observed that the flow is accelerated at the structure's upstream face (outlet key), and the flow's vertical velocity gradient is transformed into a pressure gradient, resulting in a downward flow. When the downward flow reaches the bottom, it forms vertical vortices, the ends of which are swept around the corner into the inlet key. This vortex system, also known as a horseshoe vortex, is very effective at transporting sediments. Their findings generally support the self-cleaning ability of labyrinth weirs. The flow is accelerated because of the horizontal narrowing, and the horseshoe-vortex forms, which is very effective in transporting sediments. Denys & Basson, (2018) investigated the transient hydrodynamics of piano key weirs and concluded that the development of a vortex sheet in the inlet key is caused by the formation of a recirculation zone behind a free shear layer at the entrance edge. These vortices form and roll up as they move downstream, eventually being discharged over the PKW's crest.

Karimi et al., (2019) carried out experimental investigations on symmetrical and asymmetrical shapes placed in a rectangular channel with the subcritical flow and compared the hydraulic performance for different orientations by changing the angle of the symmetric; their results revealed that the asymmetric shape has a higher discharge coefficient reach about 50% compared to the symmetric shape. Alfatlawi & Shlaash, (2021) investigated the hydraulic behaviour of stepped labyrinth side weir models located on a straight channel in subcritical conditions, and their findings revealed that the effect of small head angles could be eliminated by folding the crest length into multi-steps, as shown in Figure 2.5 to increase the effective length and crest orthogonality chance with the diverted flow. They also present a prediction equation for the discharge coefficient of the selected models.

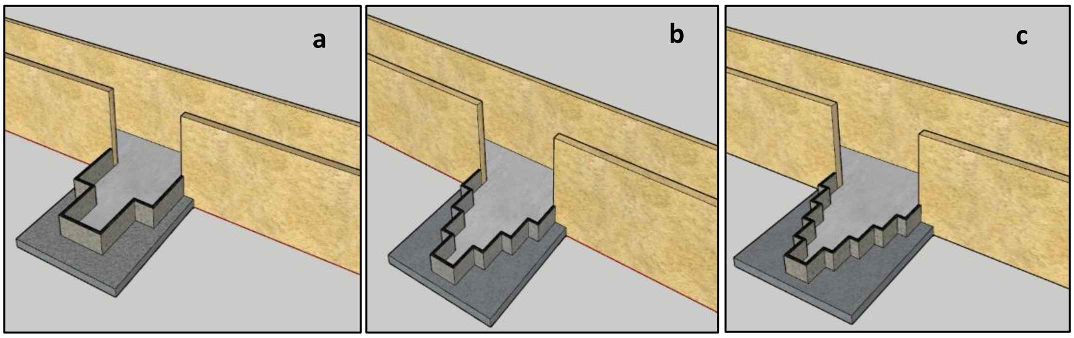

Figure 2.5: Stepped LSW adopted by (Alfatlawi & Shlaash, 2021). (a) N=4 (b) N=8 (c) N=10.

Vortices are commonly used in civil engineering and industrial applications and formed directly via the tangential inlet, guide, and spinning cylinder in most experimental experiments. Flow visualization is achieved through the application of dye. Tracer particles, measuring needles, and a hot-film anemometer are utilized to determine the velocity distribution, free surface form, and vorticity.

Li et al., (2008) analyzed experimental data and numerical results and revealed a satisfactory conclusion. The generation and evolution of the free surface vortex were studied using experimental equipment. Due to the acute changes in the core, the study suggested that the numerical simulation agrees with the practical flow field outside the vortex core. The tangential velocity distribution was found to be similar to observations, while the radial velocity in the vortex functional region was slightly different. At various depths, the vortex core was determined. The numerical model predicted the position and structure of the air core, which agreed with the physical model. (Mulligan, 2015) investigated the velocity field of strong free-surface vortex flows numerically and experimentally. According to a survey of the state of the art, a number of issues surrounding the underlying flow mechanics in these systems demand extra attention. The research focuses on experimental and numerical analysis of the flow problem and analytical studies.

Labyrinth weirs improve discharge for a given upstream head by providing a longer crest length for a waterway width. However, it is essential to remember that the flow passing through the labyrinth side weirs is connected to the vortex formation; as a result, the hydraulic performance of these structures decreases. The vortex occurrence also restricts lateral flows in specific Froude numbers, which reduces the side weirs' capacity to discharge water. The discharge capacity increases When preventing this vortex formation or lowering the possibilities of vortex formation. Many studies improved the hydraulic performance of these labyrinth weirs by installing antivortex structures.

Borghei et al., (2013) investigated triangular LSW with single and double cycles, as shown in Figure 2.6, for different flow variables and weir geometries under subcritical conditions; Vortex formation (for high velocity) and sediment deposition (for low velocity) were observed with the horizontal channel bed in front of the weir. Vertical submerged antivortex plates were utilized in the horizontal apron to avoid vortex formation. As a result, vortex generation in front of the triangular labyrinth side weir would have a small effect on the results. By extending the cycles for the triangular labyrinth side weir from one to two, the vortex effects were reduced.

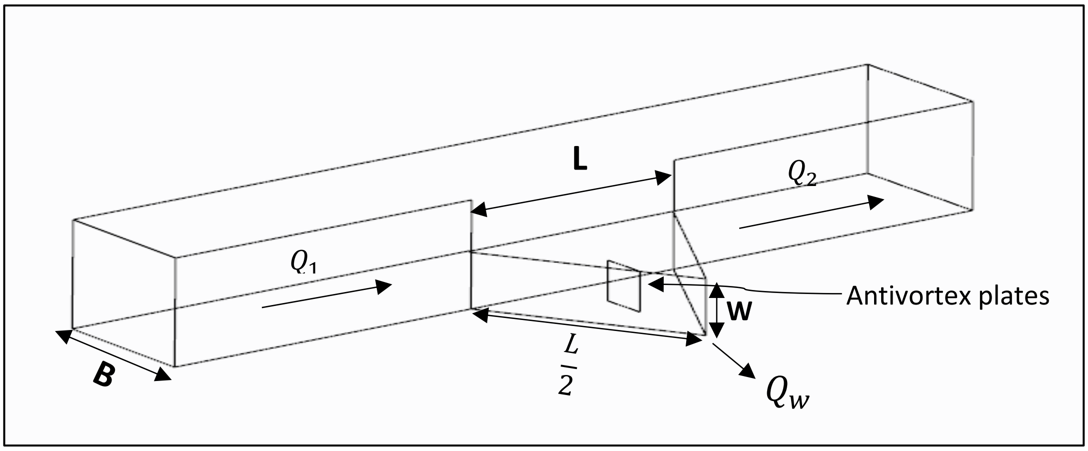

Figure 2.6: Triangular labyrinth side weir case with one cycle adopted by (Borghei et al., 2013).

Khameneh et al., (2014) investigated the effect of raising the cycle number on the discharge coefficient showed that increased flow speed in the labyrinth side weirs creates vortices and eddies, lowering the weir's discharge capacity.

Emiroglu et al., (2017) investigated the influence of antivortex structures placed in trapezoidal labyrinth side weirs on discharge capacity; their conclusions are presented below:

- The discharge capacity of the labyrinth side weir increased with increasing crest length, and a vortex was identified in the labyrinth side weir section.
- The use of antivortex structures improved the discharge capacity of the labyrinth side weirs, especially at high L/B ratios. Figure 2.7
- Among the antivortex structures examined, Type 6 in Figure 2.7 was the

most efficient in decreasing vortices in the trapezoidal labyrinth side weir section.

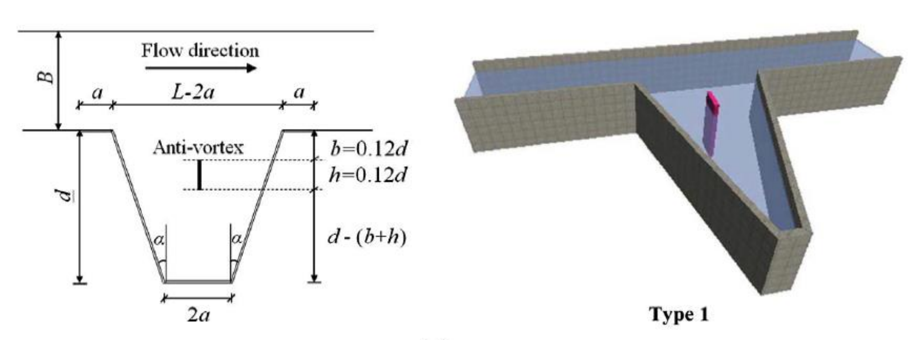

(a)

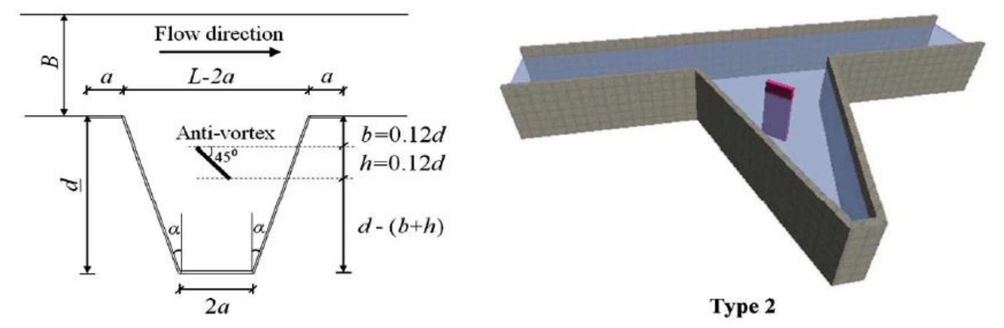

(b)

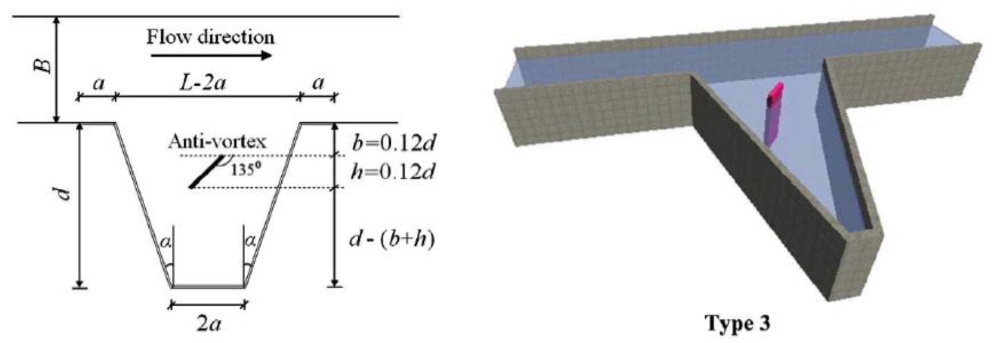

(c)

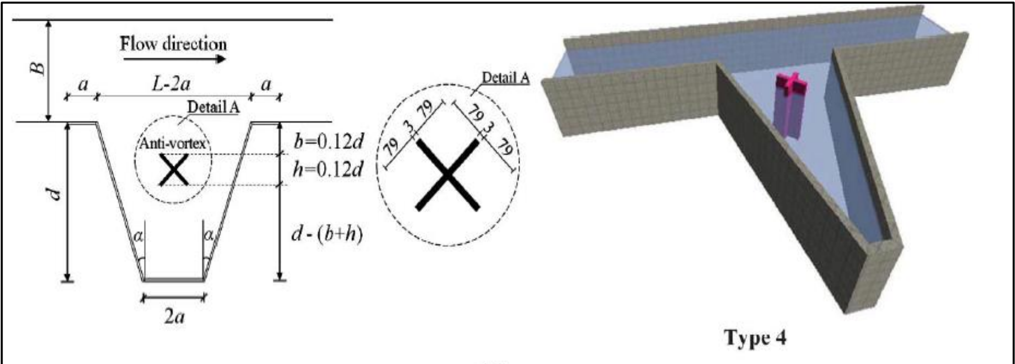

(d)

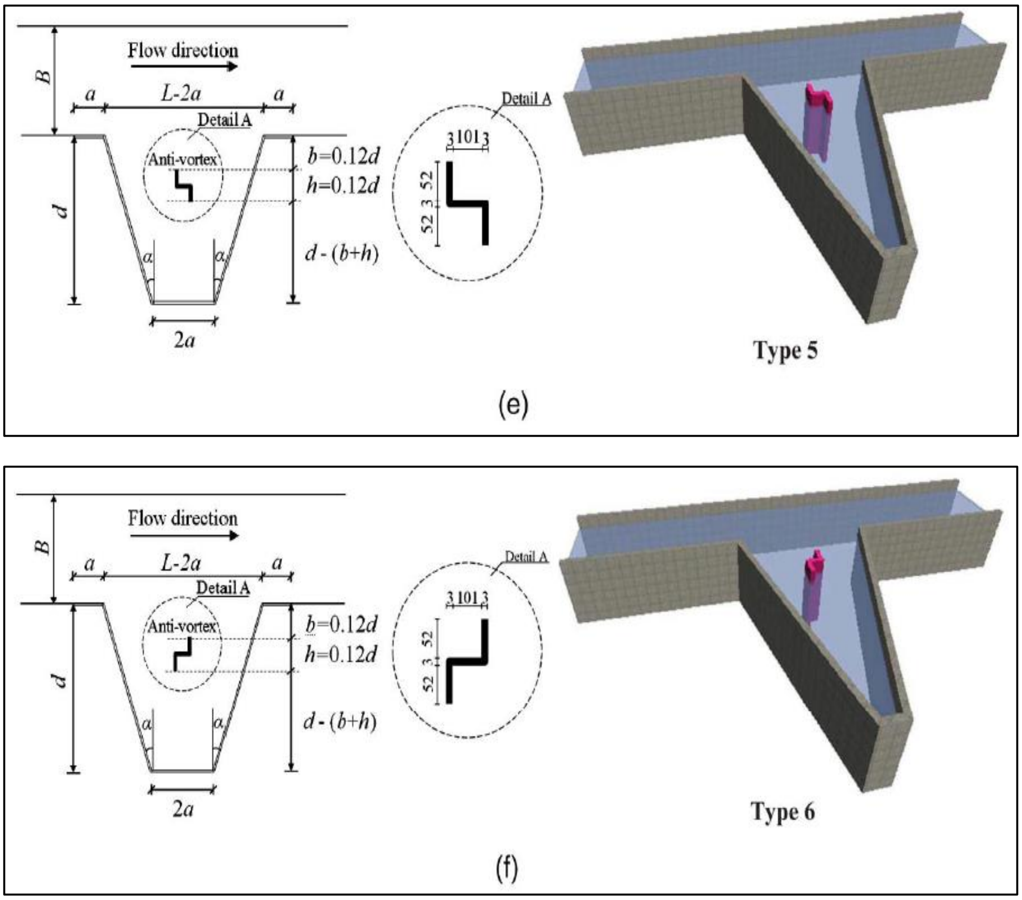

Figure 2.7: Schematic plan for antivortex structures proposed by (Emiroglu et al., 2017).

In addition to these investigations, computational fluid dynamics (CFD) has recently been shown to be particularly important in evaluating these hydraulic structures.(Aydin, 2012) used CFD to examine their side weir models and compared them to experimental data; A Volume of Fluid (VOF) numerical approach was used to simulate free-surface flow across triangular labyrinth side weirs on a straight channel. Fluent software was utilized for the CFD analysis. Their results presented the vortex formation and secondary currents in the labyrinth weir section and their effect on obstructing the discharge; the C_d coefficient reduces as nappe height increases (increases in F_1) due to secondary flow effects inside the labyrinth side weir. The CFD results were consistent with the experiments (see Figure 2.8).

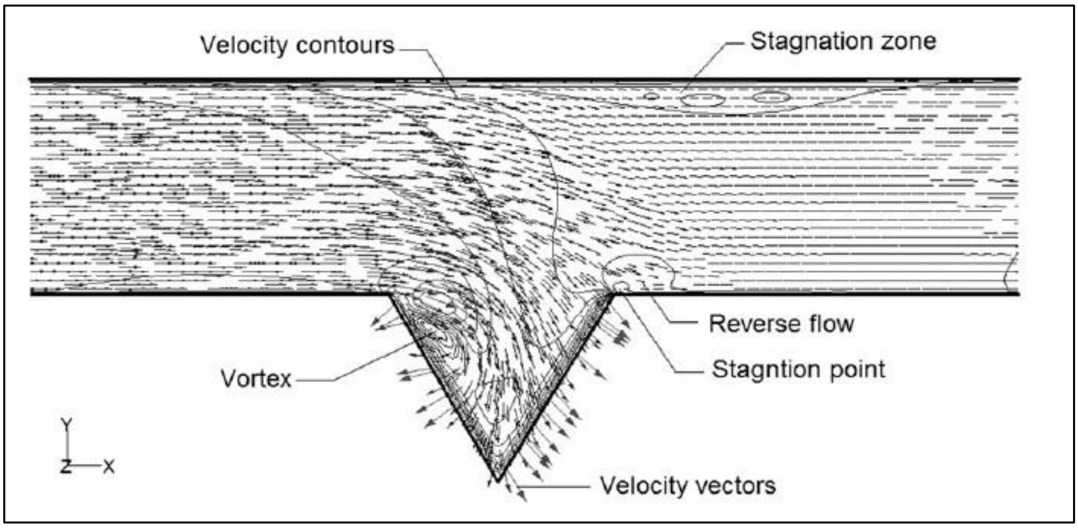

Figure 2.8: Velocity vectors on the free surface at junction location at XY-plan (Aydin, 2012).

(Azimi et al., 2016) employed the RNG turbulence model and the volume of fluid (VOF) approach to obtain the discharge coefficient relationship and specific energy variation for the circular channel under supercritical circumstances. (Aydin & Ulu, 2017) used computational fluid dynamics (CFD) software to conducted a series of numerical simulations to prevent vortices in the cycles; some antivortex elements were used in the cycles of the two-cycle labyrinth side weir. The numerical findings of the two-cycle labyrinth side weir with the antivortex were compared to the one without antivortex and some experimental observations. Their results can be summarized as indicated below:

- The use of antivortex decreases oscillations on the water's surface and the generation of vortices. Water surface fluctuations are strong at $0.40 < F1 < 0.60$, and antivortex utilization is effective against the fluctuations in this range.

- It can be used in all Froude numbers for subcritical flows, although it is more efficient when the Froude number is more significant than 0.40.

- In these weirs, the installation of antivortex improved the discharge coefficient by 16% on average.

- Based on the experimental and numerical data the average side weir discharge was also raised by 26%.

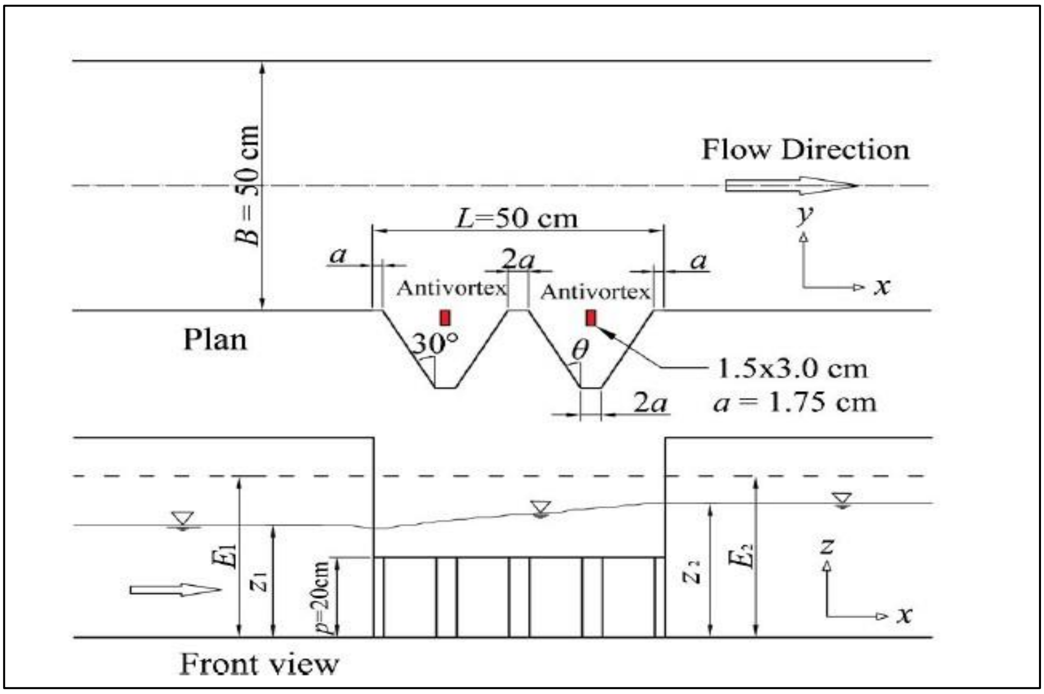

Figure 2.9: Plan and front view of the trapezoidal labyrinth side weir with antivortex (Aydin & Ulu, 2017).

(Ziaei et al., 2019) investigated the VOF tracking method to study flow across a triangular weir with three angles (θ= 45°, 60°, and 90°). Using two equations, compare experimental data to boundary conditions, modified geometric dimensions, and turbulence models to simulate depth profile data and overflows. The simulated water depth profile exhibited a root mean square error of less than 1 mm, according to their findings. The relative inaccuracy of this water diversion is less than 0.7 percent. For = 45°, 60°, and 90°, respectively, 1.7, 1.33, and 1.25 times the discharge of an equal normal side weir.(Ghaderi & Abbasi, 2019) attempted to improve the hydraulic performance of labyrinth weirs by notching the weir wall and inclining the crest edge. The RNG k-ε model was adopted in the Flow 3D software to simulate the free flow surface. The results indicate that the maximum relative error is 4.8%, which confirms that the numerical model is reasonably good for predicting flow over the labyrinth weir.

Ansari & Patil, (2022) used (CFD) to examine the influence of non-dimensional parameters obtained from dimensional analysis of triangular labyrinth side weirs in the triangular straight main channel, which are Froude number, dimensionless crest height h/p, L/l, included angle θ. They introduce an empirical equation considering all parameters for the coefficient of discharge. The generated equation was validated using experimental results, and there was good agreement between CFD and experimental results.

(Abbasi et al., 2020) investigated the hydraulic performance of triangular LSW by using CFD. The RNG k-ε model was adopted in the Flow3D software to simulate varying hydraulic conditions and Froude numbers; the triangular labyrinth side weir tested six antivortices installed inside it. Compared to a normal labyrinth side weir, they establish the best form, permeability, and height of the antivortex, and the discharge coefficient rises to (13.4%). (see Figure 2.10).

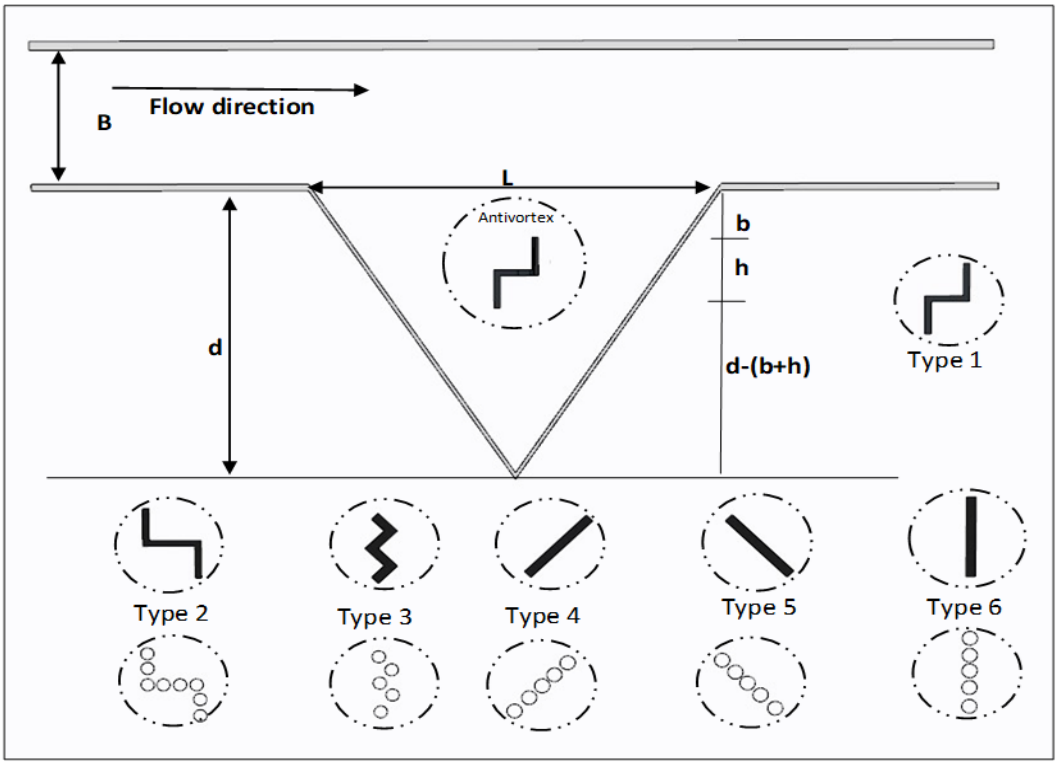

Figure 2.10: Geometric characteristics and location of permeable and impermeable antivortex (Abbasi et al., 2020).

In recent decades, researchers such as (Bombardelli et al., 2011); Aydin & Ulu, (2017); Wang et al., (2018); Ghaderi, Daneshfaraz, et al., (2020); Ghaderi, Abbasi, et al., (2020)) employed CFD in their civil and mechanical engineering studies. The comparison of simulated and experimental results provides confidence for the modelling of additional hydraulic structures using CFD.

2.7 Current Study Contribution

According to the previous literature review, some of these studies focused on modifying weir cross-section geometries to improve the discharge coefficient of a labyrinth side weir. Some approaches concentrated on preventing vortex formation by installing different antivortex structures in the labyrinth side weir section. However, it is significant to mention that the flow through the labyrinth side weirs is related to the generation of vortices for various Froude numbers, which is more productive in labyrinth side weirs. When vortex formation prevents or the dangers of vortex formation decreases, the discharge capacity increases; Thus, this study investigates the effect of geometric and hydraulic antivortex structures on discharge capacity in a stepped labyrinth side weir. Therefore, using these new devices in four shapes for different weir heights improves the labyrinth side weir performance in hydraulics. In addition, the current study uses the CFD technique to explore the effect of geometric and hydraulic characteristics of antivortex parameters. However, a numerical approach to developing an adequately validated model can be advantageous in studying and characterizing fluid properties. As a result, this study used laboratory experiments to analyze the flow characteristics of a stepped labyrinth side weir. The hydraulic performance of the antivortex within stepped labyrinth side weir was also investigated and then validated numerically using Flow 3D.

Chapter Three

Experimental Work

3.1 General Overview

This chapter will provide an overview of the experimental methodology undertaken in the project to address the problems and gaps in the current literature. The initial consideration for dimensional analysis is made as well as the design of the physical models and experimental work procedure, laboratory flume description, and labyrinth side weir (LSW) model description. The experimental approach based on the physical models is employed to investigate the hydraulic characteristics of the flow field. The laboratory work program is implemented in the Fluid Mechanics Laboratory of the Civil department at the College of Engineering of Babylon University.

3.2. Dimensional Analysis

Dimensional analysis is a technique frequently used in experimental research to identify the most important governing factors in a physical investigation. Dividing the total number of known and unknown dimensional variables into a smaller number of dimensionless Π-groups helps to simplify the experimental procedure. Previous studies such as (Crookston & Tullis, 2010) have identified the following parameters influencing the performance of Labyrinth weirs:

- Geometric parameters of labyrinth weirs, including width, crest length, and weir upstream crest elevation (measured from the upstream floor).

- Structural characteristics such as crest shape, weir aprons, and wall thickness.

- Operational parameters, such as the overall hydraulic load, the stages of weir aeration, and submersion.
- Upstream conditions such as weir inlet conditions, the design of training walls, the presence of an upstream gradient, etc.
- Downstream conditions include crest elevation, water depth, downstream gradient, etc.

The following flow parameters were investigated as part of the overall experimental program concerning Figures 3.1:

- General Hydraulic Variables: Upstream flow depth y1
- Dependent hydraulic parameters F_1, $\frac{P}{y_1}$, θ, $\frac{L}{B}$, N as a function for the flow geometry.
- Distribution of the water surface profiles.
- Distribution of the velocities in the flume
- A visual investigation of the turbulence and secondary flow fields.

3.2.1 Functional relationship

The following categories describe the characteristics that influence the hydraulic and flow conditions through LSW:

A-Geometric properties

Figure 3.1(a and b) shows the geometric shape parameters of the studied models as a definition sketch of the SLSW model located on the main flume.

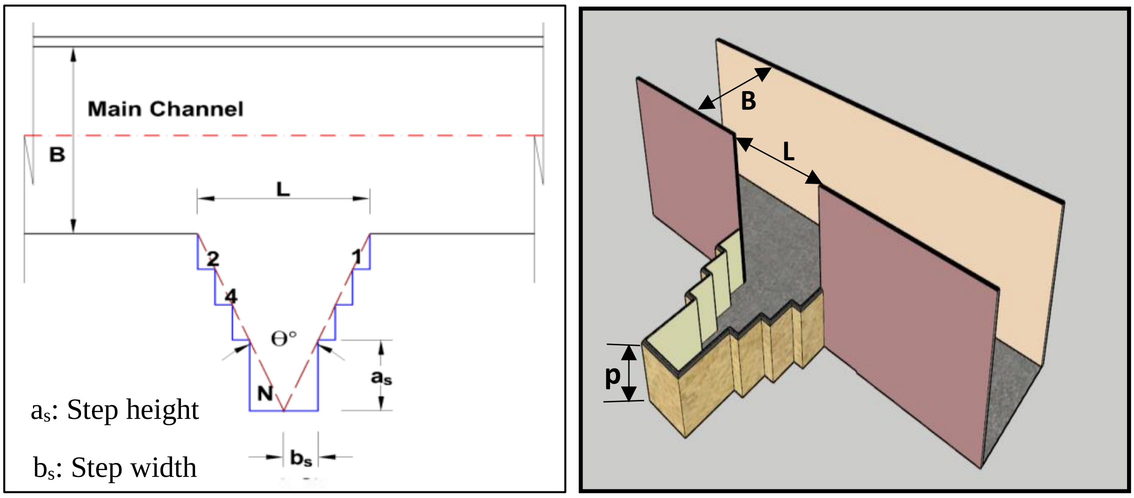

(a) (b)

Figure 3.1: Definition sketch of SLSW geometry (Alfatlawi & Shlaash, (2021))

Where:

L: Side weir opening length (L)

B: Main flume width (L)

N: Steps number (-)

θ: Internal angle (degree)

P: LSW crest height (L)

y1: Flow depth at the upstream end of side weir at main flume center (L)

B-Flow properties

v1: Main flume upstream velocity of flow (LT^{-1})

Cd: Discharge coefficient (-)

C- Fluid properties

ρ: Mass density of flowing water (ML^{-3})

μ: Dynamic viscosity of water ($ML^{-1}T^{-1}$)

g: Acceleration due to gravity (LT^{-2})

However, the following dimensional analysis will be provided with the discharge coefficient as a dependent parameter. The Buckingham theorem (Buckingham, 1915) is used by taking ρ, g, and y_1 as repeating variables. This parameter governs the following relationship as a function of the other influential geometric, flow, and fluid parameters.

$$C_d = f\,(V_1, L, B, p, y_1, \theta, \rho, g, \mu, \sigma, N) \qquad 3.1$$

Applying Buckingham Pi-Theorem by taking, Equation (3.1) can be re-written as:

$$\pi 1 = f\,(\pi 2, \pi 3, \pi 4, \pi 5, \pi 6, \pi 7, \pi 8, \pi 9) \qquad 3.2$$

$$C_d = (F_1, Re, We, \frac{P}{y_1}, \theta, \frac{L}{y_1}, \frac{B}{y_1}, N) \qquad 3.3$$

where F_1, Re, and We represent upstream Froude number, upstream Reynolds number, and upstream Weber number, respectively. In a fully turbulent flow, the influence of viscosity is small and could be ignored in comparison to the gravity effect (Henderson, 1966). therefore, the Reynolds number has an insignificant influence on the dependent variable (Kabiri-Samani et al., 2011). Furthermore, surface tension has no effect if the head above the weir crest is greater than 30 mm (Novák & Čabelka, 1981). Hence Equation 3.3 is simplified to:

$$C_d = (F_1, \frac{P}{y_1}, \theta, \frac{L}{B}, N) \qquad 3.4$$

The physical relevance of the parameters in the preceding equation can be illustrated as follows:

C_d: is a dimensionless parameter representing the labyrinth weir's discharge coefficient (dependent parameter).

$\frac{P}{y_1}$: the height of the weir crest with the flow depth at an upstream end of a side weir measured in the center of the main flume.

θ: the variation of internal angle between two tangents for the inner point of intersection of step sides.

$\frac{L}{B}$**:** the opening length of the weir to the main flume width.

N: the number of steps.

Four types of antivortex structures are used in this study to improve the performance of the stepped labyrinth side weirs. Various configurations of these structures are investigated, and the effect of raising the capacity of the labyrinth side weir is determined. The antivortex types, locations, and sizes would have a substantial effect on the weir discharge coefficient and should be considered in the corresponding Equation:

$$C_d = (F_1, \frac{P}{y_1}, \theta, \frac{L}{B}, N, \frac{x}{L}, \frac{y}{d}) \qquad 3.5$$

where:

$\frac{x}{L}$ **:** the longitudinal position of the antivortex along the opening length of the weir.

$\frac{y}{d}$ **:** the lateral position of the antivortex structure along the length of the weir.

3.3. Experimental Equipment

3.3.1. Description of Experimental Flume

Labyrinth side weir experiments are conducted at the Hydraulic Laboratory of Babylon University. Figure 3.2(a, b) and Figure 3.3c shows the laboratory flume and the labyrinth weir physical model.

In this study, laboratory prototypes of the weirs are examined in a rectangular free-flow flume with the length, width, and depth of 10m, 0.3m, and 0.45m, respectively. The flume walls are made of transparent glass; thus, the water surface profile and flow conditions are observable.

The main laboratory flume and secondary flumes make up the experimental flume, and the main flume is 12 m long with a 0.30 m wide rectangular section made of metal bed and 0.45 m depth with glass sidewalls. As a result, the water surface profile and flow conditions are visible. It includes a flow depth control gate at the end. The slope of the flume is modified to be horizontal (the bed slope was almost zero). Each component of the secondary flumes comprises one calibrated rectangular weir with a point gage device to receive lateral flow from the side weir that results in a residual at the end of the main flume and to complete the laboratory flow cycle. The main channel is fed water from a sump's supply pipe with a maximum discharge of 27 L/s. The following are the specifications of the various elements of the flume and laboratory equipment used in this experiment (Figure 3.2b): First, the pump delivered the flow from the storage tank to the head tank at the flume intake (upstream). A variable frequency device named inverter for highly accurate discharge determination is used to control the water pump's speed by adjusting the frequency as shown in Figure 3.2b(I). By using a linear equation between the frequency and flow rate as below:

The sensitivity of the discharge is 0.2 L/s, as determined by a Siemens brand electromagnetic flowmeter fitted in the supply line as shown in Figure 3.2b(II). The flow volume discharged in the channel and flowed smoothly over the stepped weir placed on the flume bed. The discharge rate is then varied to analyses and record the hydraulic conditions of the weir discharge. Finally, water flow entered the pump tank via the downstream channel and returned to the cycle. The Level meter, as shown in Figure 3.2b(III), is used to monitor water depth along the channel centreline, near the side weir, giving a highly accurate depth measurement. A sluice gate is installed at the end of the main channel to manage flow depth. The flow velocity is measured in different sections in the weir using a current meter with great sensitivity. The average distance (0.35 m) from the weir is adopted in all experiments to ensure the accuracy of flow measuring because the maximum water head over the rectangular weir crest is (H= 10cm); therefore, the range of an accurate head measuring distance is (0.30-0.40m) (Bos, 1988). Figures 3.2, 3.3a, and 3.3b demonstrate the laboratory flume's description.

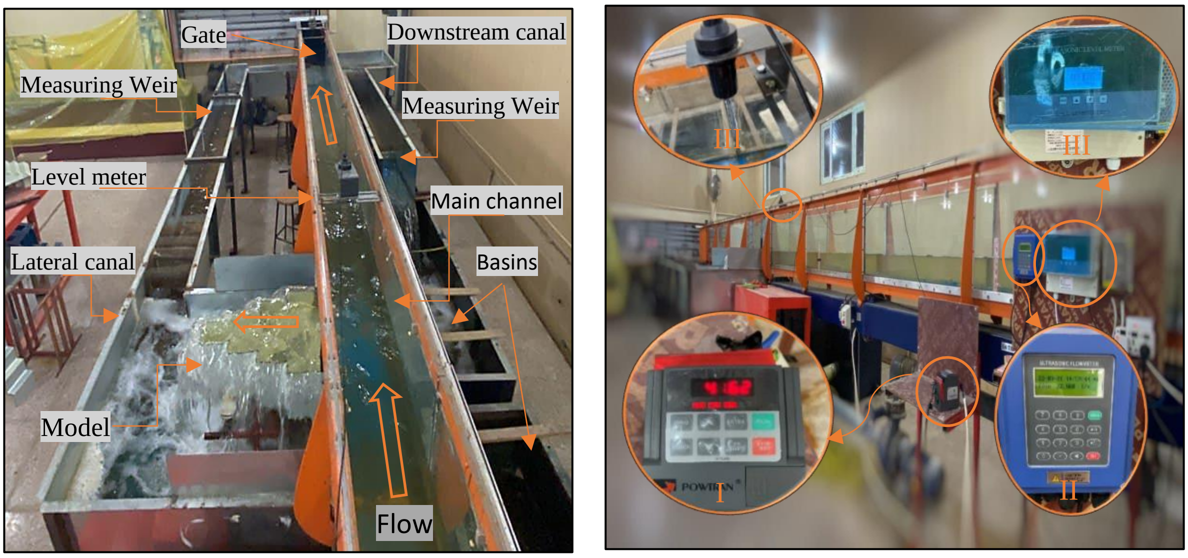

(a) (b)

Figure3.2: Details of laboratory flumes and experimental equipment.

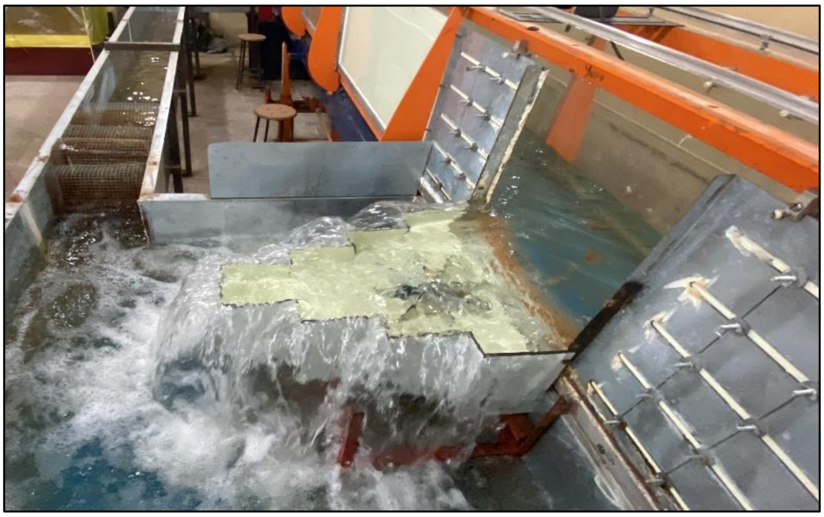

(a)

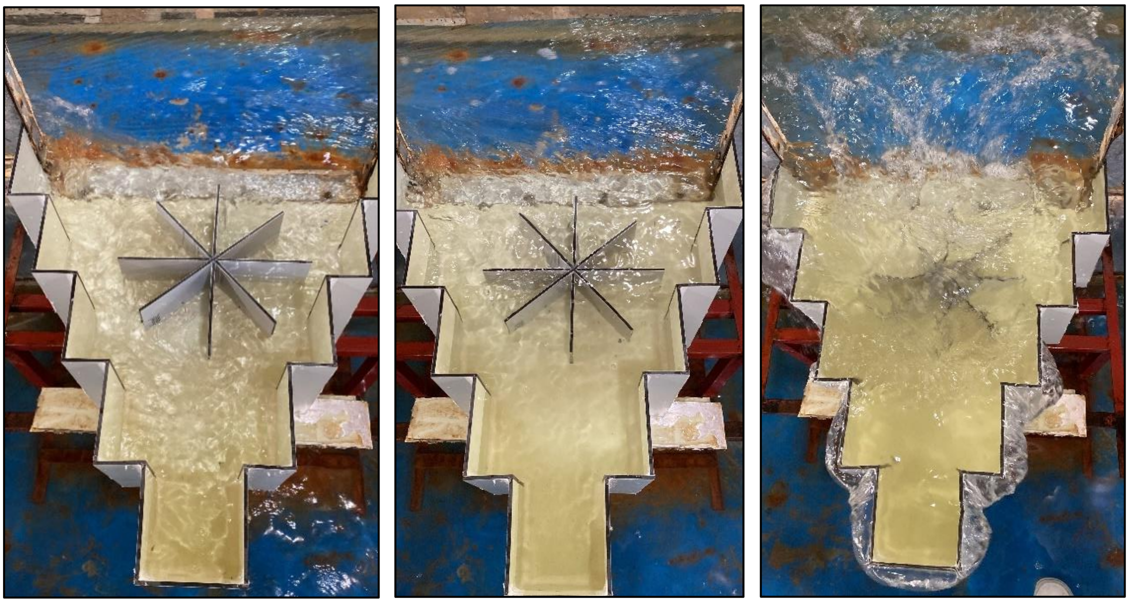

(b)

Figure 3.3: Layout of the stepped model with antivortex during experimental testing.

3.4 Experimental Testing Procedures

Laboratory experiments are explained in the following steps:

1- Adjusting the main flume at a horizontal slope

2- Installing the side weir model into the main flume sidewall and using a level meter to check the model's horizontal situation for various plans. The control gate is then adjusted to provide the initial water level for a specific weir height.

3- Turn on the pump to begin pumping water and wait for steady-state flow.

4- For the first part of the experimental work, when the steady state of flow is reached when no water depth fluctuation appears and becomes almost constant, velocity measurements are taken using the current meter device at the side-weir section to describe the hydraulic behaviour of the labyrinth side weir.

5- The flow depth in both main and auxiliary flumes, upstream water depth, and water surface profile are determined by measuring the water depth at six places in each experiment using a Level Meter Device. For each experiment, seven readings are taken. The discharge capacity is influenced by the vortices created due to the increasing Froude numbers.

6- steps (4 and 5) are repeated to apply different inward discharges using the inverter device and flowmeter.

7- Steps (2-6) are repeated for other models.

8- Steps (2-7) are applied without antivortex models to allow a comparison for the second part of the experimental work.

9- For the third part of the experimental work, steps (2-7) are repeated for the models by using antivortex structures installed in stepped weirs in different dimensions at one location at the weir (0.45d) and height (0.5p) according to (Abbasi et al., 2020) anti-vortex with half the height of the side weir (P' = 0.5 P) were found to perform best. Consequently, the most efficient antivortex type is observed and the location identified previously by CFD.

3.5 Required Measurements

3.5.1 Flow Depth

The flow depth is determined with a Level Meter Device that moves along a rail fixed along the main flume with an accuracy of ± 0.1mm. The discharge coefficient of the side weir model is determined by two measurements, which are as follows:

1- The flow depth is measured at the main flume centre at the upstream end of the side weir (y_1) and the downstream end of the side weir (y_2),as shown in Figure 3.4.

2- The height of water above a rectangular weir crest (Hs) situated within a side flume to determine the discharge that has flowed over the side weir measured 0.35m from the weir crest.

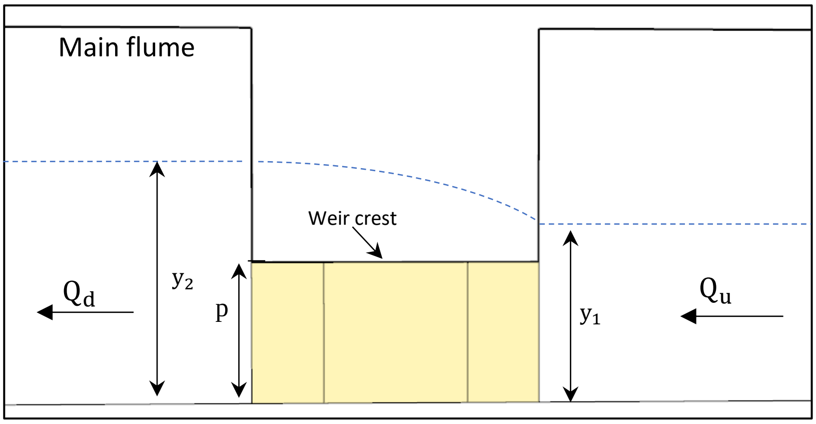

Figure 3.4: Plan of the longitudinal section along the stepped weir.

3.5.2 Water Surface Profiles

Water surface profiles are essential to describe the hydraulic performance of the stepped labyrinth side weir, the depth of the water along the centreline and the side weir of the flume are measured with a Level meter device installed on a measurement car that is able to move in both the flow (x) and lateral (y) directions by taking 8 points for each section. In practice, a level meter can be installed at the flume centre at the upstream end of the side weir (see Figure3.5). As a result, the y_1 value can be calculated from this point.

3.5.3 The Secondary Flow

A Current meter device determined the secondary flow intensity along the stepped labyrinth side weir with and without an antivortex. The velocities are measured at three sections along the stepped labyrinth weir, as shown in Figure 3.6. In sections (A-A), (B-B), and (C-C) 5, 3, and 3 points are selected in velocity measurement, as demonstrated in Figure 3.6, resulting in a total of 11 measuring points inside the weir for each testing model. The collected velocity data are evaluated and filtered, and then secondary current intensity in all sections was drawn and analysed.

3.5.4 Discharge Measurements

Two discharges are measured during the experiments as follows:

1- A flowmeter will measure the total discharge for inward discharge (Qu).

2- Measuring the lateral discharge (Q_{sw}) by the rectangular weir of the side flume using the Equation obtained by (Alfatlawi & Shlaash, 2021)

$Qs = 0.57 (Hs)^{1.5}$

Which (H_s) is water depth above side flume rectangular weir.

3-Measuring the downstream discharge (Q_d) will be ($Q_u – Q_{sw}$).

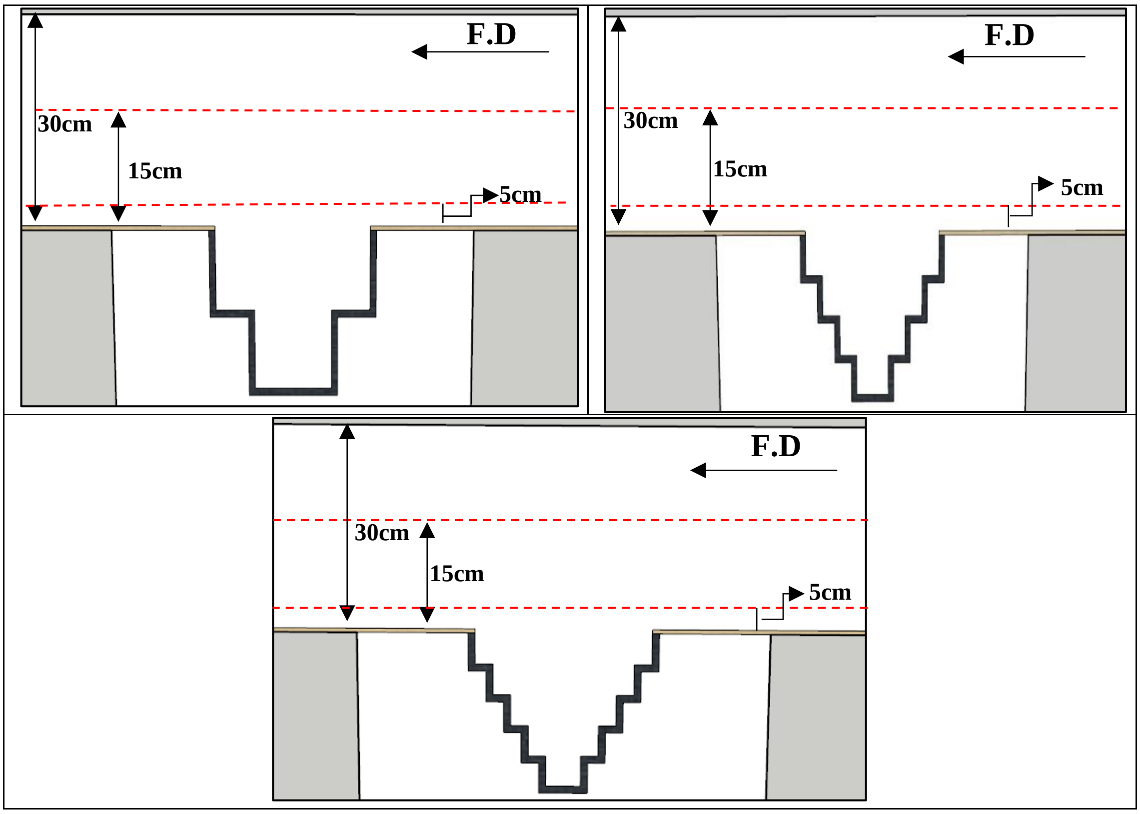

Figure 3.5: Free surface profiles on the side weir according to different step numbers.

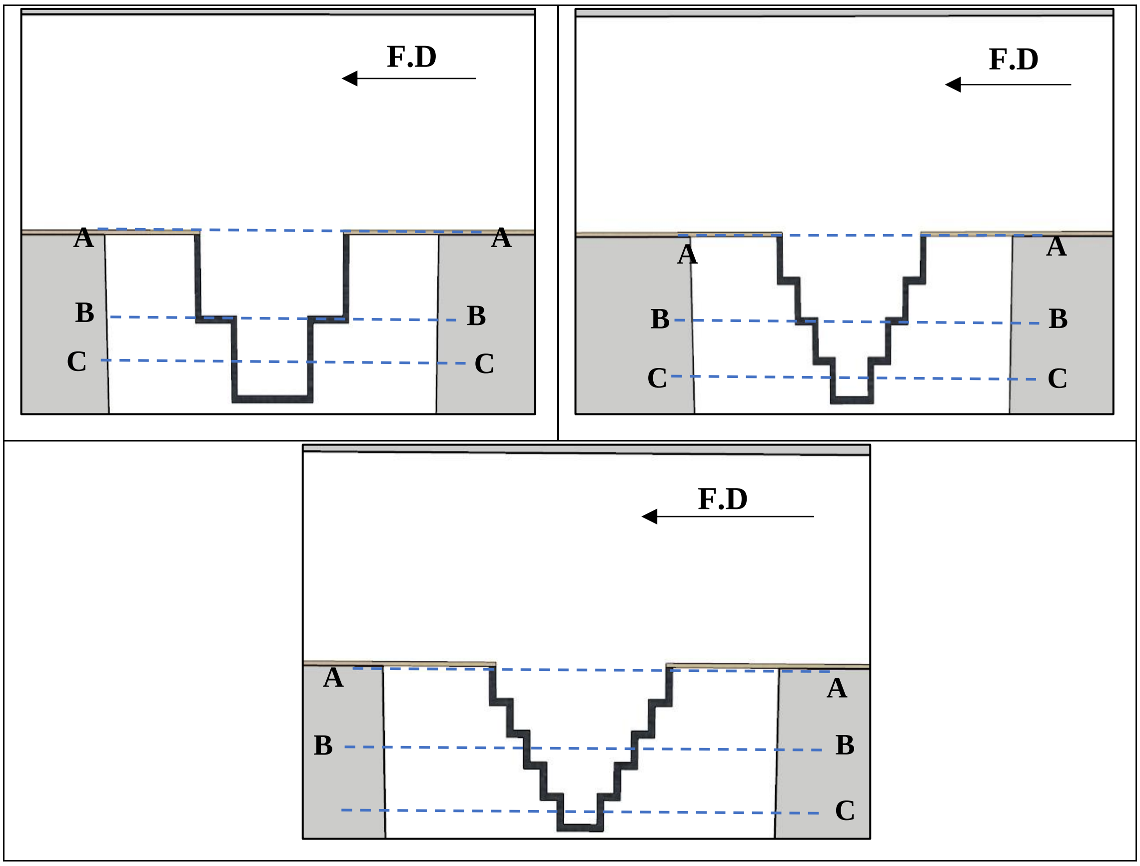

Figure 3.6: sections of velocity measurements: (a) N=4; (b) N=8; (c) N=10

3.6 Measuring the discharge coefficient of Stepped LSW

The Schmidt method is found to be a quite reliable method for estimating discharge capacity, and hydraulic designers can use it with confidence for this purpose (Emiroglu & Ikinciogullari, 2016). As far as we know, the Schmidt method is not employed to determine the stepped labyrinth side weir discharge capacity.

The Schmidt approach solved the discharge coefficient using the Poleni Equation (Emiroglu & Ikinciogullari, 2016).

$$C_d = \frac{3}{2}\frac{Q_w}{\sqrt{2g}Lh_a^{3/2}} \tag{3.1}$$

$$Q_w = \frac{2}{3}C_d\sqrt{2g}Lh_a^{3/2} \tag{3.2}$$

$$h_a = \frac{1}{2}(h_1 + h_2) \tag{3.3}$$

$${}^*h_a = \frac{1}{3}(h_1 + h_2 + h_3) \tag{3.4}$$

$$*C_d = \frac{3}{2}\frac{Q_W}{\sqrt{2g}L^* h_a^{3/2}} \qquad 3.5$$

where $*C_d$ is the discharge coefficient calculated using three points, ha is the average nappe height calculated using two points, and *ha is the average nappe height calculated using three points. The nappe heights were determined in this study based on two points using Eq. (3.1).

3.7 Models description

The stepped LSW models have a thickness of 4mm. Moreover, the crest is tapered at 45° by horizontally offsetting the external upper edge 2mm to provide an entire aerated nappe. Figure 3.7(a -d) shows the ten steps model with different shapes and dimensions of the antivortex structures used in the experiments. Tables (3.1 to 3.4) show the geometric properties of the stepped LSW and antivortex models used in this study. Figures (3.7 to 3.11) show how models are classified into three categories based on the number of steps, and the shapes, locations, and dimensions of the antivortex structures used in the experiments. The dimensions of SLSW models based on (Alfatlawi & Shlaash, (2021).

Table 3.1: Stepped LSW geometry with antivortex for (L=45cm, θ=45).

L(cm)	N	θ	P (cm)	a_s (cm)	b_s(cm)
45	4	45	8,14	27.16	11.25
45	8	45	8,14	13.58	5.62
45	10	45	8,14	10.86	4.50
Dimensions of the antivortex structures					
Type	Thickness(mm)	Width(mm)	Height(mm)	Figure	
1	3	4*a, a=230	40,70	Fig 3.8A	
2	3	2*b, b=270	40,70	Fig 3.9A	
3	3	c1, c2, c3 110,191,80	40,70	Fig 3.10A	
4	3	d1, d2, d3, d4 115,85,85,115	40,70	Fig 3.11A	

Table 3.2: Stepped LSW geometry with antivortex for (L=45cm, θ=60).

L(cm)	N	θ	P (cm)	a_s (cm)	b_s(cm)
45	4	60	8,14	19.48	11.25
45	8	60	8,14	9.74	5.62
45	10	60	8,14	7.79	4.50
Dimensions of the antivortex structures					
Type	Thickness(mm)	Width(mm)	Height(mm)	Figure	
1	3	4*a, a=180	40,70	Fig 3.8B	
2	3	2*b, b=200	40,70	Fig 3.9B	
3	3	c1, c2, c3 120,154,90	40,70	Fig 3.10B	
4	3	d1, d2, d3, d4 94,64,64,94	40,70	Fig 3.11B	

Table 3.3: Stepped LSW geometry with antivortex for (L=30cm, θ=45).

L(cm)	N	θ	P (cm)	a_s (cm)	b_s(cm)
30	4	45	8,14	18.10	7.50
30	8	45	8,14	9.05	3.75
30	10	45	8,14	7.24	3.00
Dimensions of the antivortex structures					
Type	Thickness(mm)	Width(mm)	Height(mm)	Figure	
1	3	4*a, a=150	40,70	Fig 3.8C	
2	3	2*b, b=150	40,70	Fig 3.9C	
3	3	c1, c2, c3 75,100,60	40,70	Fig 3.10C	
4	3	d1, d2, d3, d4 65,49,49,65	40,70	Fig 3.11C	

Table 3.4: Stepped LSW geometry with antivortex for (L=30cm, θ=60).

L(cm)	N	θ	P (cm)	a_s (cm)	b_s(cm)
30	4	60	8,14	12.99	7.50
30	8	60	8,14	6.49	3.75
30	10	60	8,14	3.19	3.00
Dimensions of the antivortex structures					
Type	Thickness(mm)	Width(mm)	Height(mm)	Figure	
1	3	4*a, a=120	40,70	Fig 3.8D	
2	3	2*b, b=120	40,70	Fig 3.9D	
3	3	c1, c2, c3 60,100,45	40,70	Fig 3.10D	
4	3	d1, d2, d3, d4 50,35,35,50	40,70	Fig 3.11D	

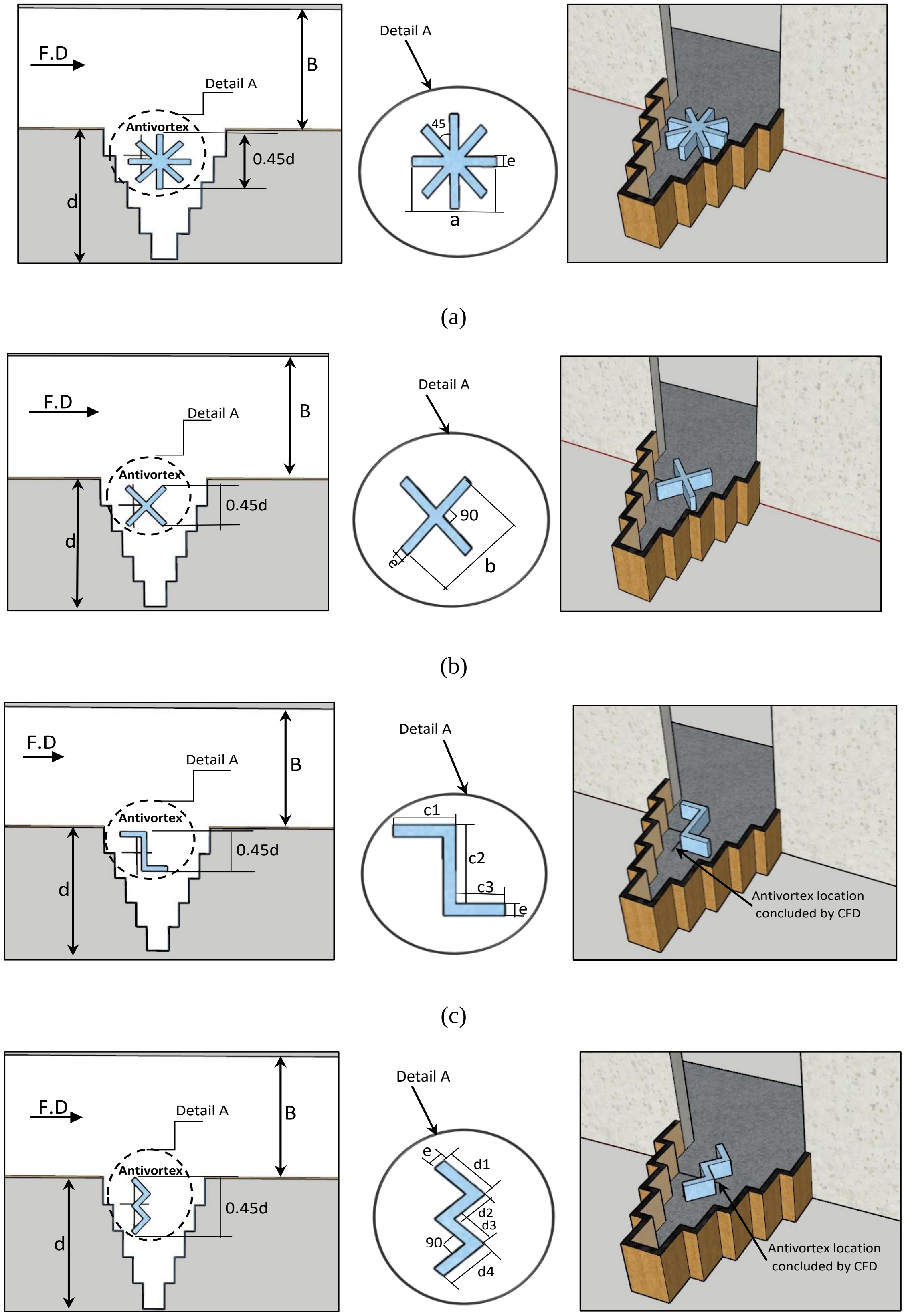

(a)

(b)

(c)

(d)

Figure 3.7: Plan and images for antivortex structures tested in the experiments: (a) type1, (b) type2, (c) type3, (d) type4.

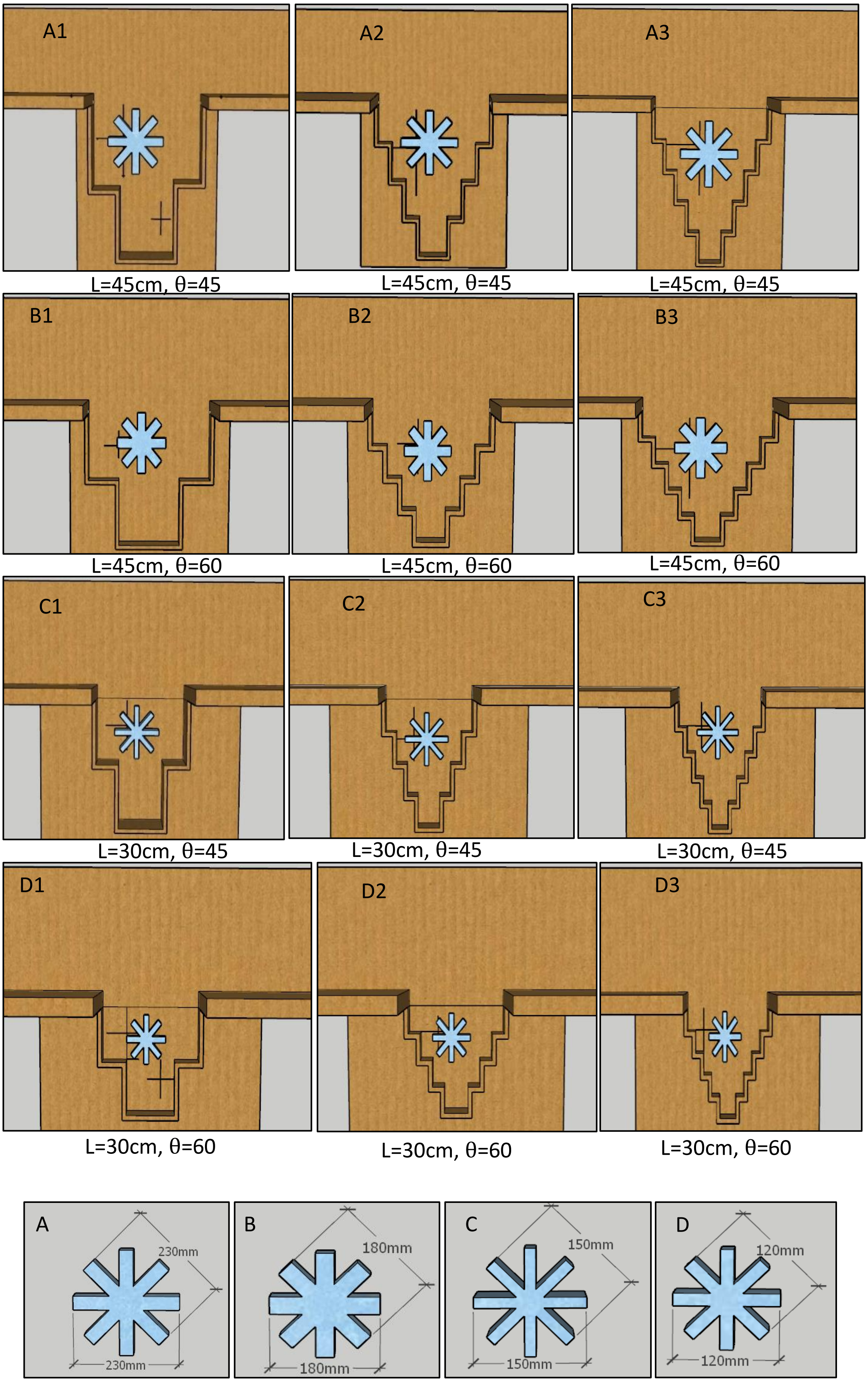

Figure 3.8: Model description.

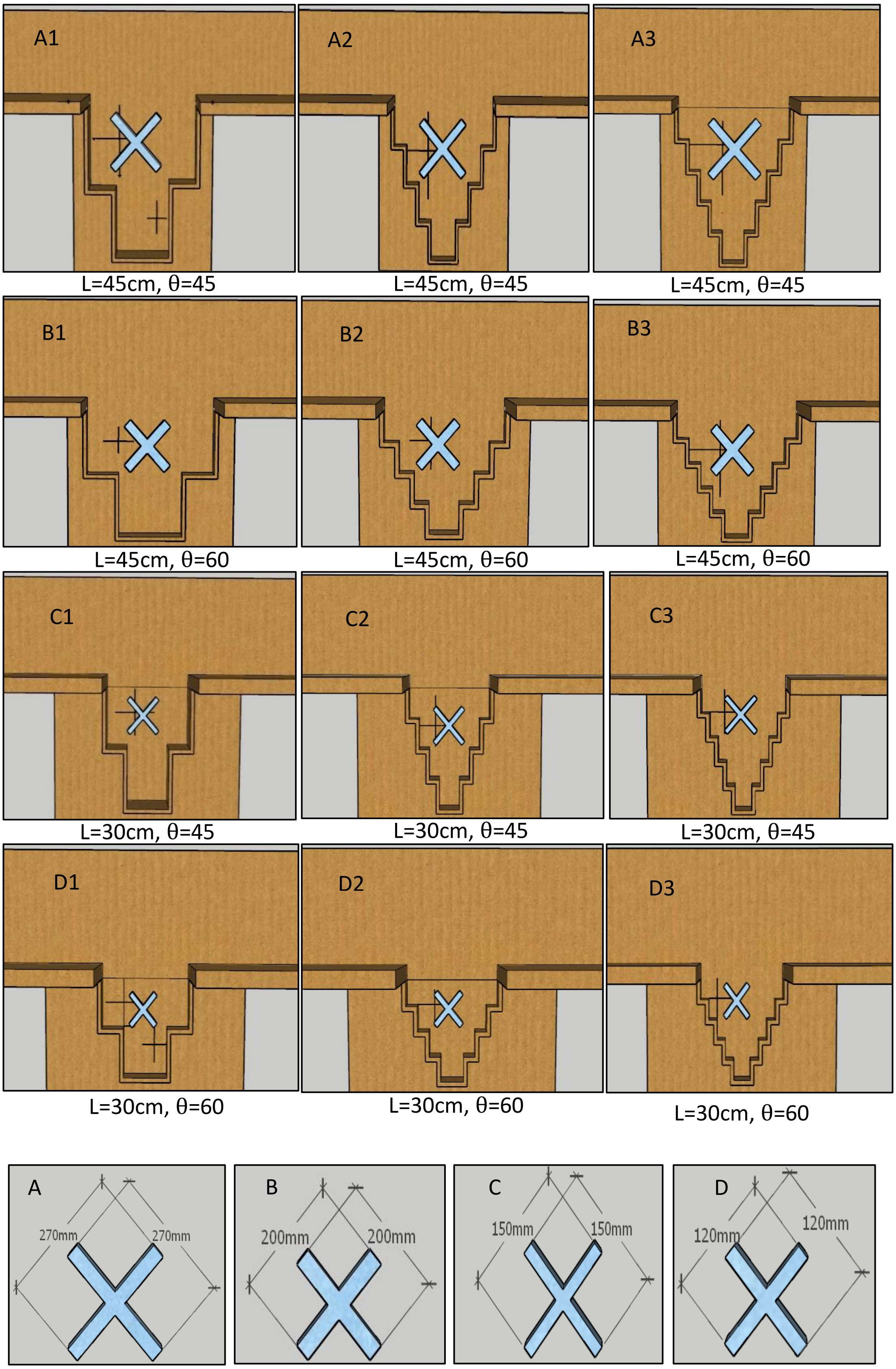

L=45cm, θ=45 L=45cm, θ=45 L=45cm, θ=45

L=45cm, θ=60 L=45cm, θ=60 L=45cm, θ=60

L=30cm, θ=45 L=30cm, θ=45 L=30cm, θ=45

L=30cm, θ=60 L=30cm, θ=60 L=30cm, θ=60

Figure 3.9: cont.

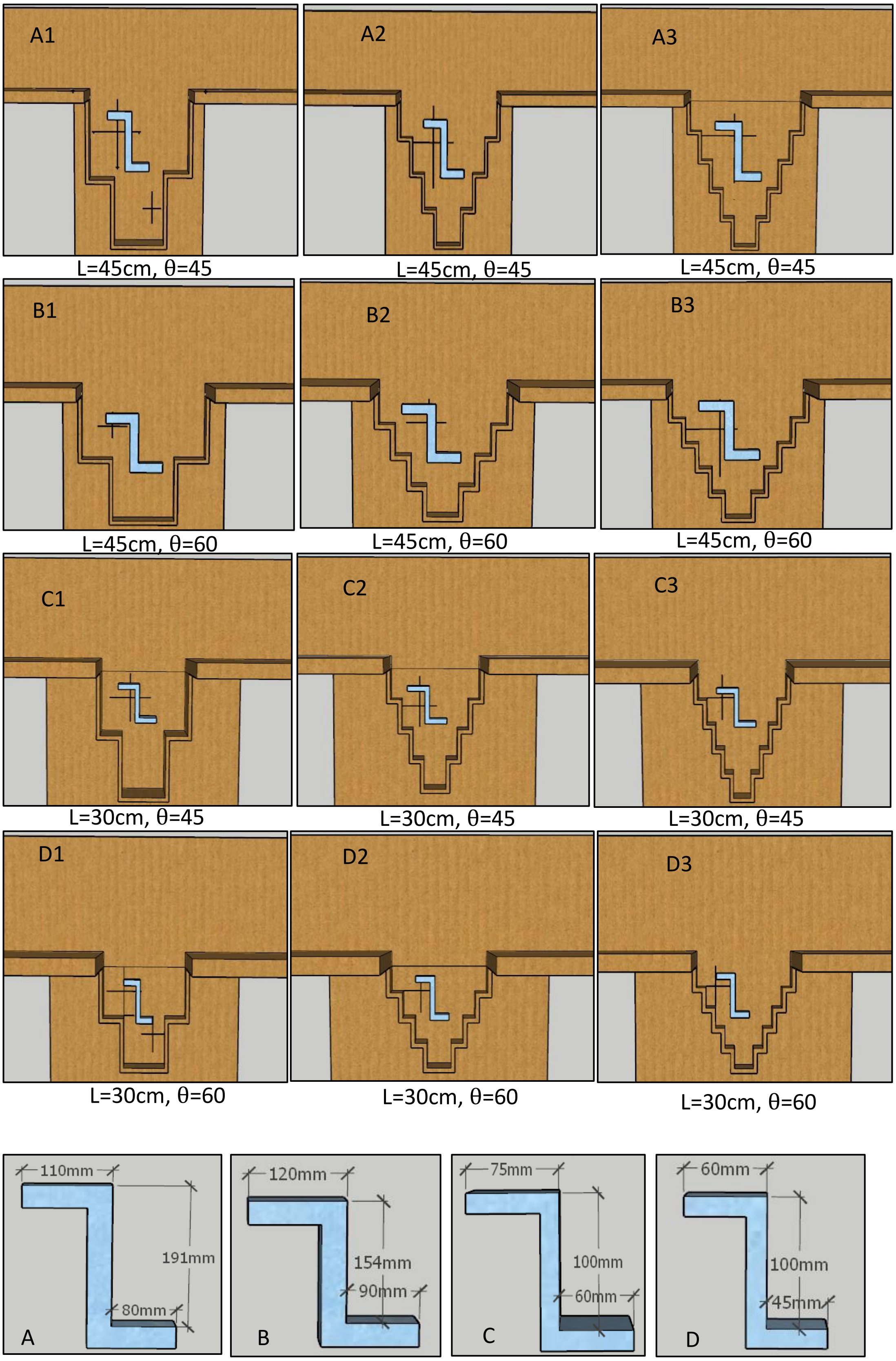

Figure 3.10: cont.

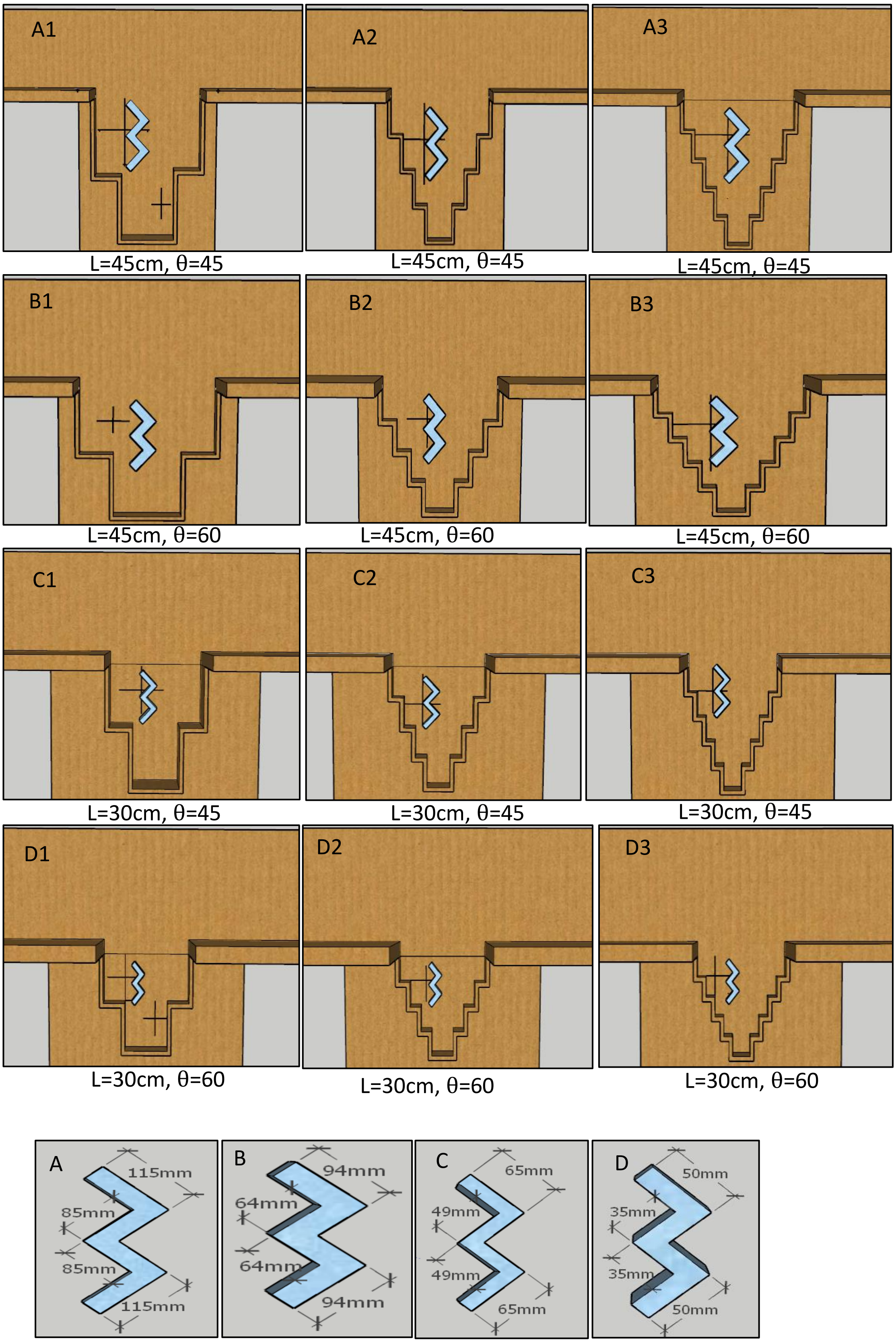

Figure 3.11: Plan and images for antivortex structures tested in the experiments (dimensions in millimetres).1: N=4, 2: N=8, 3:N=10.

Chapter Four

Experimental results

This chapter presents the overall experimental program findings, analyses, and comparisons and critically discusses them. Investigations are done into how various dimensionless parameters affected the discharge coefficient of stepped labyrinth side weir models (SLSW) with and without antivortex structures. Four models of antivortex structures for the improvement of discharge coefficient are presented, and the influence of these models on the side weir performance is evaluated by comparing the obtained findings to stepped labyrinth side weir models without antivortex structures. Secondary flows created by the lateral flow affect the water surface level along the opening length of the stepped labyrinth side weir were also investigated.

4.1 Effect of Dimensionless Parameters on the Discharge Coefficient (C_d)

4.1.1 Effect of Froude Number (F_1) and Head Angle (θ)

The Froude number is a parameter for identifying flow patterns. The variations of C_d and F_1 with side weir length ratios (L/B = 1 and 1.5) and in various weir angles (θ) are plotted in Figure 4.1((a)–(d)). Afterward, in Figure. 4.1(a, b), experiments are performed for constant dimensionless side weir length (L/B = 1) with varying various weir angles (θ). The variation of C_d with increasing F_1 demonstrates a decreasing tendency. These findings are consistent with those reported in the literature (Ikinciogullari & Emiroglu, 2019). The decreasing tendency is significant for high ratios (L/B = 1.5) of effective folded crest length (or θ = 45), as shown in Figure 4.1(c, d). This behaviour can be related to the formation of vortices and eddy flow as flow velocity increases. hence, side weir efficiency will decrease. The same results are revealed by (Alfatlawi & Shlaash, 2021) and other researchers, such as (Singh et al., (1994);Borghei et al., (1999); Emiroglu et al., (2011); Khameneh et al., (2014)). The discharge coefficient values are frequently lower in stepped labyrinth side weirs without an antivortex structure than in those with antivortex structures, according to the vortex reduction effects of antivortex structures around the labyrinth side weir area. Based on these observations, the authors suggest that using antivortex structures improves the side weir's discharge capacity. All types of antivortex structures tested yielded a higher C_d value than the no-antivortex structure controls. Type1 produced the highest C_d values with decreasing step number. Figure. 4.2((a)–(c)) shows the variation in discharge coefficient with Froude number in the SLSW with L/B = 1 with antivortex structures, together with the related data of the labyrinth weir with no antivortex structures. The discharge coefficient values in stepped labyrinth side weirs without anti-vortex structures are lower than in those with antivortex structures; this is due to the antivortex structures involving the labyrinth side weir area reducing the vortex effect. Based on these findings, the authors recommend that the antivortex structures increase the side weir's discharge capacity. Compared to the no-antivortex structure controls, the four antivortex structures produced higher C_d values. Type1 produced the highest C_d values.

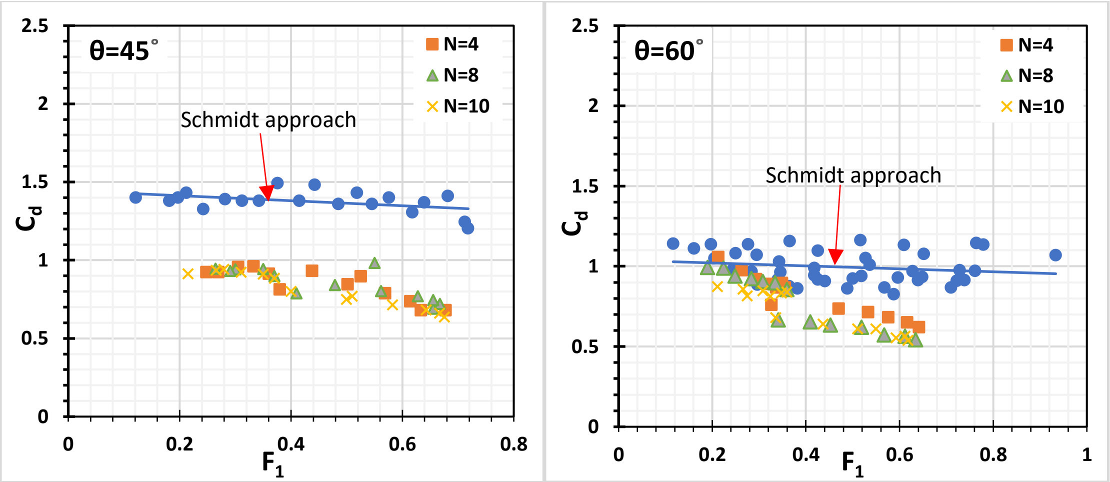

(a) L/B=1 (b) L/B=1

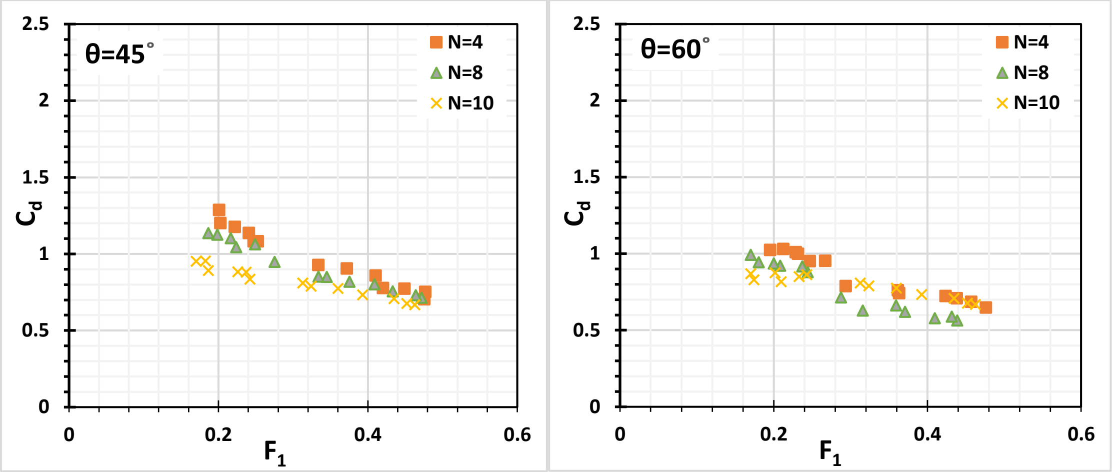

(c)L/B=1.5 (d) L/B=1.5

Figure 4.1(a-d): variation of F_1 with C_d estimated for SLSW with Cd for Schmidt approach.

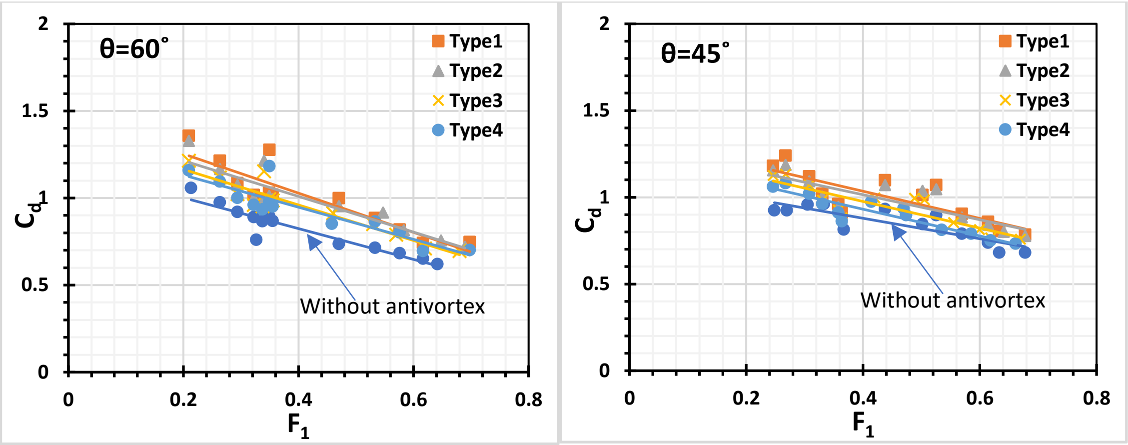

(a) N=4

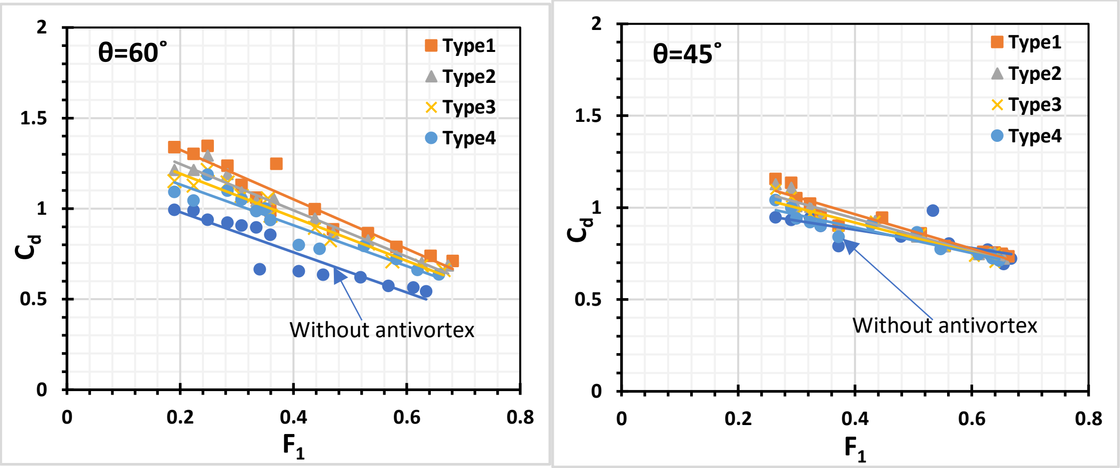

(b) N=8

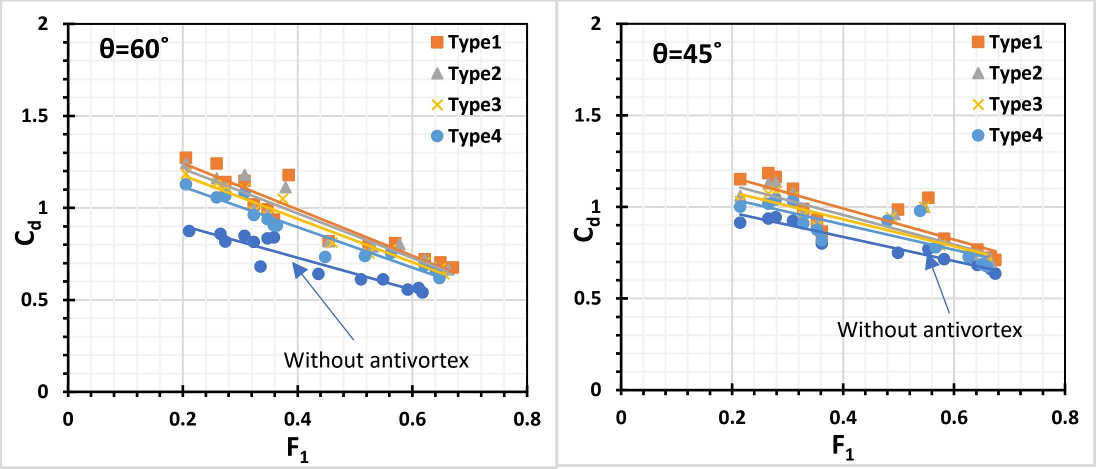

(c) N=10

Figure 4.2(a–c): Variations in C_d with F_1 for stepped labyrinth side weirs with and without antivortex structures at L/B=1.

Figure 4.3((a)–(c)) demonstrates the change in discharge coefficient with Froude number in the L/B = 1.5 in the SLSW with antivortex structures and data from side weirs without antivortex structures. Antivortex structures significantly improve the discharge coefficient with increasing step number and head angle. In head angles of 60°, all Types have greater C_d values than side weirs without antivortex structures in the ten and eight-step models. Although in the four-step model, the C_d values are greater in the side weir with no antivortex structure. At head angles of 45°, there is no general trend in the distribution of C_d with F_1 the C_d is most significant in the side weir with no antivortex structure; Except for the ten-step model, all types have greater C_d values than in the side weirs without antivortex structures as the Froude number decreases. Type1 produced the highest C_d values.

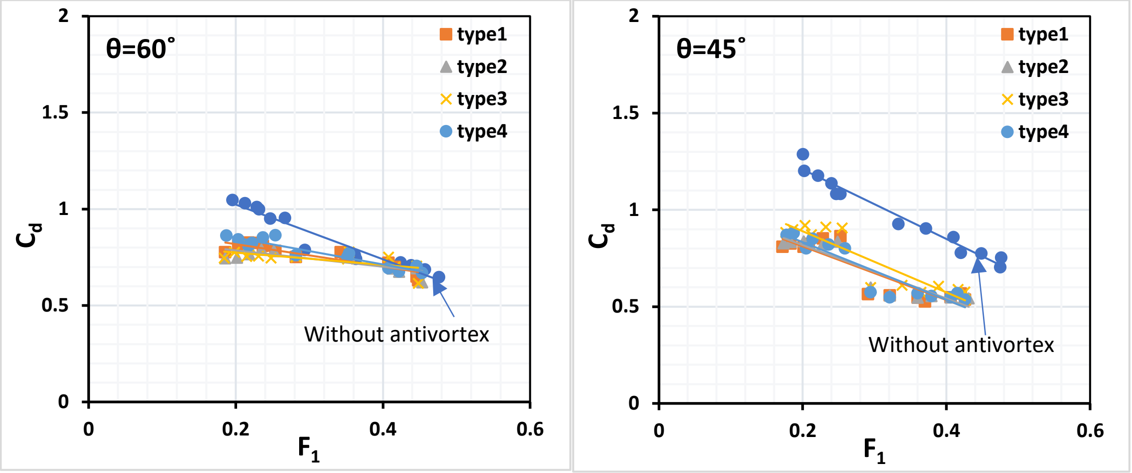

(a) N=4

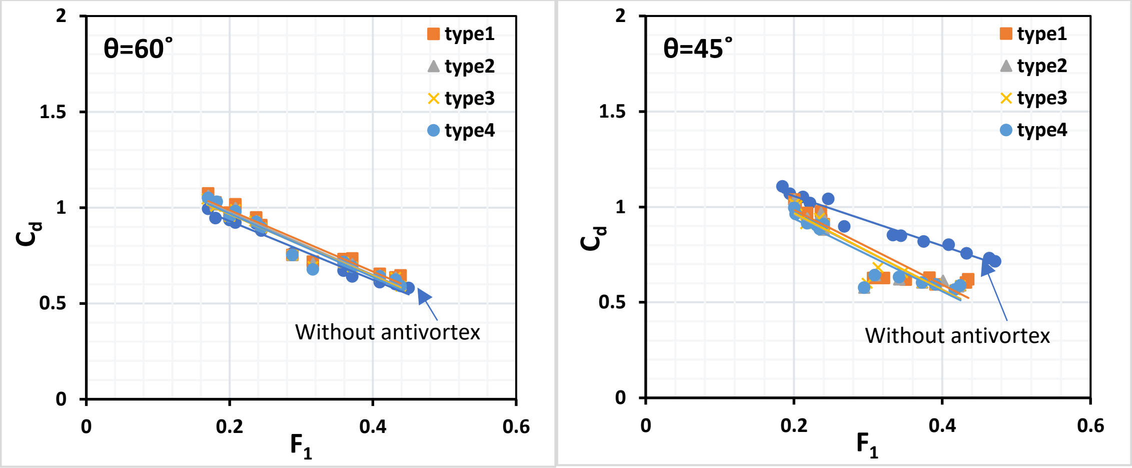

(b) N=8

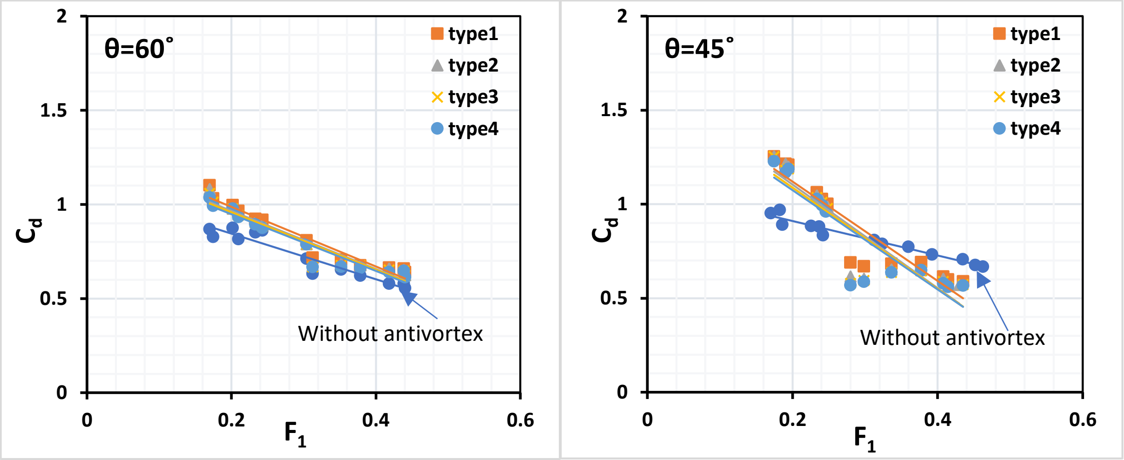

(c) N=10

Figure 4.3(a–c): Variations in C_d with F_1 for stepped labyrinth side weirs with and without antivortex structures at L/B=1.5.

To investigate the effect of step number, Figure 4.4 (a and b) shows that for different L/B ratios (1 and 1.5), with and without antivortex structures, the discharge coefficient increases as the head angle decrease for the same number of steps, and the head angle effect is significant by increasing (L/B) ratio. Emiroglu et al., (2011) reported the same results for triangle LSW ($\theta = 45°$). This behavior is related to secondary flow motion being motivated toward the most extended crest length. Consequently, the higher flow has a greater possibility of jumping the crest. For the case with antivortex, as shown in Figure (4.4a) the C_d decreased with increasing, while increased with increasing N as shown in Figure (4.4b). Thus, side weirs with (L/B = 1) produces a greater C_d value when installing the antivortex structure, and type1 in model N=4 yielded the high C_d value for any Froude number among the investigated antivortex structures.

The discharge coefficient values, relative to the SLSW with the best type of antivortex, are compared with results obtained by (Emiroglu et al., 2017) on a trapezoidal labyrinth side weir (see Figure 4.5(a)), as shown in Figure 4.5(b). The selected antivortex of the present study (Type 1 with crest height = 0.5 P) outperforms the selected antivortex (Type 6 with crest height = 1 P) of (Emiroglu et al.,2017). The discharge coefficient compared to the results of (Emiroglu et al., 2017), is 5% higher. The primary reason for this increase in the discharge coefficient of the SLSW can be attributed to the geometric shape of the antivortex structure and proper height of the antivortex used in this study.

SLSW shows in Appendix A with four different types of antivortex structures for head angles ($\theta = 60^\circ$ and $\theta = 45^\circ$) during labyrinth weir testing.

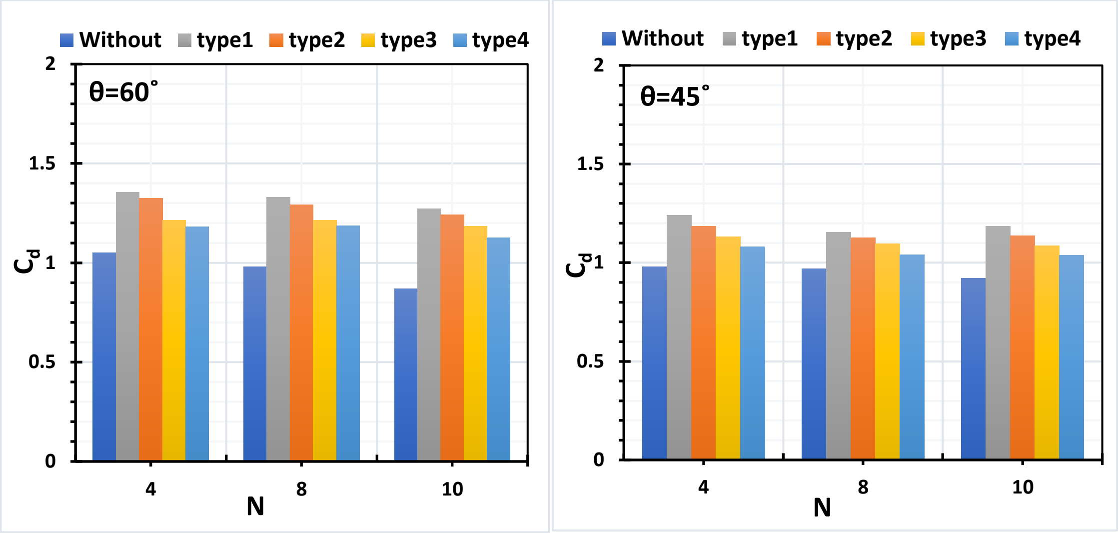

(a) L/B=1

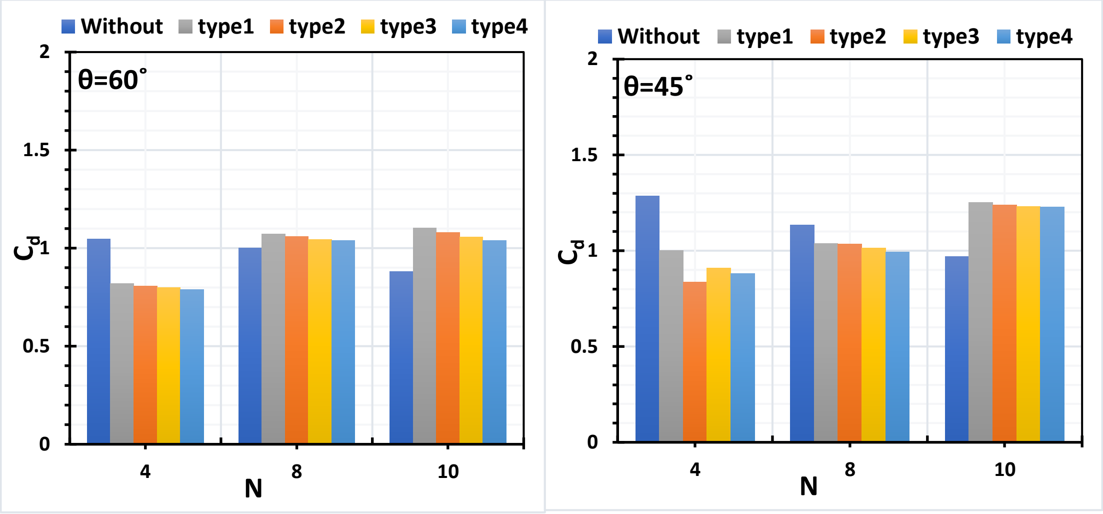

(b) L/B=1.5

Figure 4.4(a-b): Variations in discharge coefficient versus step number under different types of antivortex structures.

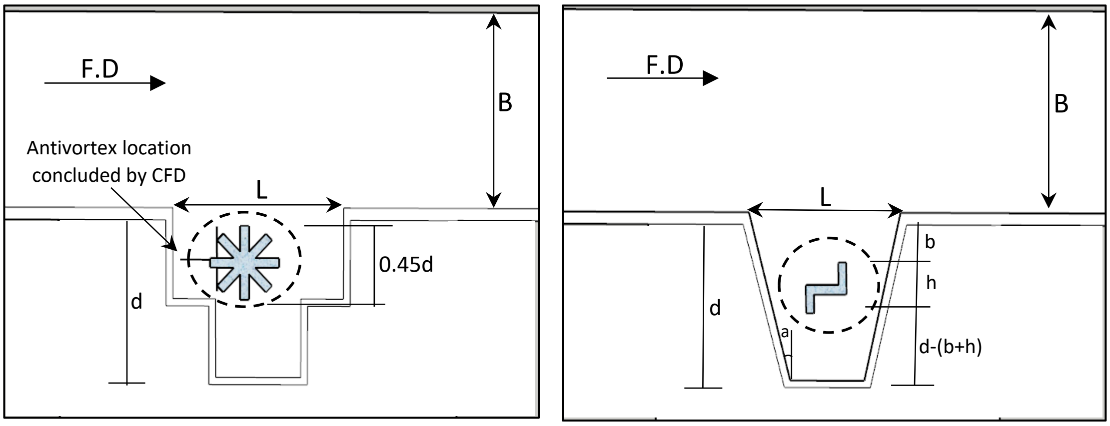

(a) present study (b) Emiroglu et al.,(2017)

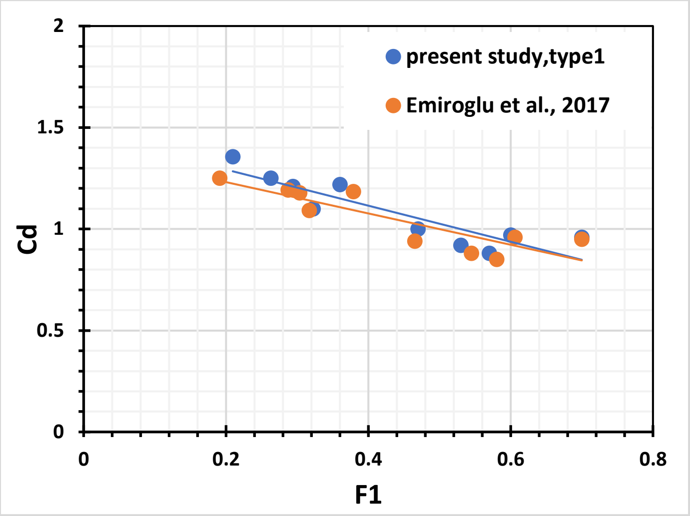

(c)

Figure 4.5: (a-b)View of the best model of the antivortex inside the labyrinth side weir.(c) comparison between present study and Emiroglu et al.,(2017) study.

4.1.2 Effect of Weir Length Ratio (L/B) and Steps Number (N)

The effect of the weir length ratio with different step numbers on the discharge coefficient (with and without antivortex structures) is studied. Also, t the antivortex results are analysed to understand its behavior and the effect on the discharge coefficient. The values of C_d is plotted versus F_1 with and without antivortex structures, with different dimensionless weir lengths (L/B = 1 and L/B = 1.5) and for different steps number and different head angles ($\theta = 45°$ and 60°), Figures (4.6 to 4.8). The results show that the influence of dimensionless weir length on the discharge coefficient is significant for lower steps. The lower internal head angle ($\theta = 45^\circ$) produces a more significant difference under the variation of the weir length ratio due to an increase in the effective crest length (relative to the other angles), which becomes useless as the steps number increase. Subramanya & Awasthy, (1972) observed that when a side weir is relatively long, secondary flow dominates. Furthermore, for four steps models, enough space for free overflow on the step dimensions is available, hence less nappe interference and less disturbance length. The effect of dimensionless weir length (L/B) on antivortex structures is significant by increasing the number of steps, and it has the best performance in the ten-step model.

Figures (4.6 to 4.8) demonstrate the change in discharge coefficient with Froude number with a variation of L/B ratio in the stepped labyrinth side weirs with and without antivortex structures. The discharge coefficient significantly improves in dimensionless weir length (L/B = 1), all Types have greater C_d values than side weirs without antivortex structures. At dimensionless weir length (L/B=1.5), the discharge coefficient increases with increasing head angle and step number, using antivortex structures in head angle ($\theta = 60°$) increases the discharge coefficient in the ten and eight-step models. While in the four-step model, the side weir with no antivortex structure produced the highest C_d value. At head angles of (θ=45°), a weir without antivortex structure control except for the ten-step model despite the data points having an almost random distribution, all types have greater C_d values than side weirs without antivortex structures. Thus, side weirs with (L/B=1) produced a greater C_d value when the antivortex structure and type 1 yielded the high C_d value for any Froude number among the investigated antivortex structures. Emiroglu et al., (2017) revealed the same result, they studied the effects of using an antivortex structure installed in trapezoidal labyrinth side weirs on the discharge capacity and concluded that when using the antivortex structure, side weirs with L/B ratios of (0.5-1.0) provided a higher C_d value.

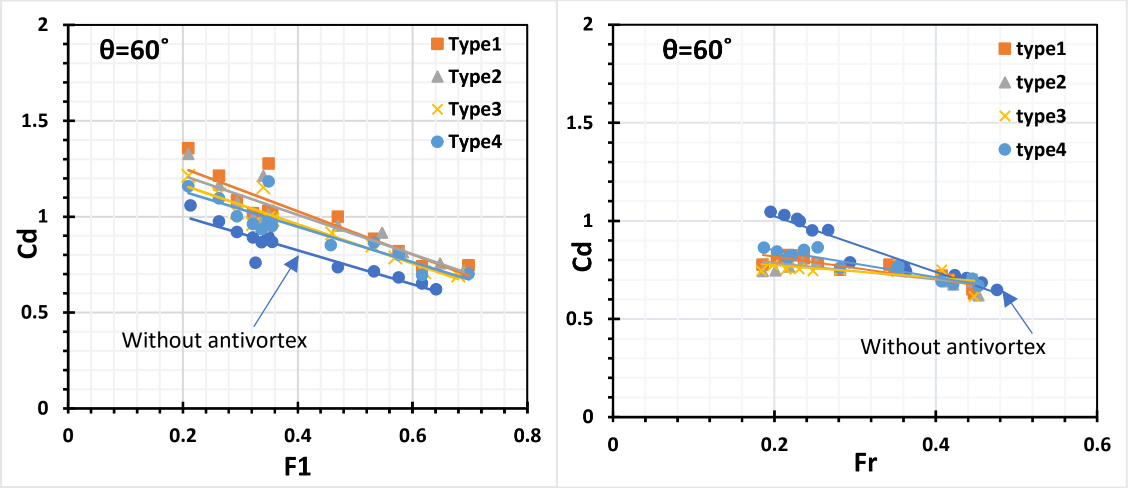

(a) L/B=1 (b) L/B=1.5

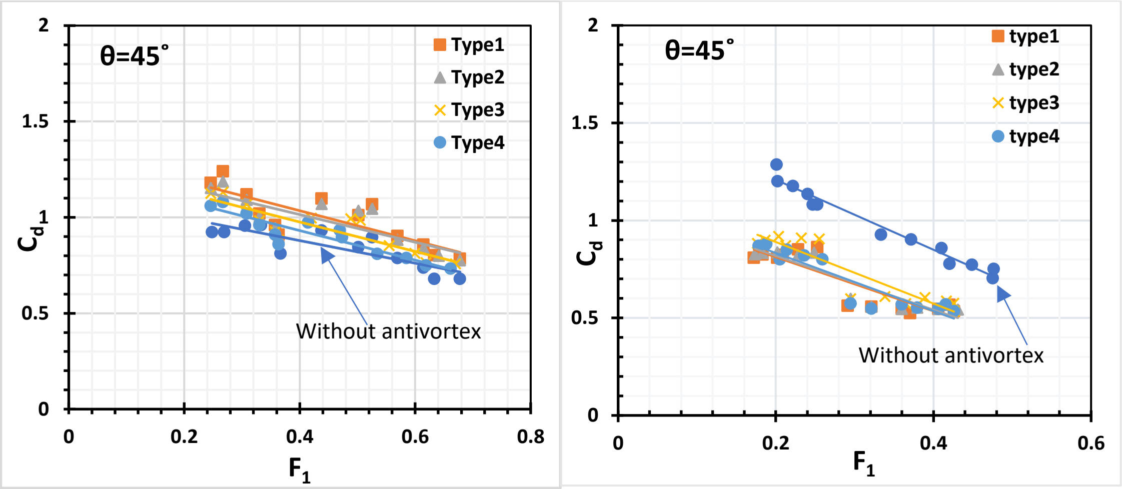

(c) L/B=1 (d) L/B=1.5

Figure 4.6(a-d): Discharge coefficient versus Froude Number with and without antivortex structures for four steps under various L/B ratios.

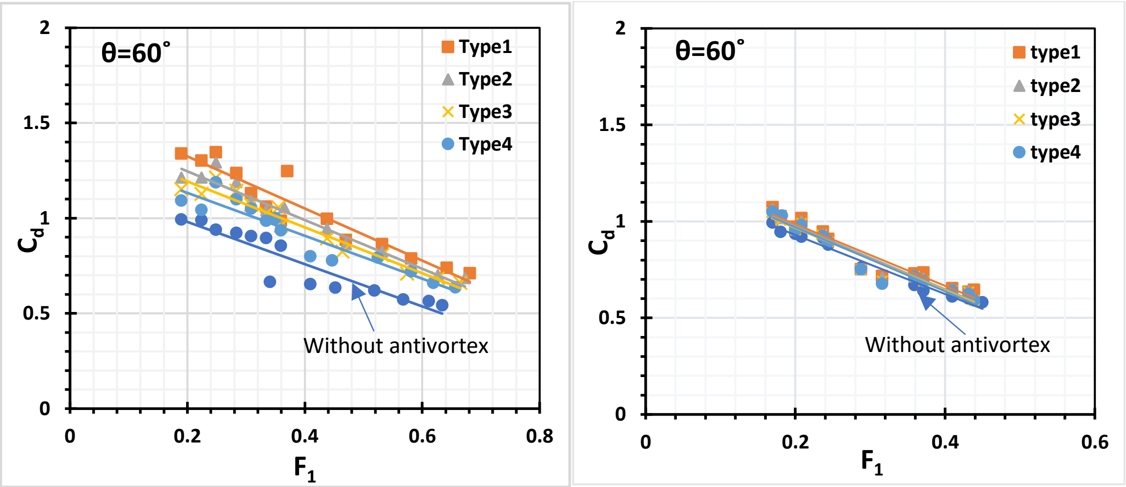

(a) L/B=1 (b) L/B=1.5

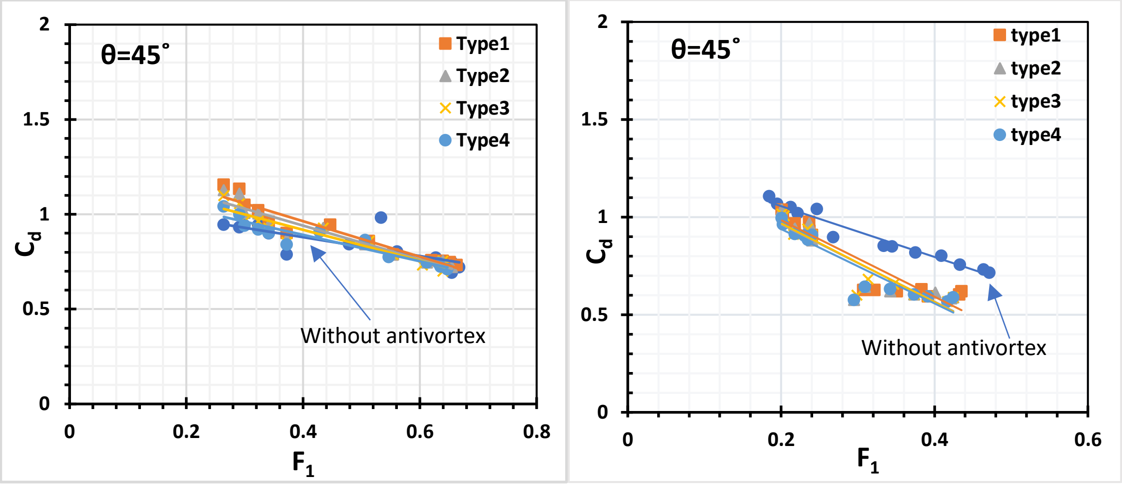

(c) L/B=1 (d) L/B=1.5

Figure 4.7(a-d): Discharge coefficient versus Froude Number with and without antivortex structures for eight steps under various L/B ratios.

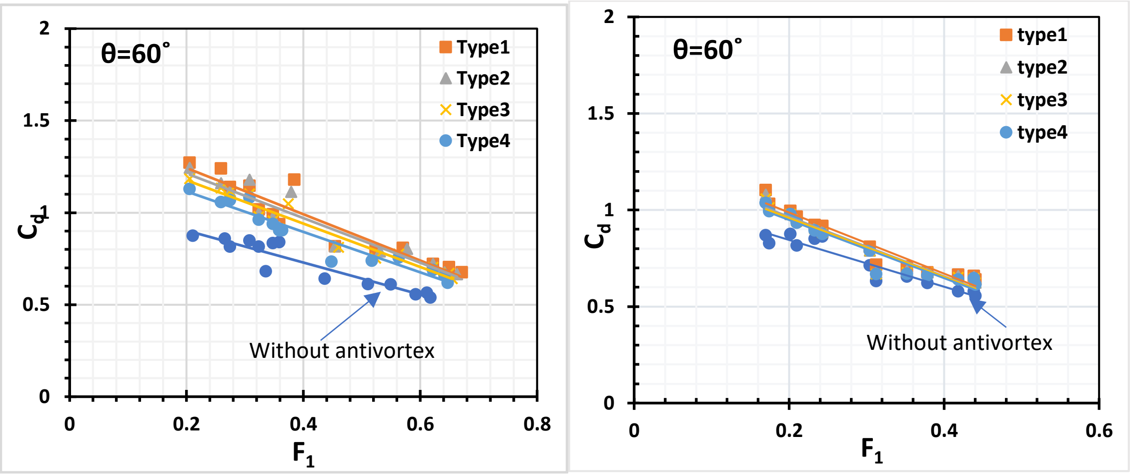

(a) L/B=1 (b) L/B=1.5

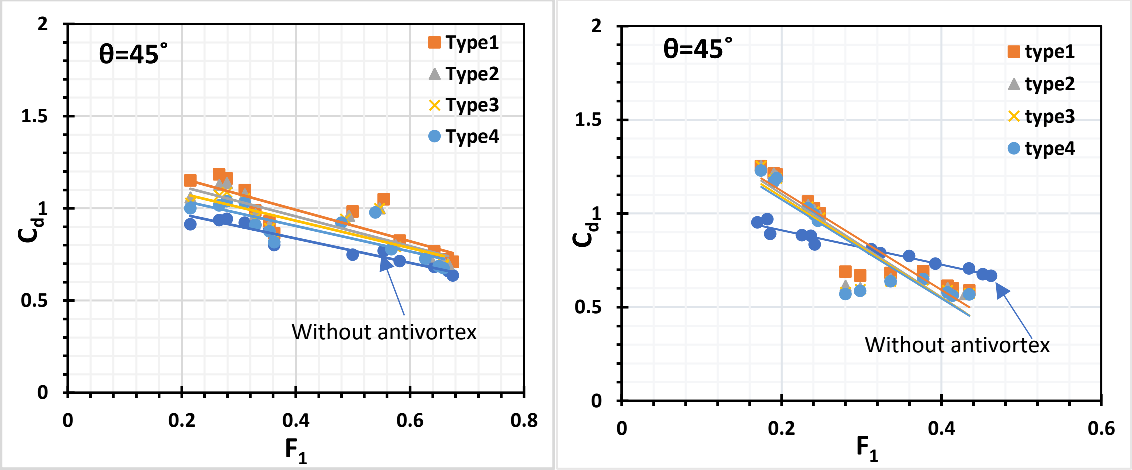

(c) L/B=1 (d) L/B=1.5

Figure 4.8(a-d): Discharge coefficient versus Froude Number with and without antivortex structures for eight steps under various L/B ratios.

Figure 4.9 shows the discharge coefficient versus the number of dimensionless step with and without antivortex structures. The discharge has a decreasing trend, and a more significant effect appears clearly for L/B ratios with a smaller ratio, and the (effect of N) decreases as this ratio increases. According to (Falvey, 2003), the discharge passing through the labyrinth weirs decreases as the number of cycles increases due to nappe interference, and the significant effect rises when the head increases and the angle between step sidewalls increases. As the number of steps increases, there are more effective crest length losses and higher detention flow on the weir apron; therefore, antivortex structures significantly improve the discharge coefficient and dissipate the vortex that extends along the Knope length (d). Figure 4.10 shows SLSW with four different types of antivortex structures for length ratios (L/B=1 and L/B=1.5) during labyrinth weir testing.

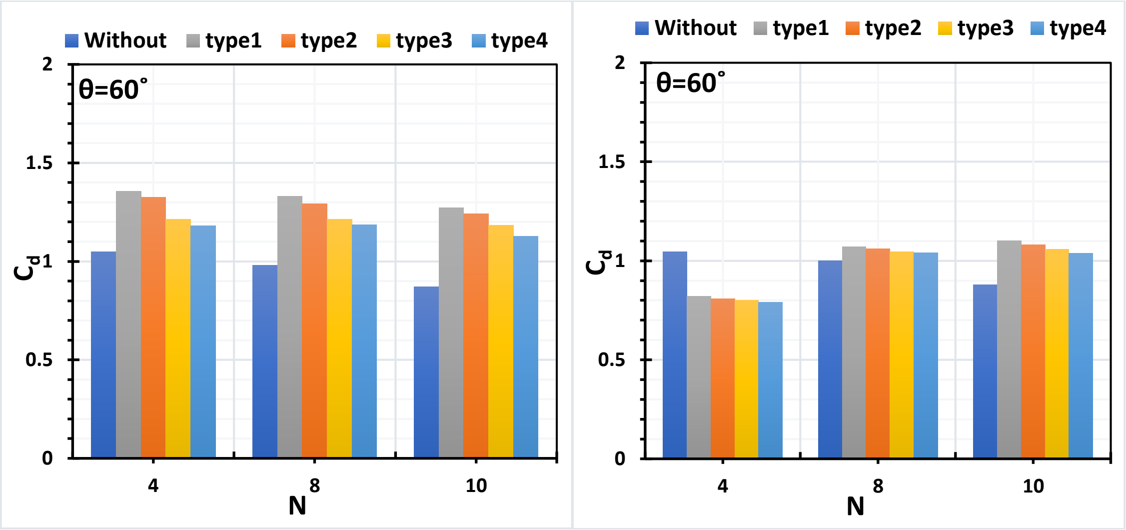

(a) L/B=1 (b) L/B=1.5

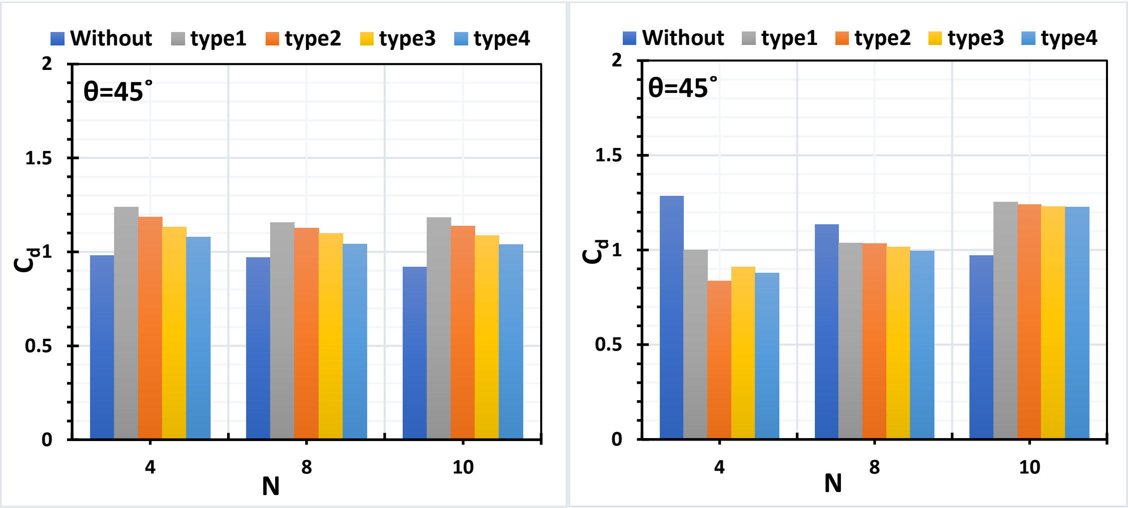

(c) L/B=1 (d) L/B=1.5

Figure 4.9: Variations in Discharge coefficient versus step number under different types of antivortex structures.

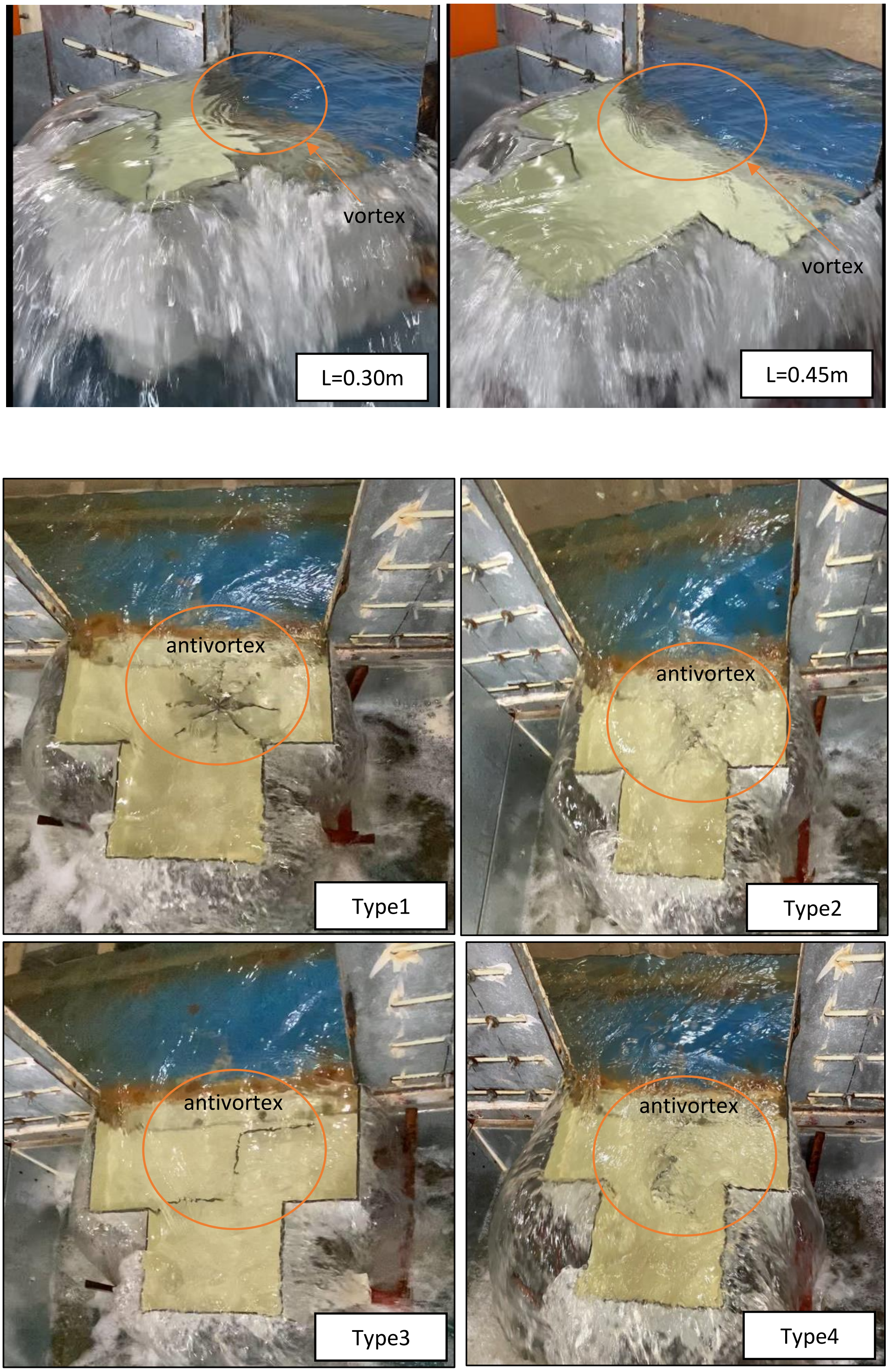

Figure 4.10a: Four step model with and without antivortex structures during experimental testing.

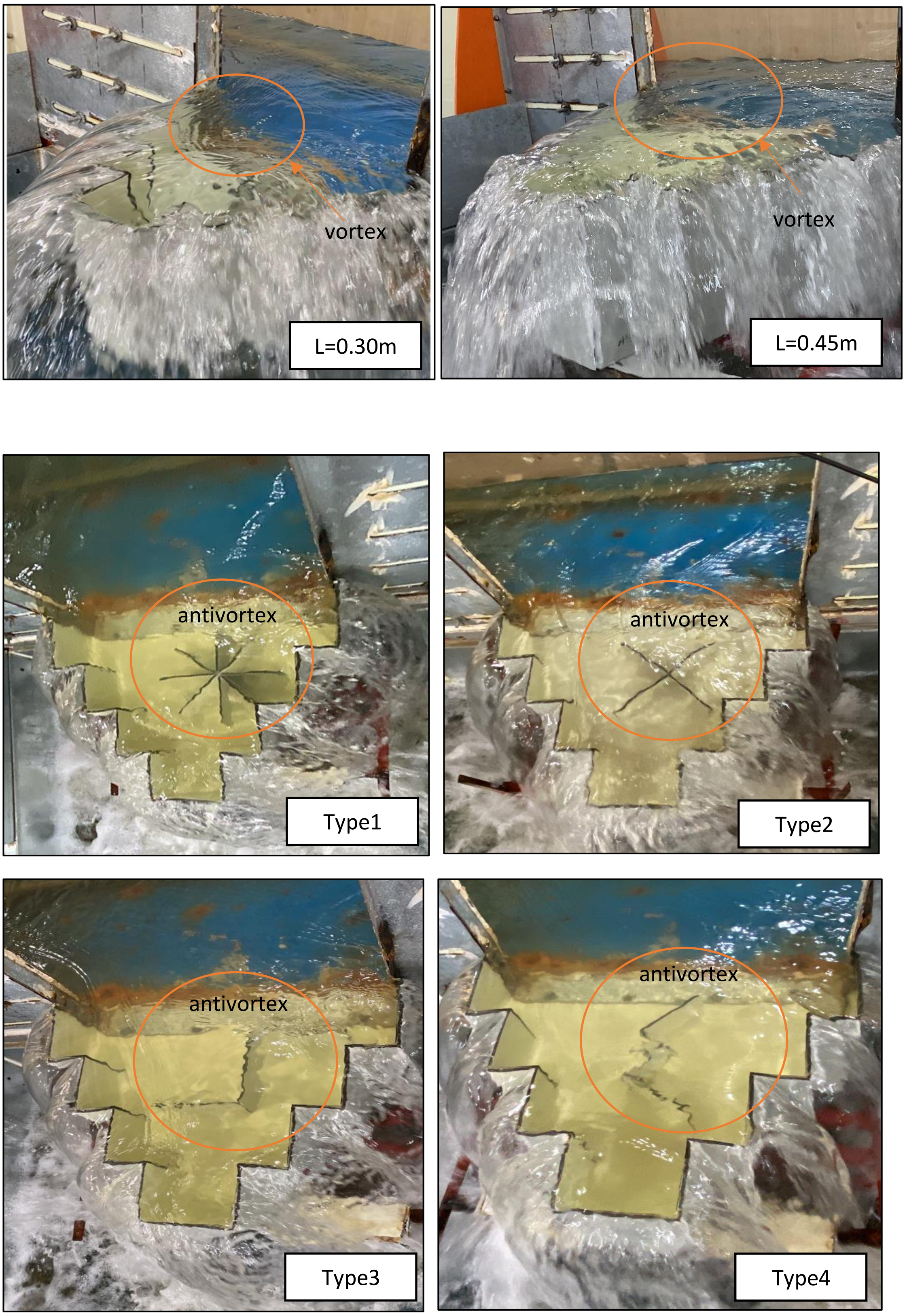

Figure 4.10b: Eight step model with and without antivortex structures during experimental testing.

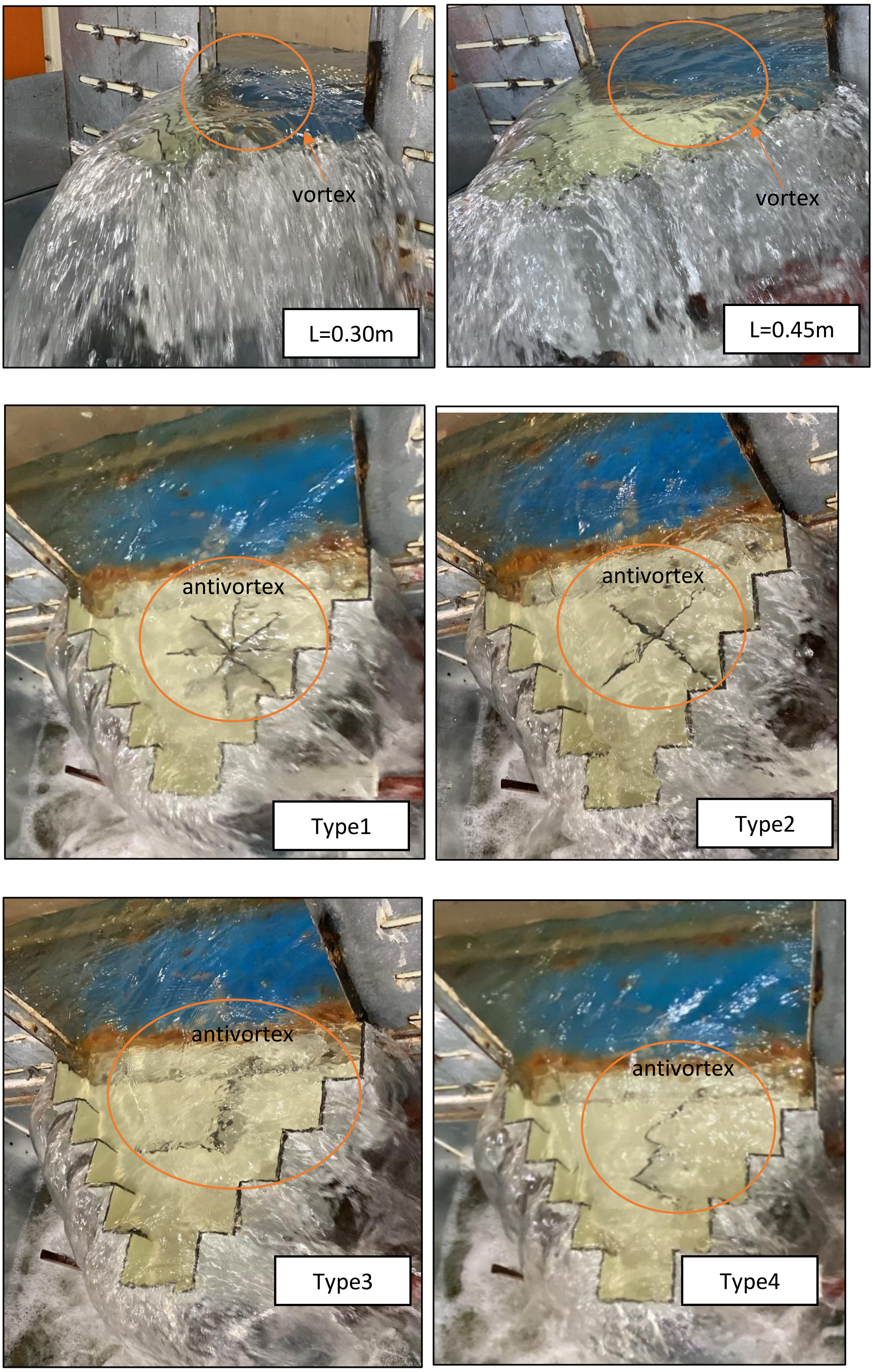

Figure 4.10c: Ten step model with and without antivortex structures during experimental testing.

4.1.3 Effect of Weir Height Ratio P/y1

The value of P/y_1 is plotted against the discharge coefficient to investigate the effect of ratio P/y_1 on the discharge coefficient (C_d) at various head angles (θ° = 45, 60), step numbers (N = 4, 8, and 10), and weir length ratios (L/B = 1 and L/B = 1.5) and compared with the case of with antivortex structures. Figures (4.11 to 4.12) show that C_d increases with the increase of dimensionless parameter (P/y_1), this behavior can be observed significantly for all weirs with and without antivortex structures, including different numbers of steps. The secondary motion can explain this behavior in the discontinuity region next to the side weir boundary. Due to friction, the secondary motion decreases as the weir height increases (Emiroglu et al., 2011), and the performance of antivortex structures improves. Due to an increase in the effective crest length and friction area, this parameter has a significant effect, especially for weirs with head angle $\theta = 45^\circ$. Antivortex structures significantly increase the discharge coefficient that improves weir performance and dissipate the vortex that extends along the length of weir because there are more effective crest length losses and higher detention flow on the weir apron as the number of steps increases (N).

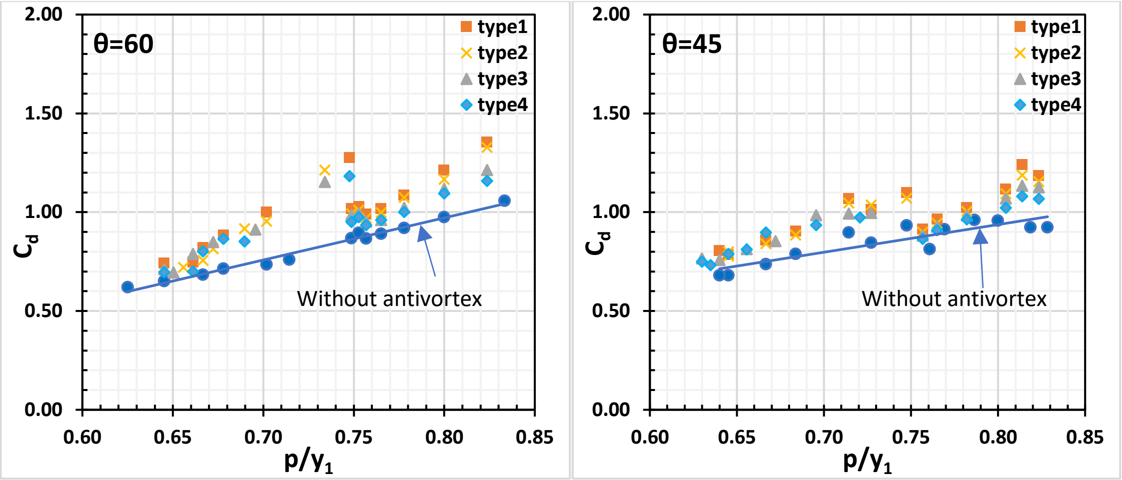

(a) N=4

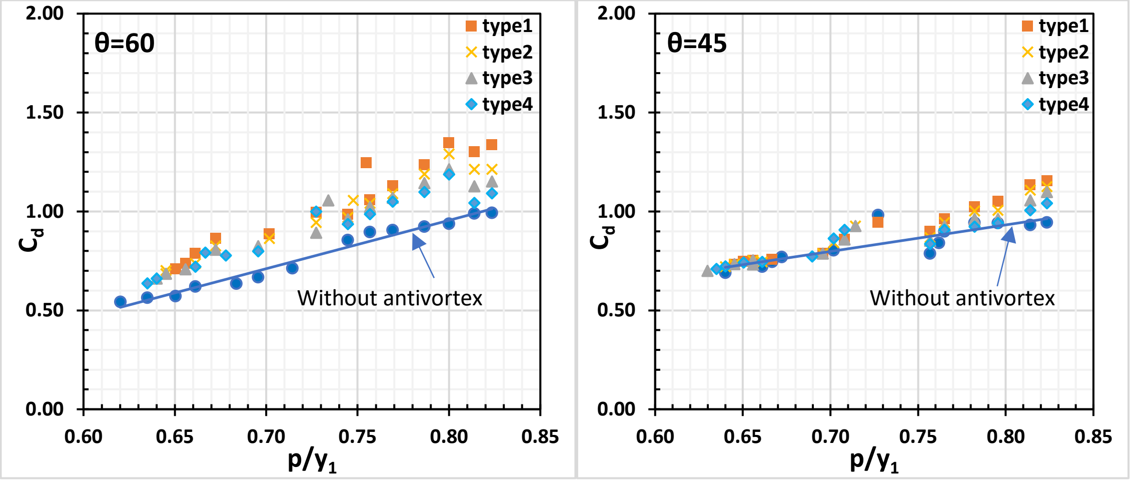

(b) N=8

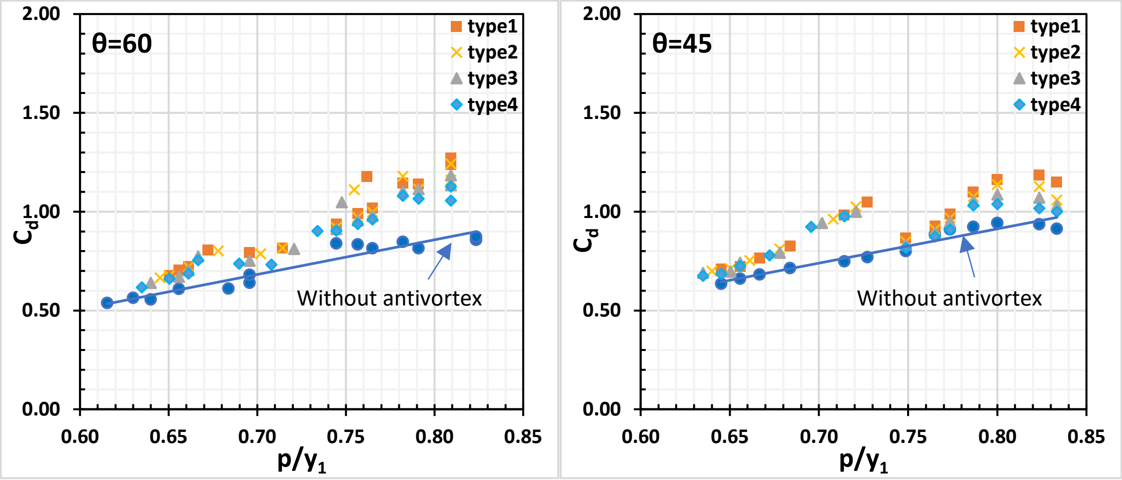

(c) N=10

Figure 4.11: Discharge coefficient against P/y_1 under various steps number with L/B=1.

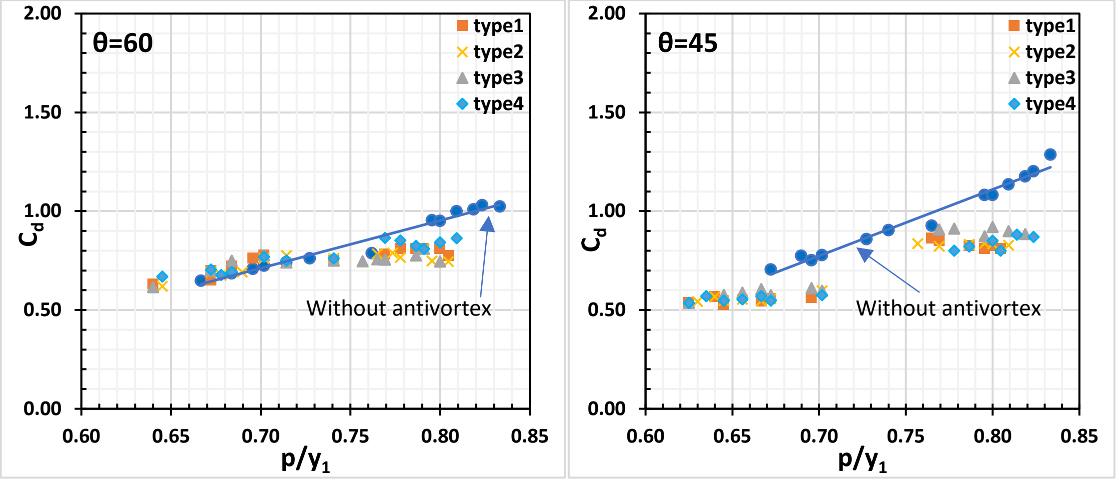

(a) N=4

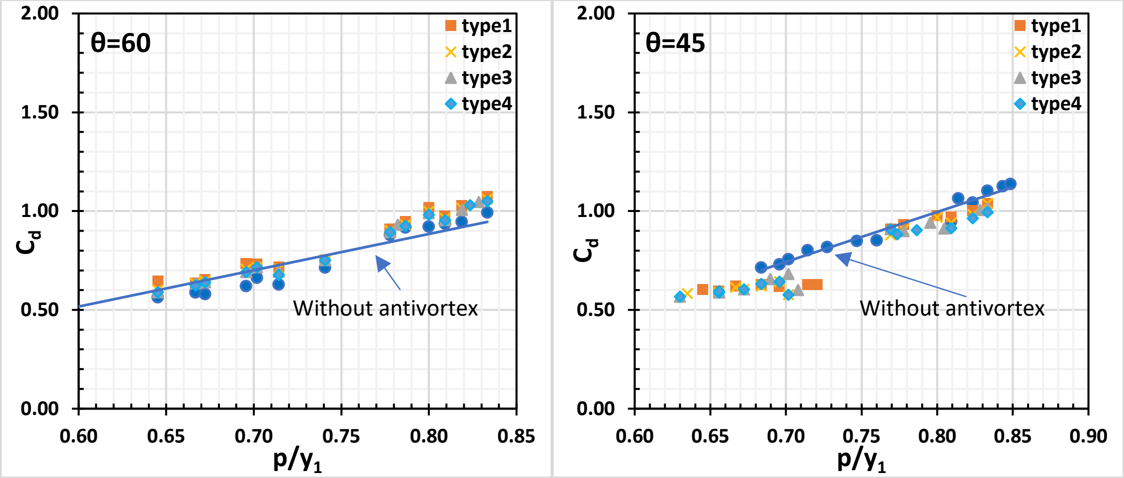

(b) N=8

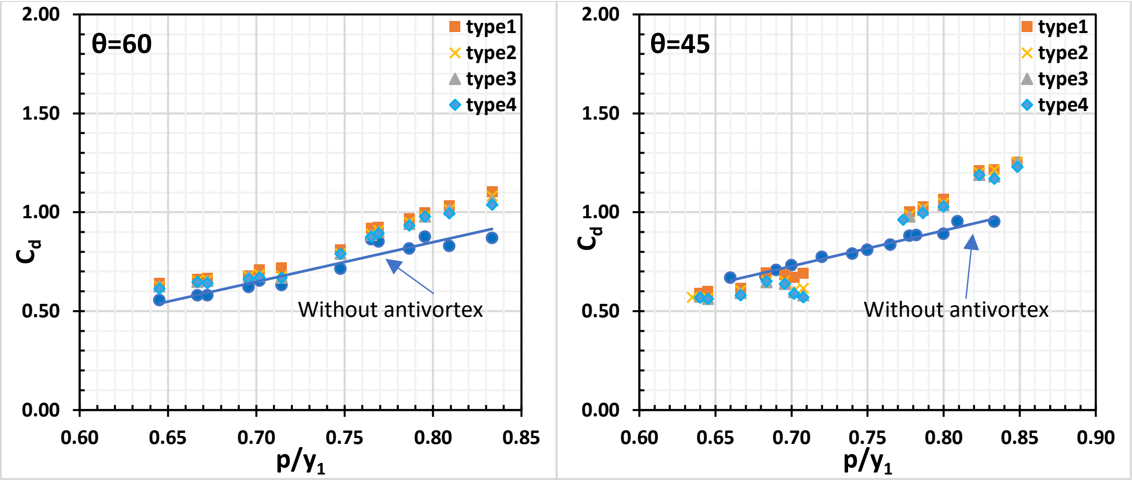

(c) N=10

Figure 4.12: Discharge coefficient against P/y_1 under various steps number with L/B=1.5.

4.2 Effect of Nappe Height (y_1-p)/p

Figures (4.13 and 4.14) show a plot of the discharge coefficient against the water depth ratio (y_1-p)/p measured at the upstream end of the weir for stepped LSW models with the same effective crest length and different step numbers at (L/B=1.5 and 1) and a range of internal head angles (θ°=45,60) compared with the case of installing antivortex structures. The relationships are shown in Figures 4.13 and 4.14 highlight the effects of essential variables separately. The descending nature of C_d against (y_1-p)/p indicates that an increase in nappe over the weir for the same height of the weir and step numbers and weir length ratio causes a decrease in C_d, which is consistent with other studies. According to Tullis et al., (1995), discharge capacity in labyrinth side weirs decreases as nappe load increases. Emiroglu et al., (2011) demonstrated empirically that discharge capacity decreased as nappe load increased. The installation of antivortex structures increases the weir discharge capacity at similar flow depths with an increase in the step number, despite the data points having an almost random distribution. Furthermore, the discharge capacity decreases as the depth of the flow increases. C_d values are higher in large L/B side weirs with antivortex structures than in small L/B side weirs.

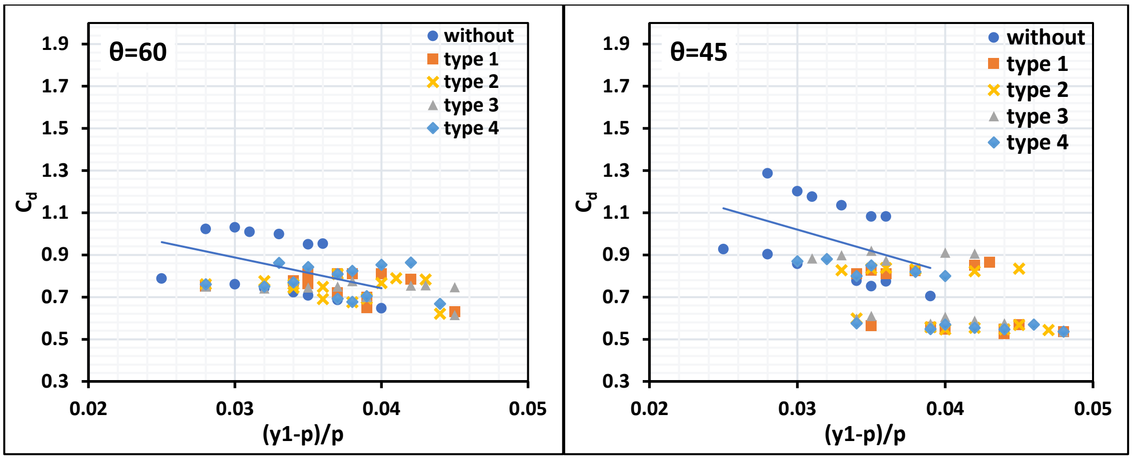

(a) N=4

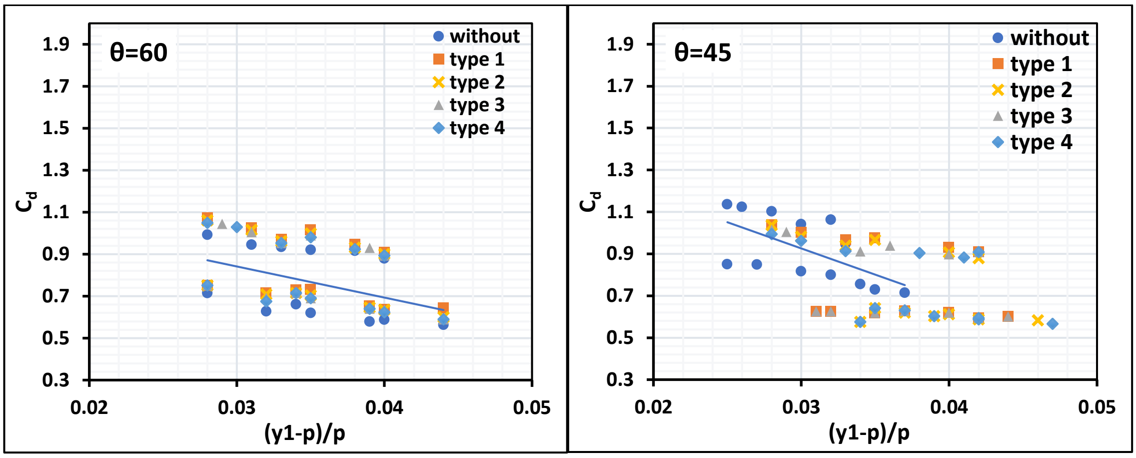

(b) N=8

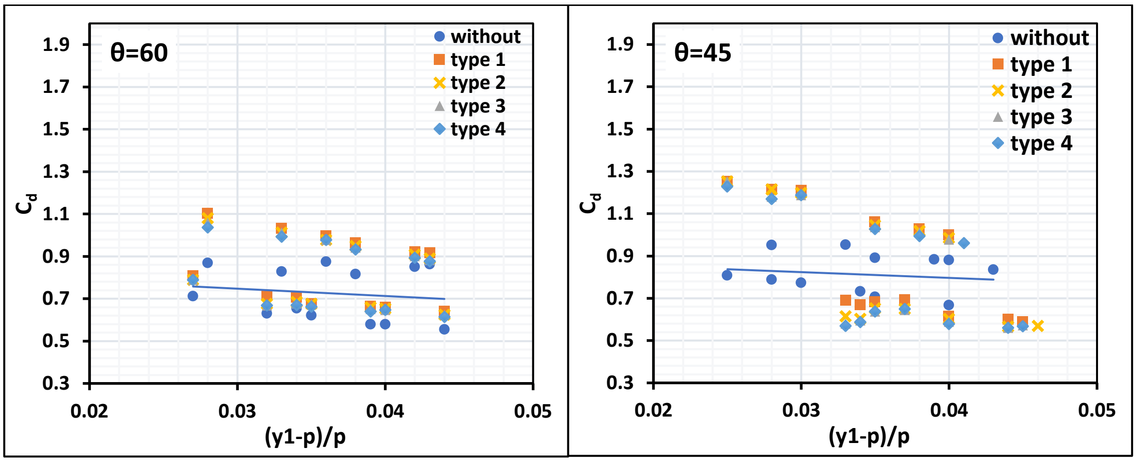

(c) N=10

Figure 4.13: Discharge coefficient versus water depth ratio $(y_1\text{-}p)/p$ compared with a case of antivortex structures under various head angles with L/B=1.5.

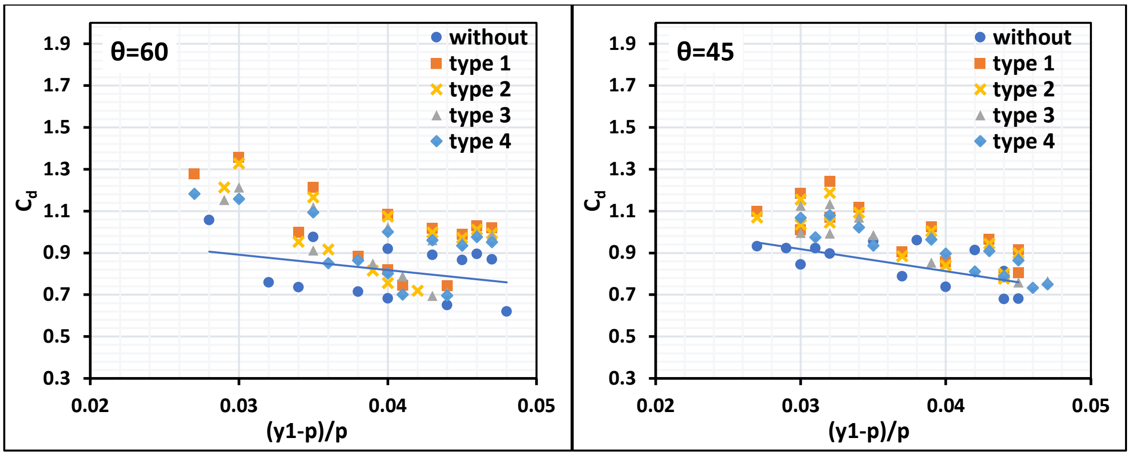

(a) N=4

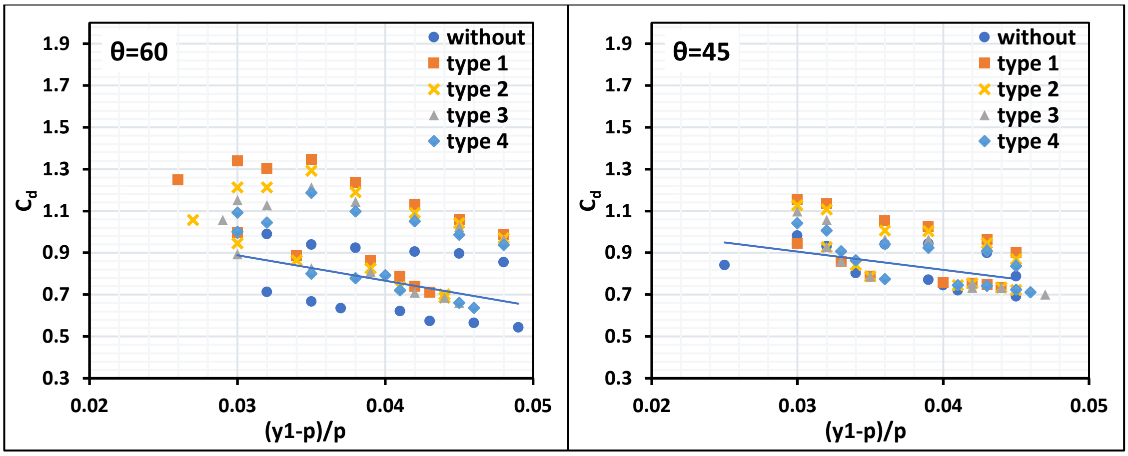

(b) N=8

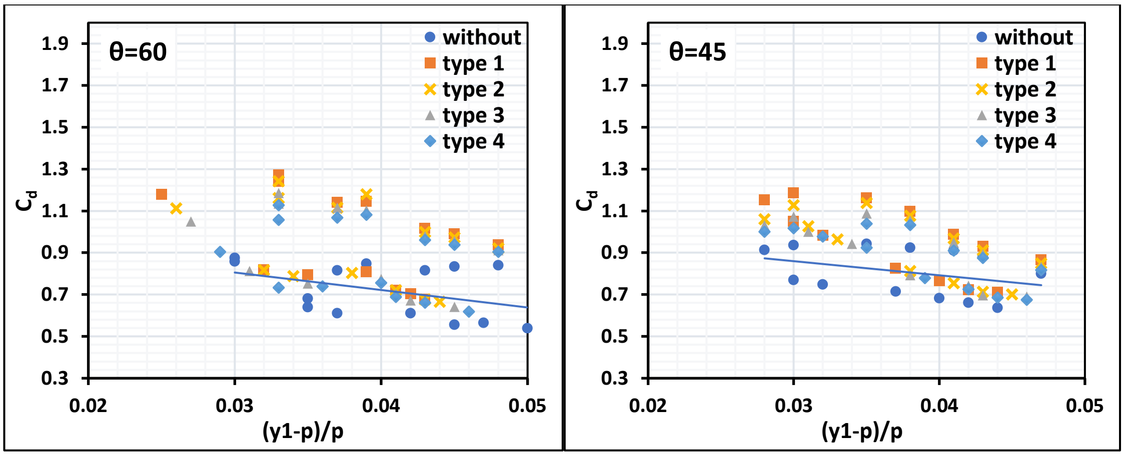

(c) N=10

Figure 4.14: Discharge coefficient versus water depth ratio $(y_1\text{-p})/p$ compared with a case of antivortex structures under various head angles with L/B=1.

4.2 Hydraulic Performance of Stepped LSW

4.2.1 Water Surface Profile of Stepped LSW Models

Water levels are measured along the main flume centreline (section B-B) and the weir side (section A-A) (as shown in Figure (3.6)). The flow pattern surface has been studied in three different models of LSW: (N= 4, 8, and 10), θ =60°; L/B=1, and compared with the two types of antivortex that showed the best performance. The water level at the upstream end of the side weir is lower than at the downstream end, as shown in Figures (4.15 to 4.17). The same effect occurred in all experiments. It is due to the influence of the upstream end of the side weir entrance. Furthermore, Emiroglu et al., (2011) and Khameneh et al., (2014) reached similar conclusions. The water level rapidly increases as it approaches the downstream weir end. This behavior of the water surface results from the secondary flow created by lateral flow. A separating zone and reverse flow are also observed at the side weir downstream end. A separation zone exists due to a deflection that occurs away from the path of the maximum velocity thread. The Froude number F_1, head angle θ, L/B ratios, and the number of steps are essential in determining where are the separation zone and the reverse flow area . With an increase in F_1, the separation zone and reverse flow area converge toward the side weir's downstream end. The results showed that as the number of steps increases, the water surface along the side weir in the main flume (sections A-A, and B-B) becomes more divergent and disturbed, moreover, the flow surface level variations at the beginning and end of the side weir increase noticeably, section A-A has a higher water surface drop at the beginning of the side weir, especially with four steps. The drop decreases as the number of steps increases. The primary cause of a fluctuating water surface profile with more steps is the steps junction points approaching in front of the weir opening, this reduces the input area and increases collision flow, which causes a poor jump on the crest weir and more returning flow into the main flume, as well as disturbance of the flow surface. At low Froude numbers, F_1 (approximately $F_1 < 0.45$), installing an antivortex does not generate significant changes in surface profiles, it simply causes a slight drop in the water surface level, which also means that side weir discharge has increased.

The variations on the water surface are reduced with antivortex for larger Froude values ($F_1 > 0.45$), resulting in the more uniform water surface on the stepped side weir, the more efficient and uniform the discharge as the number of steps increases. Aydin & Ulu, (2017) and Abbasi et al., (2020) also indicate the same results. However, beyond surface fluctuations, the vortex effects on the performance of the labyrinth side weir are more substantial, especially at larger Froude numbers. As a result, antivortex use can improve discharge efficiency by reducing vortex formation and surface fluctuation.

Figures (4.15 to 4.17), also, show that the water surface level at the main flume centreline is nearly horizontal. Furthermore, this demonstrates that the side weir entrance effect does not extend as far as the main flume centreline but occurs only near the weir crest. Because of uniform flow conditions, as previously indicated, most previous studies employed the flow depth at the upstream end of the side weir at the flume center. (for example,(Subramanya & Awasthy, (1972); Hager, (1987); Singh et al., (1994); Borghei et al., (1999); Emiroglu et al., (2011); Aydin & Ulu, (2017); Abbasi et al., (2020)). As a result, this study has considered the same flow depth (y_1) as previous research. Thus, the results of the current study are compared to those of previous studies.

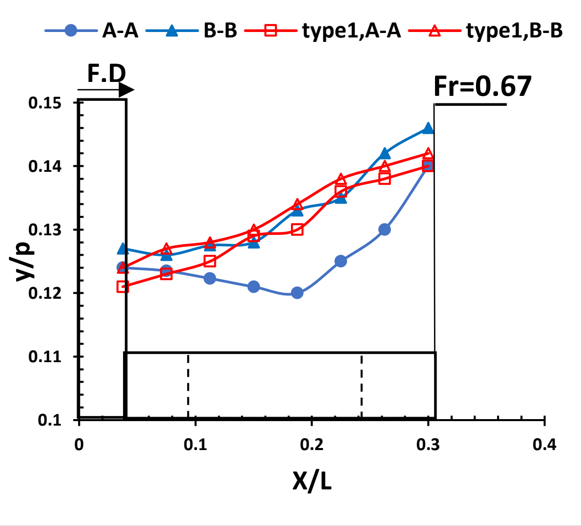
A-A
B-B
type1,A-A
type1,B-B
F.D
Fr=0.67
y/p
0.1
0.11
0.12
0.13
0.14
0.15
0
0.1
0.2
0.3
0.4
X/L

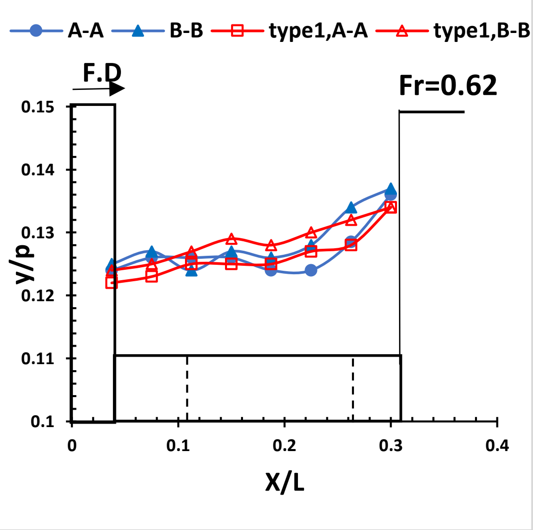
A-A
B-B
type1,A-A
type1,B-B
F.D
Fr=0.62
y/p
0.1
0.11
0.12
0.13
0.14
0.15
0
0.1
0.2
0.3
0.4
X/L

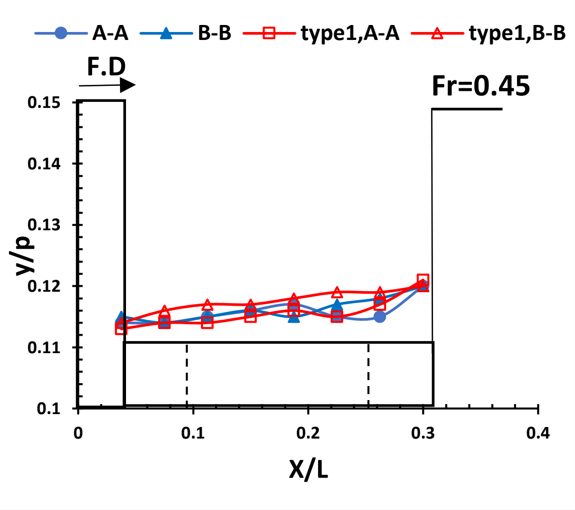
A-A
B-B
type1,A-A
type1,B-B
F.D
Fr=0.45
y/p
0.1
0.11
0.12
0.13
0.14
0.15
0
0.1
0.2
0.3
0.4
X/L

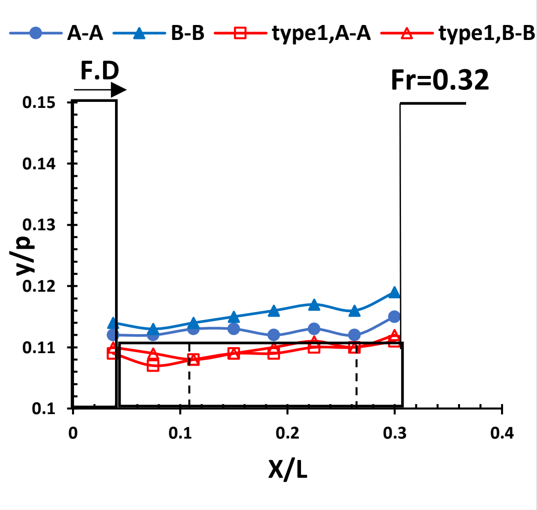
A-A
B-B
type1,A-A
type1,B-B
F.D
Fr=0.32
y/p
0.1
0.11
0.12
0.13
0.14
0.15
0
0.1
0.2
0.3
0.4
X/L

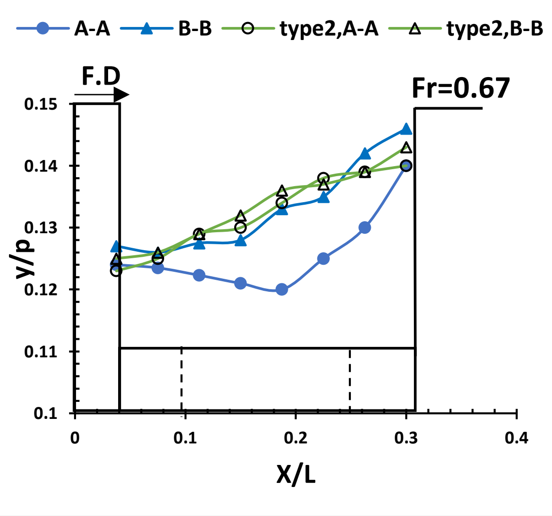
A-A
B-B
type2,A-A
type2,B-B
F.D
Fr=0.67
y/p
0.1
0.11
0.12
0.13
0.14
0.15
0
0.1
0.2
0.3
0.4
X/L

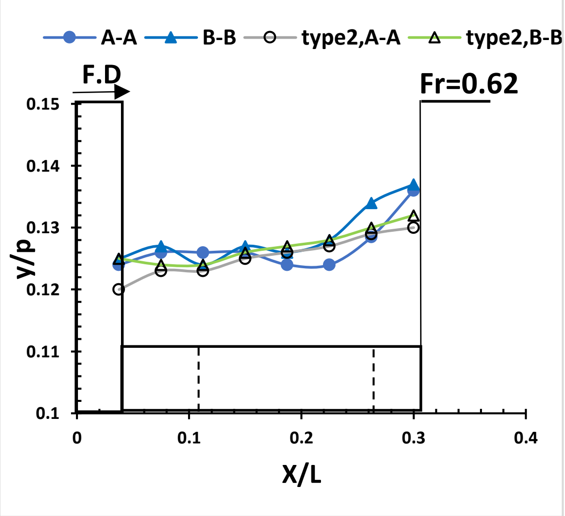
A-A
B-B
type2,A-A
type2,B-B
F.D
Fr=0.62
y/p
0.1
0.11
0.12
0.13
0.14
0.15
0
0.1
0.2
0.3
0.4
X/L

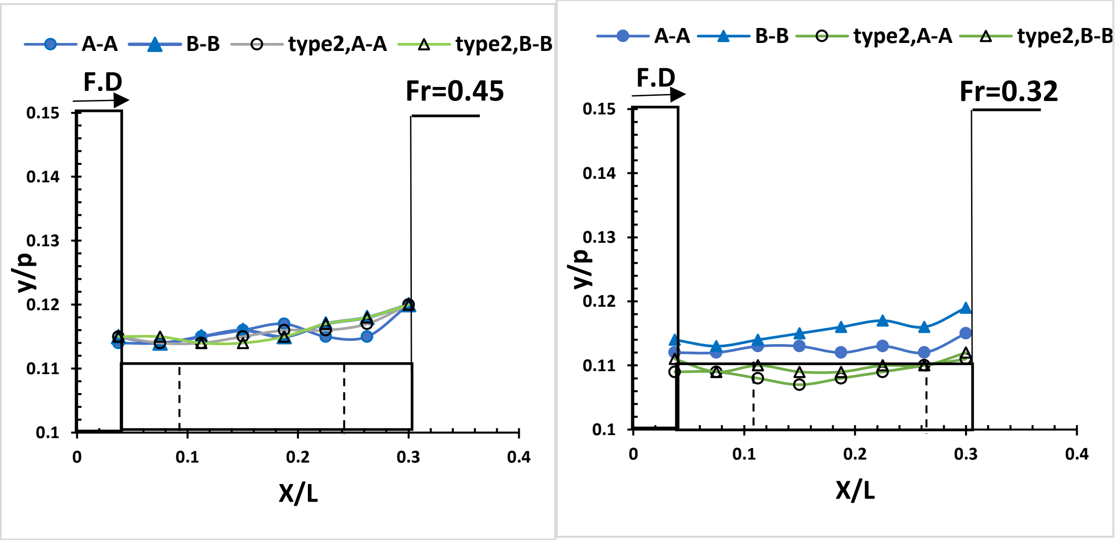

Figure 4.15: Water surface profile near the stepped labyrinth side weir with antivortex structures for four steps model.

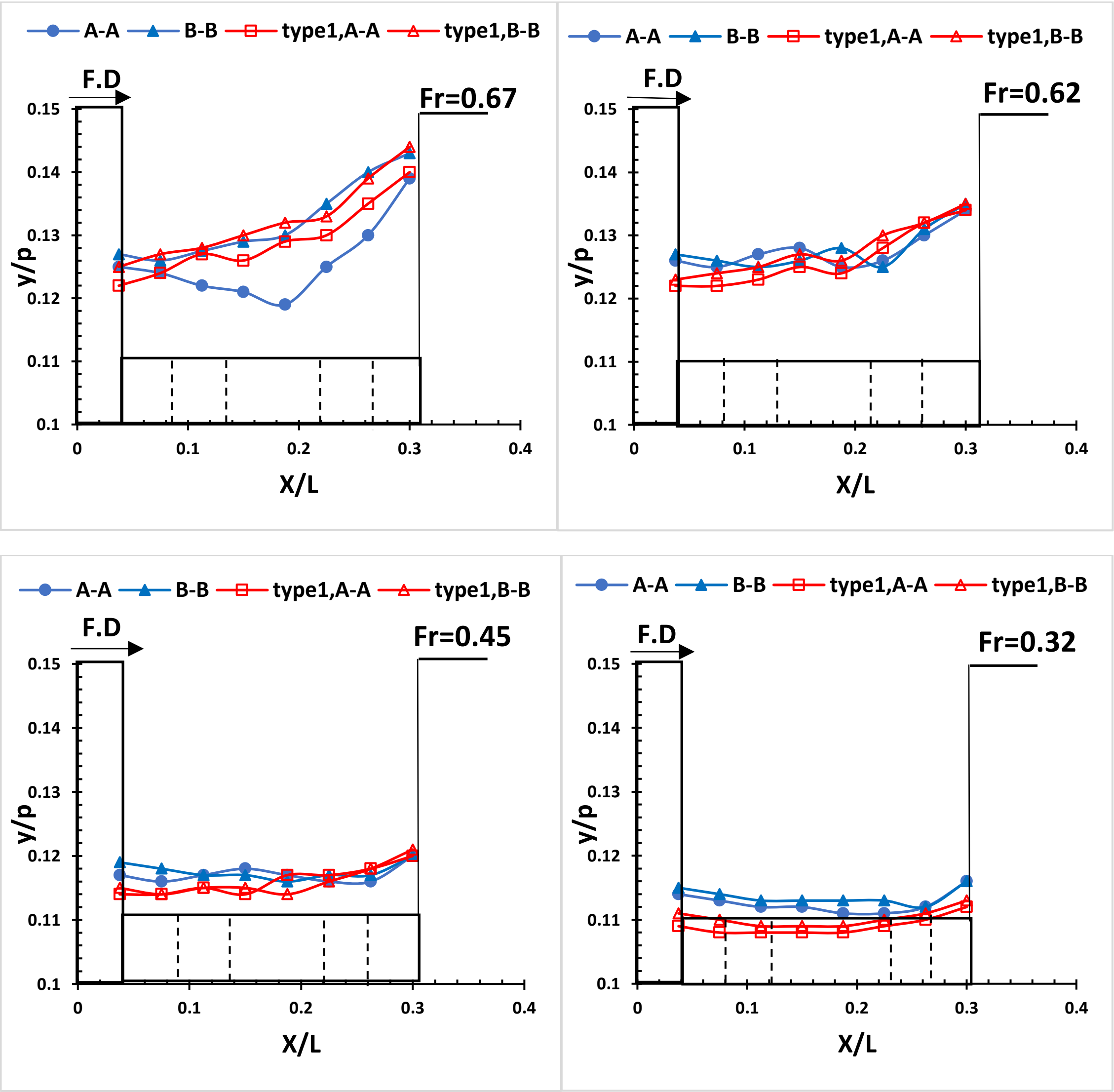

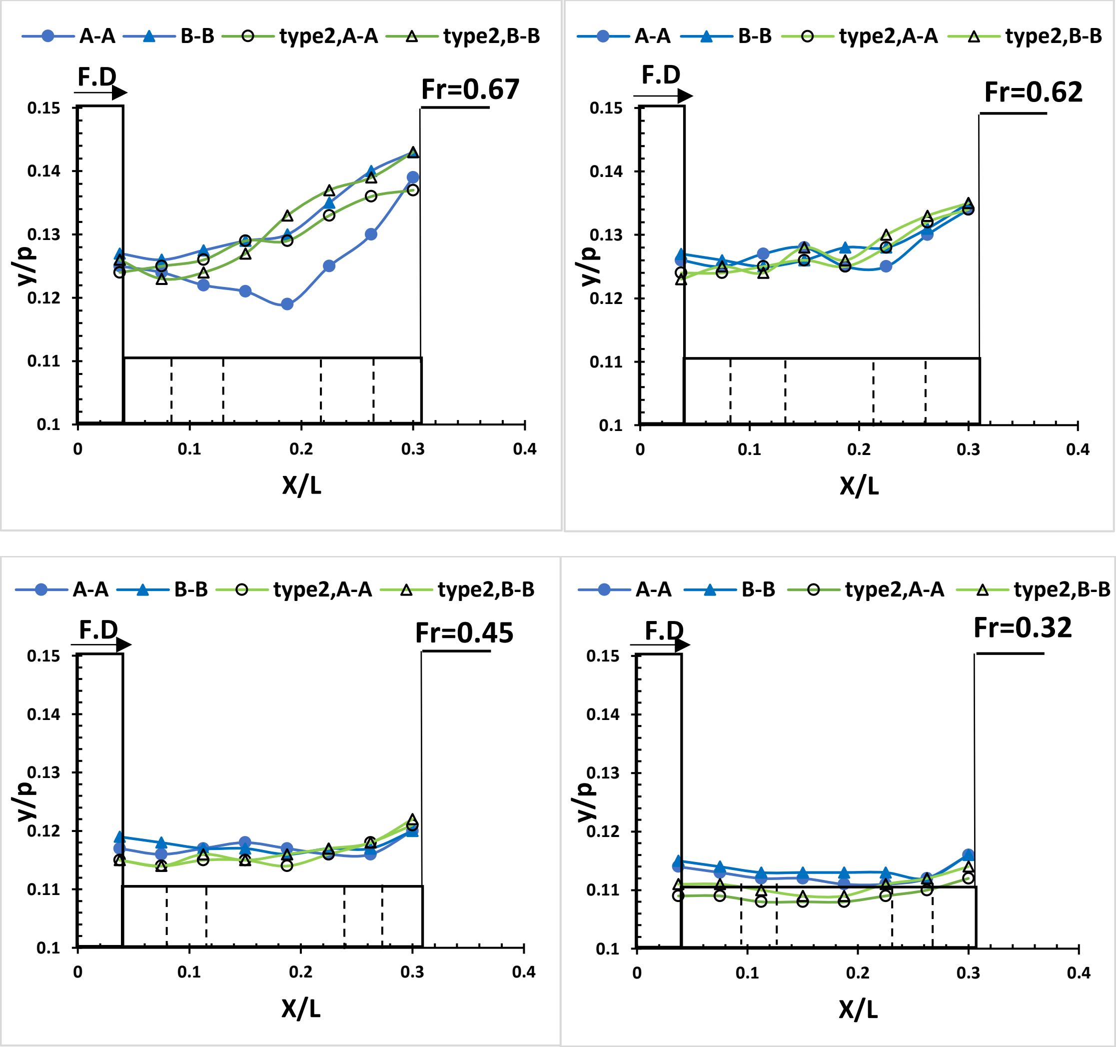

Figure 4.16: Water surface profile near the stepped labyrinth side weir with antivortex structures for eight steps model.

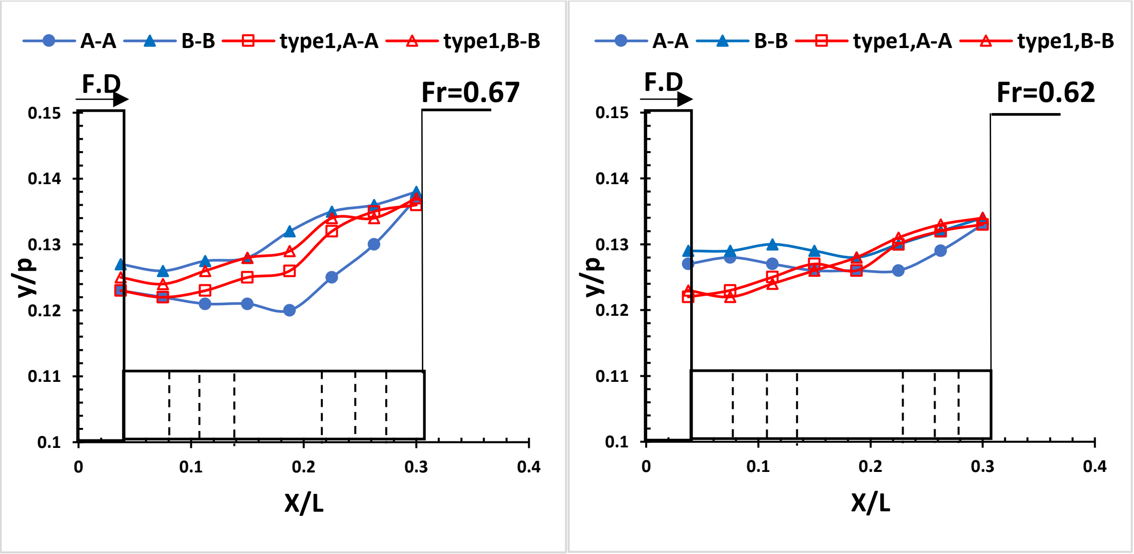

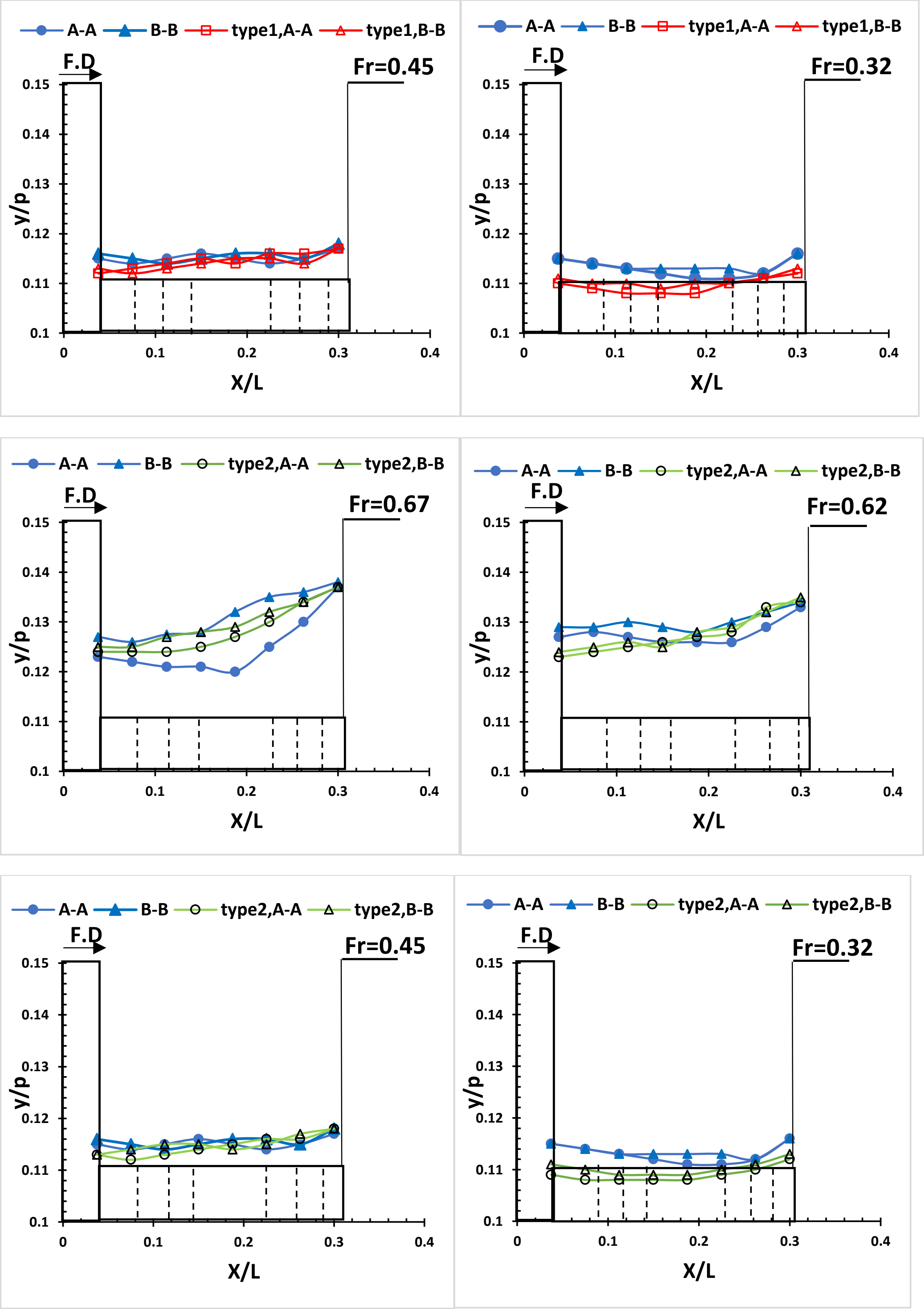

Figure 4.17: Water surface profile near the stepped labyrinth side weir with antivortex structures for ten steps model.

4.2.2 Turbulence and Secondary Flow Fields

Secondary flow in the labyrinth side weir is another critical factor influencing the discharge coefficient, as seen in Figures 4.18 to 4.30.

The intensity of secondary flow is determined by the lateral flow's kinetic energy ratio to the main flume's average kinetic energy. As a result, secondary flow intensity is a function of $(V_s\text{-}V_b)/V_1$, where V_s and V_b surface and near bed transverse velocities, respectively, and V_1 is the velocity upstream of the side weir. These currents are greater than the secondary currents in the main flume upstream of the weir because they are affected by the weir sidewalls and the accelerating flow near the weir (Oreizi et al., 2015). The secondary currents of the stepped labyrinth weirs are found to vary more significantly than those of the triangular labyrinth weirs. Figures (4.18 to 4.21) show the secondary current intensity distributions for the vortices with distance for both stepped and triangular labyrinth weirs at different dimensionless weir heights (p=0.08m and 0.14m) and head angles (θ°=60 and 45). The intensity of this secondary motion along the boundary is governed by the side weir's crest height, the number of steps, and head angle. It is increases with the decrease of the crest height and head angle. This result is similar to previous research. For instance, (Emiroglu et al., 2011) concluded that the secondary motion near the boundary is influenced by the crest height of the side weir and reduces as the crest height of the side weir increases owing to friction on the weir surface, also the intensity of secondary motion caused by lateral flow increases as the overflow length increases. When the relative side weir length grows, the deviation angle and kinetic energy toward the side weir grow as the secondary flow increases. According to these Figures (4.18 to 4.21), maximum intensity is produced at the downstream end of the side weir (section A-A) at point (2), especially in four steppes for crest height (p=0.08m) and weir angle (θ=45), because the sides of the step restrict the vortices, their area of influence is limited to the length of the side weir. In sections (B-B) and(C-C) as shown in Figure (3.6), the influence is more significant in point (2) that has the lowest value because of vortex formation, preventing entering currents from reaching the entire length of the downstream crest. The secondary flow intensity near the side weir's beginning is higher than at the side weir's apex. Abbasi et al., (2020) and Ansari & Patil, (2022) also found the same pattern of variation in their investigations in triangle LSW. However, given the same conditions, the average turbulence intensity of the stepped weir is approximately 15% higher than that of the triangular weir. According to these findings, the shape of the weirs increases the turbulence intensity and secondary currents.

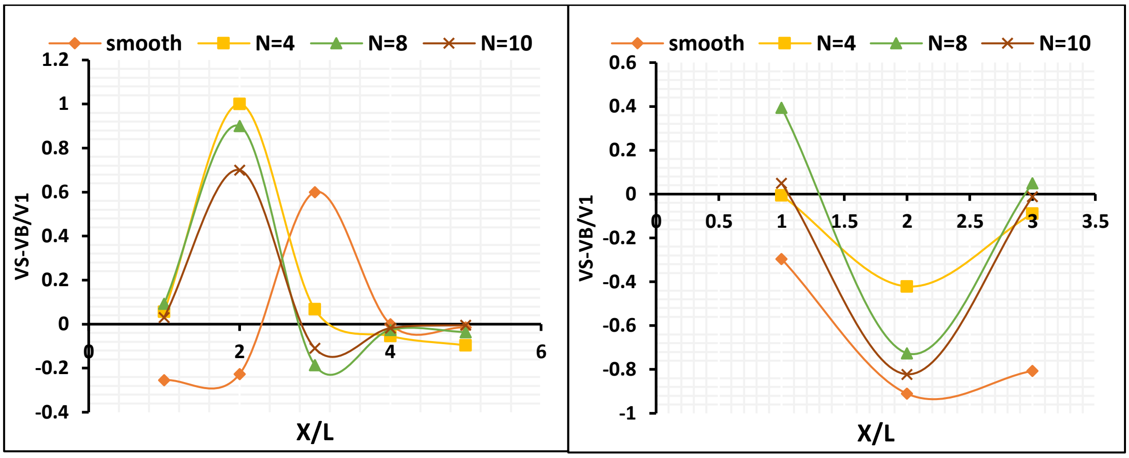

Section(A-A) Section(B-B)

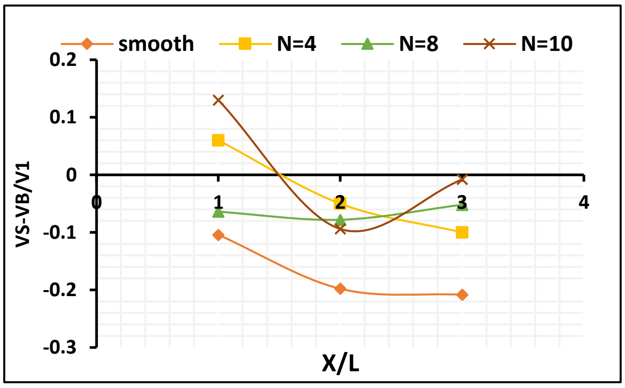

Section(C-C)

Figure 4.18: The secondary flow intensity along the stepped and triangular labyrinth side weir (p=0.08m, θ=45).

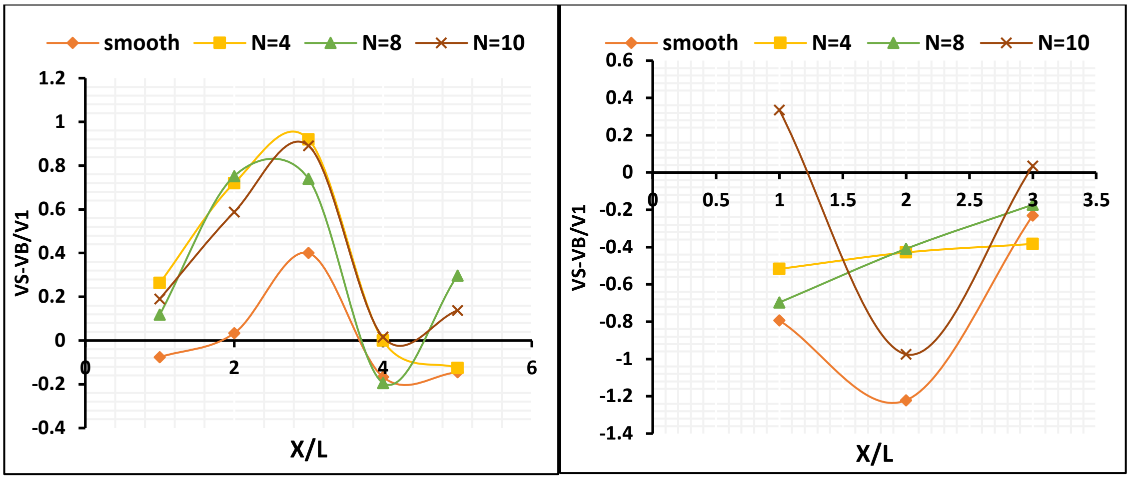

Section(A-A) Section(B-B)

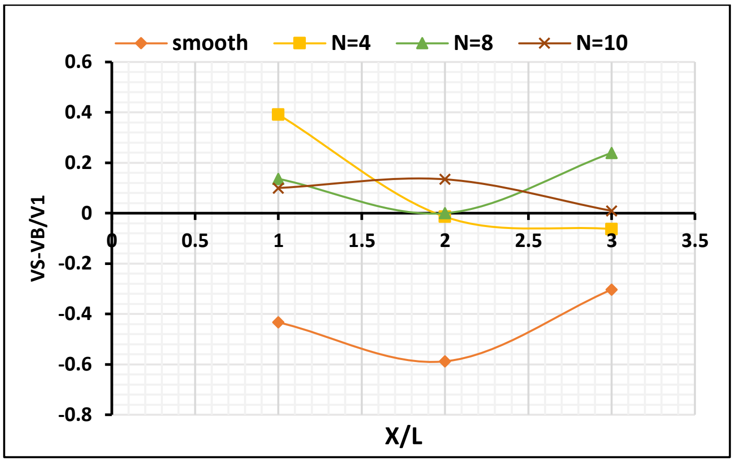

Section(C-C)

Figure 4.19: The secondary flow intensity along the stepped and triangular labyrinth side weir (p=0.14m, θ=45).

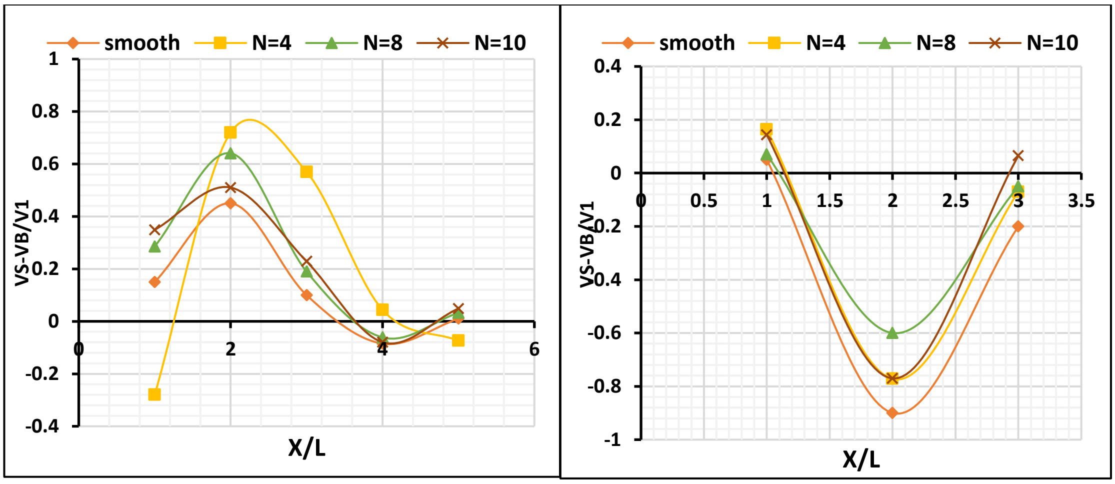

Section(A-A) Section(B-B)

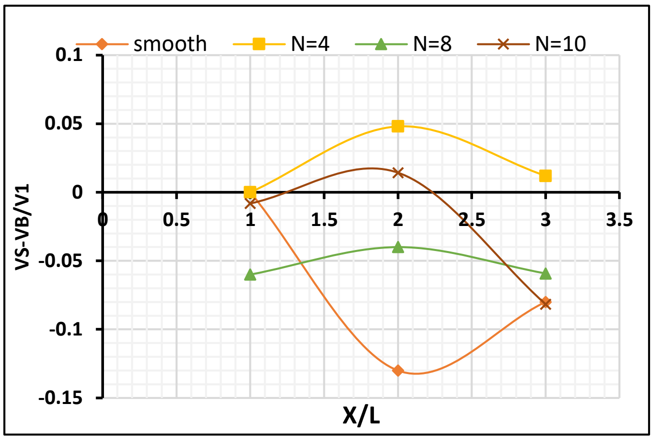

Section(C-C)

Figure 4.20: The secondary flow intensity along the stepped and triangular labyrinth side weir (p=0.08m, θ=60).

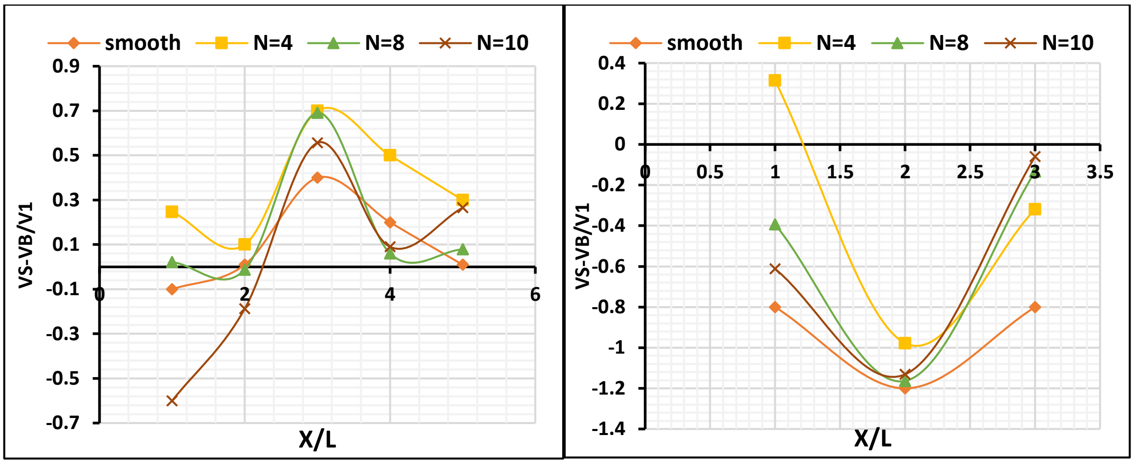

Section(A-A) Section(B-B)

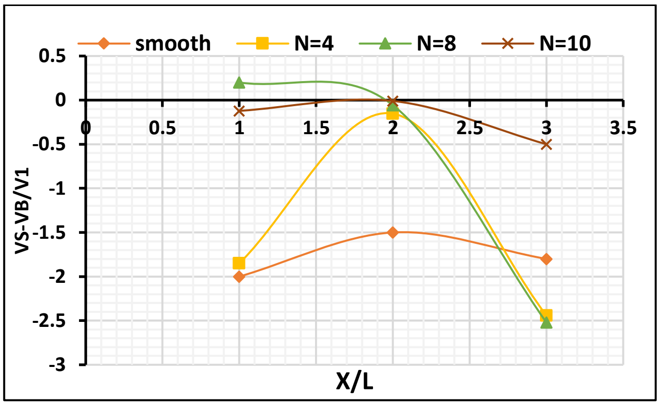

Section(C-C)

Figure 4.21: The secondary flow intensity along the stepped and triangular labyrinth side weir (p=0.14m, θ=60).

The antivortex decreases the velocity of flow inside the side weir. The intensity of the secondary flow inside the side weir decreases as the flow velocity lowers, which significantly affects the discharge performance. A vortex forms at the upstream end of the labyrinth side weir, with a larger diameter in sections A-A than in the other sections. The hydraulic performance of the side weir decreases when the intensity of the secondary motion caused by lateral flow increases as the Froude number increases. By lowering secondary motion, the antivortices increase the side weir's discharge coefficient, improving the side weir's performance, and preventing surface fluctuations and vortex formation from occurring in the downstream crest. By comparing different types of antivortex structures, the type1 outperforms other types by decreasing the amount of secondary motion by approximately 9%. Abbasi et al., (2020) also concluded the same results and mentioned that the flow path changed from the main channel to the side weir, and the flow entering the side weir generated significant vortices inside the triangular LSW. Thus, installing antivortex structures improved the hydraulic performance of the triangular LSW and reduced the intensity of the secondary flow. see Figures (4.23 to 4.31).

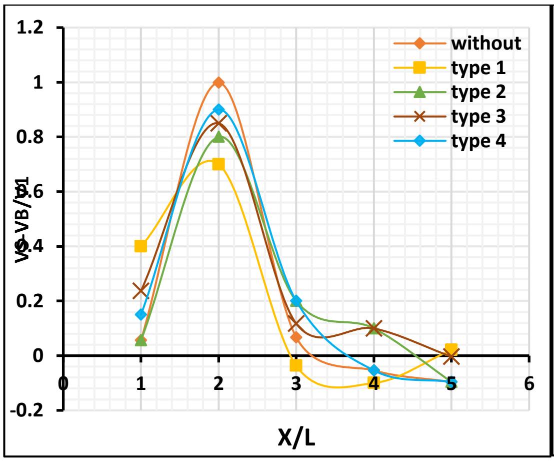

Section(A-A)

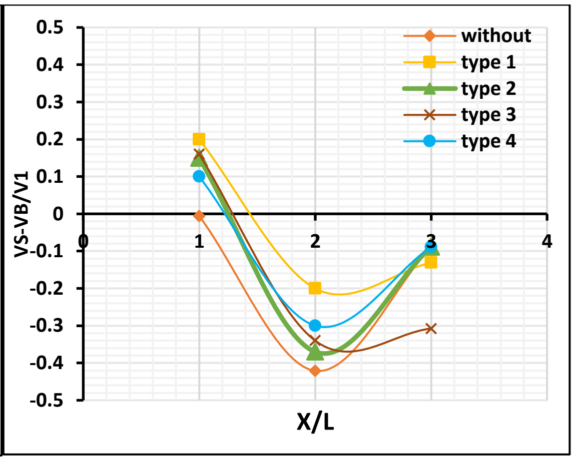

Section(B-B)

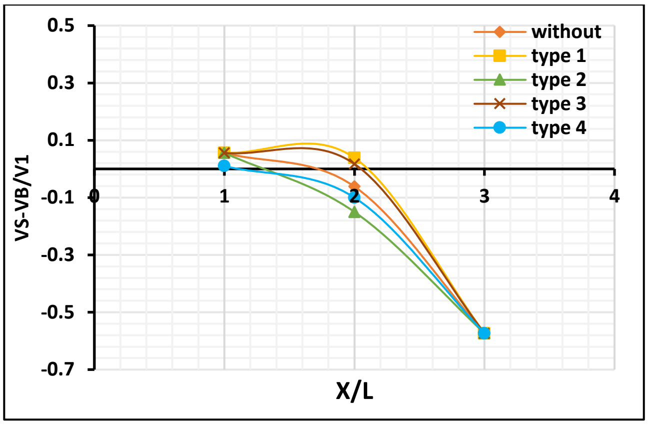

Section(C-C)

Figure 4.22: The secondary flow intensity along the stepped labyrinth side weir with and without antivortex for four steps (p=0.08m, θ=45).

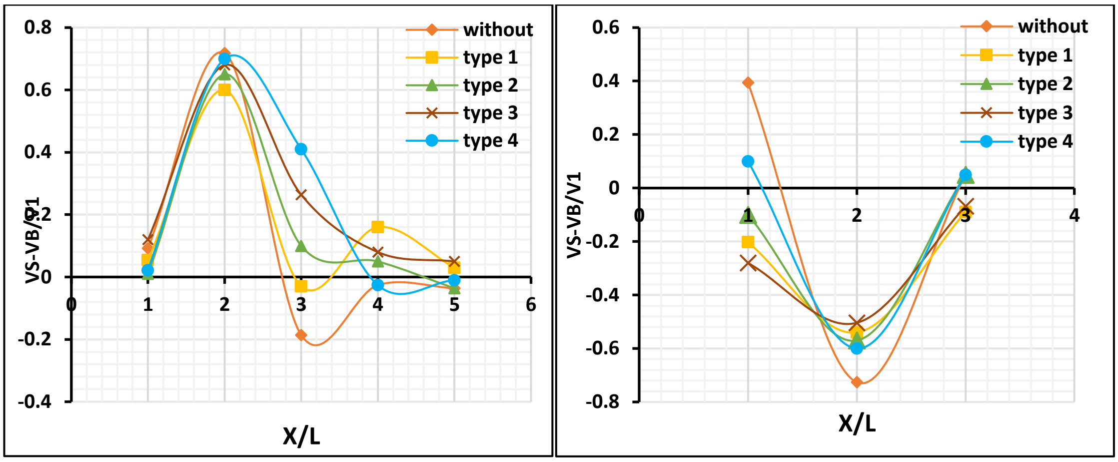

Section(A-A) Section(B-B)

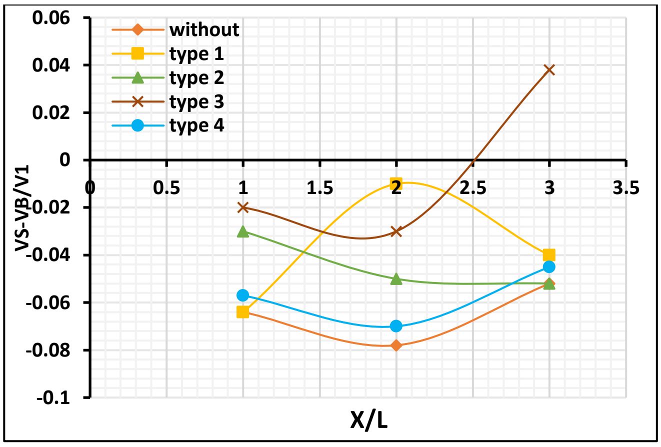

Section(C-C)

Figure 4.23: The secondary flow intensity along the stepped labyrinth side weir with and without antivortex for eight steps (p=0.08m, θ=45).

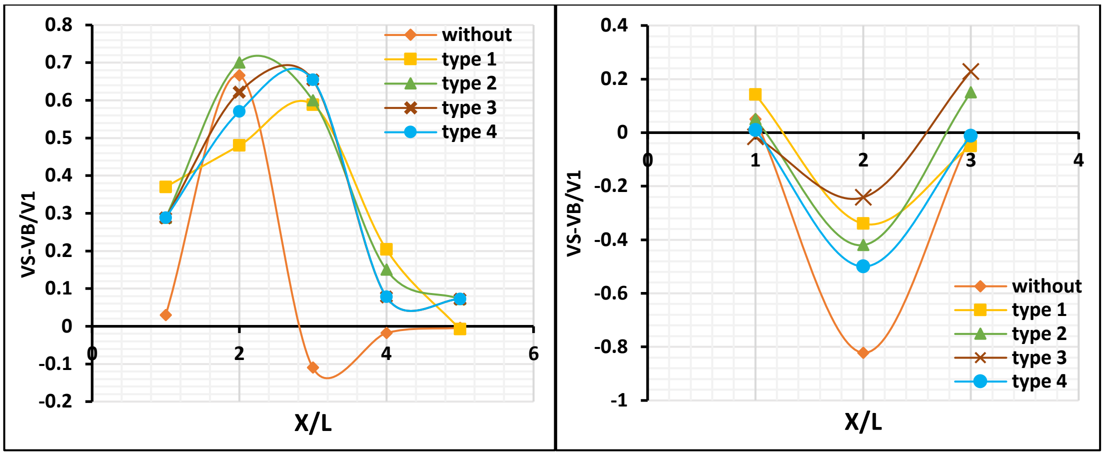

Section(A-A) Section(B-B)

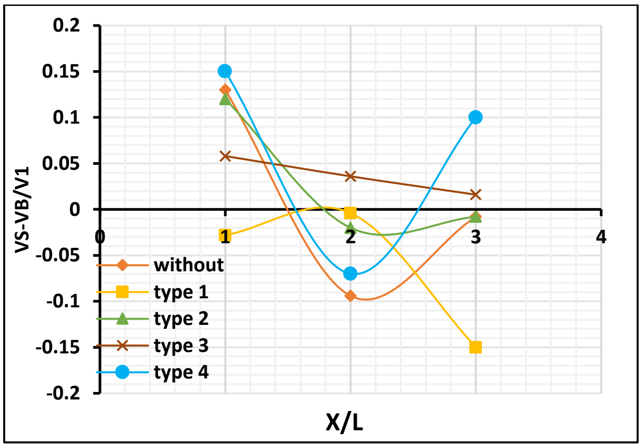

Section(C-C)

Figure 4.24: The secondary flow intensity along the stepped labyrinth side weir with and without antivortex for ten steps (p=0.08m, θ=45).

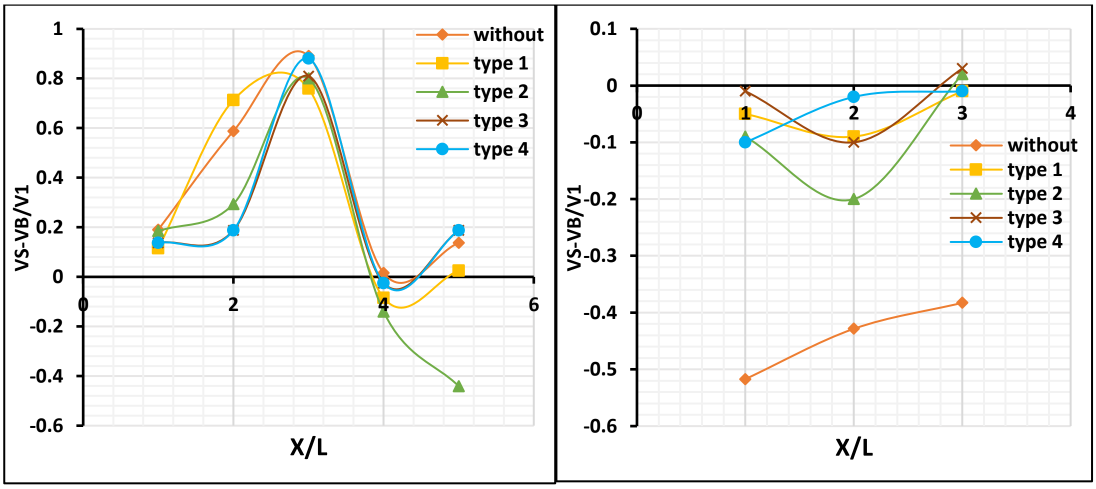

Section(A-A) Section(B-B)

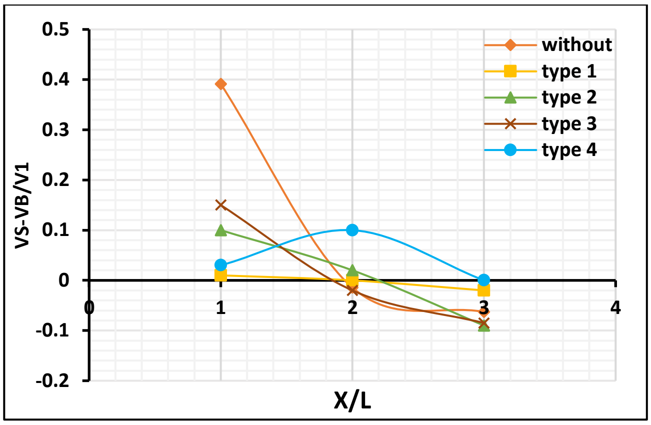

Section(C-C)

Figure 4.25: The secondary flow intensity along the stepped labyrinth side weir with and without antivortex for four steps (p=0.14m, θ=45).

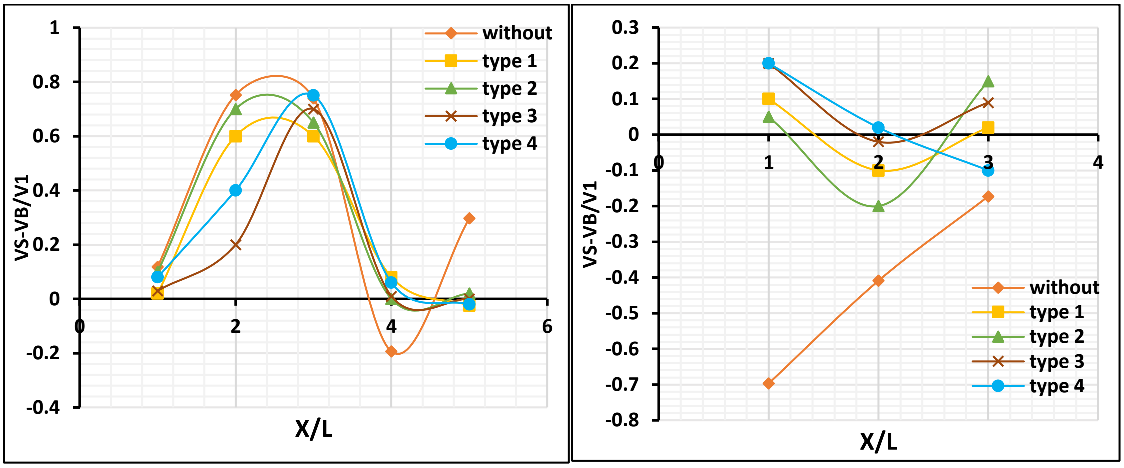

Section(A-A) Section(B-B)

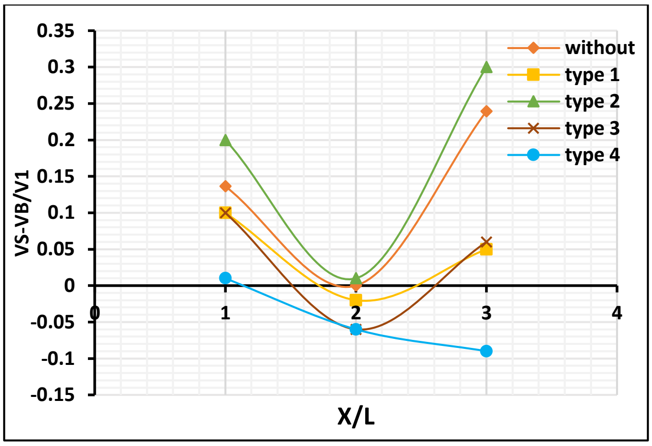

Section(C-C)

Figure 4.26: The secondary flow intensity along the stepped labyrinth side weir with and without antivortex for eight steps (p=0.14m, θ=45).

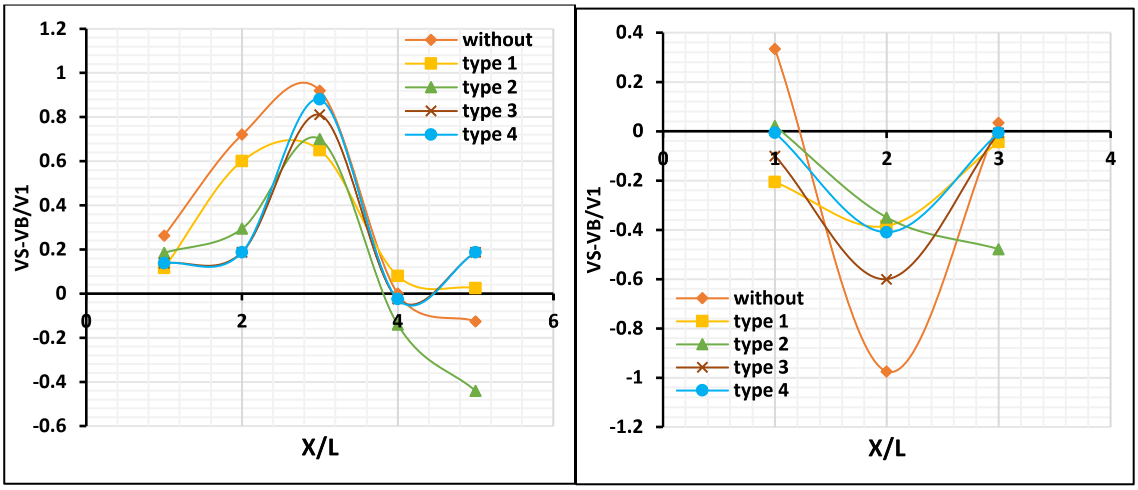

Section(A-A) Section(B-B)

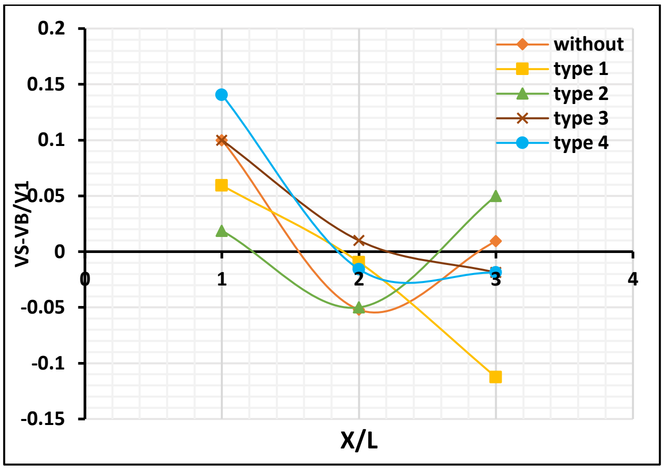

Section(C-C)

Figure 4.27: The secondary flow intensity along the stepped labyrinth side weir with and without antivortex for ten steps (p=0.14m, θ=45).

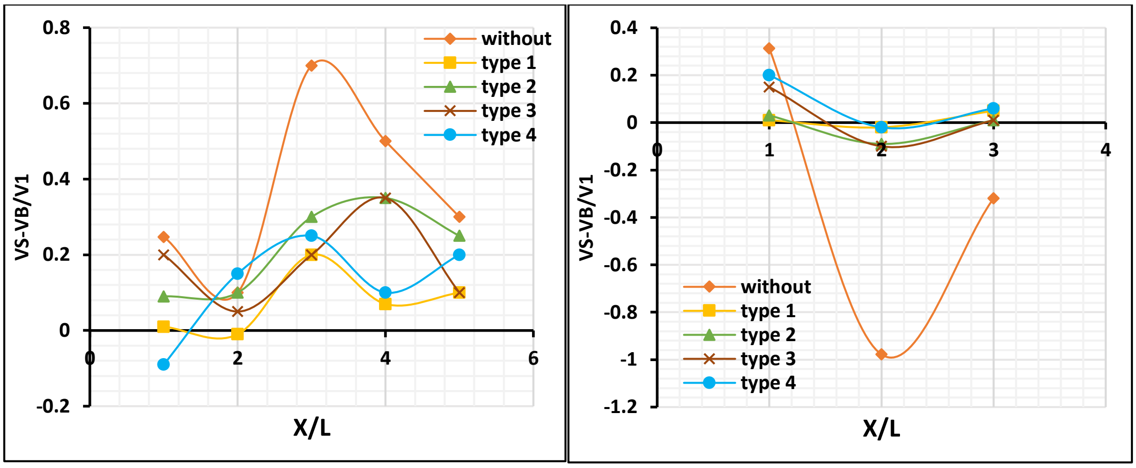

Section(A-A) Section(B-B)

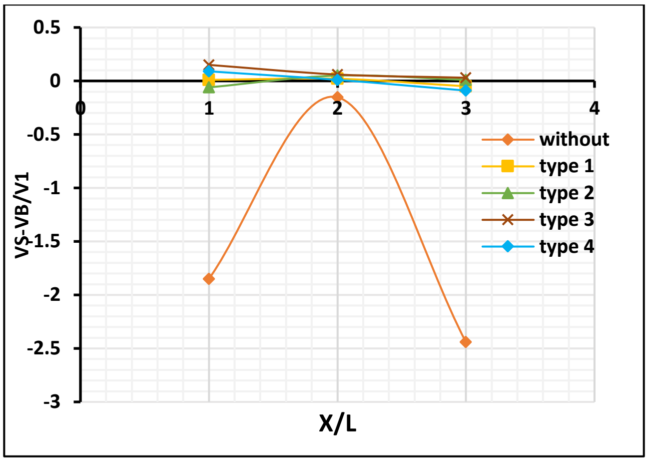

Section(C-C)

Figure 4.28: The secondary flow intensity along the stepped labyrinth side weir with and without antivortex for four steps (p=0.14m, θ=60).

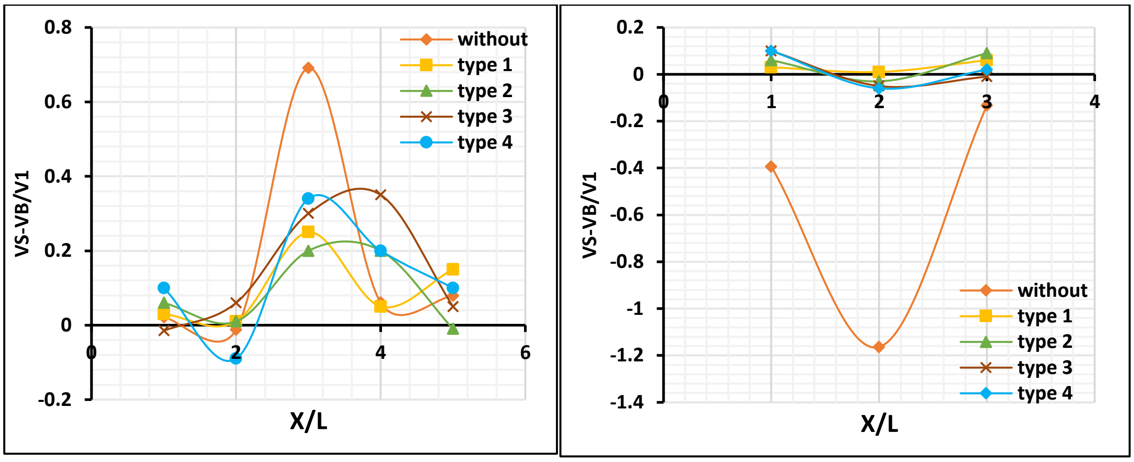

Section(A-A) Section(B-B)

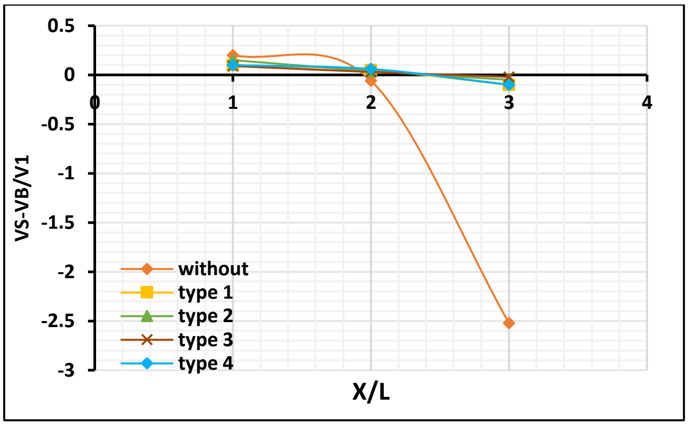

Section(C-C)

Figure 4.29: The secondary flow intensity along the stepped labyrinth side weir with and without antivortex for eight steps (p=0.14m, θ=60).

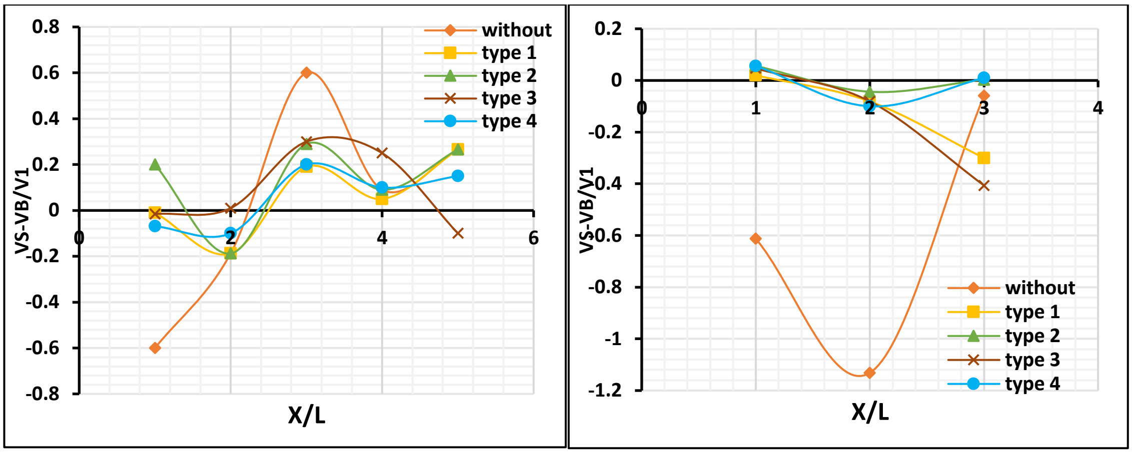

Section(A-A) Section(B-B)

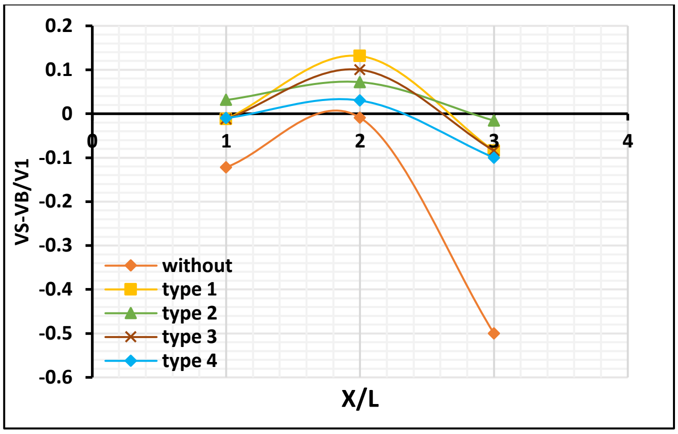

Section(C-C)

Figure 4.30: The secondary flow intensity along the stepped labyrinth side weir with and without antivortex for ten steps (p=0.14m, θ=60).

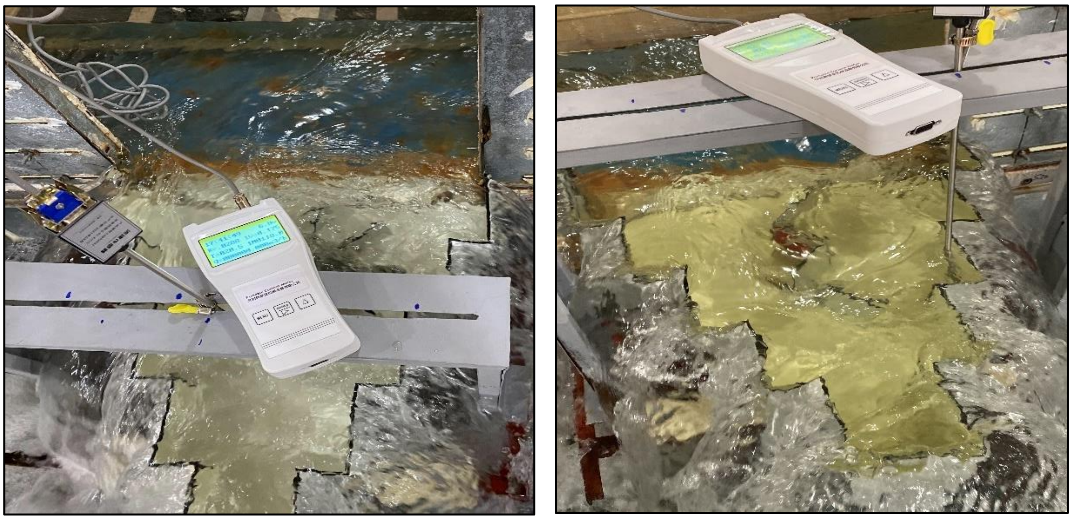

Figure 4.31: Samples of stepped LSW models during the experiment.

Chapter Five

Numerical Simulation

5.1. General Description

A comprehensive experimental, numerical comparison utilizes Computational Fluid Dynamics (CFD) techniques for modeling free surface vortices and the effect of antivortex structures for tracking and specifying flow conditions in a system. The simulations are created using data from the experimental study described in Chapter 4.

CFD simulations are carried out using powerful computers. The flow environment in CFD applications is limited by boundary conditions to simulate the surrounding influences on the specific investigation area. Almost all CFD applications are based on the solution of Navier Stokes Equations. Flow 3D, like many other commercial codes, is a strong computational fluid dynamics (CFD) code that solves the Navier Stokes Equations. The program contains advanced features that allow it to simulate while reducing computing time. Flow 3D specializes in modeling free surface flows. The application expands its capabilities by utilizing free gridding, fractional area volume obstacle representation (FAVOR), the modified volume of fluid approach (truVOF), and multi-block meshing ("Flow Science.," 2016). The process of creating unstructured grids is time consume. The free gridding method generates mesh blocks from rectangular parts. This method allows for faster meshing and shorter computing times.

Creating meshes without taking geometry into account may result in low resolution and roughness in the system. This condition is solved by the use of FAVOR, which allowed the computer to fractionally separate sections with the solid and fluid regions. Furthermore, FAVOR can connect both structured and unstructured grid elements.

("Flow Science.," 2016). The momentum and continuity of the Navier Stokes equations for three dimensional incompressible flow, including FAVOR variables, are expressed as follows:

$$\frac{\partial}{\partial x_i}(\bar{u}_i A_i) = 0, \qquad 5.1$$

$$\frac{\partial \bar{u}_i}{\partial t} + \frac{1}{V_f}\left(\bar{u}_j A_j \frac{\partial \bar{u}_i}{\partial x_j}\right) = -\frac{1}{\rho}\frac{\partial \bar{P}}{\partial x_i} + G_i + f_i \qquad 5.2$$

$$f_i = \frac{1}{V_f}\left[\frac{\tau_{w,i}}{\rho} + \frac{\partial}{\partial x_j}\left(\frac{\partial \bar{u}_i}{\partial x_j} + \frac{\partial \bar{u}_j}{\partial x_i}\right)\right] \qquad 5.3$$

where P denotes pressure, V_f the volume fraction of fluid in each cell, A_i denotes the fractional areas open to flow, f_i denotes viscous acceleration, G_i denotes body acceleration, ρ is water density, and $\tau_{w,i}$ denotes wall shear stress in the subscript directions. Flow 3D employs an advanced algorithm known as the VOF (Volume of Fluid) technique to identify the position of the free surface. The determination of the volume of a fluid function, the imposition of boundary conditions, and the use of an accurate numerical scheme are the three aspects that make up this technique. The VOF transport equation writes as follows:

$$\frac{\partial F}{\partial t} + \frac{1}{V_F}\left[\frac{\partial(FA_x u)}{\partial x} + \frac{\partial(FA_y v)}{\partial y} + \frac{\partial FA_z w}{\partial z}\right] = 0 \qquad 5.4$$

Flow 3D employs the Volume of Fluid (VOF) approach, which is established by (Hirt & Nichols, 1981). For sharp interfaces, VOF is a powerful free surface tracking approach. Gas and liquid flow freely, but the interface generates a thin viscous boundary layer. Rather than computing flow in gas and liquid regions, VOF defines air with a boundary condition and applies it to the surface. The VOF consists of three components, according to the developers of Flow 3D: a method to locate the surface, an algorithm to follow the surface as a sharp interface traveling over a computational grid, and a method to apply boundary conditions to the surface. ("Flow Science.," 2016). As previously stated, VOF is used to demonstrate fluid performance on a free surface, but FAVOR is used to represent surfaces and rigid bodies, such as complicated geometric boundaries. The program enables multi block meshing, which offers flexibility for mesh geometry fitting and dense mesh construction at specific locations where precise and accurate results are required. The following are the primary benefits and justifications for utilizing Flow 3D to model the hydraulic flow conditions in this study:

Accuracy:

The finite difference approach is used to solve the governing equations using a second order upwind scheme. The flow fields in the stepped labyrinth side weir are simulated using TruVOF. Using the TruVOF approach, empty cells are assigned a value of zero, filled cells are assigned a value of one, and cells containing the free surface are assigned a value representing the fluid volume to cell volume ratio. In both time and space, Flow 3D can follow free surfaces. Only the fluid value is calculated, not the air value. This strategy is utilized to decrease time and graphically characterize the form of the free surface. Thus, Flow 3D only supports automatic time steps for this method, with no specified time steps.

Efficiency:

Flow 3D employs the FAVOR meshing technique, which improves issue setup by embedding geometry directly into the mesh, enabling rapid parametric modifications without the time consuming re-meshing necessary by other computational fluid dynamics tools. Engineers invest their time in visualizing, optimizing, and developing design concepts with faster run times and improved accuracy.

High-Performance Computing:

Flow 3D quickly moves from desktop workstation solutions to high performance on demand cloud computing and group solutions to satisfy the industry's most demanding simulations.

The user will navigate the five primary tabs while designing the appropriate model. The following are the tabs:

1- Navigator: The user can view the simulation files, a summary, and the location of the simulation files on this screen.

2- Model Setup: This is the section in which the numerical model is performed. In the simulate tab, users may specify the simulation order and track variables such as time step, fluid surface area, mean kinetic energy, etc. The model setup tab includes six sub-tabs.

2.1- General: This subtab determines the simulation's finish time, fluid compressibility, interface type, unit type, the number of fluids, and degree of precision.

2.2- Physics: Depending on the situation, there are numerous physics-related alternatives available, including air entrainment, gravity, fluid supply, sediment, cavitation, heat transfer, viscosity and turbulence, and moving objects.

2.3- Fluids: This sub-tab allows the user to select the working fluid and its properties.

2.4- Meshing & Geometry: The domain geometry and the initial and boundary conditions are established in this tab. The user can choose to use the software's drawing options or import an executable drawing file with the STL extension. Flow 3D allows the user to construct a primitive mesh that fits the geometry.

2.5- Output: Here, the user can specify the output file.

2.6- Numerics: Options for stability factors, convergence controls, viscous stress and pressure solvers, momentum advection, and fluid flow solvers are available in this sub-tab.

3- Simulation: This screen displays information about the simulation's progress. When necessary, graphics are connected to simulations, such as time step size, pressure iteration count, etc.

4- Analyze: This tab allows the user to study the results as text or in 1D, 2D, and 3D charts. Among the choices are iso surface and color variables.

5- Display: This screen displays the visual results depending on the criteria selected in the analyze tab. It is possible to take a screenshot of the screen or make a movie.

5.2. Numerical Model Setup

5.2.1. Geometry:

Geometry is created in different geometric models of the stepped weir are developed utilizing computer software in the form of stereo lithographic (STL) pictures drawn in sketch-up pro and exported in STL format. The imported (STL) files are examined, and any geometric mistakes are fixed. Figure 5.1 demonstrates the geometry of the stepped labyrinth side weir. The pre-processor then inserts the flow geometry in the computational grid using FAVOR, an acronym for fractional area/volume obstacle representation. This approach computes open area and open volume fractions on cell faces and reconstructs the geometry based on these parameters. This method provides a simple and accurate representation of complicated surfaces in the domain without needing a body fitted grid.

5.2.2 Grid Generation:

The Flow 3D grid generation technique employs structured, rectangular, and cartesian meshes independent of the geometry employed to provide the user with simplicity and flexibility. After constructing the geometry, a suitable computational domain size must be determined before beginning grid generation. The computational domain must include a sufficiently enough area of the flow area so that the boundary conditions applied at the upstream and downstream ends do not restrict the free expansion of the flow inside the computational domain. On the other hand, an oversized domain will increase computational time and the number of the computational mesh.

In this study, the domain length is set at 5 m, while the width sets at 0.30 m. To begin grid generation, a mesh block that suits the geometry is constructed. The grid size should be kept in the logarithmic region regardless of the type of viscous solver.

Mesh analysis is essential to CFD analysis since it affects how accurate the results become. Aydin, (2012) used three different mesh sizes to calculate the numerical error for a 60° triangular labyrinth side weir with a 0.25 m side weir opening, he obtained a 3 percent error in terms of velocity with a 10 mm mesh. Wang et al., (2018) observed good agreement between CFD and experimental results with a 5 percent error when modeling flow through trapezoidal side weirs using a grid with units of 20 mm in height, width, and depth. The spatial domain subject of this study is meshed using a structured rectangular hexahedral mesh. A contained mesh block was created first for the entire spatial domain, followed by a nested mesh block with refined cells for the area of interest, which includes the weir and flow over the weir. (Figure 5.1). This method, which uses nested mesh blocks, is adapted from previous researchers (Abbasi et al., (2020); Ghaderi, Abbasi, et al., (2020). The appropriate mesh is selected by testing various computational meshes, a well-established and approved method for evaluating discretization error applied to several CFD situations. Using three different meshes with fine, medium, and coarse cells, the effect of grid size on the validity of numerical results is investigated.

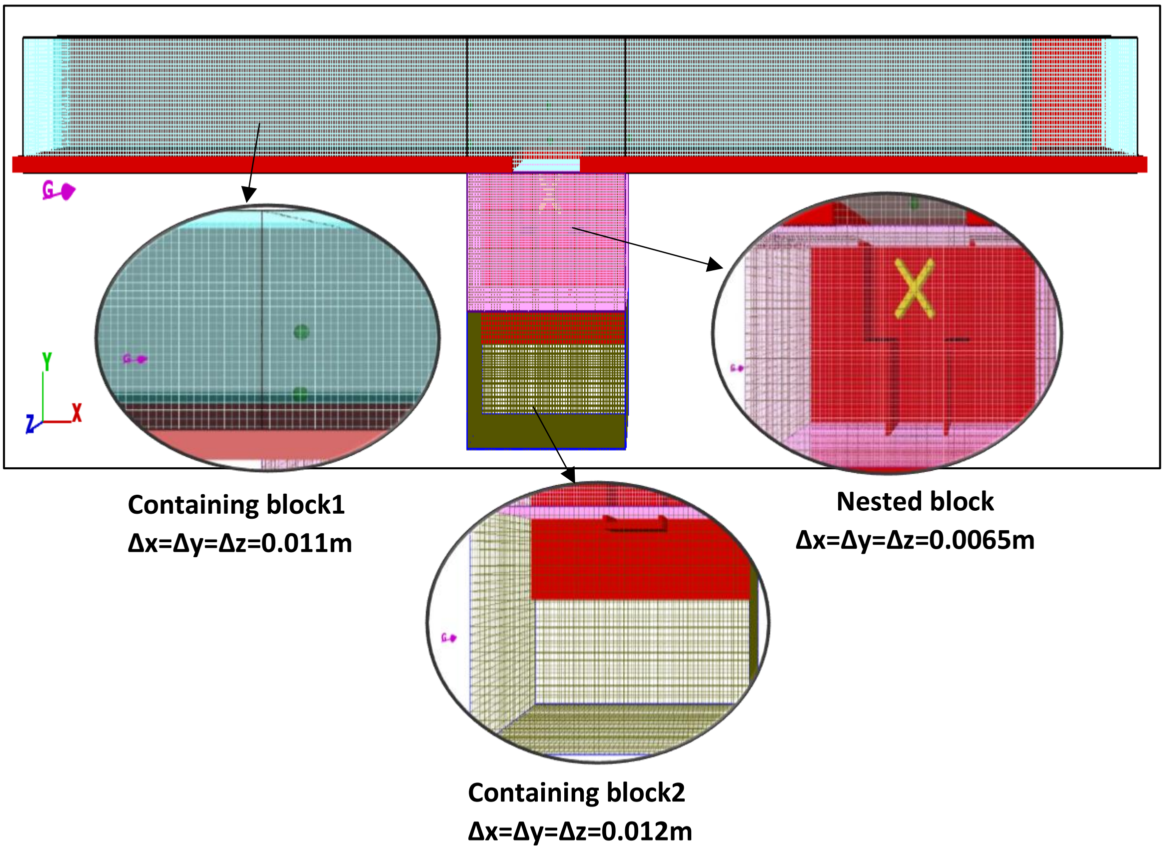

Figure 5.1: Gridding for FLOW 3D simulations.

Table 5.1. summarizes sensitivity studies of four different mesh sizes used in the area of the labyrinth weir by comparing the weir discharge produced by a numerical solution with experimental results. Finally, several appropriate and efficient meshes are selected. Figure 5.2 demonstrates the mean relative error for the weir discharge as a function of cell size. We can see that the simulated discharge agrees better with the measured discharge for the finer cell size of 0.0065 m. The authors used the same mesh in all the research models to minimize the effects of the computational mesh on simulation results.

Table 5.1: Mesh sensitivity analysis in this study.

Test no.	model	Containing 1 (m)	Containing 2 (m)	Nested mesh (m)	Total cell number	Time of run	MAPE
1	LES	0.0115	0.0125	0.0085	674,410	5h and 19m	22
2	LES	0.011	0.012	0.0075	943,942	8h and 15m	14
3	LES	0.011	0.012	0.0065	1,344,468	11h and 16m	3.84
4	LES	0.01	0.011	0.0055	1,988,432	15h and 20m	2.9

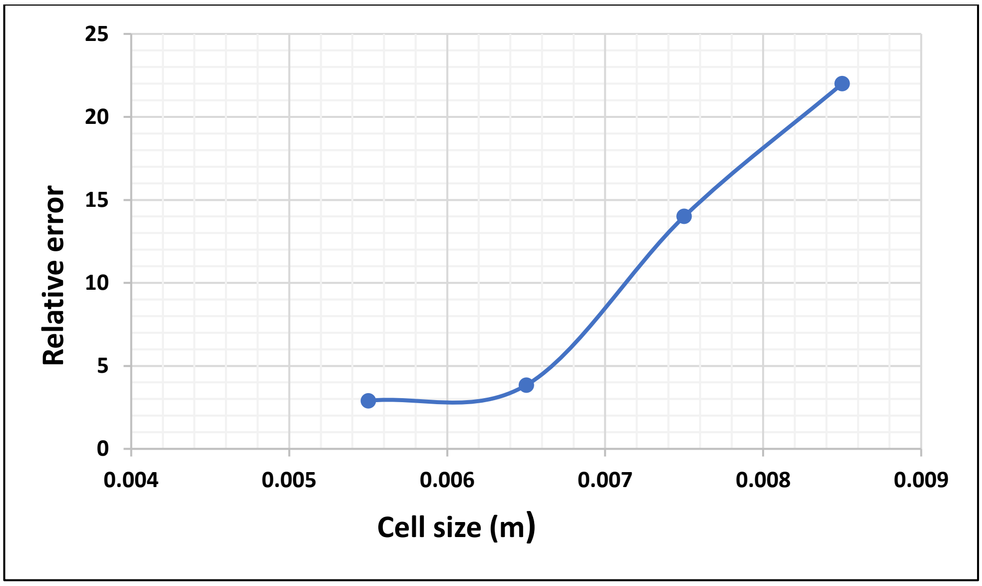

Figure 5.2: Variations of the relative error of the weir discharge versus cell size.

5.2.3 FAVOR:

The Fractional Area-Volume Obstacle Rendering (FAVOR) is an effective technique for introducing geometry influence into the governing equations and allows the program to partition parts fractionally into solid and fluid regions. However, it likes all discrete methods, is affected by the resolution of the computational grid. Therefore, the FAVOR selection is a method for determining whether the mesh size allows the solver to perceive the system's entire geometry accurately. It is because the pre-processor generates area fractions for each cell face in the grid by detecting whether the corners of the face are within a defined geometry. Similarly, if all corners are outside the geometry, the entire face is considered outside. When certain face corners are inside geometry, and others are outside, the geometry's intersection with face edges is computed.

Figure 5.3 demonstrates a 3d representation of the favored flume, and the Figures shows that all components are adequately captured in the mesh space. Furthermore, Figure 5.4 depicts the installation of the Antivortex structures in the stepped labyrinth side weir.

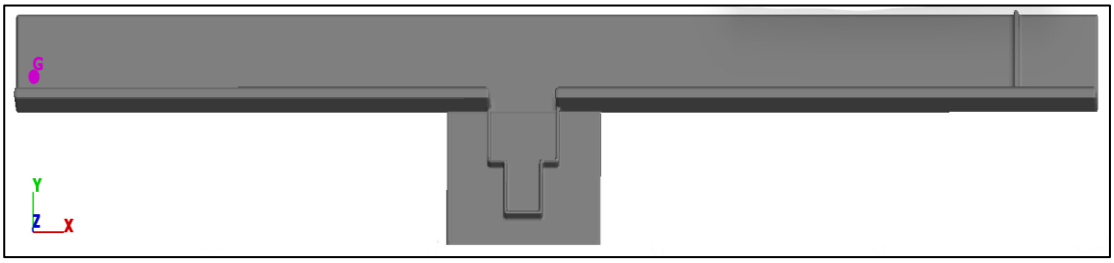

Figure 5.3: The 3D favored view of the channel.

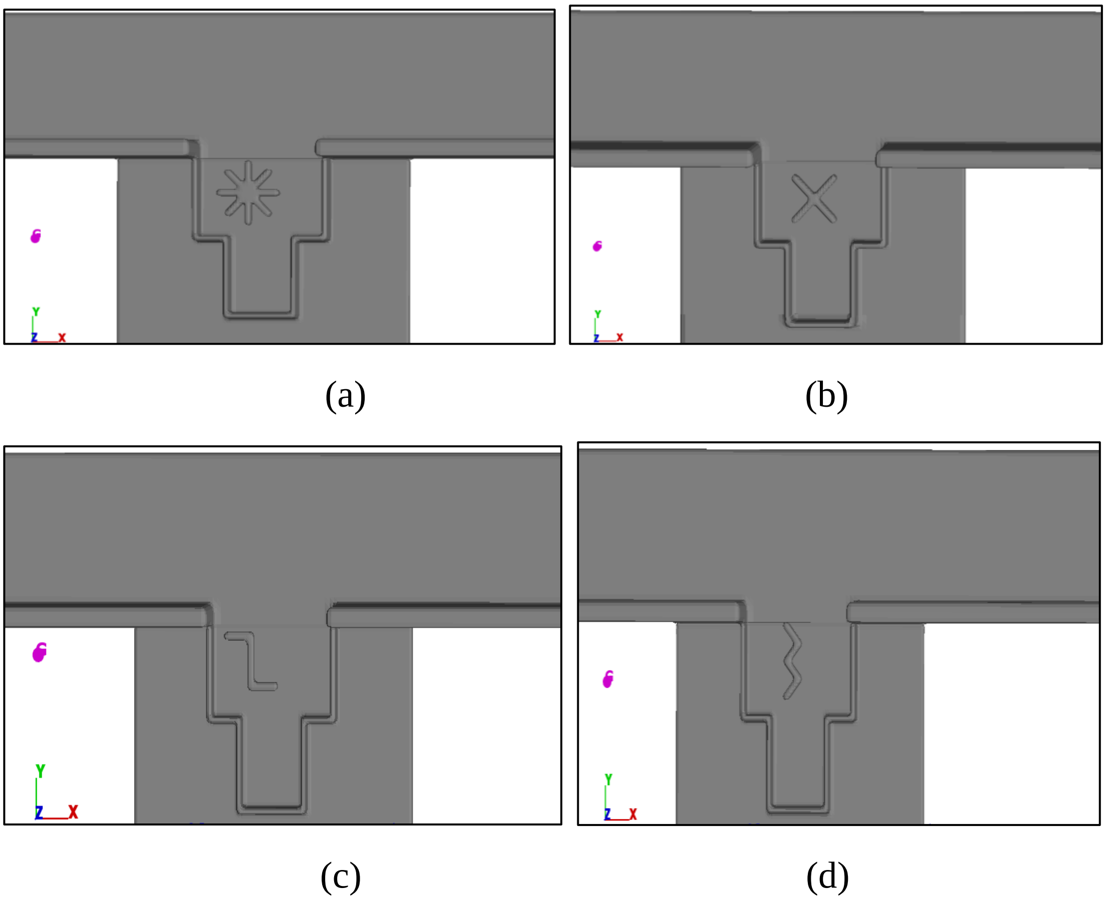

(a) (b)

(c) (d)

Figure 5.4: Antivortex installation in stepped labyrinth side weir.

5.2.4 Boundary Conditions:

It is almost impossible to define every component of a flow domain in CFD, so the computers only solve the desired regions. Boundary conditions are essential for achieving identical flow conditions with the physical model, and they must be set after grid creation and utilizing the FAVOR algorithm to finish the model's design precisely. The numerical model with mesh planes and boundary conditions is presented in Figure 5.5. Each mesh block face must describe a boundary condition. Based on the experimental conditions, the following boundary conditions used in this study:

1- Volume flow rate(Q) is used for the input flow at the inlet with a constant-depth subcritical flow. The solver will maintain the discharge on the "Q" face at the specified rate. And the downstream face of the outer mesh is set to an outlet(O)

2- The lower Z (Z_{min}) and both side boundaries are treated as a rigid wall (W). No-slip conditions are applied at the wall boundaries. No-slip is defined as zero tangential and normal velocities ($u = v = w = 0$). The boundary "Wall" refers to how the solution considers "W" faces as solid components with the no-slip condition.

3- An atmospheric boundary condition sets the channel's upper boundary, allowing the flow to enter and leave the domain, as null von Neumann conditions are imposed on all variables except for pressure, which is set to zero (i.e., atmospheric pressure).

4- Asymmetry boundary condition (S) is imposed at the inner boundaries, allowing flow-through. Symmetry indicates that there is no flow across the "S" plane and that the velocity normal to the symmetry line is zero.

Finally, the numerical model is ready to conduct numerous simulations with changing situations after different models and mesh designs are examined to obtain the most accurate template for the model. Several simulations can be generated by varying the parameters such as weir height, weir length, discharge, and step number.

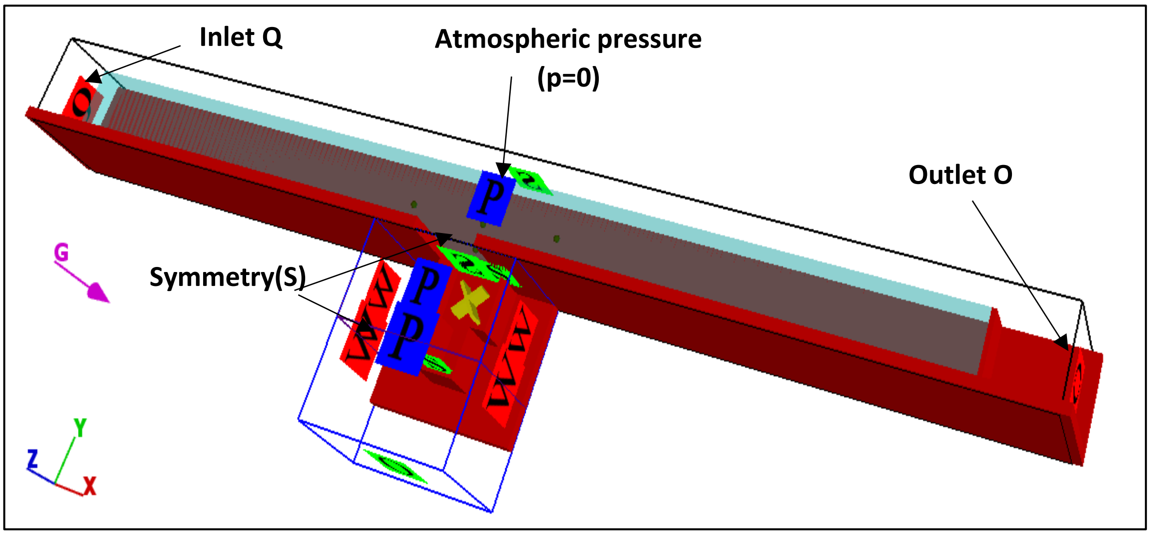

Figure 5.5: Weir with antivortex and boundary conditions.

5.3 Turbulence Model Solver

In flow 3D, turbulence models have five types: Large Eddy Simulation (LES), Renormalization-Group (RNG), and the two-equation (k −ε), one Equation turbulent energy (k), and Prandtl's mixing length theory ("Flow Science.," 2016). The swirling flows is recommended to be solved with eddy-resolving methods (Koken & Constantinescu, 2008). Consequently, this study used the LES turbulence model to perform the CFD via Flow 3D.

This model can reduce the computational cost by ignoring the shortest length scales, where most computations are difficult to resolve. In addition, the storage and analysis of extensive data also create significant logistical problems. Also, according to the Flow 3D User Manual (2013), the LES model usually offers more information than models based on Reynolds averaging. The LES model is based on computing all large-scale turbulent structures within the computational grid and modeling the smaller structures outside the grid resolution.

For the length scale, a geometric mean of the grid cell dimensions is used (Smagorinsky, 1963). The influence of turbulence on smaller structures is represented in the model by a value called eddy viscosity, which is proportional to the length scale times a measure of velocity variations on that scale.

$$L^{*} = \left(\partial_x \, \partial_y \, \partial_z\right)^{1/3} \qquad 5.5$$

The value of L* is effective grid scale by the mean shear stress determines the scale of velocity changes. The LES kinematic eddy viscosity calculates by packing these values together, which is as follows:

$$v_T = (cL)^2 \times \sqrt{2e_{ij}e_{ij}} \qquad 5.6$$

Where v_T Represents turbulent kinematic viscosity, c is a constant with an expected value of 0.1 to 0.2, cL is the length scale, and e_{ij} the strain rate tensor components.

5.4. Results and Discussion

5.4.1 Convergence and Validation

Using experimental data, researchers can use CFD to understand flow behavior and quantify essential flow parameters if the CFD solver has been adequately validated. The 3D numerical model, once validated, can be used to analyze the flow characteristics at the stepped labyrinth side weir. The experimental data collected at Hydraulic Laboratory allows for comparing this numerical model with laboratory test results. Table 5.2. Show the geometric characteristics of the tested stepped labyrinth side weir. The rectangular horizontal channel utilized in the experiment has dimensions of 12m in length, 0.3m in width, and 0.45m in height, respectively. Weir angles of 45 and 60 degrees and a ratio of L/B = 1 and 1.5 (L: The weir opening length; B: Channel width). Although the experimental flume was 12 m long, the current numerical analysis shortens it to 5 m to improve computing efficiency and minimize the total number of cells. The model had to be validated before it could be used in different scenarios. After that, the anti-vortices are placed inside the stepped labyrinth side weir at one height (0.5p), as recommended by (Abbasi et al., 2020), and their performance evaluates using the discharge coefficient.

Table 5.2: Geometric characteristics of stepped labyrinth side weir.

Model	L(m)	P(m)	θ	B(m)	N
Numerical and Physical Models	0.30,0.45	0.08,0.14	45°,60°	0.3	4,8,10

As a result, the three-dimensional model of the labyrinth weir is solved for four scenarios:

Scenario I: The Flow 3D discharge coefficient results and water surface profile without antivortex structures are compared to experimental data to validate the simulation results. After validation, the location of the vortex is identified by streamlines.

Scenario II: Simulations are carried out with four different types of anti-vortex structures installed in a stepped labyrinth side weir. The simulations are run by varying the position and dimensions of the antivortex structures with height (p=0.08m,0.14m), length (L=0.30m,0.45m), and steps (N=4,8,10) in order to choose the most efficient location and dimensions.

Scenario III: Different hydraulic characteristics such as secondary flow and air core forming process are investigated to track and specify flow conditions in the stepped labyrinth side weir.

Scenario IV: Four types of antivortex structures are installed in stepped labyrinth side weir to determine the effects of discharge capacity at different discharges, weir lengths, and crest heights for L =0.30 and 0.45 m.

Scenario I:

5.4.1.1 Discharge Coefficient of the Stepped Labyrinth Side Weir

The weir discharge coefficients obtained from the numerical simulations are compared with those from experimental simulations. during the simulation, the flow rate at the outlet boundary and the free surface elevation at the inlet boundary does monitor in every iteration. The solution becomes fully converged, and the steady state condition does control for all values after a 40s simulation of the flow.

The goodness of fit between the observed and simulated values are evaluated using the R^2 representation as shown in Figure 5.6 and the data from Table 5.3.

Figure 5.6 shows that there is good agreement between the predicted discharge coefficient and the experimental observations of the stepped weir.

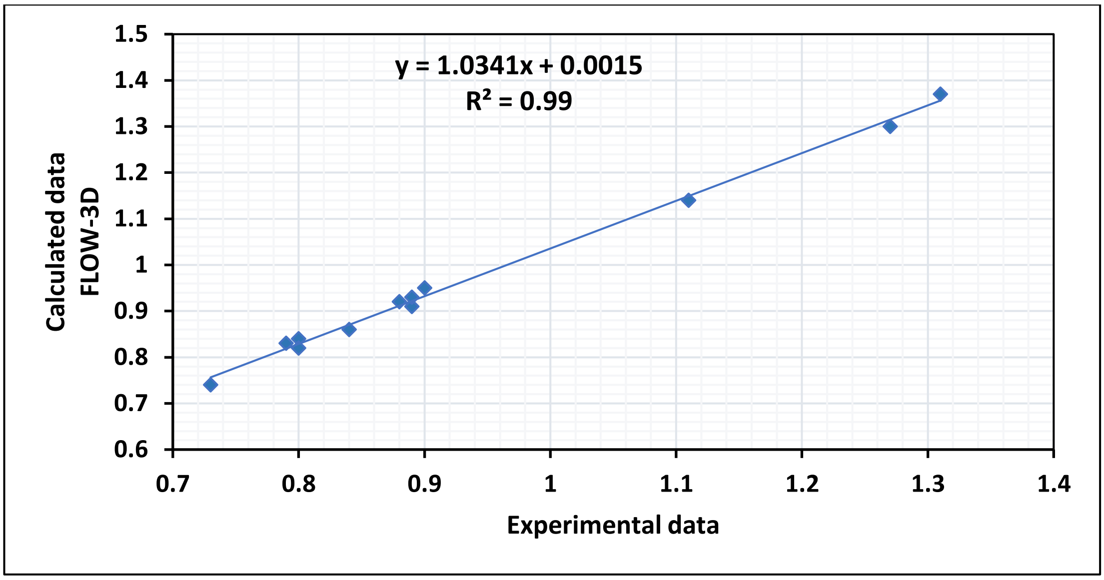

Figure 5.6: Comparison of the discharge coefficient obtained from numerical solutions with experimental data.

Table5.3: Numerical simulations without antivortex structures.

Steps (N)	L (m)	Head angle θ°	Weir height (m)	Qt m^3/s	F_1	C_d flow3d	C_d experimental
4	0.45	45	0.14	0.027 0.020	0.25 0.20	1.13 1.35	1.08 1.28
4	0.45	45	0.08	0.027 0.019	0.48 0.37	0.75 0.94	0.70 0.90
8	0.45	45	0.14	0.027 0.019	0.28 0.20	1.07 1.34	1.02 1.12
8	0.45	45	0.08	0.027 0.017	0.47 0.34	0.73 0.90	0.71 0.85
10	0.45	45	0.14	0.027 0.019	0.24 0.18	0.87 0.99	0.83 0.95
10	0.45	45	0.08	0.027 0.019	0.46 0.36	0.70 0.81	0.67 0.77
4	0.45	60	0.14	0.027 0.019	0.27 0.20	1.12 1.09	0.95 1.02
4	0.45	60	0.08	0.027 0.019	0.48 0.36	0.70 0.80	0.65 0.76
8	0.45	60	0.14	0.027 0.018	0.24 0.18	0.90 0.97	0.88 0.95
8	0.45	60	0.08	0.027 0.020	0.44 0.36	0.58 0.69	0.56 0.66
10	0.45	60	0.14	0.027 0.018	0.24 0.17	0.84 0.88	0.86 0.83
10	0.45	60	0.08	0.027 0.019	0.44 0.35	0.59 0.67	0.55 0.65
4	0.30	45	0.14	0.027 0.018	0.37 0.27	0.87 0.95	0.84 0.92

Steps (N)	L (m)	Head angle θ°	Weir height (m)	Qt m^3/s	F_1	C_d flow3d	C_d experimental
4	0.30	45	0.08	0.027 0.019	0.68 0.52	0.72 0.93	0.68 0.89
8	0.30	45	0.14	0.027 0.018	0.37 0.26	0.83 1	0.78 0.96
8	0.30	45	0.08	0.027 0.018	0.66 0.53	0.75 1.02	0.71 0.98
10	0.30	45	0.14	0.027 0.018	0.36 0.27	0.85 0.97	0.80 0.94
10	0.30	45	0.08	0.027 0.018	0.67 0.49	0.69 0.79	0.65 0.76
4	0.30	60	0.14	0.027 0.020	0.36 0.26	0.95 0.96	0.92 0.98
4	0.30	60	0.08	0.027 0.017	0.65 0.47	0.69 0.75	0.64 0.72
8	0.30	60	0.14	0.027 0.015	0.36 0.22	0.88 1.02	0.86 0.98
8	0.30	60	0.08	0.027 0.015	0.63 0.41	0.60 0.67	0.55 0.65
10	0.30	60	0.14	0.027 0.018	0.36 0.27	0.88 0.90	0.85 0.86
10	0.30	60	0.08	0.027 0.016	0.62 0.44	0.61 0.65	0.55 0.64

After examining various models, the suitable duration for results extraction in the analyzed numerical model is determined to be 45 s. Figure 5.7 shows the flow path through the weir at different points in time. After entering a stepped crested labyrinth weir, the flow exits the channel after 45 seconds in a steady state.

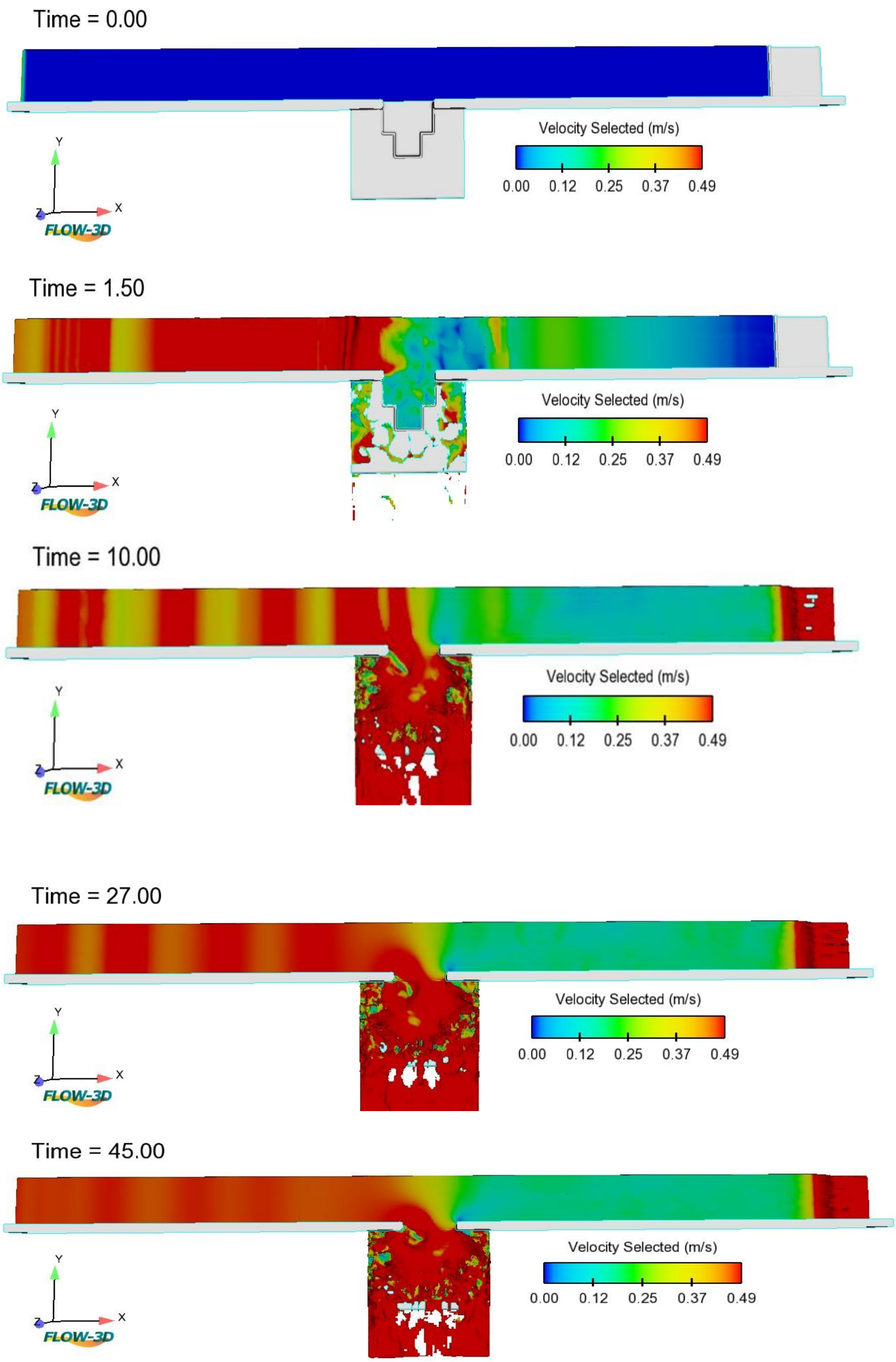

Figure 5.7: Flow path through the weir at different points in time (sec).

5.4.1.2 Water Surface Profiles

The water surfaces produced from numerical simulation and experiment are compared for the F_1 = 0.34 and 0.67, as shown in Figure 5.8(a-c), to confirm the Flow 3D simulation results in the stepped labyrinth side weir on the axis A-A. The computational and experimental surface profiles are pretty similar in Figure 5.8.

In this Figure, the vertical axis is the water depth ratio to the side weir height (y/P), and the horizontal axis is the dimensional ratio of the location in the direction of the channel length over the weir opening length (x/L). The water depth upstream of the side weir opening is slightly lower than the water depth downstream of the side weir opening. Secondary flow resulting from the lateral flow causes this water surface condition, and the flow diversion causes the separation zone at the downstream end of the side weir. The same effect is observed in studies by (Emiroglu et al., 2011) and (Abbasi et al., 2020), and according to them, the reason for this occurrence is the result of the current deviating from the main channel and entering the side weir, they have noticed how the head angle affects the separation zone. Because of the increased effective length of the 45° labyrinth side weir, the difference in water surface levels upstream and downstream is the largest. The findings demonstrated that as the number of steps increases, the water surface along the side weir in the main flume (sections A-A, and B-B) gets more divergent and disturbed. Additionally, the surface level fluctuations at the side weir's beginning and end increase noticeably. According to Figure 6, section A-A, the water surface drop is higher at the start of the side weir, particularly with four steps, and the drop decreases as the number of steps increases.

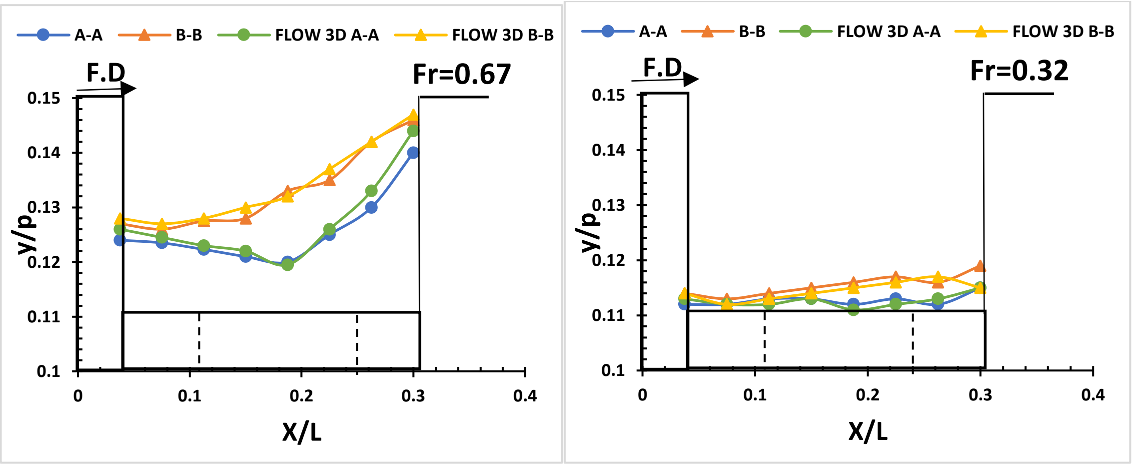

Figure 5.8a: Water surface profiles along the stepped weir side and centre-line at the straight channel for four steps.

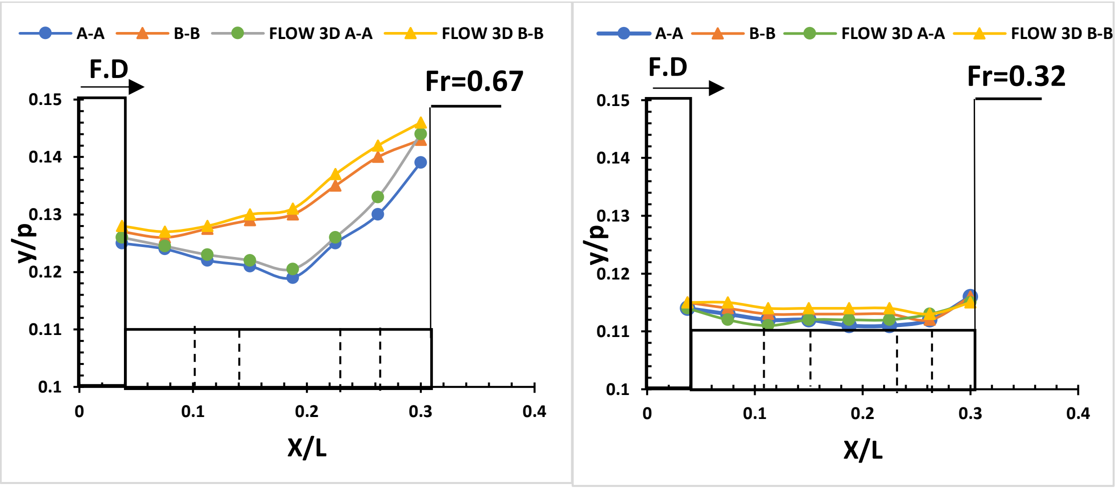

Figure 5.8b: Water surface profiles along the stepped weir side and centre-line at the straight channel for eight steps.

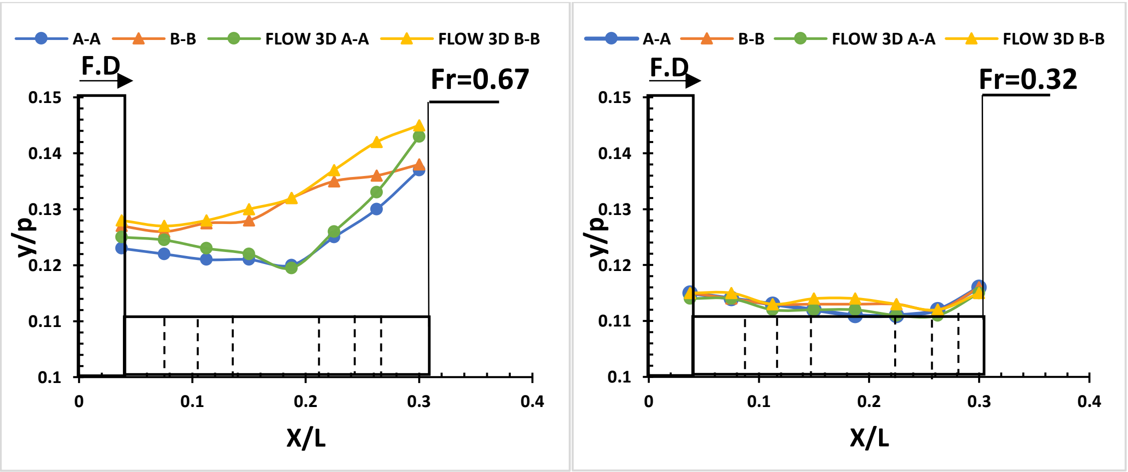

Figure 5.8c: Water surface profiles along the stepped weir side and centre-line at the straight channel for ten steps.

Scenario II:

In this scenario, all types of antivortex structures are used because engineering design accuracy is required. The simulations are run by installing the antivortex in the location of the vortex and varying the location and dimensions of the antivortex structures with height (p=0.08m,0.14m), length (L=0.30m,0.45m), and steps (N=4,8,10). All anti-vortex structures are installed at 35%, 60%, and 45% of "d," and the most efficient distance "d" is determined to be 45%. These simulations are then repeated by increasing the dimensions of the antivortex structures by 30-40% while keeping a stationary "d" of 45%. Figure 5.9 shows a three-dimensional flow field model for simulation. The layout design of antivortex structure dimensions is demonstrated in Figure 5.9 by streamlines and reported in Table 5.4 by comparing with results of the model (N=4, P=0.14m, L=0.45m).

Table 5.4: Selecting the efficient hydraulic geometry of antivortex structures.

Description of anti-vortex model	C_d before adjustment	C_d after adjustment	Nots	Fig.
Type1 with full length of the crest height (p) and 0.35d	0.79	0.89	Low distraction for the vortex	5.9a
Type2 with (0.5p) and (0.35d)	0.83	0.87	Low distraction for the vortex	5.9b
Type4 with (0.5p) and (0.60d)	0.82	0.85	More turbulent flow	5.9c

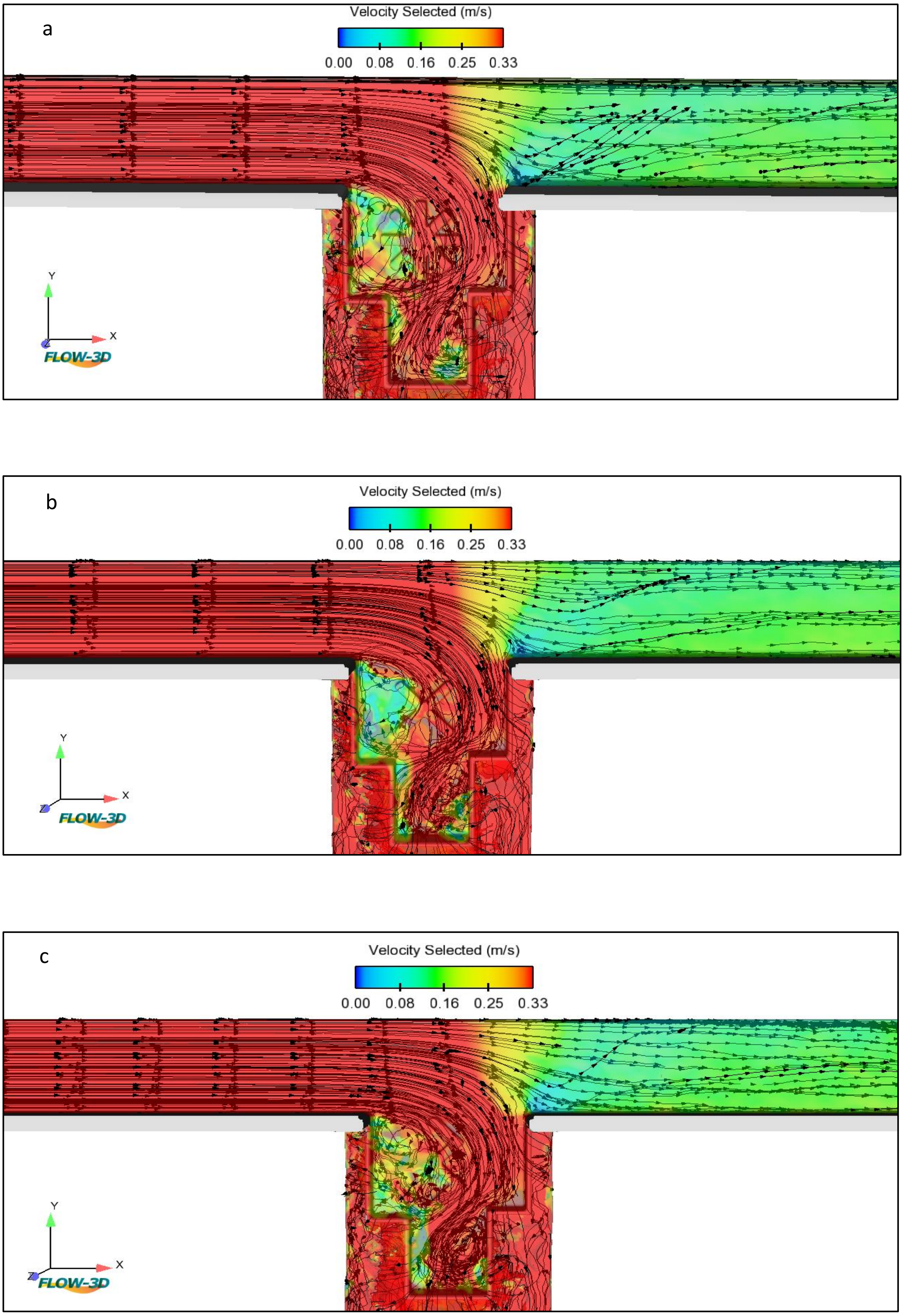

Figure 5.9: Flow field models with antivortex for selecting most efficient hydraulic geometry.

Figure 5.10 show the vortex position at F_1=0.67 for each model used in this study and the rest of them in appendix A. based on the ease of construction and the engineering judgment of the authors. These simulations present the exact position of the vortex. In all cases, the vortex location in upstream of the weir, and its effect extent when the number of steps increased, it is observed that the vortex core become wider and extend with decreasing in weir height.

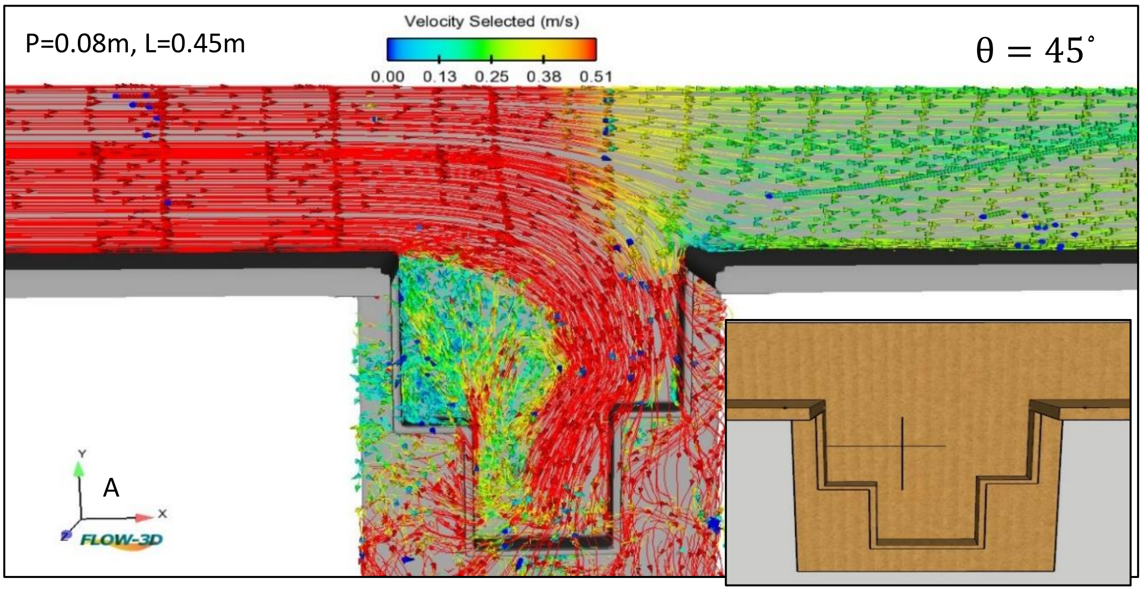

Figure 5.10: Cont.

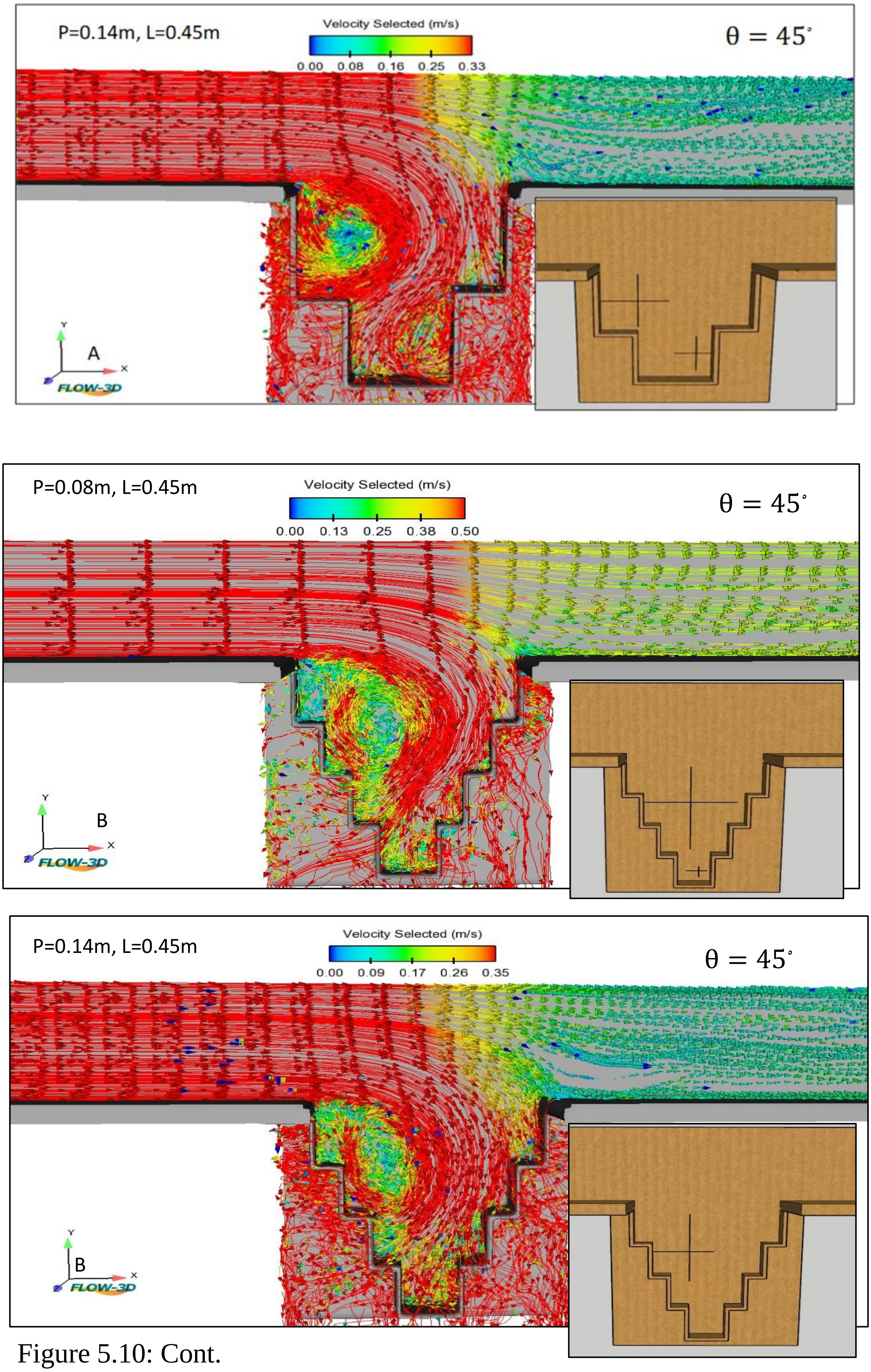

Figure 5.10: Cont.

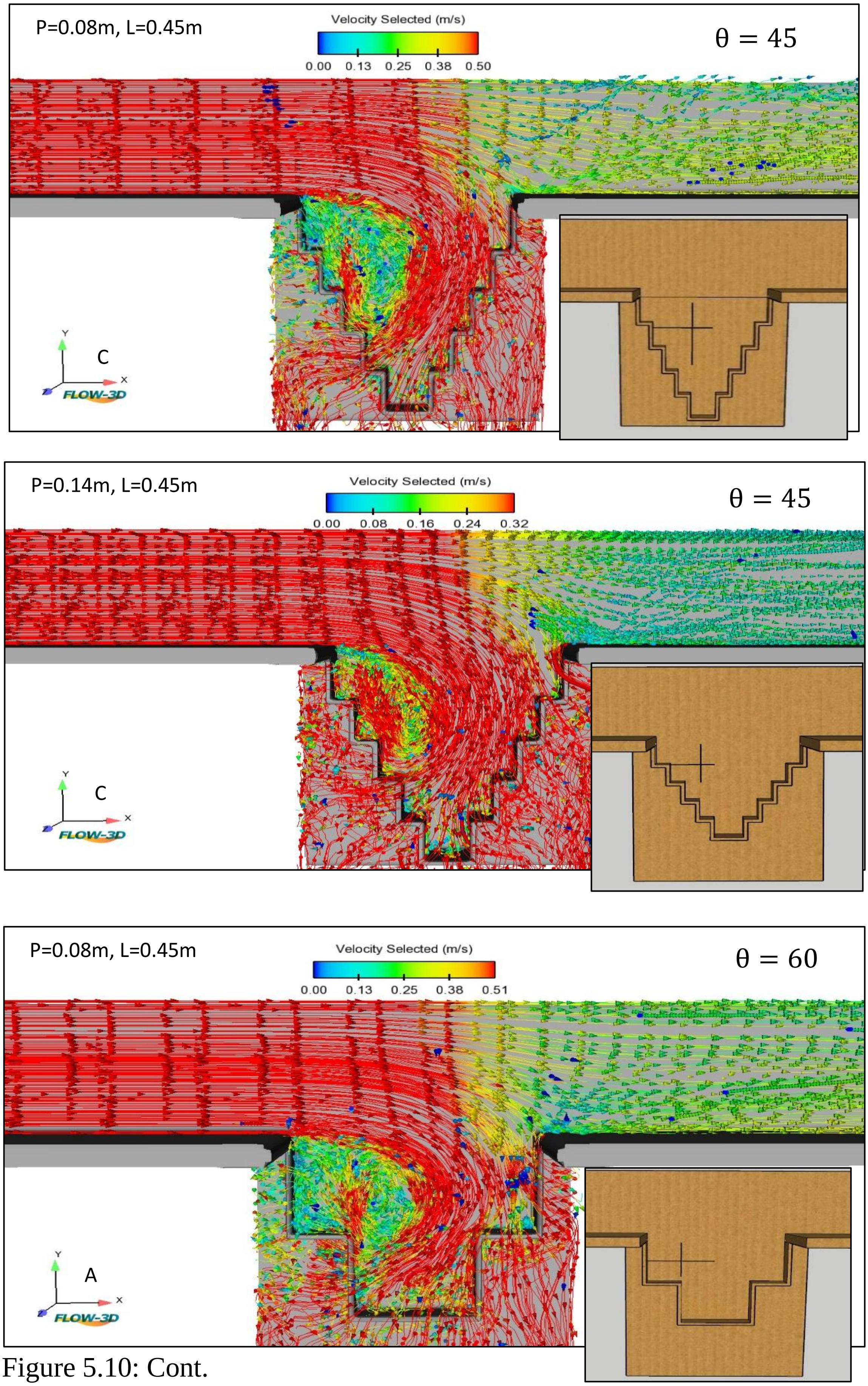

Figure 5.10: Cont.

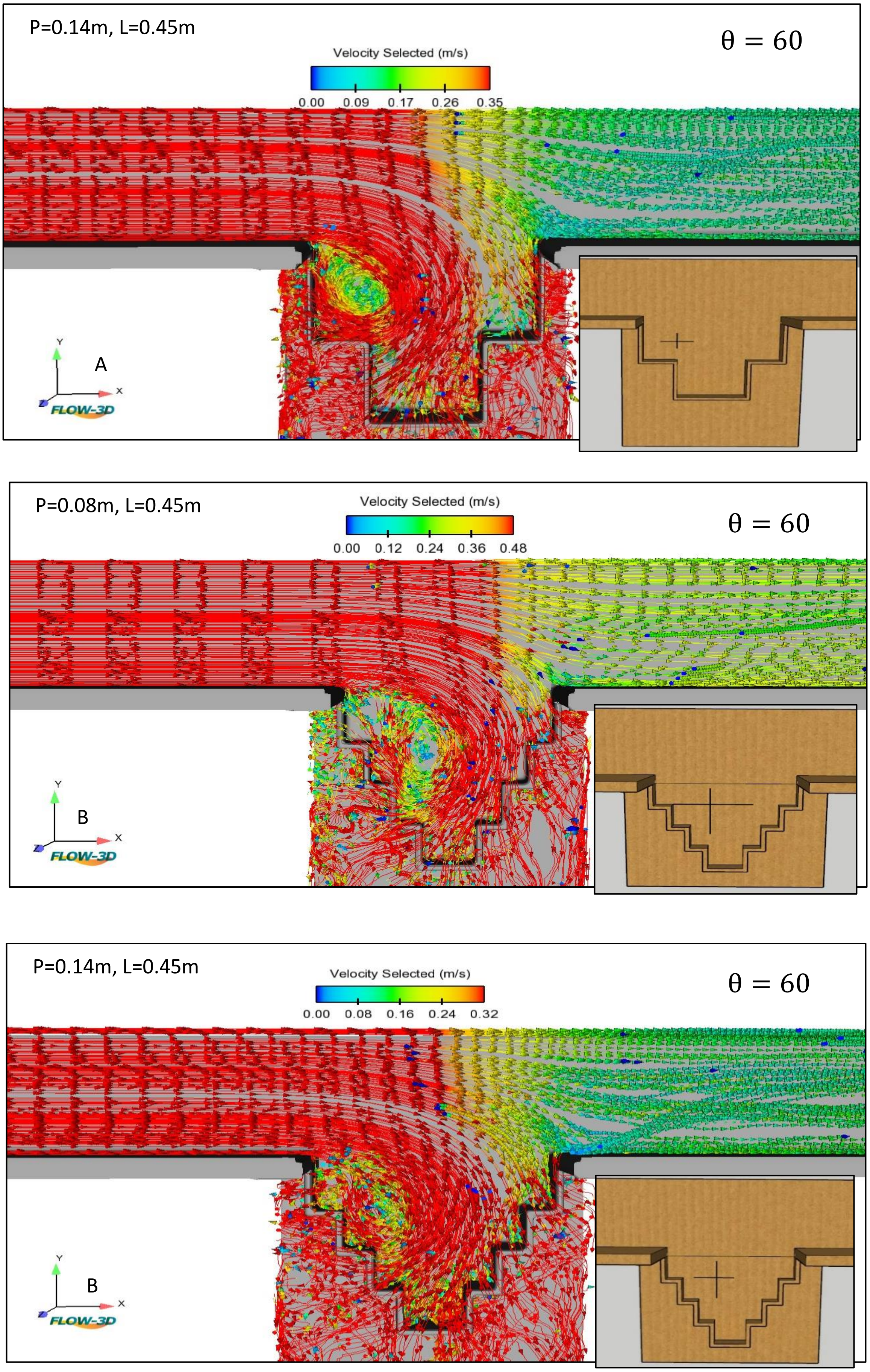

Figure 5.10: Cont.

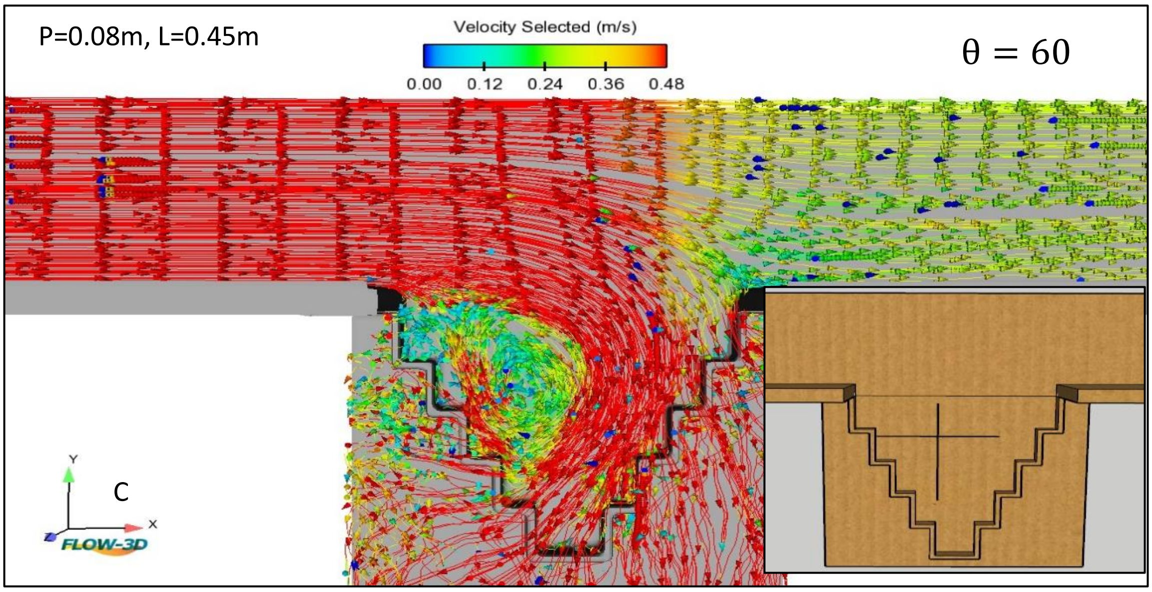

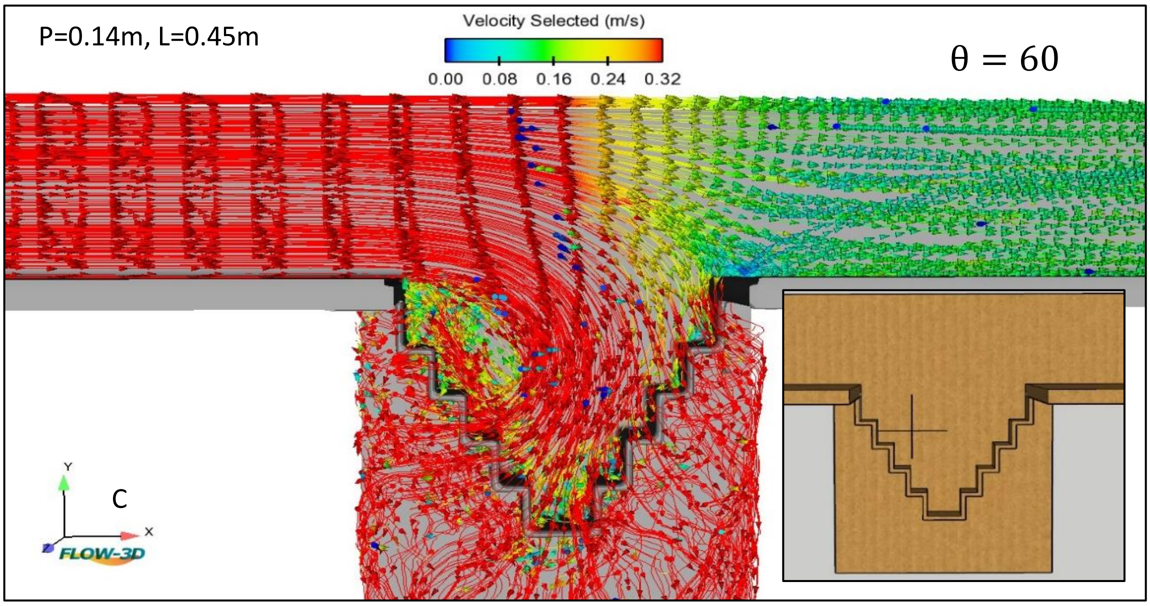

Figure 5.10: the vortex position for the stepped models. (A): N=4, (B): N=8, (C)N=10.

Scenario III:

In this scenario, simulations of a stepped labyrinth weir included angles of 45˚ and 60˚, runs by changing the crest height (P), side weir length (L), and step number (N) for the Froude number 0.67. The intensity of the secondary currents is another essential factor influencing the discharge coefficient in labyrinth side weirs, in Figures 5.11 to 5.13, the flow entering the side weir forms vortices, because the flow path is changed from the main channel to the side weir, collisions with the weir wall, and side weir geometry. The secondary flow formed by the lateral flow leads to a separation zone, and the reversed flow area at the length of the side weir, causes the water surface level fluctuations along the opening length (L) of the stepped labyrinth side weir. The vortex generation complicates the secondary flow near the apex of the stepped labyrinth side weir as shown in Figure 5.11a and the cross-section vortex development at the bed of the channel represented by the 2D clip in Figure 5.11b. As the flow deviates from the X to the Y direction in lateral flow, vortex generation plays an essential role in flow interaction. Vortex development is due to the y component of velocity, as indicated in sections I, II, and III. The diameter of a vortex is larger at the upstream end of the labyrinth side, whereas weir velocity vectors indicate vortex development near the side weir bed in section II, i.e., in the center of the labyrinth side. The lateral flow depends upon the opening length of the side weir, crest height, Froude number, step number, and head angle as follows:

A-length of Side Weir:

Secondary flow increases as the length of the side weir increase due to: a greater value of deviation angle, kinetic energy, and extending further along the length. To represent this effect, Figure 5.11(a,b) illustrates simulations of a stepped labyrinth weir, including angles 60°, runs with the crest height (P=0.14m), side weir length (L=0.30 and 0.45m), and step number (N=4) for the Froude number 0.67. For (L/B =1 and 1.5), the flow collides with the first step and then rises to splits into two parts, either reverse flow to create a vortex or outflow. Consequently, the vortices are bounded by the sides of the step preventing the area of influence of these vortices from extending more toward the entire length of the side weir. However, in section I, Figure 5.11, based on two different values of L/B, the vortex core for L/B = 1.5 is significantly bigger than the other value along the crest height because of the area of influence of these vortices increases with the increasing opening length of the SLSW. Emin Emiroglu et al., (2014) concluded similar results and mentioned that the intensity of secondary motion caused by lateral flow increases as the overflow length increases. When the relative side weir length rises, the deviation angle and kinetic energy develop toward the side weir as the secondary flow increases. Aydin et al., (2015) and Ansari & Patil, (2022) also found a similar pattern of variation. In contrast, weir velocity vectors indicate vortex formation near the side weir bed in sections II, and III, i.e., in the center and downstream of the labyrinth side.

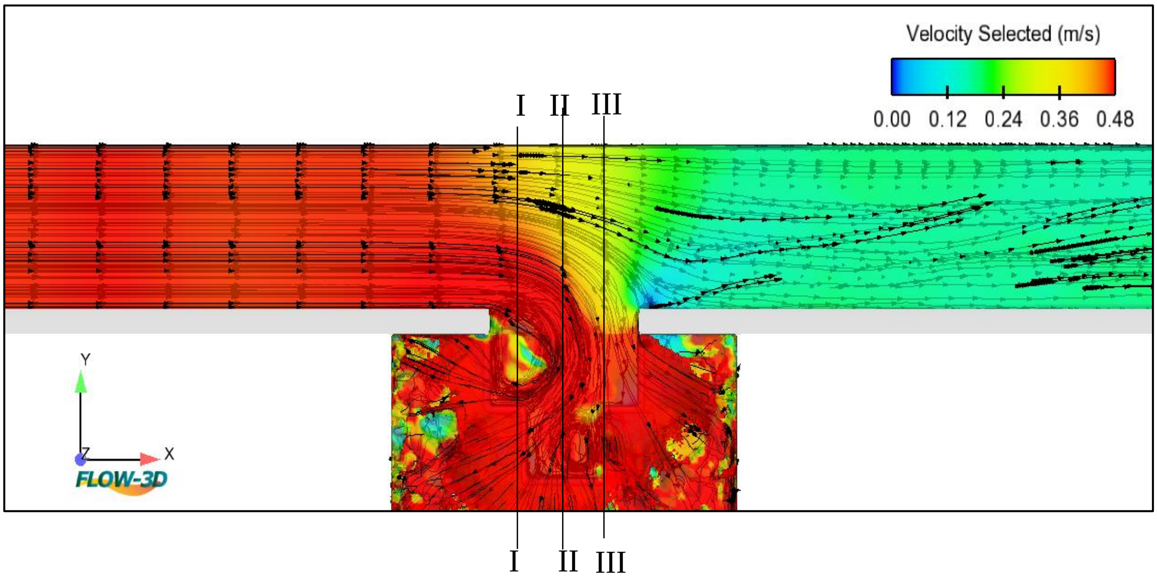

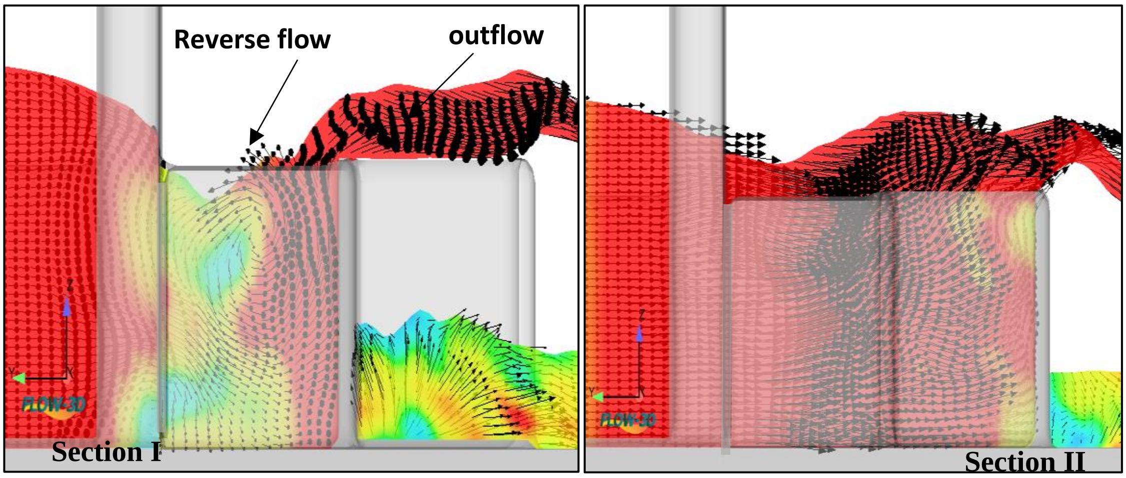

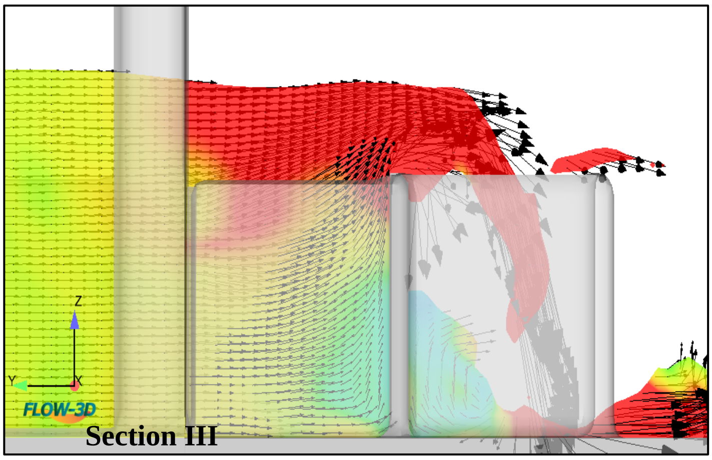

Figure 5.11a: Secondary flow in the four-step cross-section with L/B=1, θ°=60, F_1=0.67, p=0.14m.

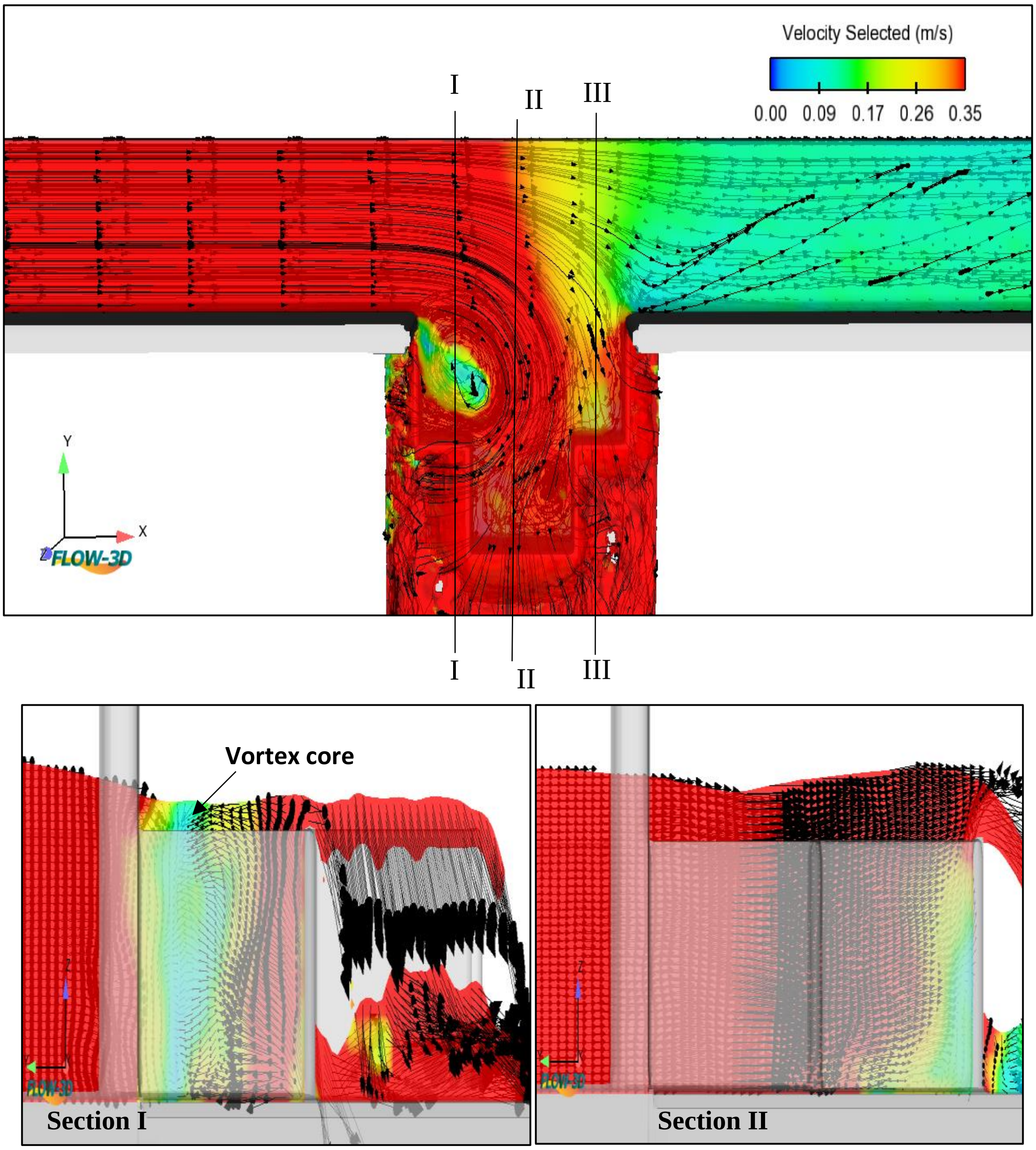

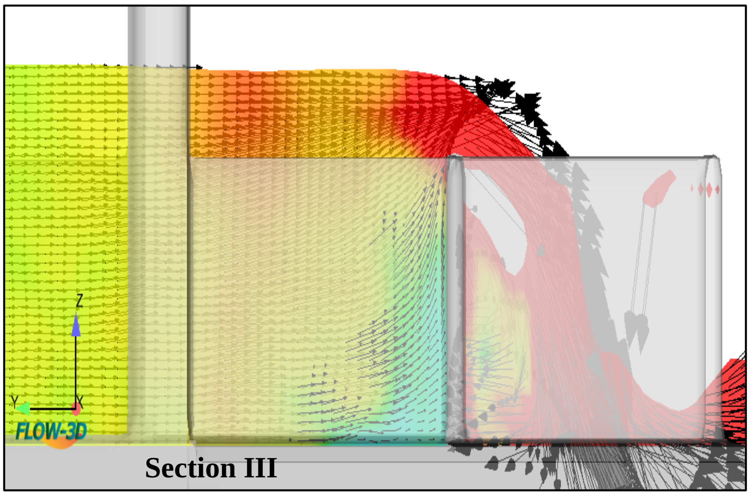

Figure 5.11b: Secondary flow in the four-step cross-section with L/B=1.5, θ°=60, F_1=0.67, p=0.14m.

2-Crest Height Effect:

Figure 5.12 (a,b) illustrates simulations of a stepped labyrinth weir, including angles 60°, runs with the crest height (P=0.14,0.08m), side weir length (L/B=1), and step number (N=8) for the Froude number 0.67. The flow collides with the second step and then rises to splits into two parts, either reverse flow to create a vortex or outflow. Therefore, the influence is more extended within the side weir, preventing incoming currents from crossing over the entire length of the downstream crest. as shown in Figure 5.12b, in section I, it can be observed that the vortex core for P=0.08m is significantly wider and more extending than the other value along the crest height leading to strong secondary motion near the weir side boundary. The strength of this secondary motion next to the boundary depends on the crest height of the side weir and reduces as the crest height of the side weir increases due to weir surface friction of the SLSW. The same results revealed by (Aydin, (2012); Aydin & Emiroglu, (2013); Emiroglu & Kaya, (2011)), they concluded that the intensity of this secondary motion near the boundary is influenced by the crest height of the side weir and reduces as the crest height of the side weir increases due to friction on the weir surface. In contrast, weir velocity vectors indicate vortex formation near the side weir bed in sections II, and III, i.e., in the center and downstream of the labyrinth side.

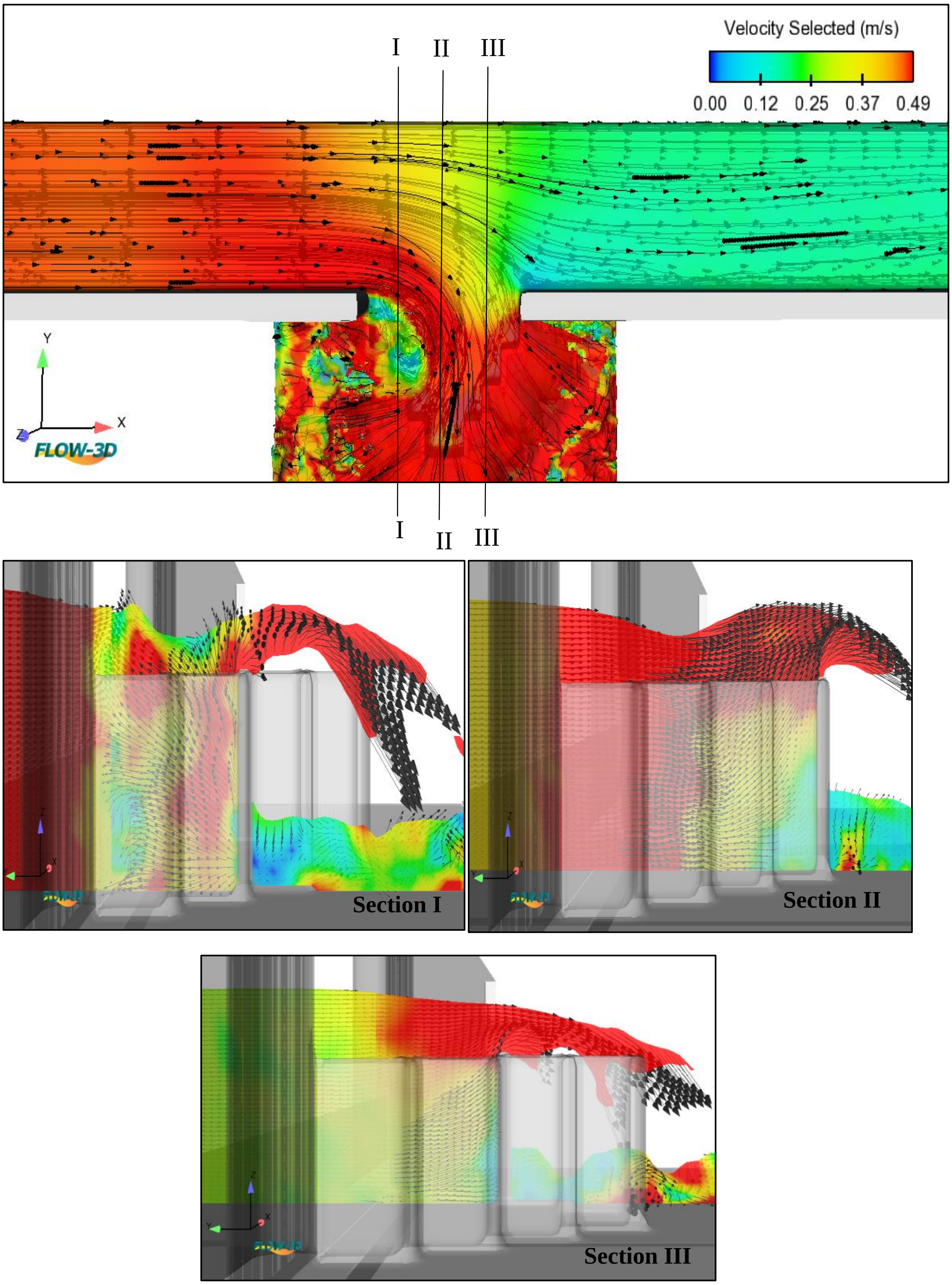

Figure 5.12a: Secondary flow in the eight-step cross-section with L/B=1, $\theta^{\circ}=60$, $F_1=0.67$, p=0.14m.

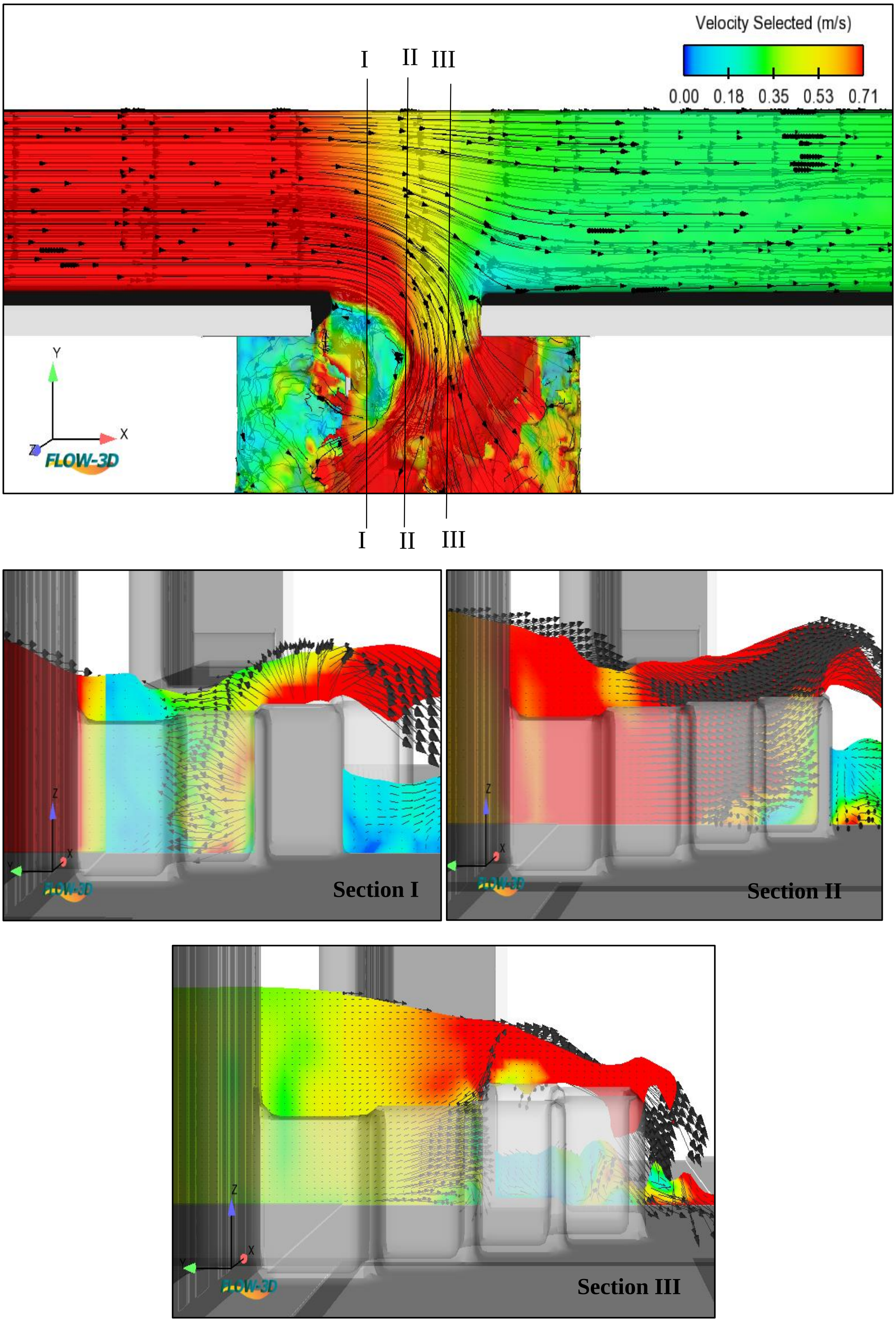

Figure 5.12b: Secondary flow in the eight-step cross-section with L/B=1, $\theta^{\circ}=60$, $F_1=0.67$, p=0.08m.

3-Head Angle Effect

Two representative views of the velocity vectors are shown in Figure 5.13 (a,b) . these figures represented the simulations of a stepped labyrinth weir, including angles 45˚ and 60˚, runs with the crest height (P=0.14m), side weir length (L/B=1), and step number (N=10) for the Froude number 0.67. the flow collides with the third step and then rises to splits into two parts, either reverse flow to create a vortex or outflow. Therefore, the influence is more extended within the side weir, preventing incoming currents from crossing over the entire length of the downstream crest. as shown in figure 5.13a, in section I, it can be observed that the vortex for $\theta=45$ is significantly more extending along labyrinth weir length than the other value leading to increasing the secondary motion. On the other hand, weir velocity vectors show vortex formation along the side weir bed in sections II and III, i.e., in the middle and downstream of the labyrinth side. Abbasi et al., (2020); Ansari & Patil, (2022); Emiroglu et al., (2011) also revealed the same results.

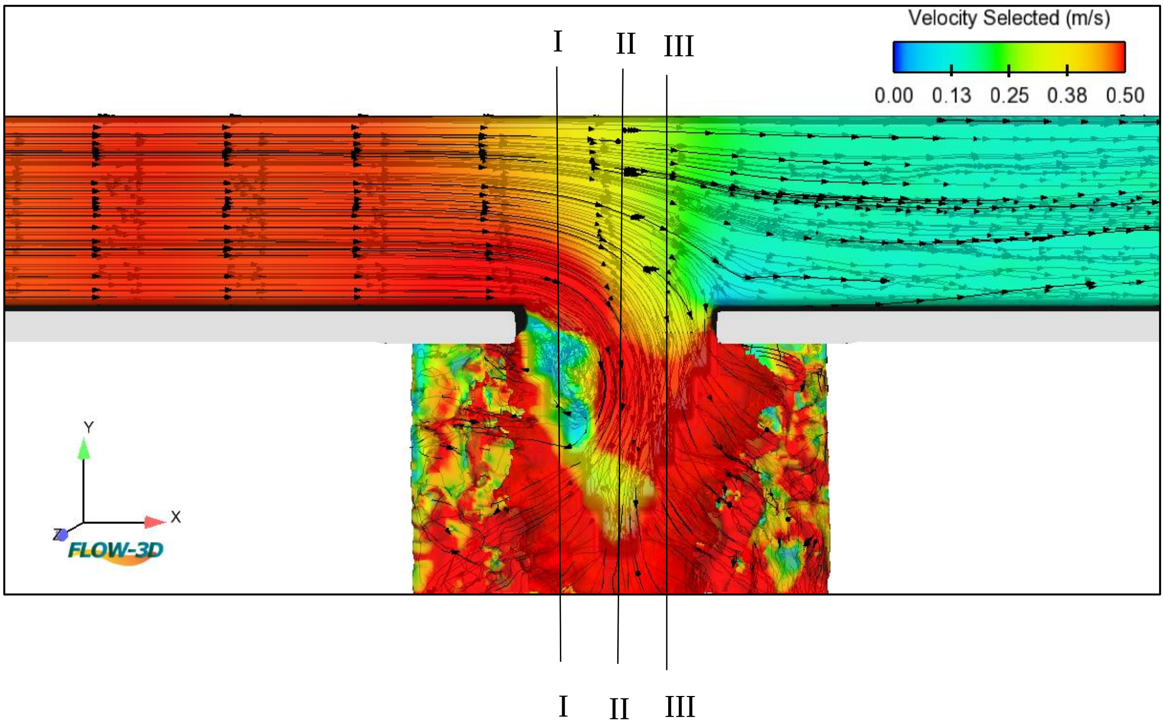

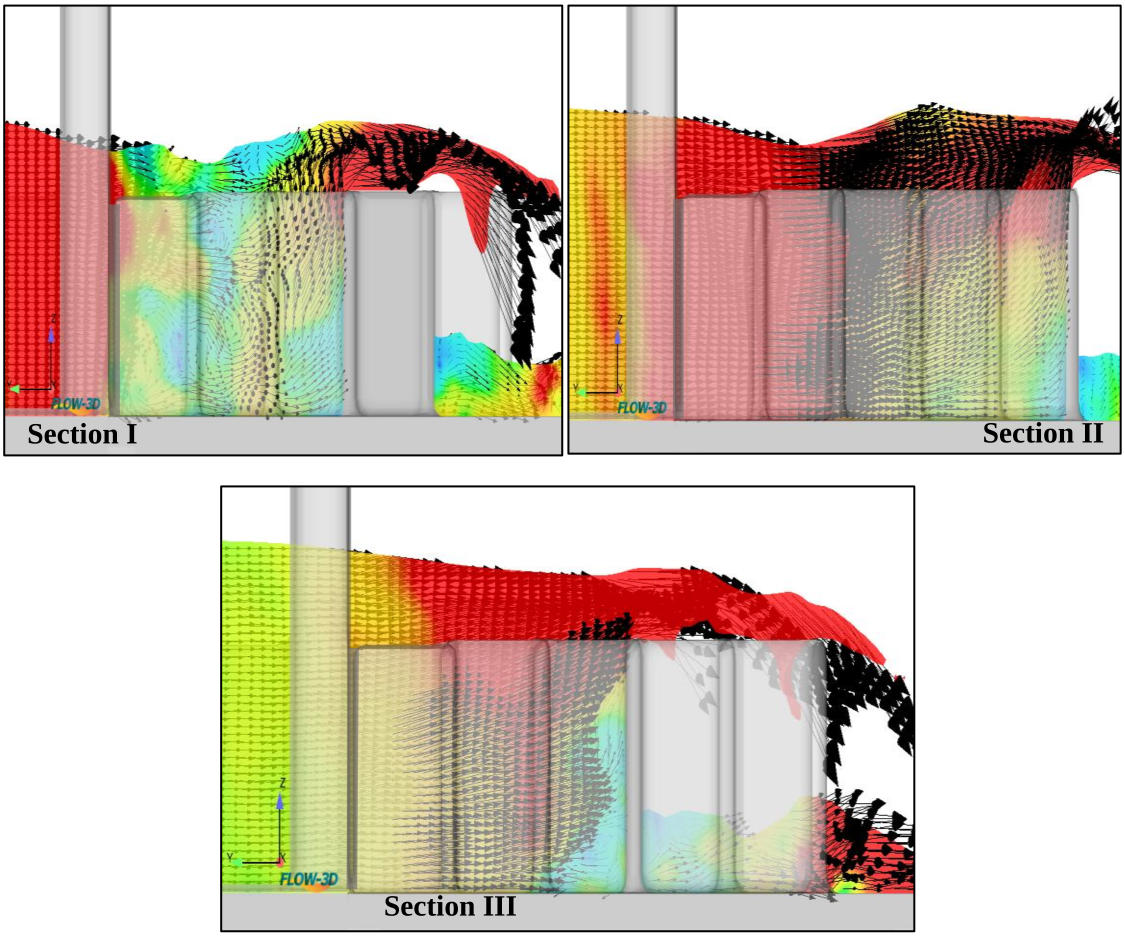

Figure 5.13a: Secondary flow in the ten step cross-section with L/B=1, $\theta^{\circ}=45$, $F_1=0.67$, p=0.14m.

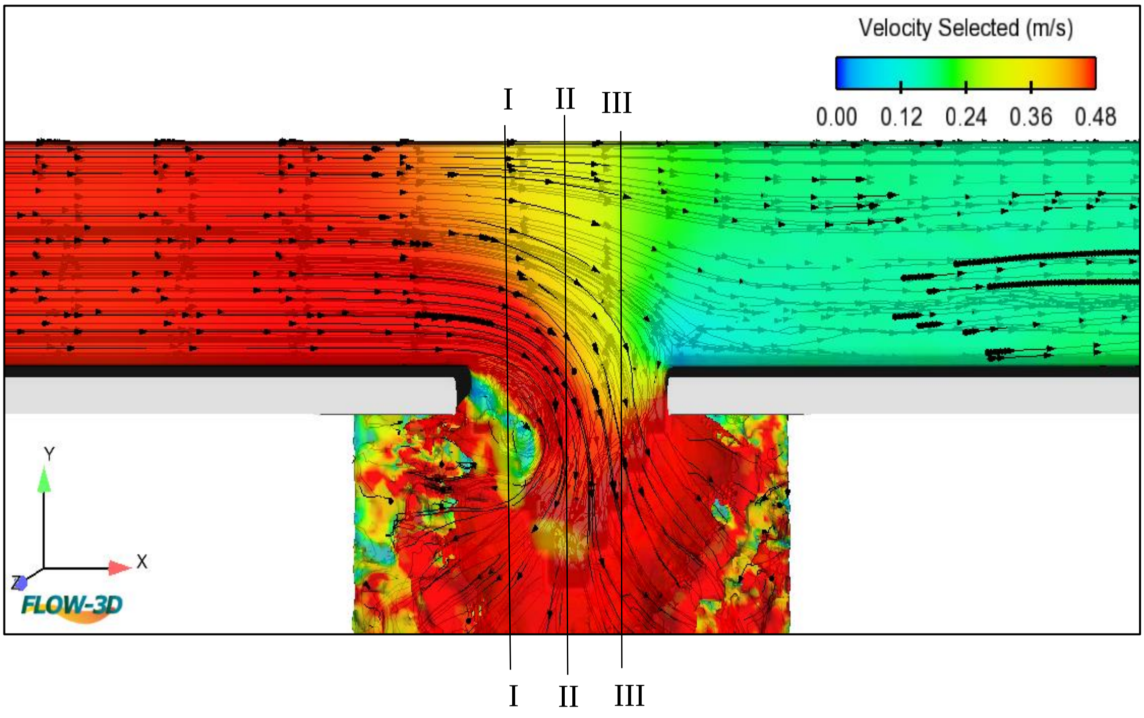

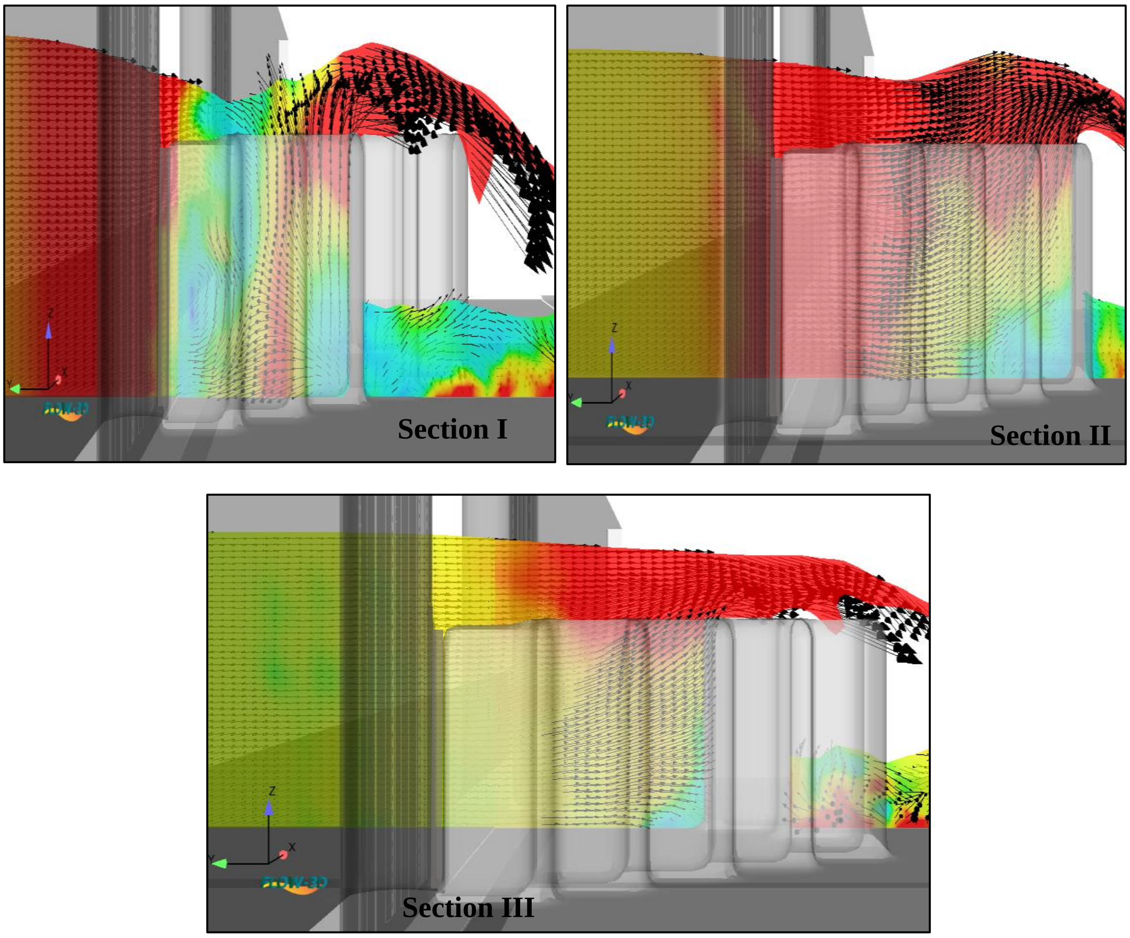

Figure 5.13b: Secondary flow in the ten-step cross-section with L/B=1, θ°=60, F_1=0.67, p=0.14m.

3.2.3 Air-Core Forming Process

The secondary flow motion will develop above the crest of the weir at upstream when the main flow is split up to the entire side weir. The simulation shows that the red colors have the highest velocity, while the blue colors have the lowest velocity. as shown in Figure 5.14a, the vortex indicates a slight drop, and the surface profile displayed a smooth curve as well at L/B=1, θ°=60, Q=17 L/s, p=0.14m, N=4.

The vortex is formed when the water level overflowed the crest of the weir. The entire vortex had a small core to the bottom of the weir, with a degree of depth proportionate to the amount of inflow. Figure 5.14 (b) and

Figure5.14 (c) are the results of inflows Q = 19 L/s and Q = 27 L/s, respectively and L/B=1, θ°=60, p=0.14m, N=4.

when the inflow is small, the air core takes a restrictive shape with little deformation, as shown in Figure 5.14(b). However, as the inflow is gradually increased, the air core became wider and deeper, and it begin to form a spiral surface profile that circled the vortex, as shown in Figure 5.14(c).

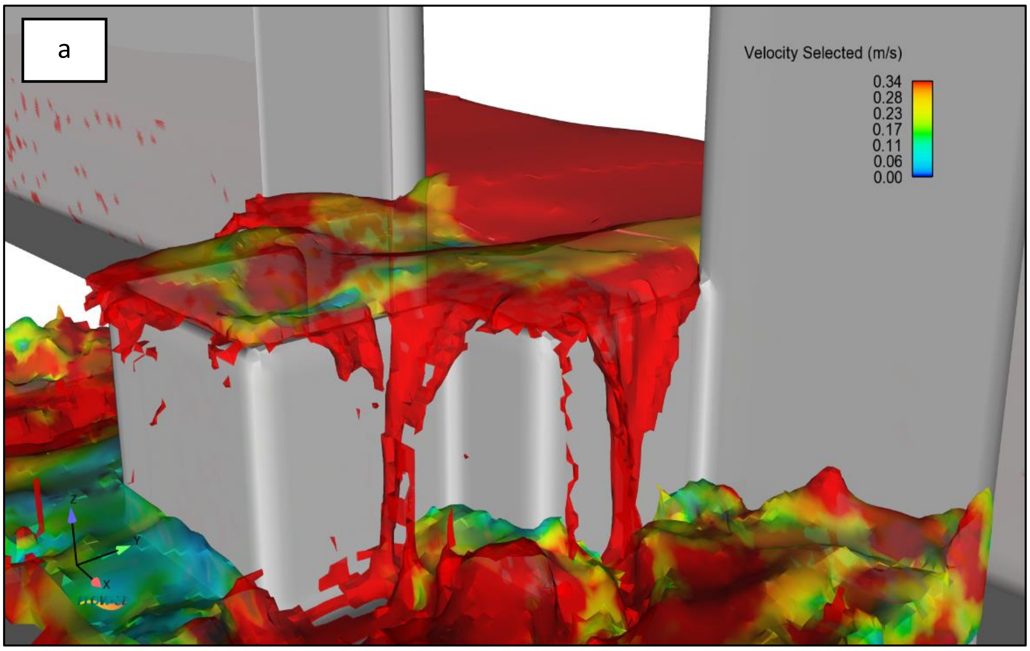

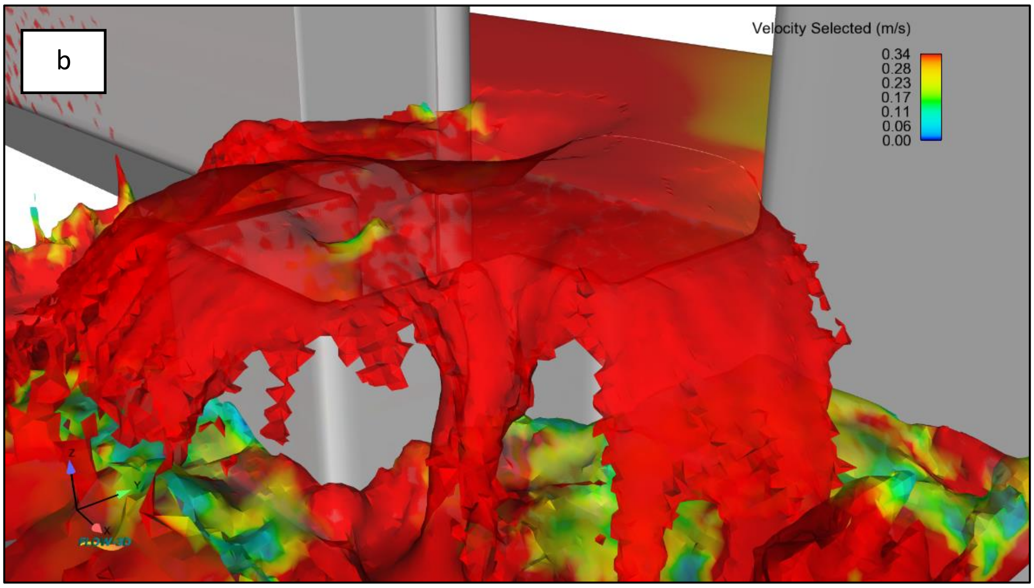

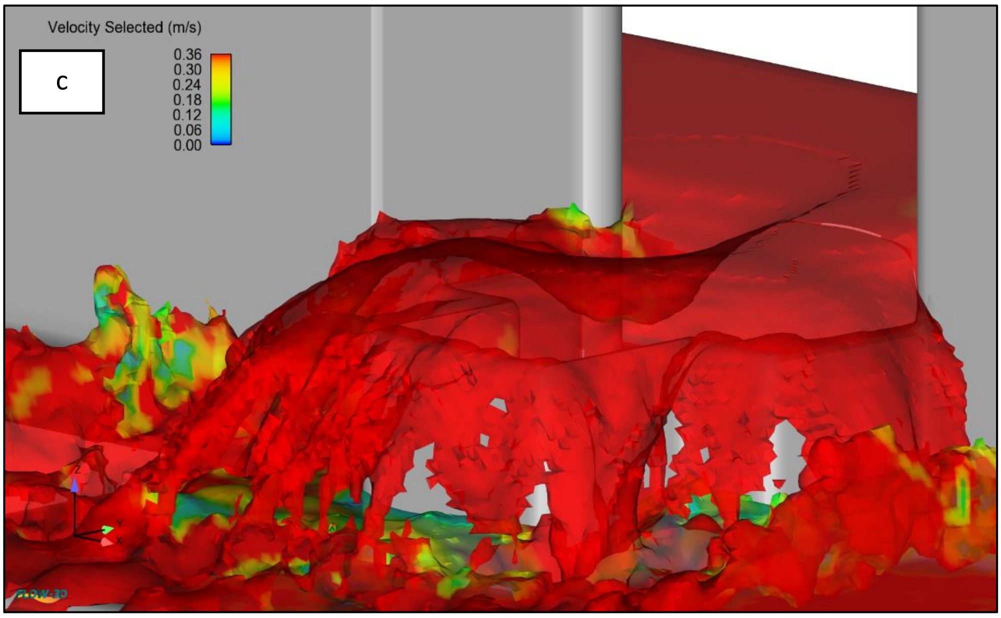

Figure 5.14: Air core forming process display in four model of a SLSW.

The swirl flow gradually intensified, and its center began to drop, at low Froude numbers, (approximately F1 < 0.17), it only causes a small drop in the water surface level. The fluctuation in the water surface increased as the Froude number increased (F1 > 0.17). Three types of vortices are observed at a fixed flow rate by changing the water level in the flume. Figure 5.15 (a,c) shows the vortices observed in the experiments. Figure 5.15(a) shows the surface swirl at L/B=1, θ°=60, p=0.14m, N=4, and F_1=0.16, Figure 5.16(b) the surface dimple at L/B=1, θ°=60, p=0.14m, N=4 and F_1=0.40, Figure 5.15(c) the dye core to the weir at L/B=1, θ°=60, p=0.14m, N=4 and F_1=0.67.

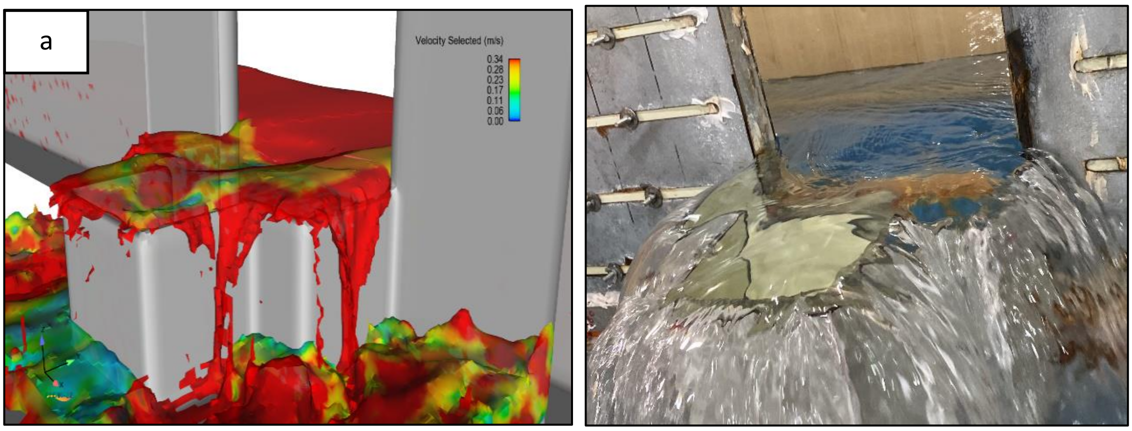

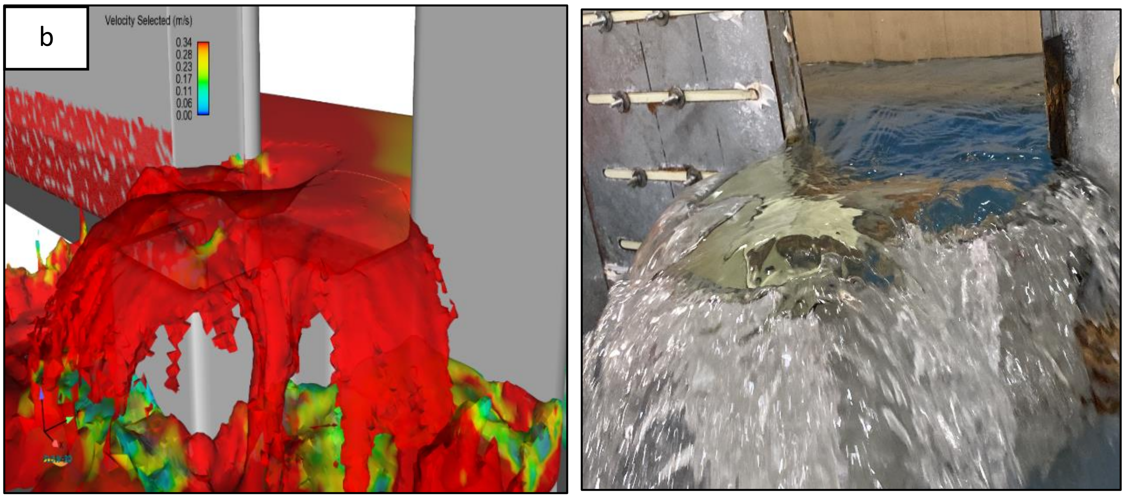

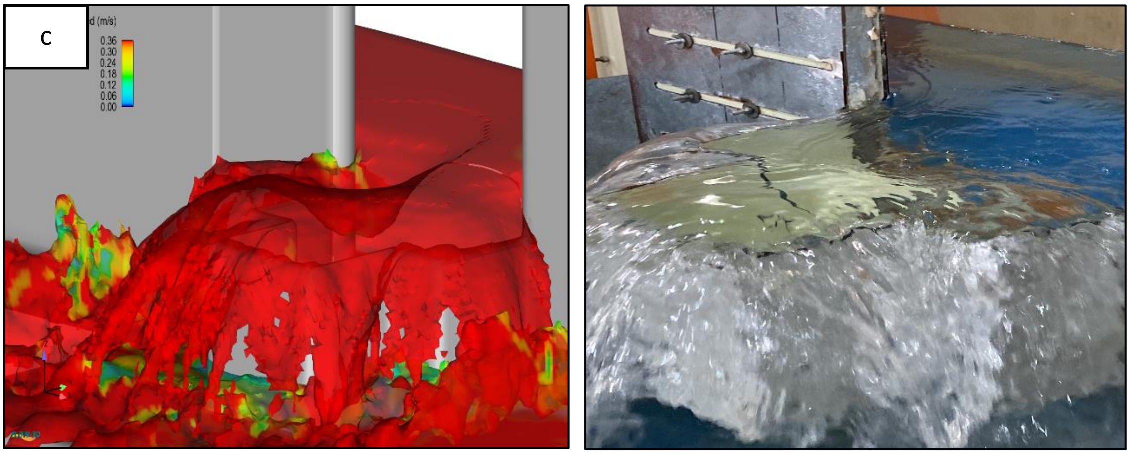

Figure 5.15: Types of vortices observed in experiments.

Figure 5.16 demonstrates the lateral flow over the labyrinth side weir represented by velocity vectors. In Figure 5.16a four-step model, the vortices are bounded by the sides of the step preventing the area of influence of these vortices from extending more toward the entire length of the side weir. In the case of an increase in the number of steps (Figure 5.16 b and c), the influence is more extended within the side weir, preventing incoming currents from crossing over the entire length of the downstream crest, resulting in decreased side weir performance. Although, in the case of the triangular labyrinth side weir (Figure 5.16d), changes in the flow direction and collisions with the triangular wall cause vortices. Abbasi et. al., (2021) also concluded the same results and mentioned that the flow path changed from the main channel to the side weir, and the current entering the side weir generated significant vortices inside the triangular LSW, thus, the hydraulic performance of the LSW was reduced. These vortices disrupt the side weir flow direction in all cases, reducing the discharge capacity, especially in SLSW. It can view vertical flow patterns in the y-direction by using a 3D clip to define the location where plot values are along with the fluid.

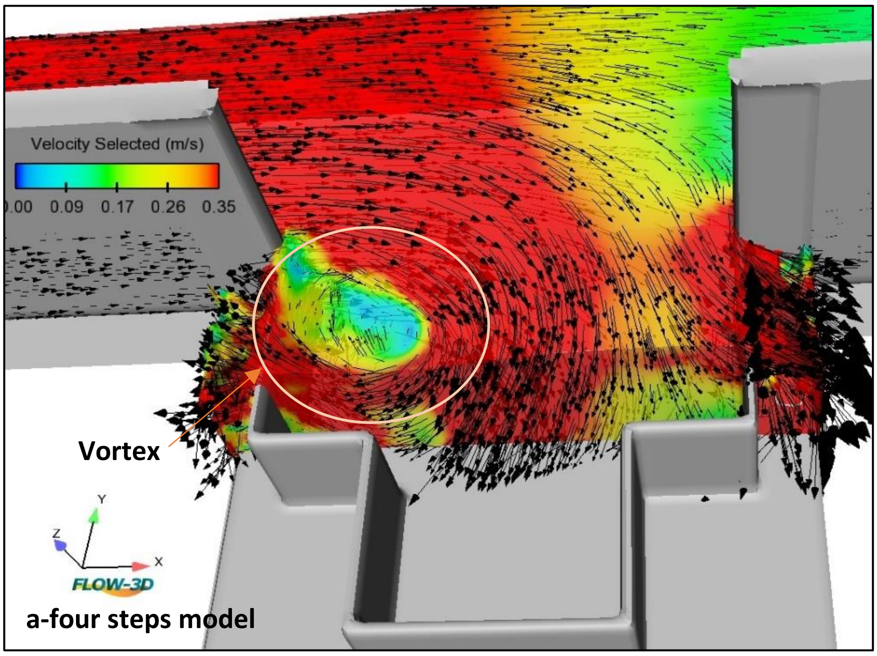

a-four steps model

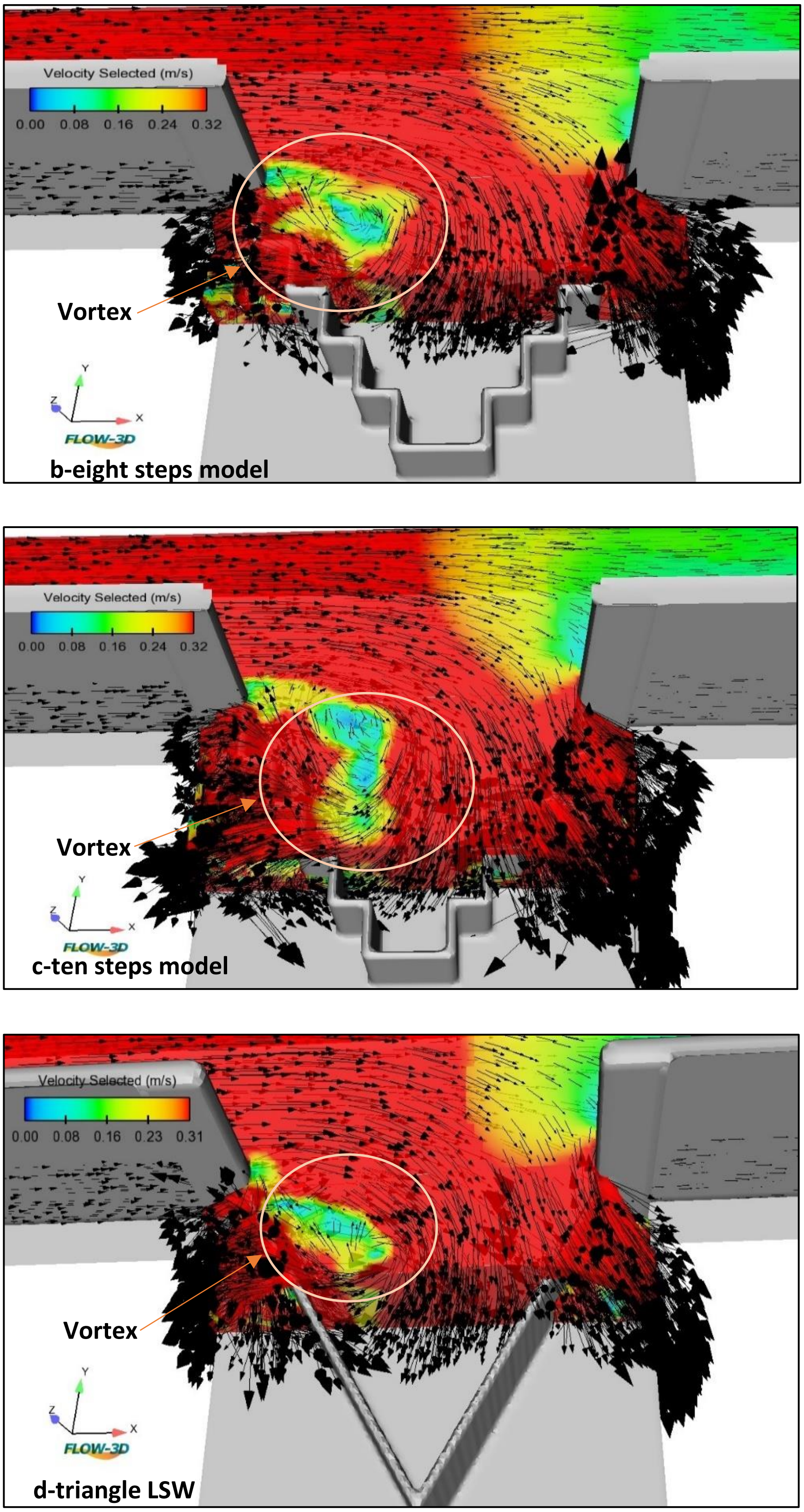

Figure 5.16: Lateral flow along the opening length of the LSW represented by velocity vectors at L/B=1, ϴ˚=60, p=0.08m, and F_1=0.67.

Scenario IV

In this scenario, simulations of a stepped labyrinth weir included angles of 45˚ and 60˚, runs by changing the crest height (P), side weir length (L), and step number for the Froude number range from 0.35 to 0.67. The discharge coefficient is calculated using Schmidt method, and the results are reported in Table 5.5.

As shown in Figure 5.17, the simulation shows that the red colors have the highest velocity while the blue colors have the lowest rate, it can view vertical flow patterns in the y-direction, as shown in sections I, and II, by using a 3D clip and velocity vectors to define the location where plot values are along with the fluid. Only a four-step model is presented here to maintain clarity in the presentation. A graphical presentation with the eight and ten-step models is presented in Appendix B. As shown in Figure 5.17 vortices are bounded by the sides of the step, preventing the area of influence of these vortices from extending more toward the entire length of the side weir. The antivortex structures decrease vortices and flow velocity inside and around the labyrinth side apex by tracking the flow direction, resulting in a more uniform lateral flow as shown in Figure 5.18. Abbasi et al., (2020) also concluded the same results and mentioned that the flow path changed from the main channel to the side weir, and the current entering the side weir generated significant vortices inside the triangular LSW. Consequently, the hydraulic performance of the LSW is reduced. Moreover, they concluded that using an antivortex inside the side weir improves the hydraulic performance by decreasing secondary flow motion intensity and increasing the discharge coefficient.

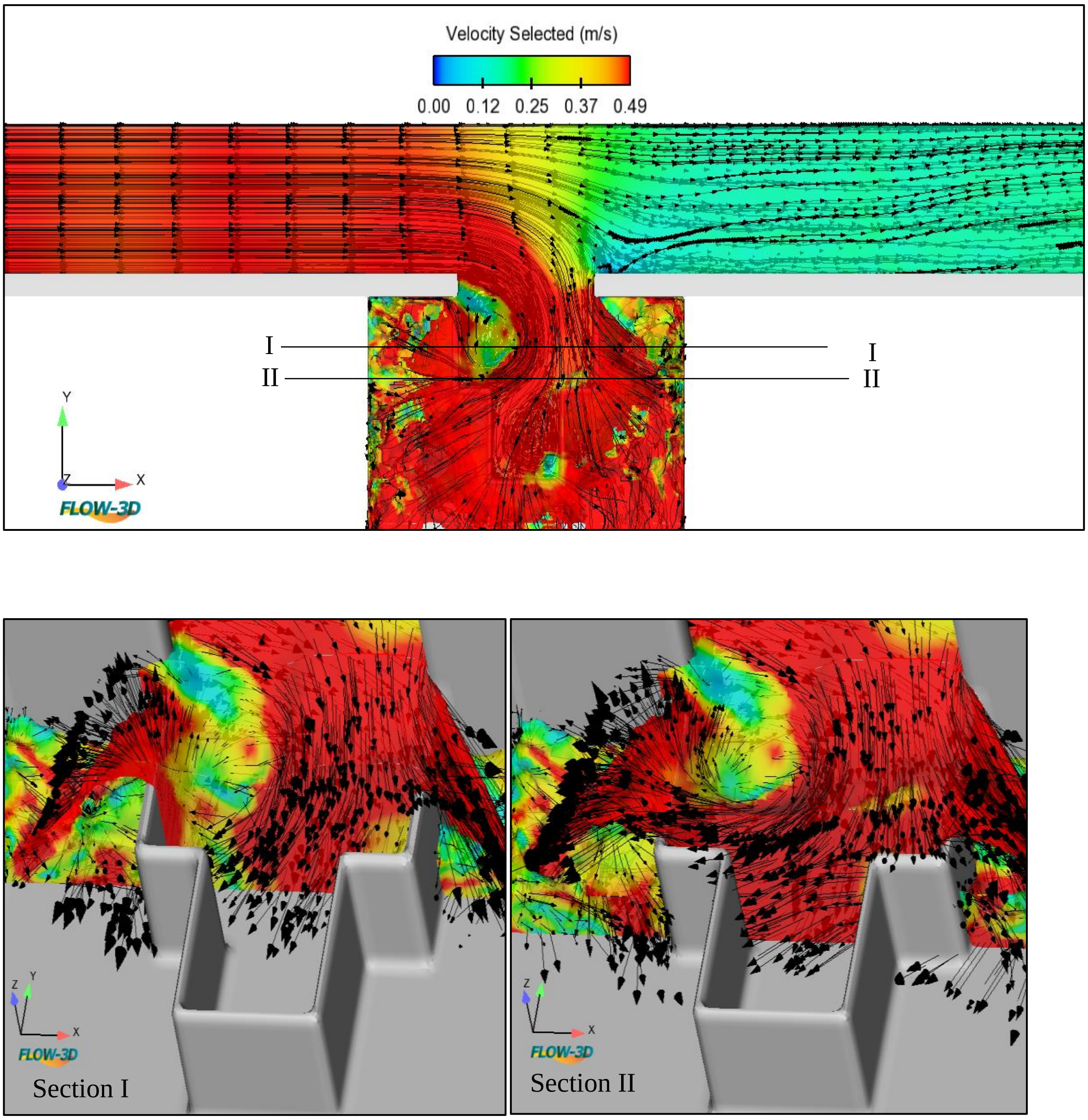

Figure 5.17: Vortex formation in four step model representing by velocity vectors at L/B=1, $\theta^{\circ}=45$, p=0.14m, and $F_1=0.67$, N=4.

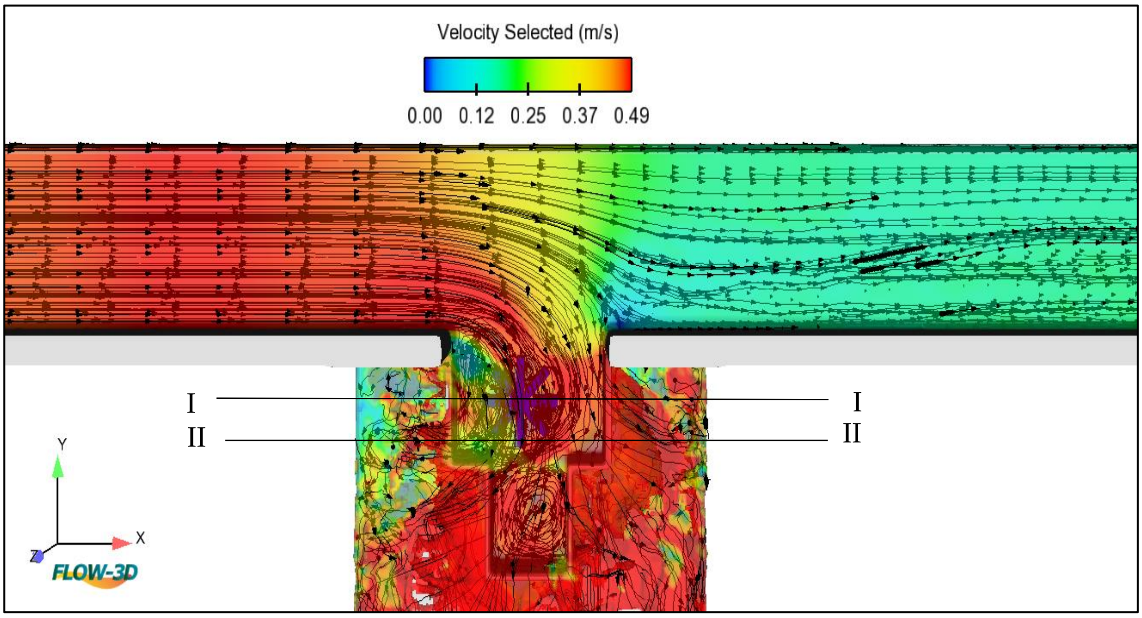

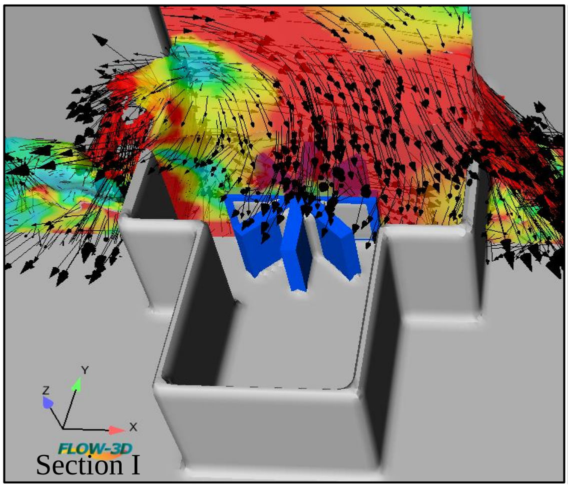

Section I

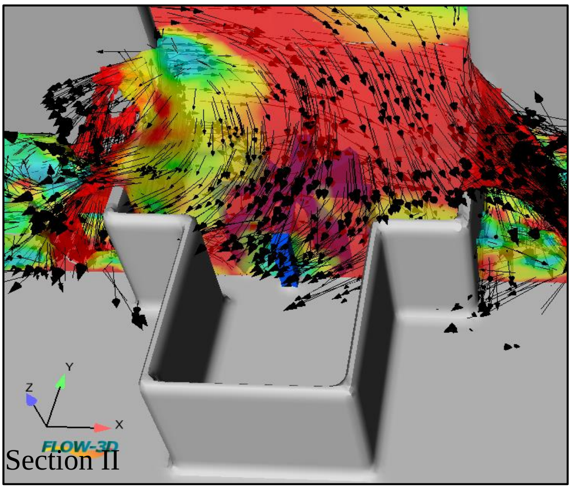

Section II

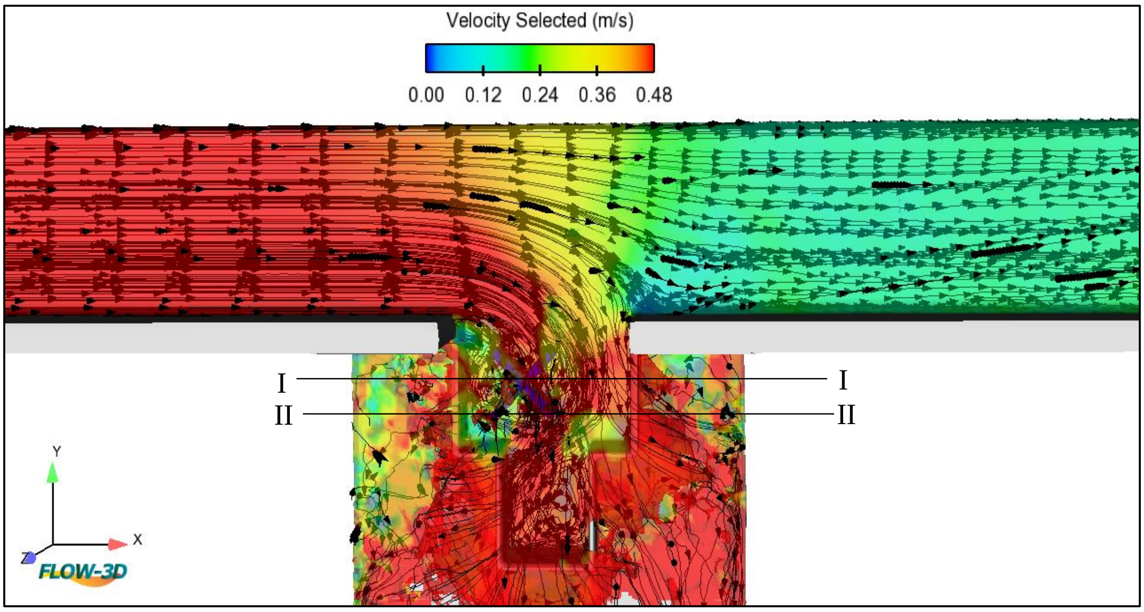

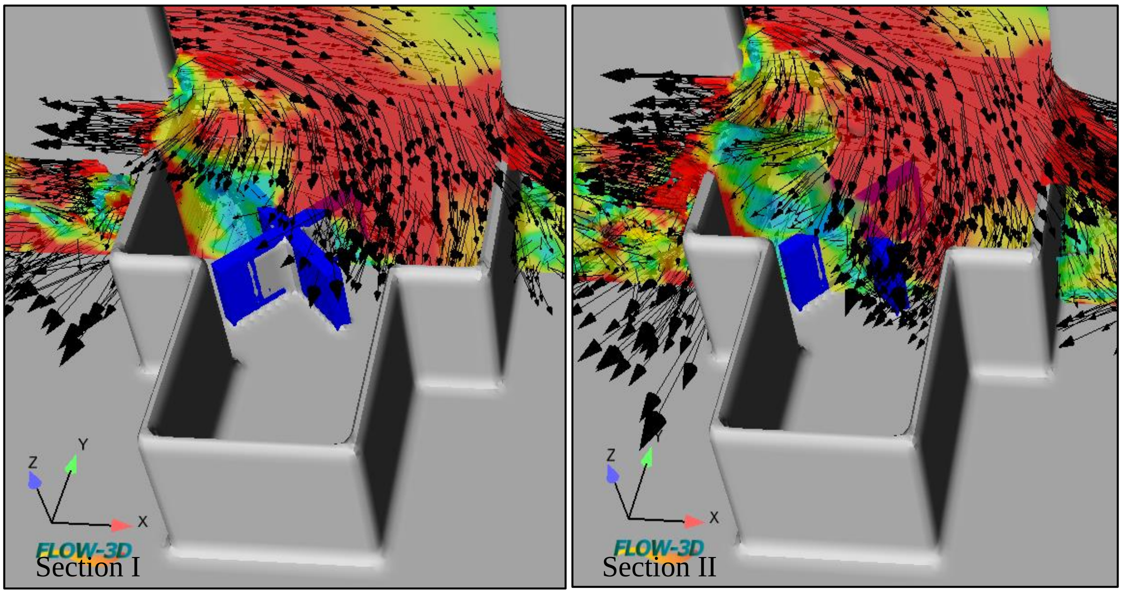
Z
Y
X
FLOW-3D
Section I
Z
Y
X
FLOW-3D
Section II

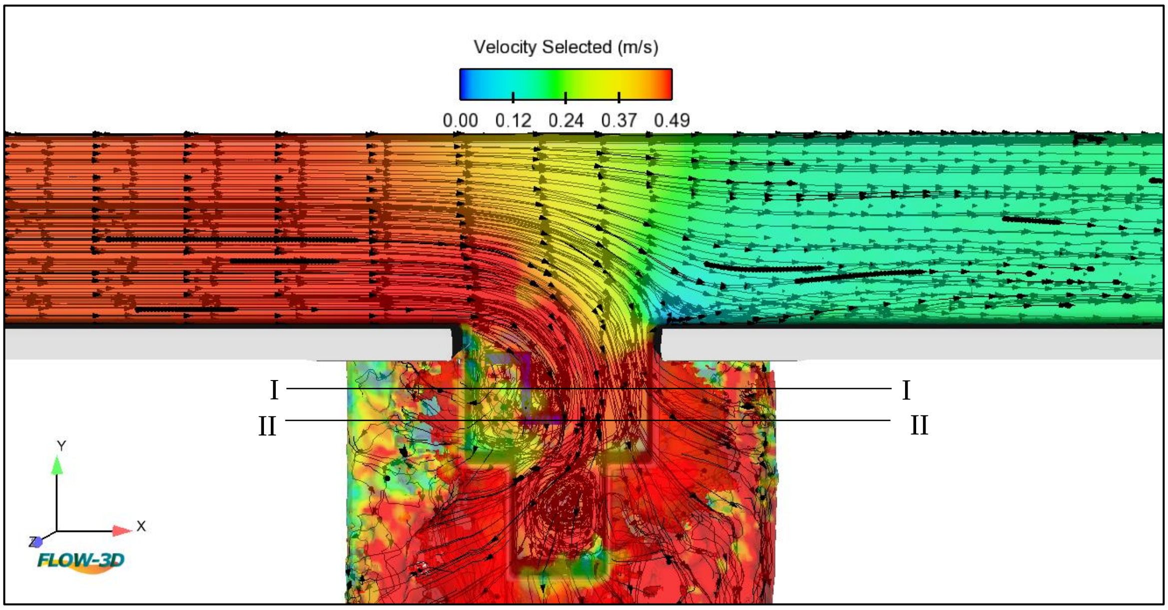
Velocity Selected (m/s)
0.00
0.12
0.24
0.37
0.49
I
I
II
II
Y
X
Z
FLOW-3D

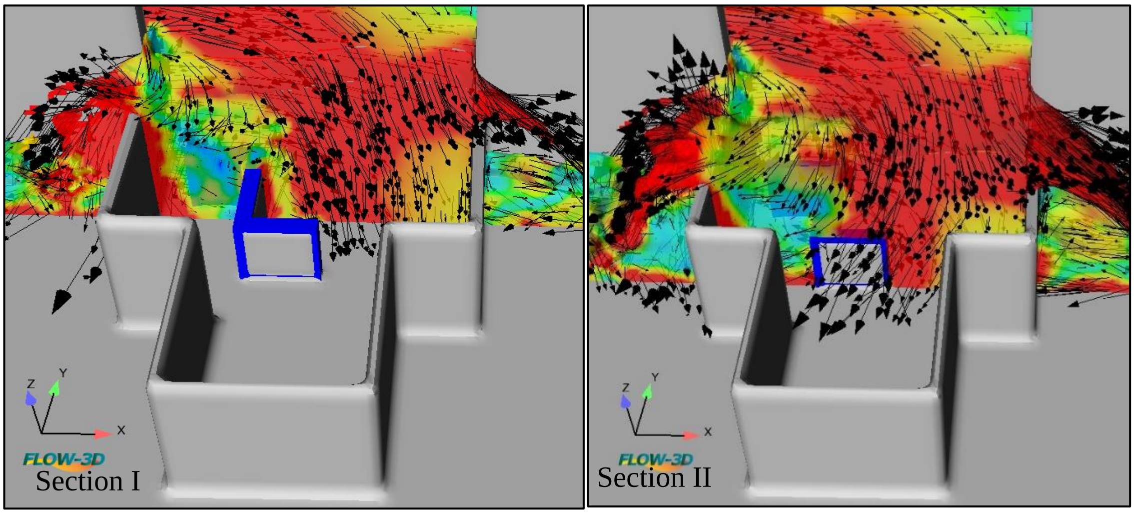
Z
Y
X
FLOW-3D
Section I
Z
Y
X
FLOW-3D
Section II

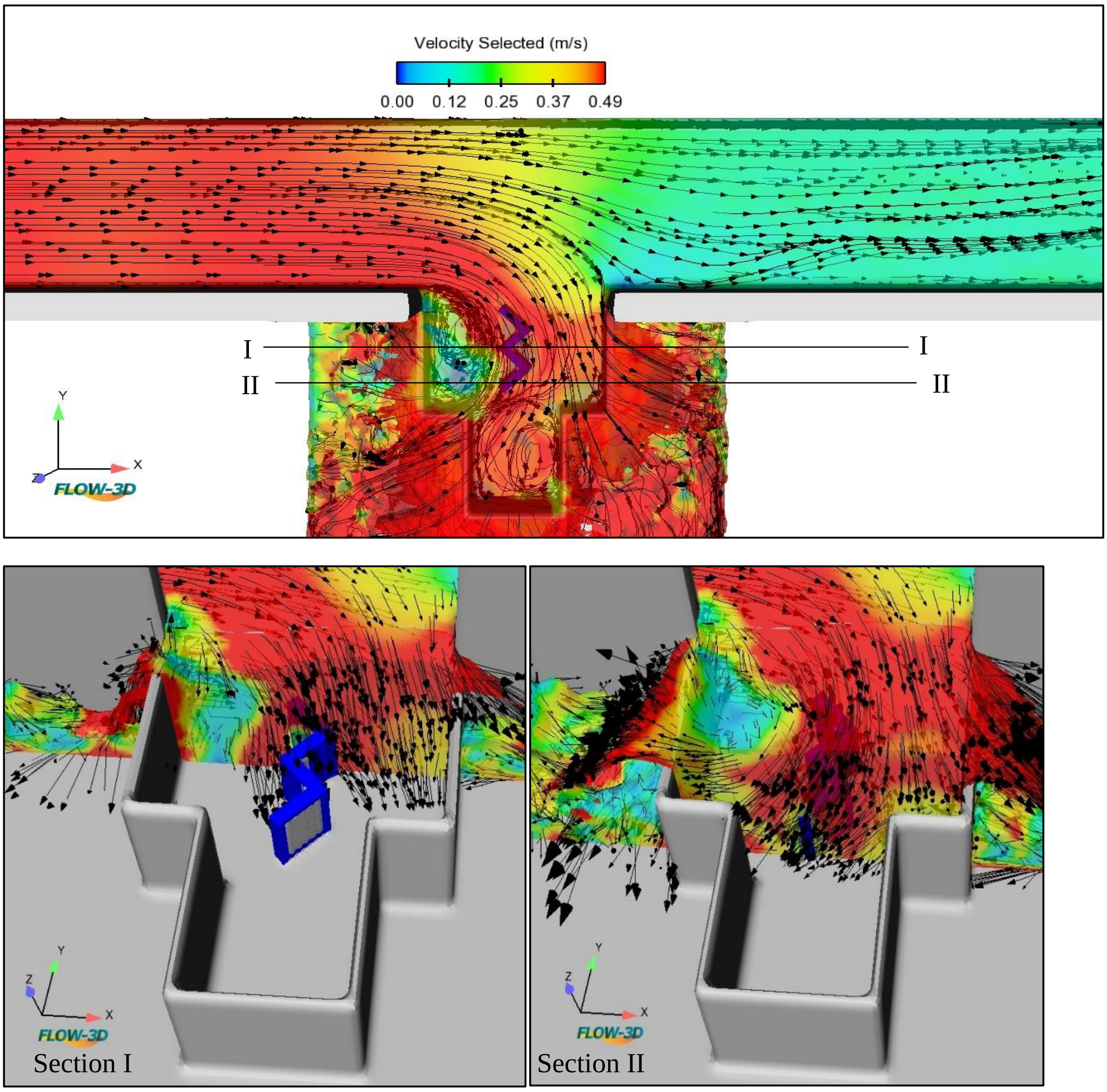

Section I

Section II

Figure 5.18: Vortex prevention by using antivortex structures at L/B=1, θ°=45, p=0.14m, and F_1=0.67, N=4.

Table5.5: Numerical simulations with antivortex structures.

N	P (m)	L (m)	θ	Q m^3/s	Antivortex type	F_1	Cd flow 3D	Cd experiment
4	0.14	0.30	45	0.027	1	0.36	0.96	0.91
4	0.14	0.30	45	0.027	2	0.35	0.91	0.88
4	0.14	0.30	45	0.027	3	0.36	0.92	0.88
4	0.14	0.30	45	0.027	4	0.36	0.91	0.87
8	0.14	0.30	45	0.027	1	0.37	0.95	0.90
8	0.14	0.30	45	0.027	2	0.37	0.98	0.95
8	0.14	0.30	45	0.027	3	0.36	0.93	0.88
8	0.14	0.30	45	0.027	4	0.36	0.94	0.88
10	0.14	0.30	45	0.027	1	0.35	0.92	0.88
10	0.14	0.30	45	0.027	2	0.35	0.90	0.86
10	0.14	0.30	45	0.027	3	0.34	0.89	0.85
10	0.14	0.30	45	0.027	4	0.34	0.89	0.84
4	0.08	0.30	60	0.027	1	0.70	0.77	0.75
4	0.08	0.30	60	0.027	2	0.68	0.75	0.72
4	0.08	0.30	60	0.027	3	0.68	0.72	0.70
4	0.08	0.30	60	0.027	4	0.68	0.74	0.70
8	0.08	0.30	60	0.027	1	0.68	0.75	0.71
8	0.08	0.30	60	0.027	2	0.67	0.73	0.69
8	0.08	0.30	60	0.027	3	0.66	0.71	0.67
8	0.08	0.30	60	0.027	4	0.66	0.70	0.65
10	0.08	0.30	60	0.027	1	0.66	0.72	0.68
10	0.08	0.30	60	0.027	2	0.66	0.69	0.67
10	0.08	0.30	60	0.027	3	0.65	0.70	0.66
10	0.08	0.30	60	0.027	4	0.65	0.69	0.66

Chapter Six

Conclusions and Recommendations

6.1. Conclusions

1- Free-surface vortex developed upstream of stepped labyrinth side weir as the number of steps decreased at specific Froude numbers.

2- The swirl flow gradually intensified, and its center began to drop at low Froude numbers (approximately F1 < 0.17), it only caused a slight drop in the water surface level. The fluctuation in the water surface increased as the Froude number increased (F1 > 0.17).

3- The area of influence of these vortices increases with the increasing number of steps, in four steps model, the vortices are bounded by the sides of the step, which restricts the area of influence of these vortices against extending more toward the length of the side weir, contrary to the case of an increase in the number of steps where the influence is more extended within the side weir. As a result, the side weir performance is decreased.

4- The performance of the antivortex structures improves the discharge coefficient with increasing step number and head angle, which is significant with decreasing weir length ratio (L/B=1).

5- Among the selected models of the antivortex structures, type1 is the most effective model in decreasing the vortices in the stepped labyrinth side weir area.

6-Type1 increases the discharge coefficient by about (19%) as an average as compared with the case of no antivortex under the same range of Froude Number. While Type4 increased it by 11% and had a minor effect among all other types.

7-The discharge coefficient values of the stepped weirs with antivortex structure that have the best performance (Type1 with crest height P = 0.5 P) outperform the selected antivortex (Type 6 with crest height P = 1 P in the study of Emiroglu et al.,2017) in the literature with 5% higher.

8-Antivortex structures significantly increase the discharge coefficient with the increase of the weir height ratio (P/y_1) that lead to improve weir performance and dissipating the vortex that extends along the length of the weir as the number of steps increases (N), especially for weirs with head angle $\theta = 45^\circ$.

9-The installation of antivortex structures increases the weir discharge capacity at similar flow depths with an increase in the step number.

10- The antivortex inside the stepped labyrinth side weir increases hydraulic performance by reducing secondary flow motion intensity. The antivortex decreases the velocity of flow inside the side weir. The intensity of the secondary flow inside the side weir decreases as the flow velocity lowers, which significantly affects the discharge performance.

11- Results indicate that the water surface profile has a higher water surface drop at the beginning of the side weir, especially with four steps, and the drop decreases as the number of steps increases. As a result, the antivortex installation improves discharge efficiency by reducing vortex formation and surface fluctuation.

12- The most significant error for the stepped labyrinth side weir between experimental data and numerical results is 3.07 percent, which supports the capability of the numerical model to estimate flow requirements across a stepped labyrinth side weir.

13- It can be suggested that the LES model gives better solutions for small values. because the laminar solver cannot capture the vorticity near the walls caused by low turbulence values, which affects the formation of the vortex.

14- Several simulations are investigated for cases to select the most efficient shape and dimensions of the antivortex structures. The comparison showed that the Flow 3D and the LES turbulence model are the most suitable for modelling free surface rotating flows where the former was the most economical and the latter was the most accurate.

15- The numerical model confirms its capacity to estimate flow requirements across the side weir.

6.2 Recommendations

1- Studying the hydraulic performance of asymmetrical SLSW in subcritical flow.

2- Studying the discharge coefficient of stepped trapezoidal piano key side weir.

3- Improving the efficiency of stepped trapezoidal piano key side weir using anti-vortices in subcritical flow.

4- Refinement of the velocimetry technique to resolve the vortex core velocity profiles in greater detail. The result would lead to resolving the dependence of the tangential velocity field on the $z-$axis in this region as well as other trends.

5- Investigating, in detail, the growth of the turbulent vortex core by measuring the maximum tangential velocities as a means to indirectly observe the turbulent eddy viscosity.

References

References

Abbasi, S., Fatemi, S., Ghaderi, A., & Di Francesco, S. (2020). The effect of geometric parameters of the antivortex on a triangular labyrinth side weir. *Water*, *13*(1), 14. https://doi.org/https://doi.org/10.3390/w13010014

Aǵaçcioǵlu, H., & Önen, F. (2005). Clear-water scour at a side-weir intersection along the bend. *Irrigation and Drainage: The Journal of the International Commission on Irrigation and Drainage*, *54*(5), 553–569. https://doi.org/https://doi.org/10.1002/ird.209

Aghayari, F., Honar, T., & Keshavarzi, A. (2009). A study of spatial variation of discharge coefficient in broad-crested inclined side weirs. *Irrigation and Drainage: The Journal of the International Commission on Irrigation and Drainage*, *58*(2), 246–254. https://doi.org/https://doi.org/10.1002/ird.416

Alfatlawi, & Shlaash. (2021). Experimental Study of the Hydraulic Performance of Stepped Labyrinth Side Weir. *Master Thesis*.

Ansari, U. S., & Patil, L. G. (2022). Numerical analysis of triangular labyrinth side weir in triangular channel. *ISH Journal of Hydraulic Engineering*, *28*(sup1), 141–148. https://doi.org/https://doi.org/10.1080/09715010.2020.1715269

Aydin, M. C. (2012). CFD simulation of free-surface flow over triangular labyrinth side weir. *Advances in Engineering Software*, *45*(1), 159–166. https://doi.org/https://doi.org/10.1016/j.advengsoft.2011.09.006

Aydin, M. C., & Emiroglu, M. E. (2013). Determination of capacity of labyrinth side weir by CFD. *Flow Measurement and Instrumentation*, *29*, 1–8. https://doi.org/https://doi.org/10.1016/j.flowmeasinst.2012.09.008

Aydin, M. C., Öztürk, M., & Yücel, A. (2015). Experimental and numerical investigation of self-priming siphon side weir on a straight open channel. *Flow Measurement and Instrumentation*, *45*, 140–150. https://doi.org/https://doi.org/10.1016/j.flowmeasinst.2015.06.014

Aydin, M. C., & Ulu, A. E. (2017). Antivortex effects on two-cycle trapezoidal labyrinth side weirs. *Journal of Irrigation and Drainage Engineering*, *143*(7), 6017004. https://doi.org/https://doi.org/10.1061/(ASCE)IR.1943-4774.0001182

Azimi, H., Shabanlou, S., Ebtehaj, I., & Bonakdari, H. (2016). Discharge coefficient of rectangular side weirs on circular channels. *International Journal of Nonlinear Sciences and Numerical Simulation*, *17*(7–8),

References

391–399. https://doi.org/https://doi.org/10.1515/ijnsns-2016-0033

Bagheri, S., Kabiri-Samani, A. R., & Heidarpour, M. (2014). Discharge coefficient of rectangular sharp-crested side weirs Part II: Domínguez's method. *Flow Measurement and Instrumentation, 35,* 116–121. https://doi.org/https://doi.org/10.1016/j.flowmeasinst.2013.10.006

BINNIE, G. M. (1938). MODEL-EXPERIMENTS ON BELLMOUTH AND SIPHON-BELLMOUTH OVERFLOW SPILLWAYS.(INCLUDES PLATES AND PHOTOGRAPHS). *Journal of the Institution of Civil Engineers*, *10*(1), 65–90. https://doi.org/https://doi.org/10.1680/ijoti.1938.14576

Bombardelli, F. A., Meireles, I., & Matos, J. (2011). Laboratory measurements and multi-block numerical simulations of the mean flow and turbulence in the non-aerated skimming flow region of steep stepped spillways. *Environmental Fluid Mechanics, 11*(3), 263–288. https://doi.org/https://doi.org/10.1007/s10652-010-9188-6

Borghei, S. M., Jalili, M. R., & Ghodsian, M. (1999). Discharge coefficient for sharp-crested side weir in subcritical flow. *Journal of Hydraulic Engineering*, *125*(10), 1051–1056.

Borghei, S. M., Nekooie, M. A., Sadeghian, H., & Ghazizadeh, M. R. J. (2013). Triangular labyrinth side weirs with one and two cycles. *Proceedings of the Institution of Civil Engineers-Water Management*, *166*(1), 27–42. https://doi.org/https://doi.org/10.1680/wama.11.00032

Bos, M. G. (1988). *Discharge measurement structures*. Int. Institute for Land Reclamation and Improvement, Wageningen, The Netherlands, 399.

Buckingham, E. (1915). The principle of similitude. *Nature, 96*(2406), 396–397.

Cheong, H.-F. (1991). Discharge coefficient of lateral diversion from trapezoidal channel. *Journal of Irrigation and Drainage Engineering*, *117*(4), 461–475. https://doi.org/https://doi.org/10.1061/(ASCE)0733-9437(1991)117:4(461)

Coşar, A., & Agaccioglu, H. (2004). Discharge coefficient of a triangular side-weir located on a curved channel. *Journal of Irrigation and Drainage Engineering*, *130*(5), 410–423. https://doi.org/https://doi.org/10.1061/(ASCE)0733-9437(2004)130:5(410)

Crookston, B. M., & Tullis, B. (2010). Labyrinth weirs. *Hydraulic*

Structures, 59.

Crookston, B. M., & Tullis, B. P. (2012). Arced labyrinth weirs. *Journal of Hydraulic Engineering*, *138*(6), 555–562. https://doi.org/https://doi.org/10.1061/(ASCE)HY.1943-7900.0000553

De Marchi, G. (1934). Essay on the performance of lateral weirs. *L'Energia Elettrica, Milan, Italy*, *11*, 849–860.

Denys, F., & Basson, G. (2018). Transient hydrodynamics of Piano Key weirs. *7th International Symposium on Hydraulic Structures*. https://doi.org/10.15142/T30M0J

Emin Emiroglu, M., Cihan Aydin, M., & Kaya, N. (2014). Discharge characteristics of a trapezoidal labyrinth side weir with one and two cycles in subcritical flow. *Journal of Irrigation and Drainage Engineering*, *140*(5), 4014007. https://doi.org/https://doi.org/10.1061/(ASCE)IR.1943-4774.0000709

Emiroglu, & Ikinciogullari. (2016). Determination of discharge capacity of rectangular side weirs using Schmidt approach. *Flow Measurement and Instrumentation*, *50*, 158–168. https://doi.org/https://doi.org/10.1016/j.flowmeasinst.2016.06.021

Emiroglu, M. E., Gogus, M., Tunc, M., & Islamoglu, K. (2017). Effects of antivortex structures installed on trapezoidal labyrinth side weirs on discharge capacity and scouring. *Journal of Irrigation and Drainage Engineering*, *143*(6), 4017006. https://doi.org/https://doi.org/10.1061/(ASCE)IR.1943-4774.0001158

Emiroglu, M. E., & Kaya, N. (2011). Discharge coefficient for trapezoidal labyrinth side weir in subcritical flow. *Water Resources Management*, *25*(3), 1037–1058. https://doi.org/https://doi.org/10.1007/s11269-010-9740-7

Emiroglu, M. E., Kaya, N., & Agaccioglu, H. (2011). *Discharge Capacity of Labyrinth Side Weir Located on at straight channel*. *January*, 37–46. https://doi.org/https://doi.org/10.1061/(ASCE)IR.1943-4774.0000112

Falvey, H. T. (2003). *Hydraulic design of labyrinth weirs*.

Fares, Y. R., & Herbertson, J. G. (1993). Behaviour of flow in a channel bend with a side overflow (flood relief) channel. *Journal of Hydraulic Research*, *31*(3), 383–402. https://doi.org/https://doi.org/10.1080/00221689309498833

Flow Science. (2016). *FLOW-3D V 11.2 User's Manual.Inc.: Santa Fe, NM, USA,*.

References

Gebhardt, M., Herbst, J., Merkel, J., & Belzner, F. (2018). Sedimentation at labyrinth weirs–an experimental study of the self-cleaning process. *Journal of Hydraulic Research*, *57*, *2019*(4), 579–590. https://doi.org/https://doi.org/10.1080/00221686.2018.1494053

Ghaderi, A., & Abbasi, S. (2019). CFD simulation of local scouring around airfoil-shaped bridge piers with and without collar. *Sādhanā*, *44*(10), 1–12. https://doi.org/https://doi.org/10.1007/s12046-019-1196-8

Ghaderi, A., Abbasi, S., Abraham, J., & Azamathulla, H. M. (2020). Efficiency of trapezoidal labyrinth shaped stepped spillways. *Flow Measurement and Instrumentation*, *72*, 101711. https://doi.org/https://doi.org/10.1016/j.flowmeasinst.2020.101711

Ghaderi, A., Daneshfaraz, R., Abbasi, S., & Abraham, J. (2020). Numerical analysis of the hydraulic characteristics of modified labyrinth weirs. *International Journal of Energy and Water Resources*, *4*(4), 425–436.

Hager, W. H. (1987). Lateral outflow over side weirs. *Journal of Hydraulic Engineering*, *113*(4), 491–504.

Henderson, V. (1966). *The nature of nursing a definition and its implications for practice, research, and education*.

Hirt, C. W., & Nichols, B. D. (1981). Volume of fluid (VOF) method for the dynamics of free boundaries. *Journal of Computational Physics*, *39*(1), 201–225.

Ikinciogullari, &Emiroglu. (2019). Estimation of triangular labyrinth side weir discharge capacity using schmidt approach. *Sigma Journal of Engineering and Natural Sciences*, *37*(1), 289–303.

Jalili, M. R., & Borghei, S. M. (1996). Discussion: discharge coefficient of rectangular side weirs. *Journal of Irrigation and Drainage Engineering*, *122*(2), 132. https://doi.org/https://doi.org/10.1061/(ASCE)0733-9437(1996)122:2(132)

Kabiri-Samani, A., Borghei, S. M., & Esmaili, H. (2011). Hydraulic performance of labyrinth side weirs using vanes or piles. *Proceedings of the Institution of Civil Engineers-Water Management*, *164*(5), 229–241. https://doi.org/https://doi.org/10.1680/wama.2011.164.5.229

Karimi, M., Ghazizadeh, M. J., Saneie, M., & Attari, J. (2019). Flow characteristics over asymmetric triangular labyrinth side weirs. *Flow Measurement and Instrumentation*, *68*, 101574. https://doi.org/https://doi.org/10.1016/j.flowmeasinst.2019.101574

Khameneh, H. Z., Khodashenas, S. R., & Esmaili, K. (2014). The effect of increasing the number of cycles on the performance of labyrinth side weir. *Flow Measurement and Instrumentation*, *39*, 35–45. https://doi.org/https://doi.org/10.1016/j.flowmeasinst.2014.05.002

Koken, M., & Constantinescu, G. (2008). An investigation of the flow and scour mechanisms around isolated spur dikes in a shallow open channel: 1. Conditions corresponding to the initiation of the erosion and deposition process. *Water Resources Research*, *44*(8). https://doi.org/10.1029/2007WR006491

Li, H., Chen, H., Ma, Z., & Zhou, Y. (2008). Experimental and numerical investigation of free surface vortex. *Journal of Hydrodynamics*, *20*(4), 485–491. https://doi.org/https://doi.org/10.1016/S1001-6058(08)60084-0

Maatooq, J. S., & Ojaimi, T. Y. (2014). Evaluation the Hydraulic Aspects of Stepped Labyrinth Spillway. *Engineering and Technology Journal*, *32*(9), 2174–2185.

May, R. W. P. (2003). *Hydraulic design of side weirs*. Thomas Telford.

Mulligan, S. (2015). Experimental and numerical analysis of three-dimensional free-surface turbulent vortex flows with strong circulation. *Ireland: Institute of Technology Sligo*.

Nadesamoorthy, T., & Thomson, A. (1972). Discussion of “spatially varied flow over side-weirs.” *Journal of the Hydraulics Division*, *98*(12), 2234–2235. https://doi.org/https://doi.org/10.1061/JYCEAJ.0003529

Novák, P., & Čabelka, J. (1981). Models in hydraulic engineering: Physical principles and design applications. *Monographs & Surveys in Water Resources Engineering*.

Oreizi, Z., Heidarpour, M., & Bagheri, S. (2015). Hydraulic characteristics of flow over sinusoidal sharp-crested weirs. *Journal of Irrigation and Drainage Engineering*, *141*(3), 6014003. https://doi.org/https://doi.org/10.1061/(ASCE)IR.1943-4774.0000808

Parvaneh, A., & Borghei, S. M. (2009). Oblique side weir. *Proceedings of the 33th Congress of the International Association for Hydraulic Research, Vancouver*, 9–14.

Ranga Raju, K. G., Gupta, S. K., & Prasad, B. (1979). Side weir in rectangular channel. *Journal of the Hydraulics Division*, *105*(5), 547–554. https://doi.org/https://doi.org/10.1061/JYCEAJ.0005207

Sangsefidi, Y., Mehraein, M., & Ghodsian, M. (2018). Experimental study on flow over in-reservoir arced labyrinth weirs. *Flow Measurement and Instrumentation*, *59*, 215–224.

https://doi.org/https://doi.org/10.1016/j.flowmeasinst.2017.12.002

Schmidt, M. (1954). Zur Frage des abflusses uber streichwehre. *Techaniv Berlin-Charlottenbury, Mitteilung, NY41*, 1–68.

Singh, R., Manivannan, D., & Satyanarayana, T. (1994). Discharge coefficient of rectangular side weirs. *Journal of Irrigation and Drainage Engineering*, *120*(4), 814–819. https://doi.org/https://doi.org/10.1061/(ASCE)0733-9437(1994)120:4(814)

Smagorinsky, J. (1963). General circulation experiments with the primitive equations: I. The basic experiment. *Monthly Weather Review*, *91*(3), 99–164. https://doi.org/https://doi.org/10.1175/1520-0493(1963)091<0099:GCEWTP>2.3.CO;2

Subramanya, K., & Awasthy, S. C. (1972). Spatially varied flow over side-weirs. *Journal of the Hydraulics Division*, *98*(1), 1–10. https://doi.org/https://doi.org/10.1061/JYCEAJ.0003188

Swamee, P. K., Pathak, S. K., Mohan, M., Agrawal, S. K., & Ali, M. S. (1994). Subcritical flow over rectangular side weir. *Journal of Irrigation and Drainage Engineering*, *120*(1), 212–217.

Tullis, J. P., Amanian, N., & Waldron, D. (1995). Design of labyrinth spillways. *Journal of Hydraulic Engineering*, *121*(3), 247–255. https://doi.org/10.1061/(ASCE)0733-9429(1995)121:3(247), 247–255.

Venutelli, M. (2008). Method of solution of nonuniform flow with the presence of rectangular side weir. *Journal of Irrigation and Drainage Engineering*, *134*(6), 840–846. https://doi.org/https://doi.org/10.1061/(ASCE)0733-9437(2008)134:6(840)

Vyzikas, T., Deshoulières, S., Giroux, O., Barton, M., & Greaves, D. (2017). Numerical study of fixed Oscillating Water Column with RANS-type two-phase CFD model. *Renewable Energy*, *102*, 294–305.

Wang, Y., Wang, W., Hu, X., & Liu, F. (2018). Experimental and numerical research on trapezoidal sharp-crested side weirs. *Flow Measurement and Instrumentation*, *64*, 83–89. https://doi.org/https://doi.org/10.1016/j.flowmeasinst.2018.10.005

Yamini, O. A., Movahedi, A., Mousavi, S. H., Kavianpour, M. R., & Kyriakopoulos, G. L. (2022). Hydraulic Performance of Seawater Intake System Using CFD Modeling. *Journal of Marine Science and Engineering*, *10*(7), 988. https://doi.org/; https://doi.org/10.3390/jmse10070988

References

Yu-Tek, L. (1972). Discussion of "Spatially Varied Flow over Side-Weirs." *Journal of the Hydraulics Division*, *98*(11), 2047–2048.

Ziaei, A. N., Nikou, N. S. R., Beyhaghi, A., Attarzadeh, F., & Khodashenas, S. R. (2019). Flow simulation over a triangular labyrinth side weir in a rectangular channel. *Progress in Computational Fluid Dynamics, An International Journal*, *19*(1), 22–34. https://doi.org/https://www.inderscienceonline.com/doi/abs/10.1504/PCFD.2019.097599#pane-pcw-details

Appendix A

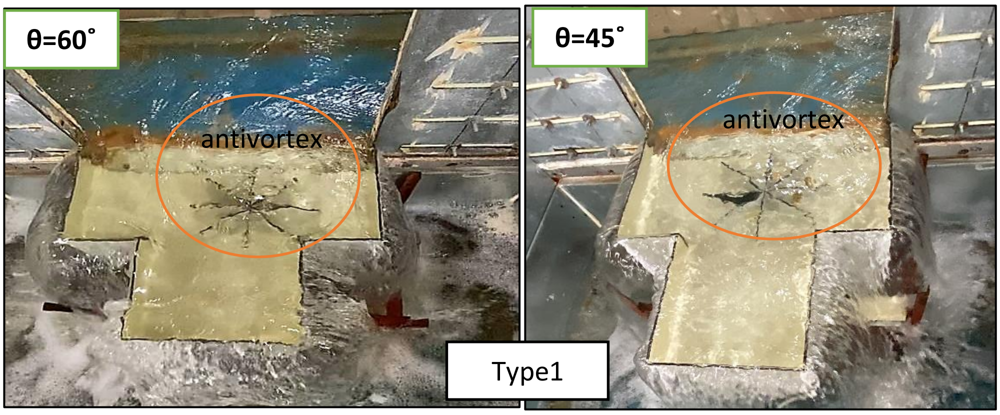

Type1

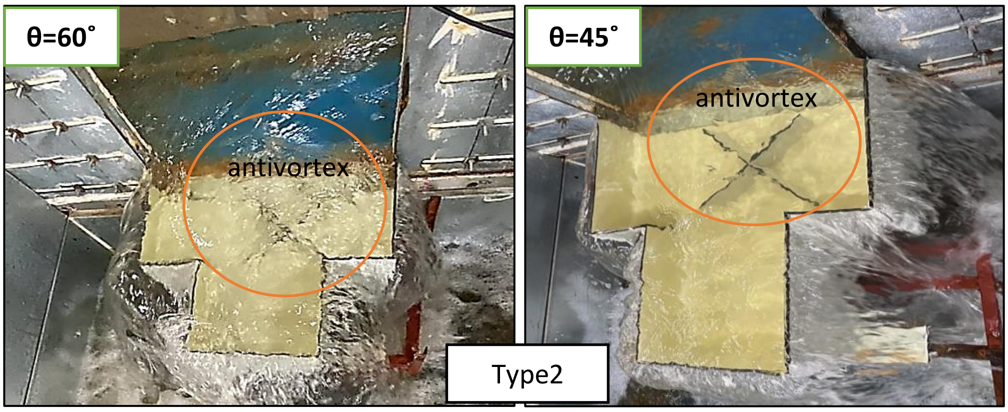

Type2

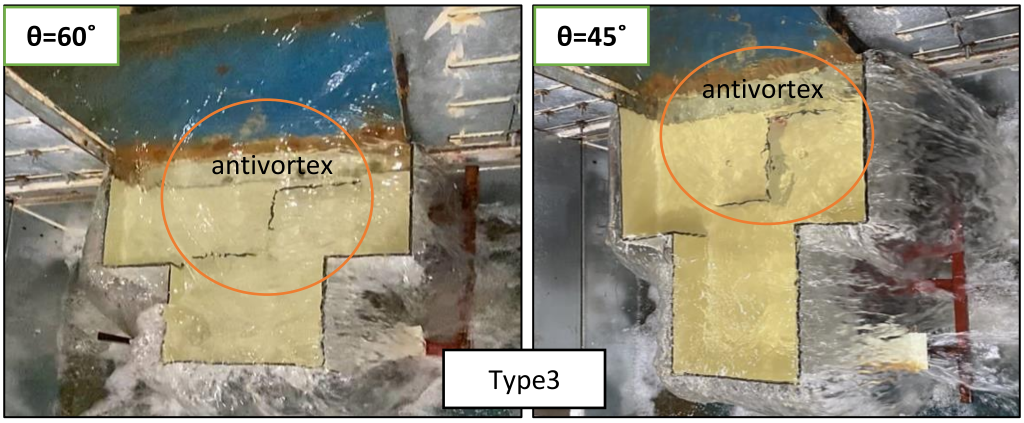

Type3

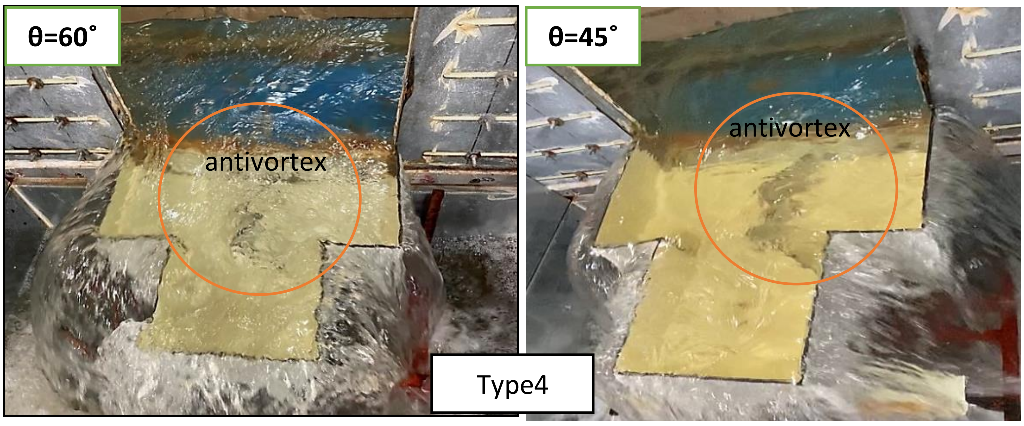

Type4

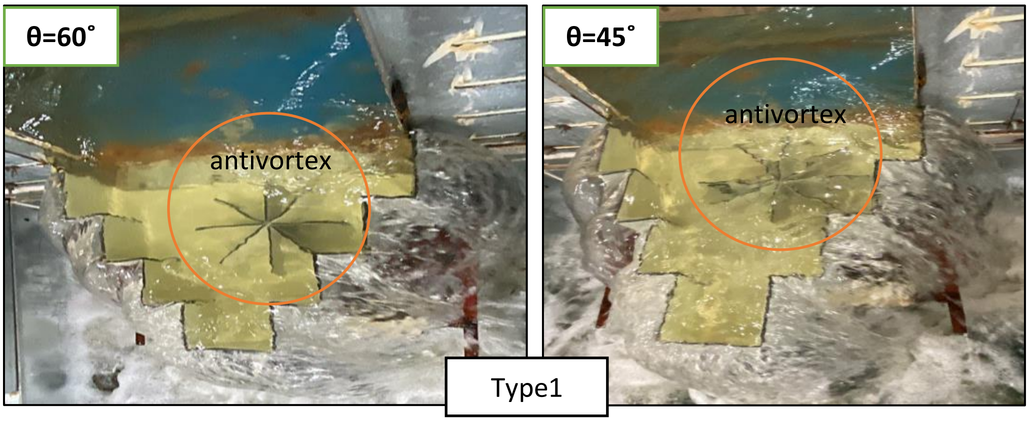
θ=60˚
antivortex
θ=45˚
antivortex
Type1

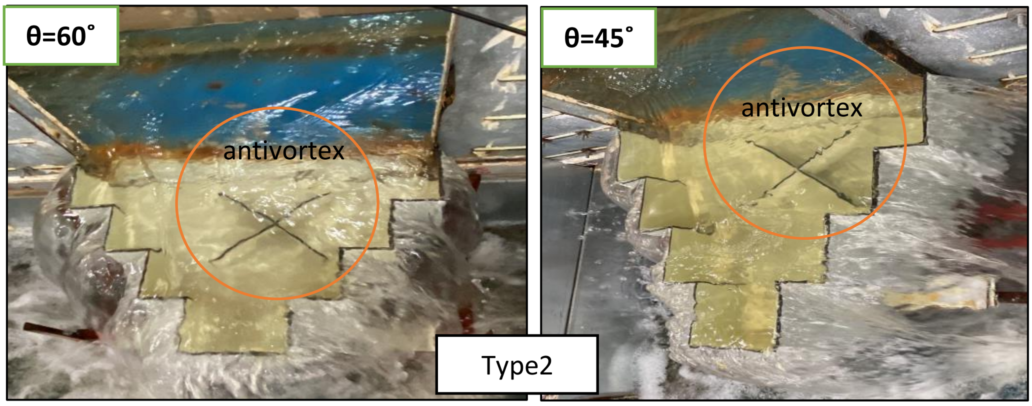
θ=60˚
antivortex
θ=45˚
antivortex
Type2

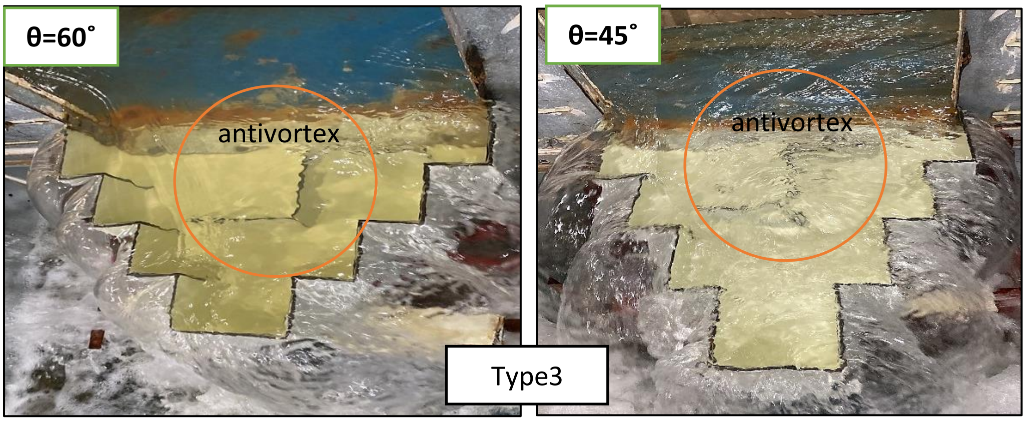
θ=60˚
antivortex
θ=45˚
antivortex
Type3

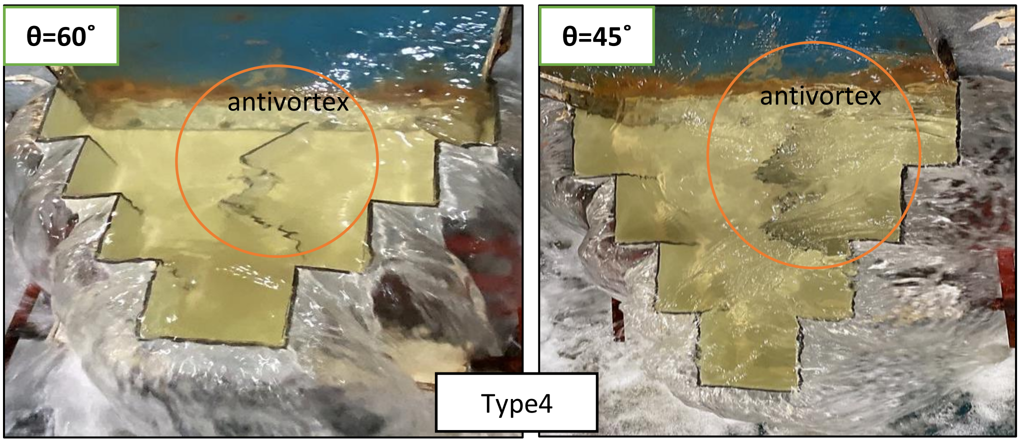
θ=60˚
antivortex
θ=45˚
antivortex
Type4

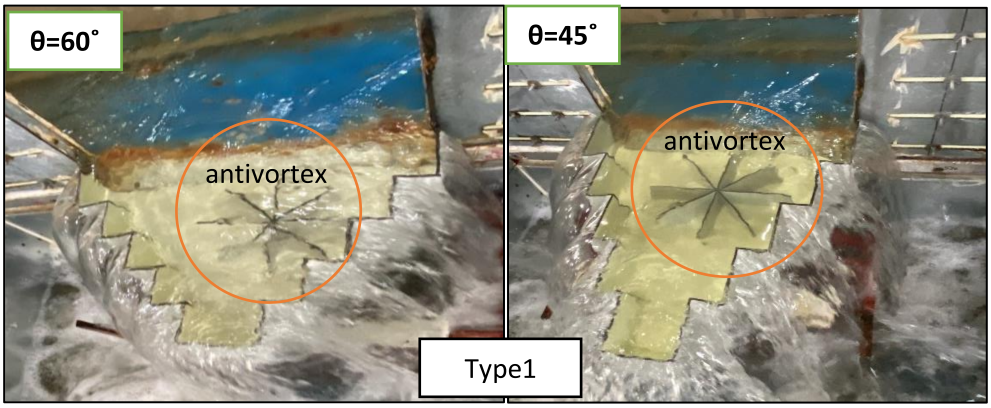

Type1

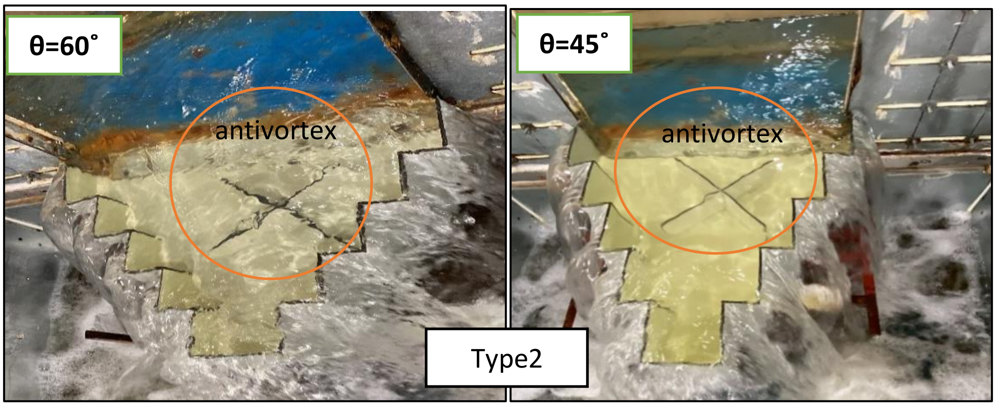

Type2

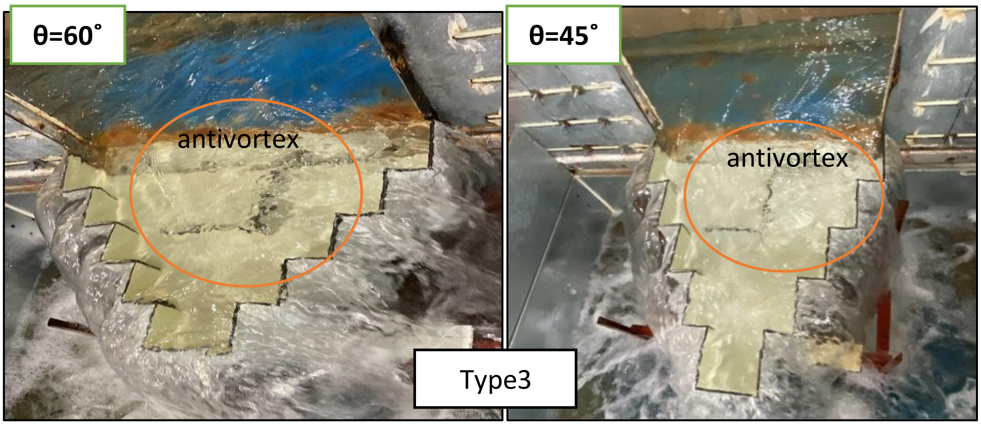

Type3

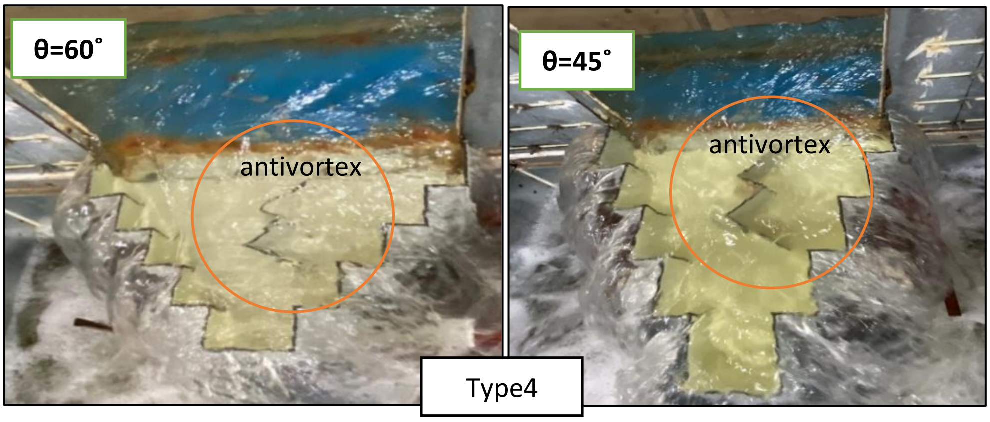

Type4

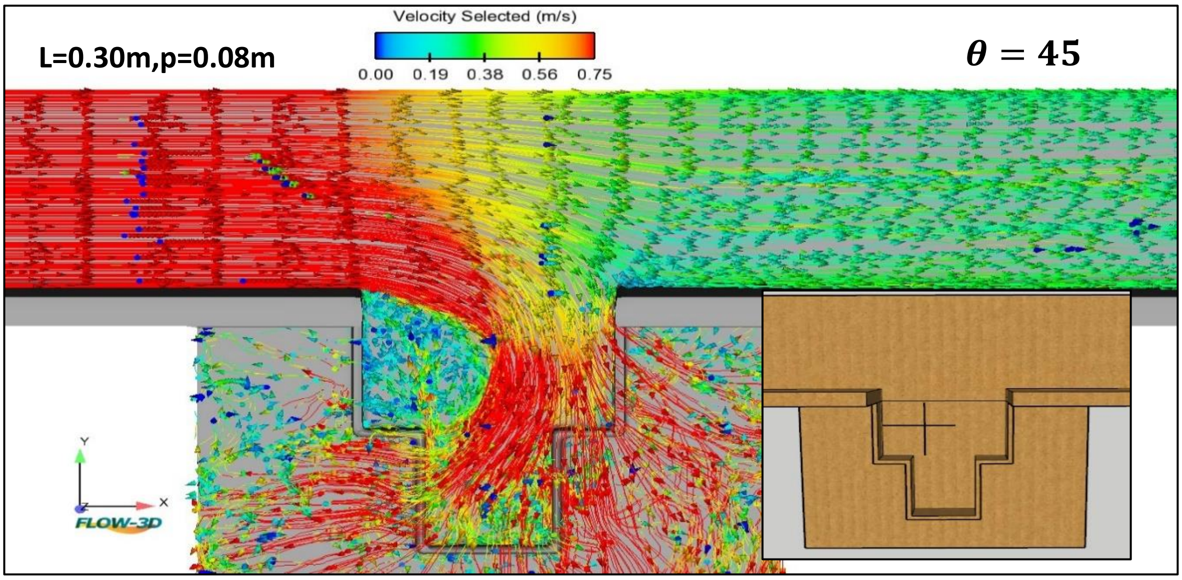
Velocity Selected (m/s)
L=0.30m,p=0.08m
0.00 0.19 0.38 0.56 0.75
$\theta = 45$
Y
X
FLOW-3D

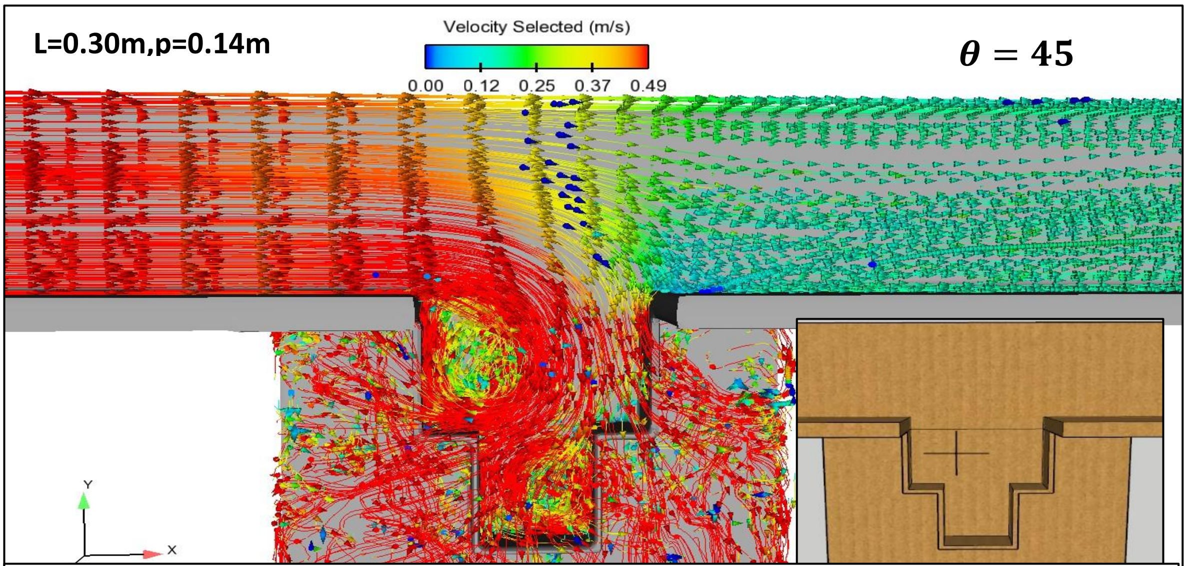
L=0.30m,p=0.14m
Velocity Selected (m/s)
0.00 0.12 0.25 0.37 0.49
$\theta = 45$
Y
X

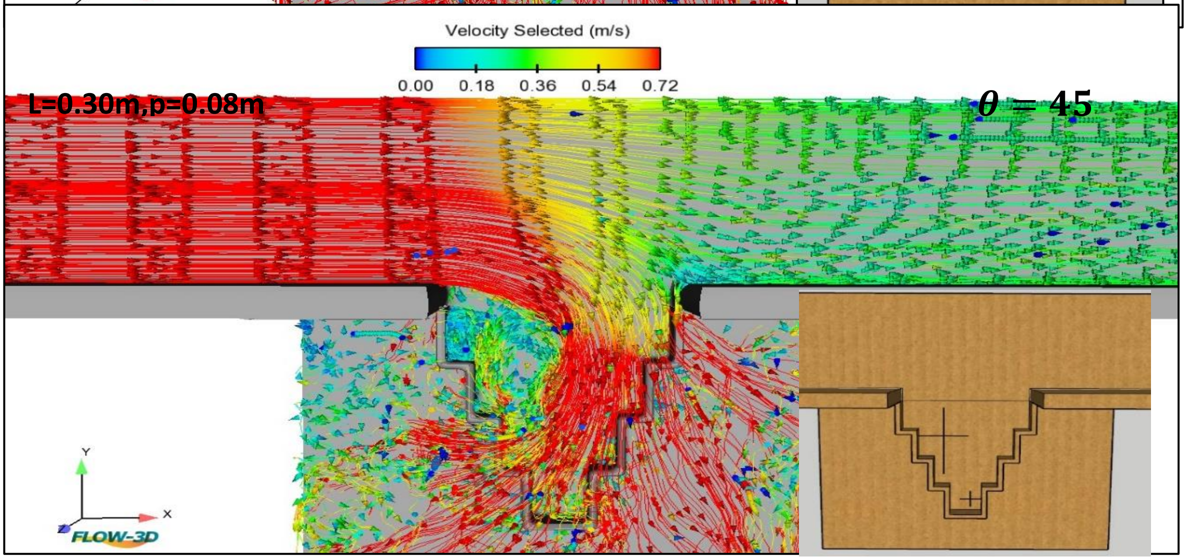
Velocity Selected (m/s)
0.00 0.18 0.36 0.54 0.72
L=0.30m,p=0.08m
$\theta = 45$
Y
X
FLOW-3D

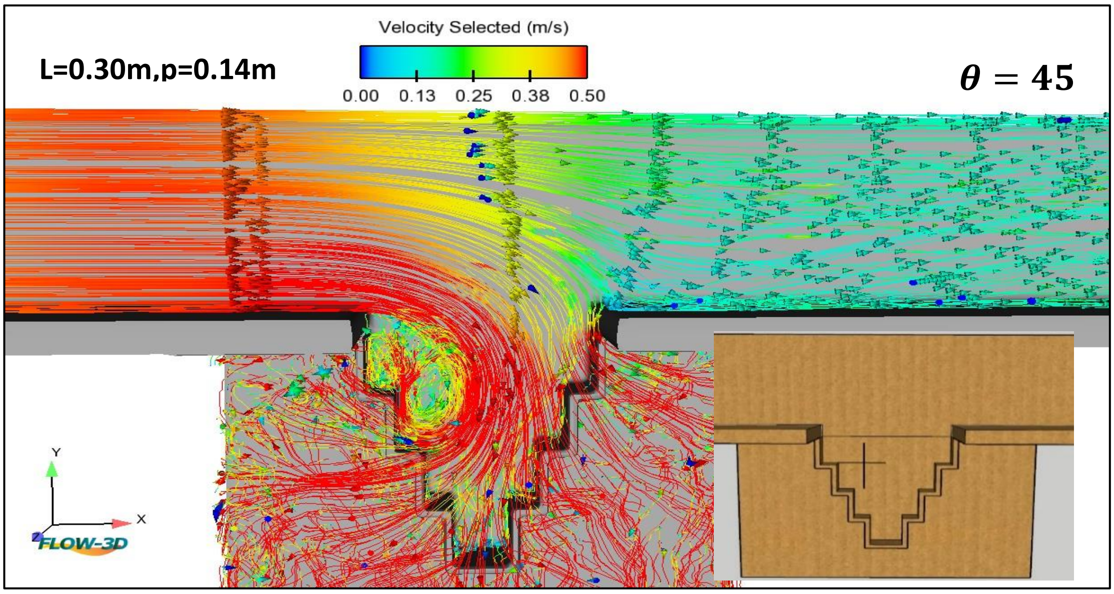
L=0.30m,p=0.14m
Velocity Selected (m/s)
0.00 0.13 0.25 0.38 0.50
$\theta = 45$
Y
X
FLOW-3D

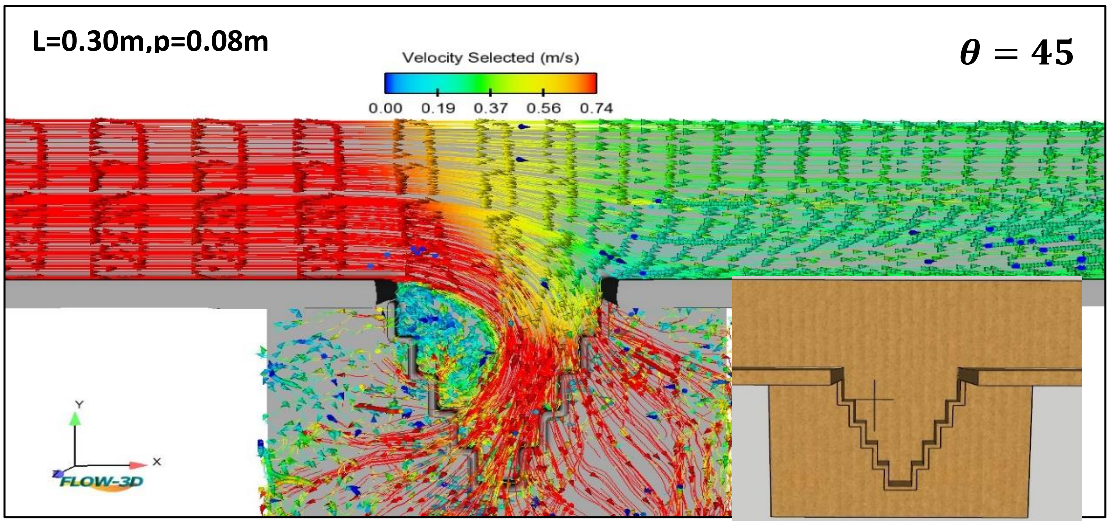
L=0.30m,p=0.08m
Velocity Selected (m/s)
0.00 0.19 0.37 0.56 0.74
$\theta = 45$
Y
X
FLOW-3D

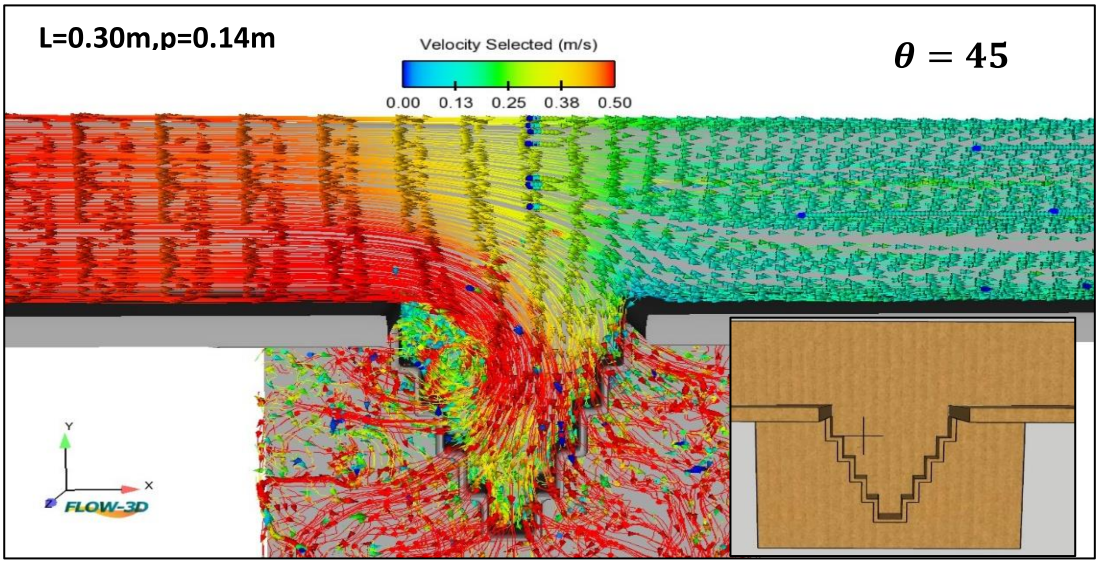
L=0.30m,p=0.14m
Velocity Selected (m/s)
0.00 0.13 0.25 0.38 0.50
$\theta = 45$
Y
X
FLOW-3D

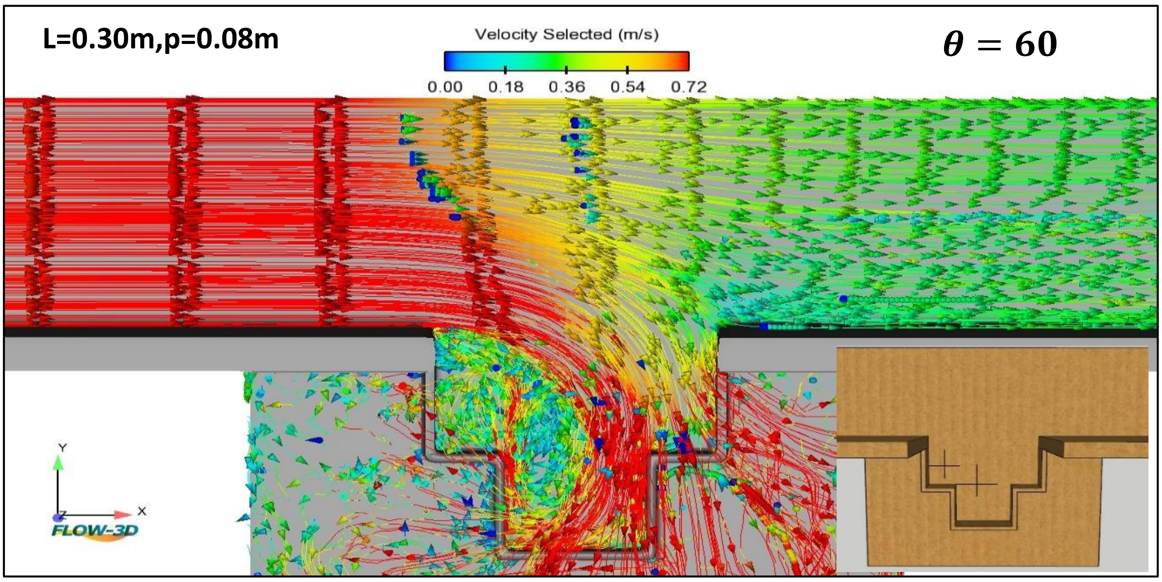
L=0.30m,p=0.08m
Velocity Selected (m/s)
0.00 0.18 0.36 0.54 0.72
$\theta = 60$
Y
X
FLOW-3D

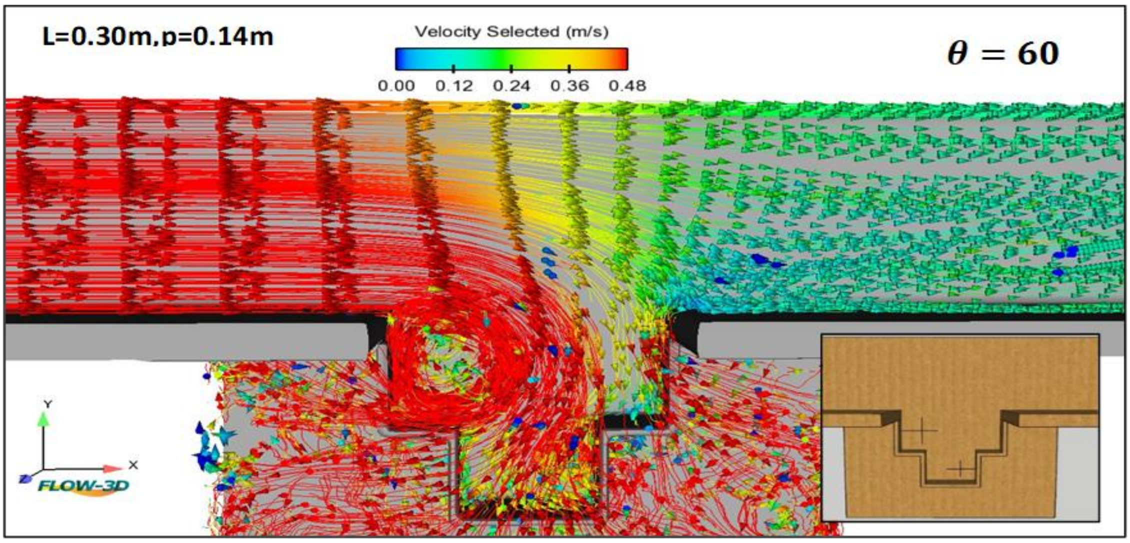
L=0.30m,p=0.14m
Velocity Selected (m/s)
0.00 0.12 0.24 0.36 0.48
$\theta = 60$
Y
X
FLOW-3D

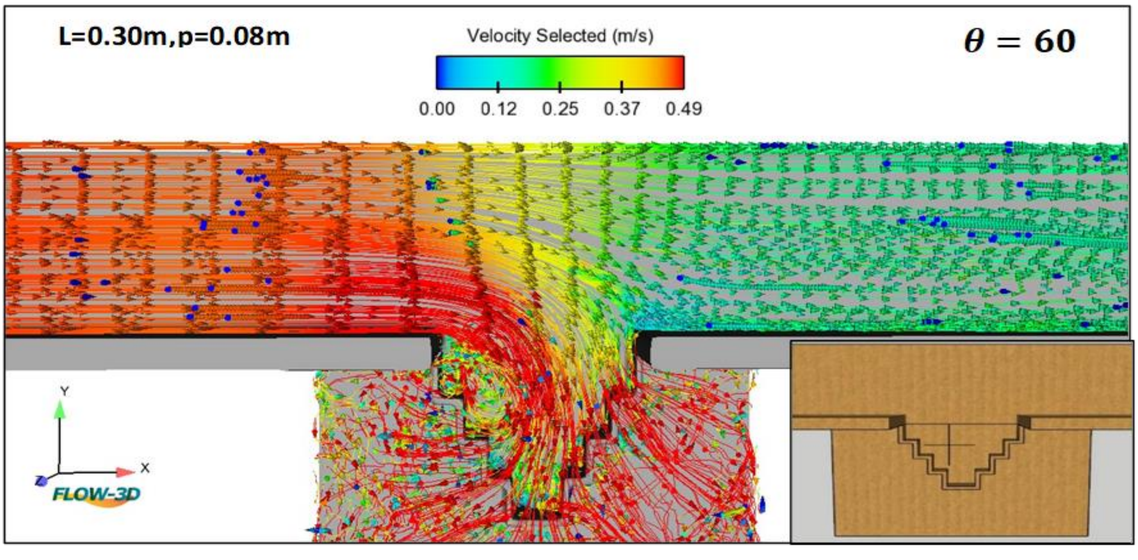
L=0.30m,p=0.08m
Velocity Selected (m/s)
0.00 0.12 0.25 0.37 0.49
$\theta = 60$
Y
X
FLOW-3D

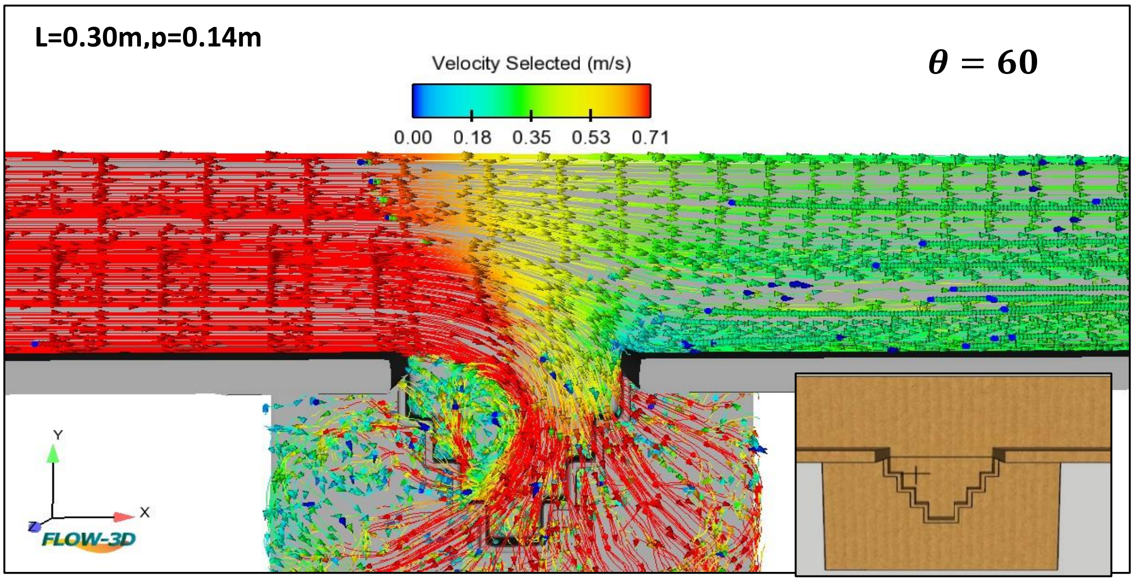
L=0.30m,p=0.14m
Velocity Selected (m/s)
0.00 0.18 0.35 0.53 0.71
$\theta = 60$
Y
X
FLOW-3D

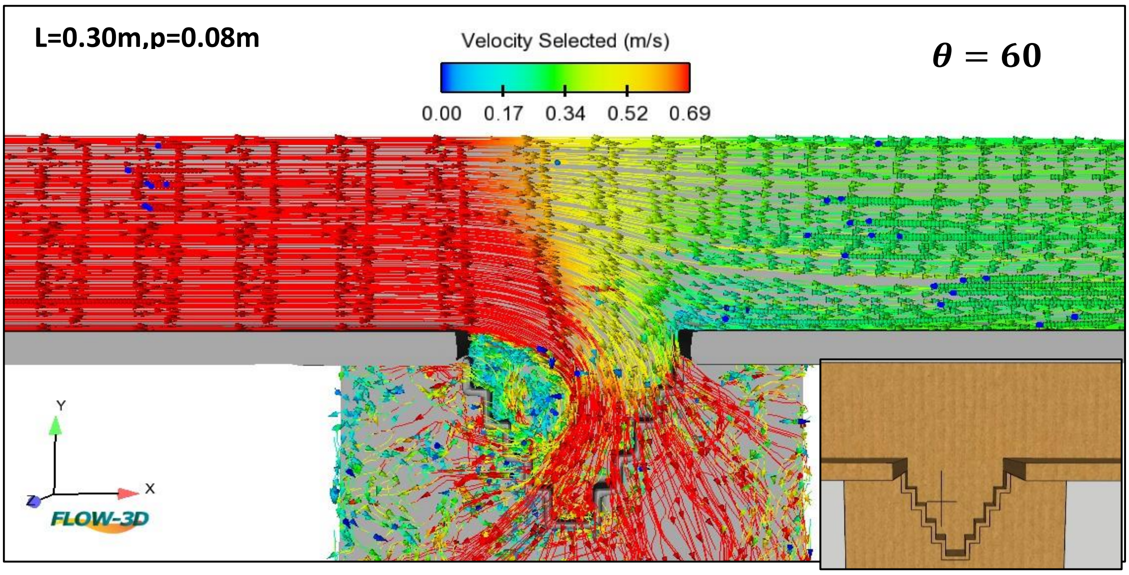
L=0.30m,p=0.08m
Velocity Selected (m/s)
0.00 0.17 0.34 0.52 0.69
$\theta = 60$
Y
X
FLOW-3D

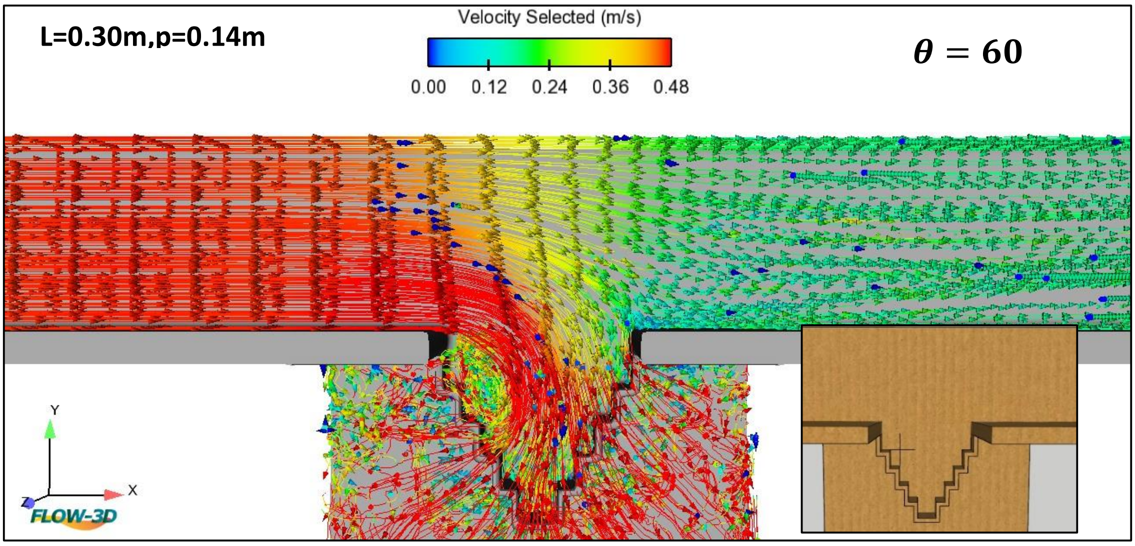
L=0.30m,p=0.14m
Velocity Selected (m/s)
0.00 0.12 0.24 0.36 0.48
$\theta = 60$
Y
X
FLOW-3D

Appendix B

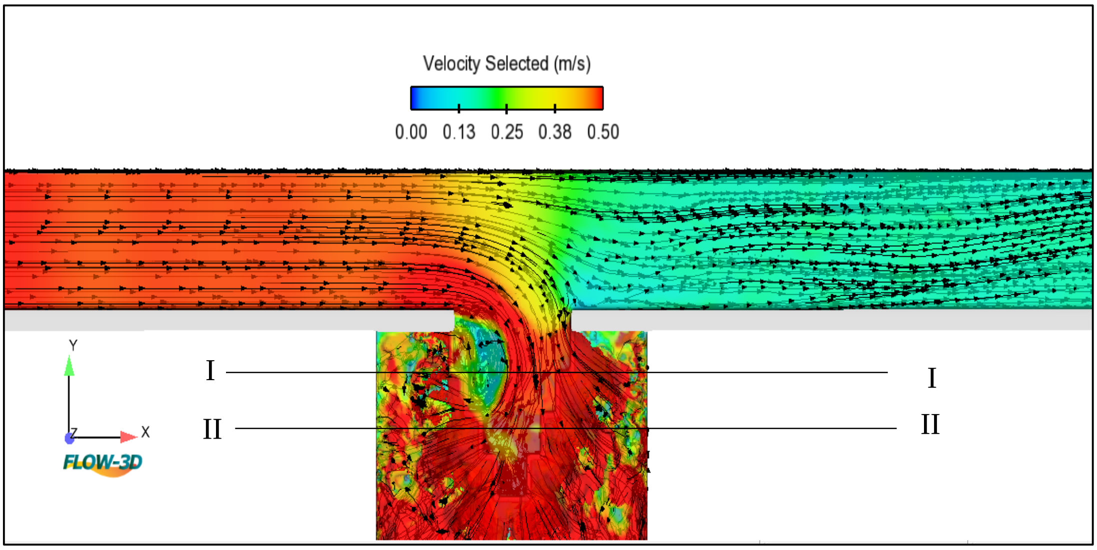
Velocity Selected (m/s)
0.00 0.13 0.25 0.38 0.50
I
I
II
II
Y
Z
X
FLOW-3D

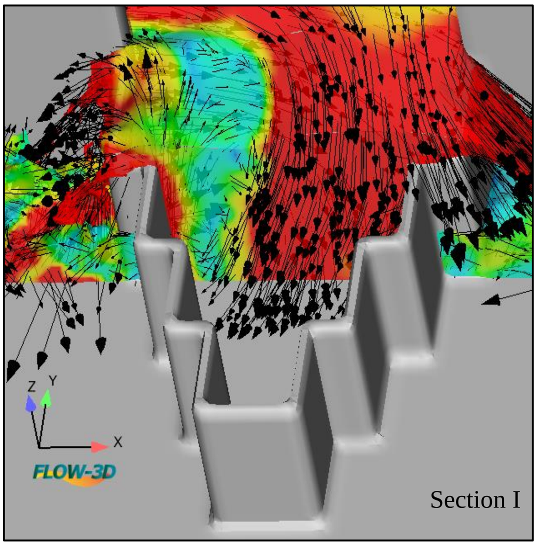
Z
Y
X
FLOW-3D
Section I

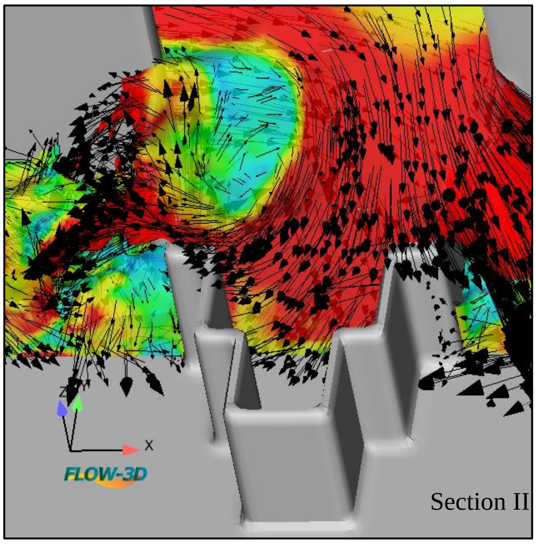
Z
X
FLOW-3D
Section II

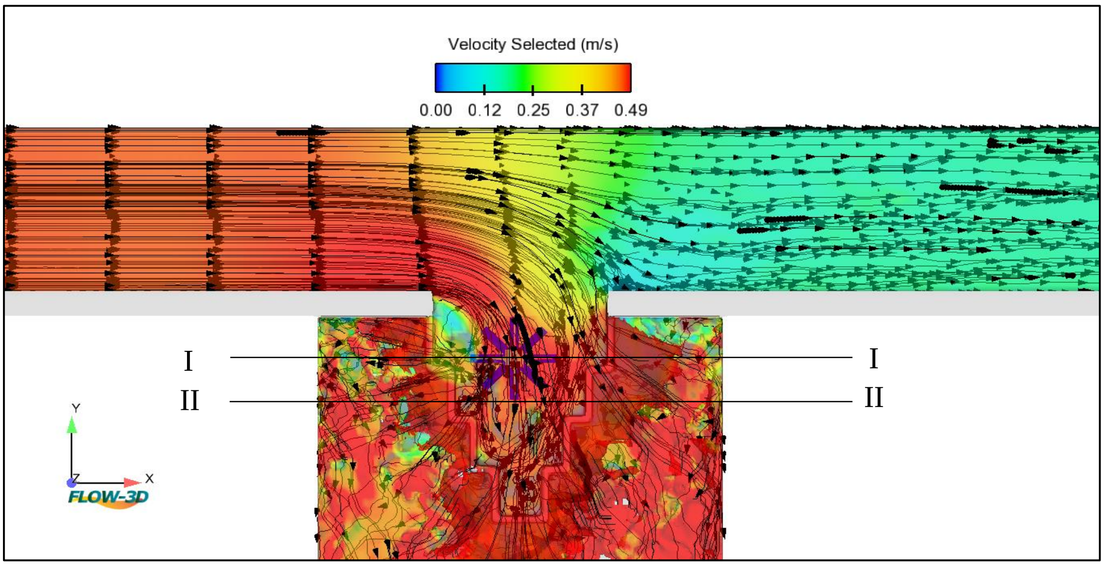
Velocity Selected (m/s)
0.00 0.12 0.25 0.37 0.49
I
I
II
II
Y
Z
X
FLOW-3D

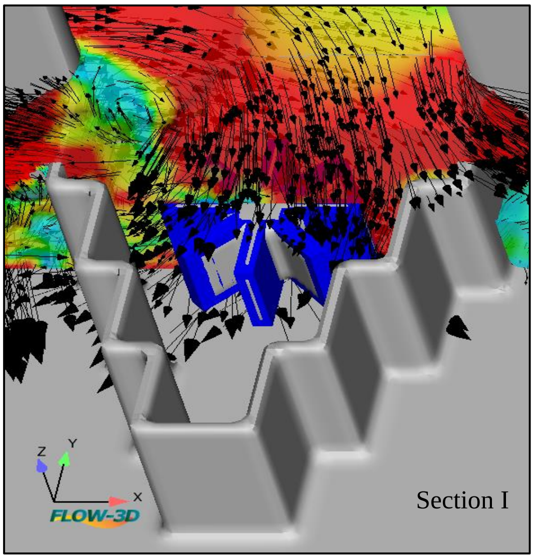
Z
Y
X
FLOW-3D
Section I

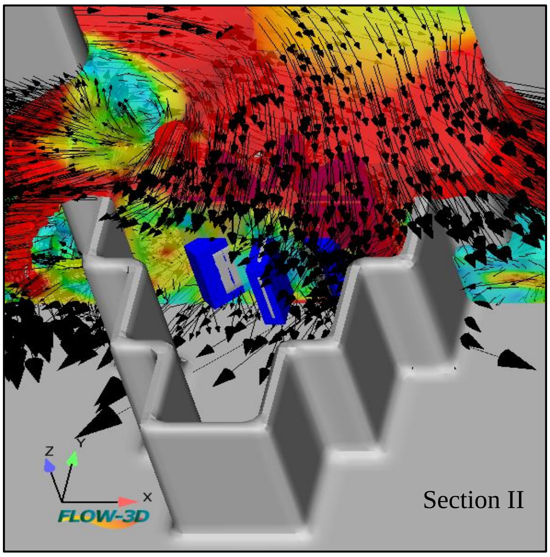
Z
Y
X
FLOW-3D
Section II

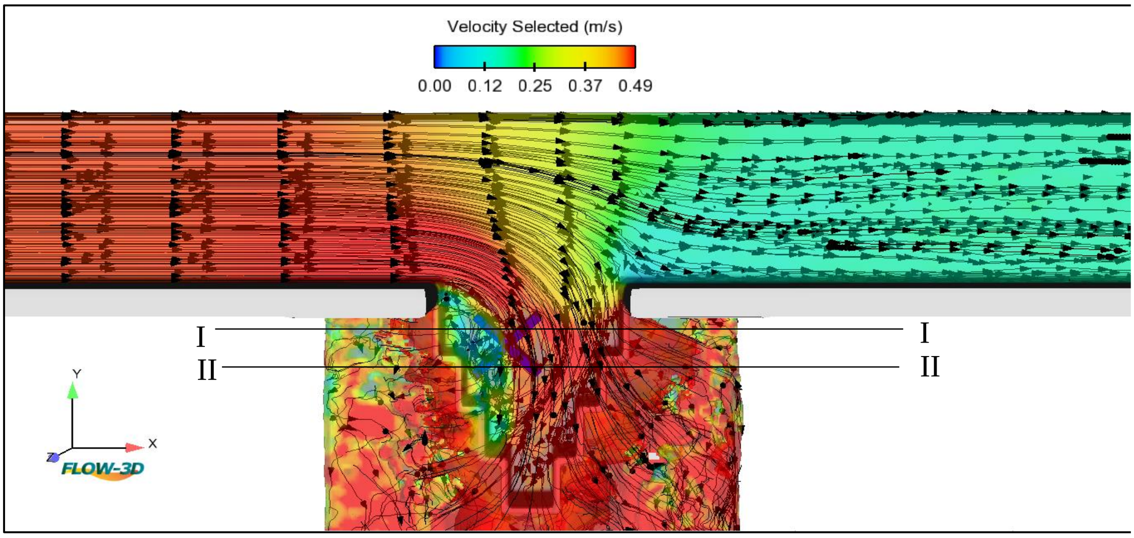
Velocity Selected (m/s)
0.00
0.12
0.25
0.37
0.49
I
II
I
II
Y
X
FLOW-3D

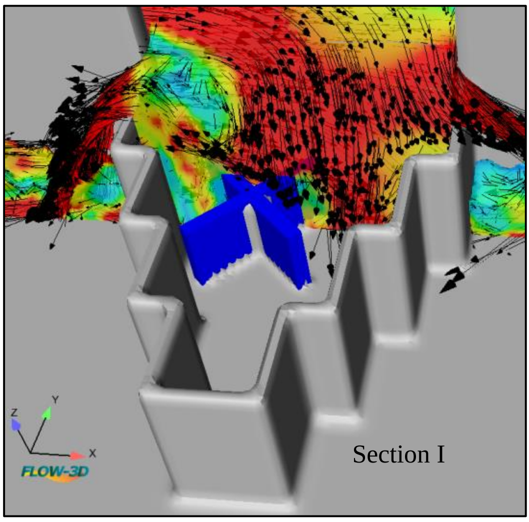
Z
Y
X
FLOW-3D
Section I

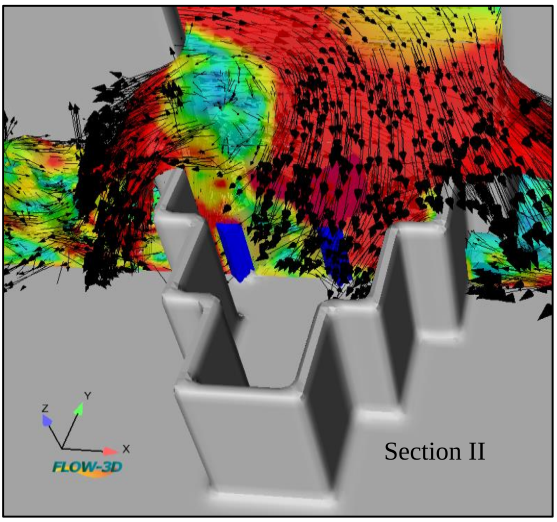
Z
Y
X
FLOW-3D
Section II

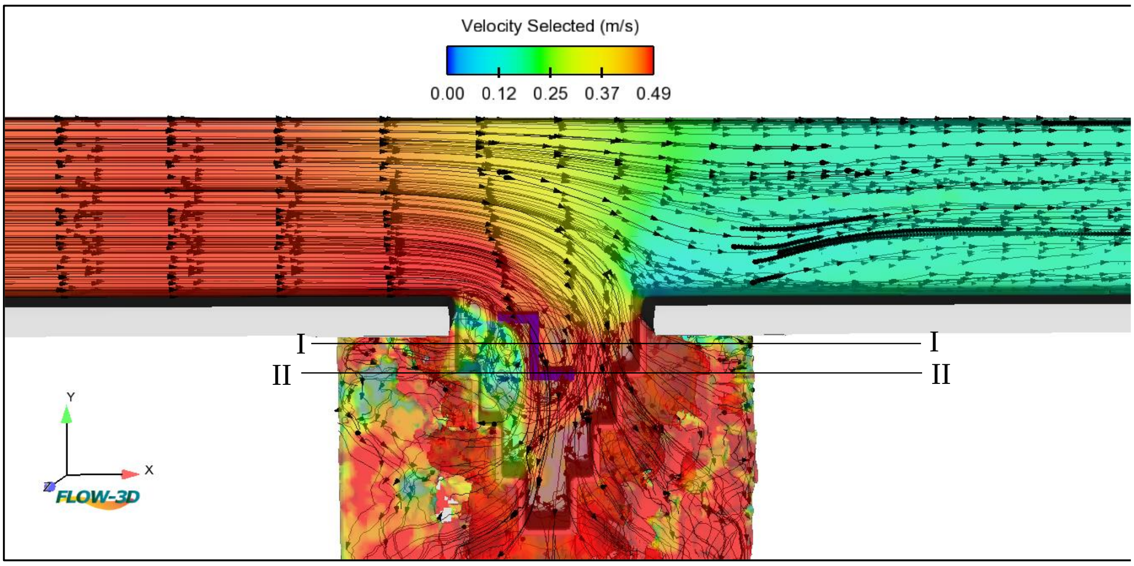
Velocity Selected (m/s)
0.00 0.12 0.25 0.37 0.49
I
II
I
II
Y
X
FLOW-3D

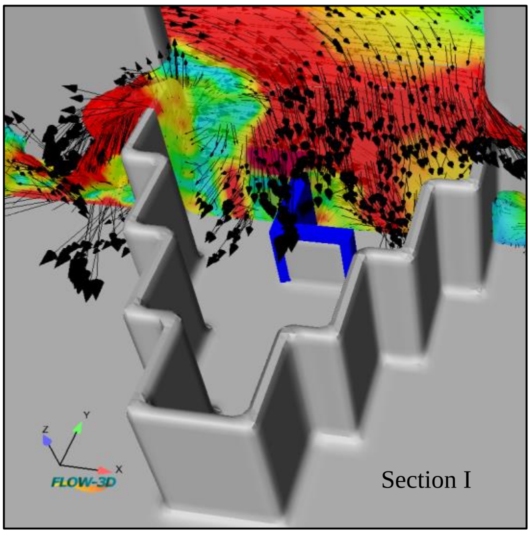
Z
Y
X
FLOW-3D
Section I

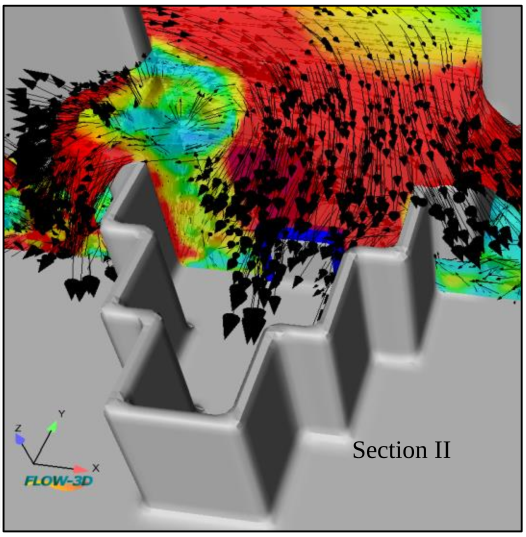
Z
Y
X
FLOW-3D
Section II

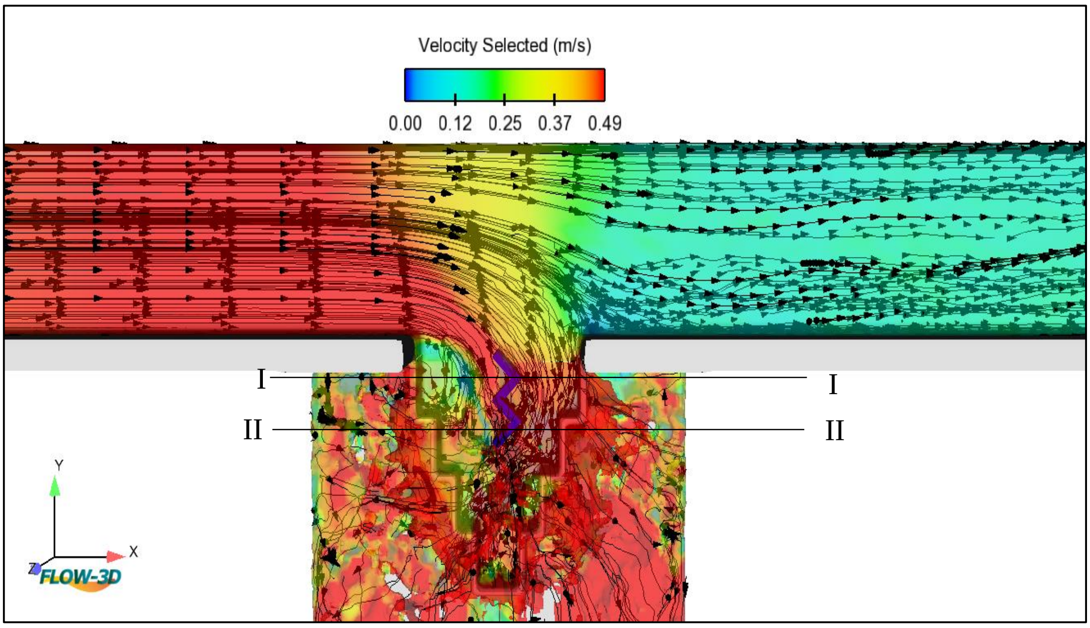
Velocity Selected (m/s)
0.00 0.12 0.25 0.37 0.49
I
II
I
II
Y
X
FLOW-3D

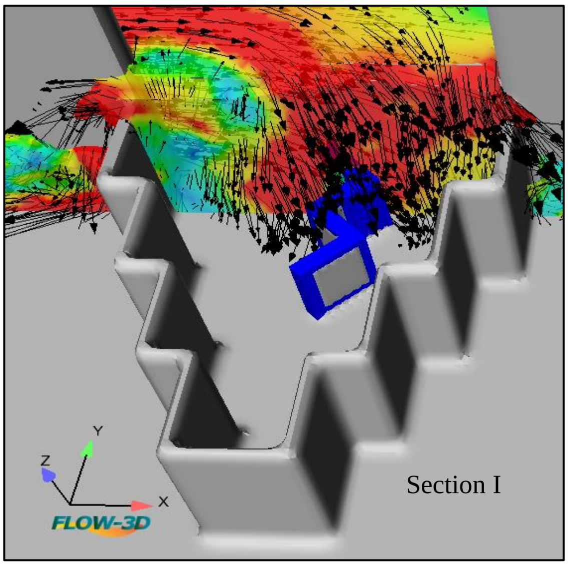
Y
Z
X
FLOW-3D
Section I

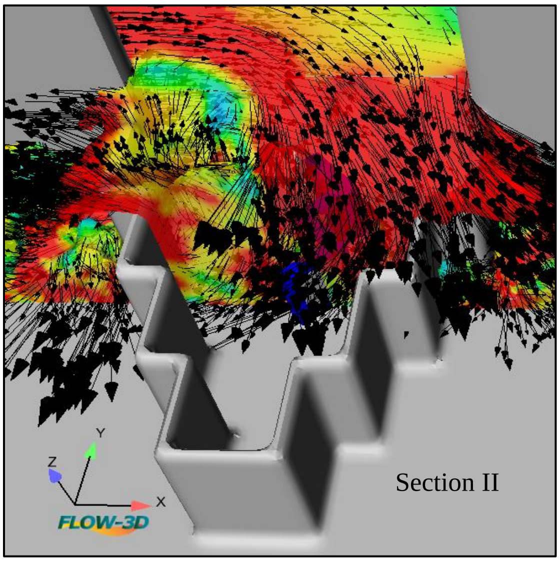
Y
Z
X
FLOW-3D
Section II

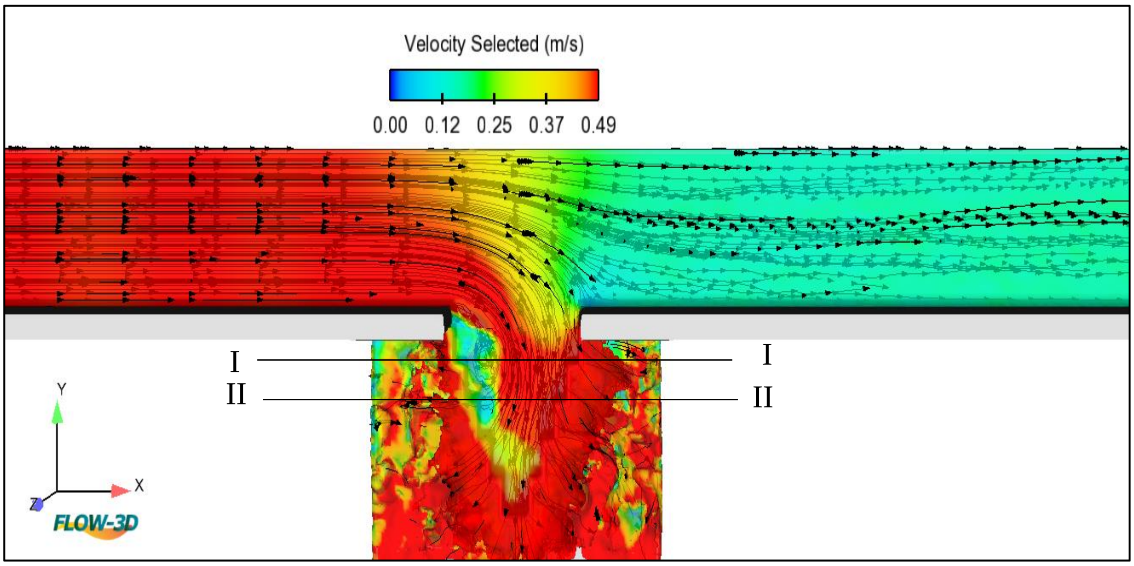
Velocity Selected (m/s)
0.00
0.12
0.25
0.37
0.49
I
II
I
II
Y
X
Z
FLOW-3D

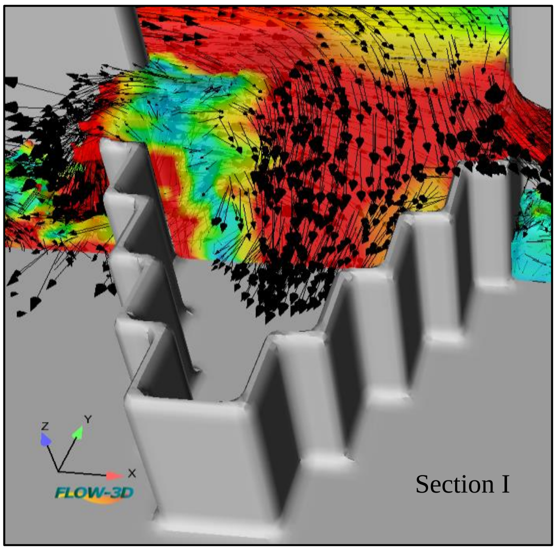
Z
Y
X
FLOW-3D
Section I

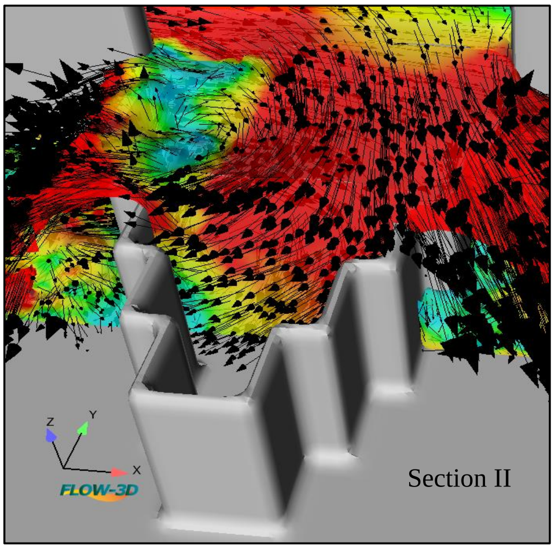
Z
Y
X
FLOW-3D
Section II

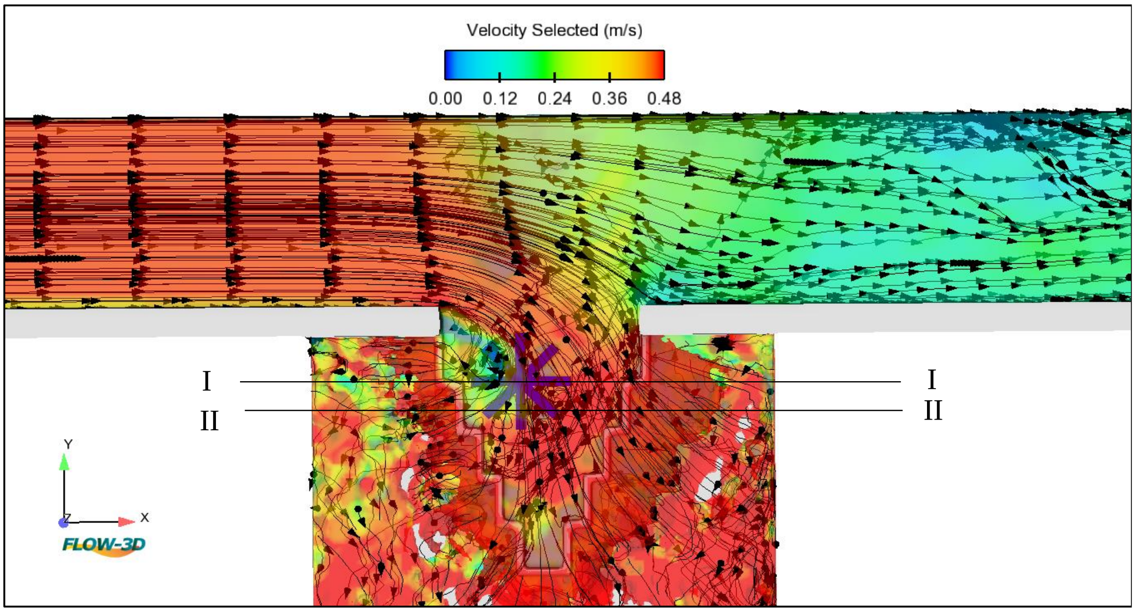
Velocity Selected (m/s)
0.00 0.12 0.24 0.36 0.48
I
II
I
II
Y
X
FLOW-3D

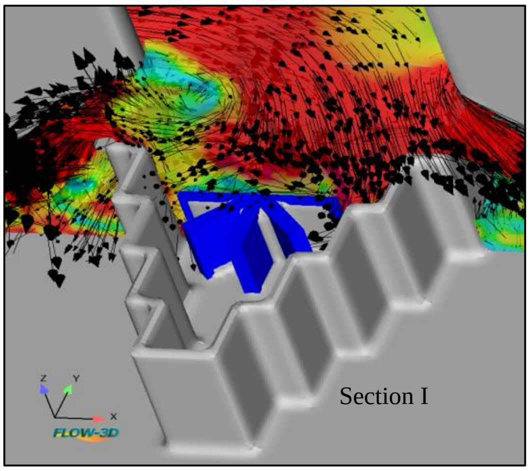
Z
Y
X
FLOW-3D
Section I

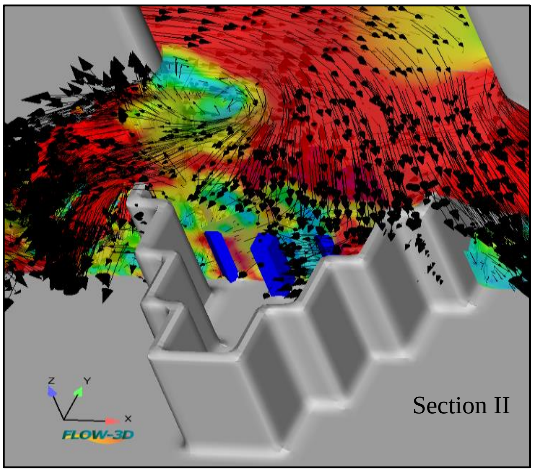
Z
Y
X
FLOW-3D
Section II

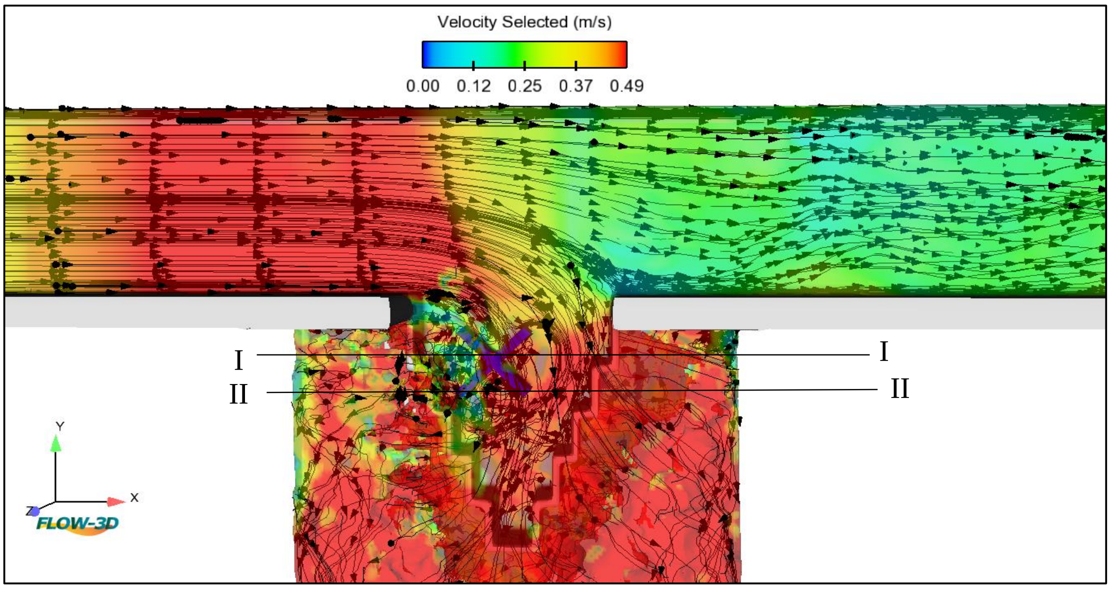
Velocity Selected (m/s)
0.00 0.12 0.25 0.37 0.49
I
II
I
II
Y
X
FLOW-3D

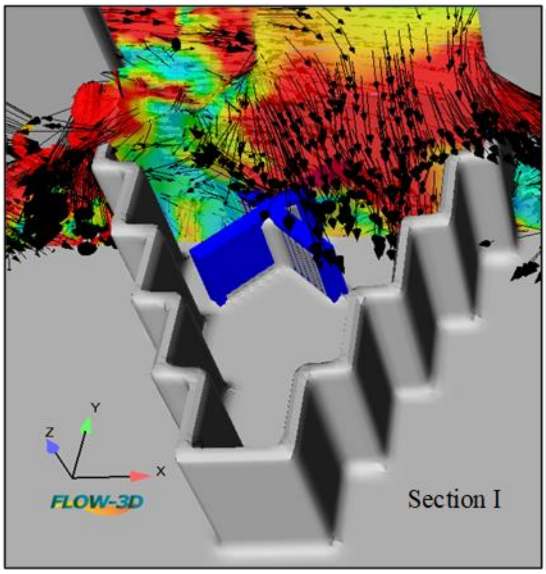
Y
Z
X
FLOW-3D
Section I

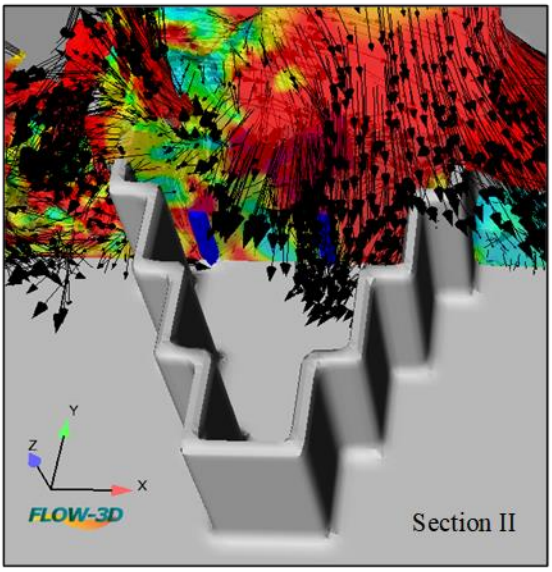
Y
Z
X
FLOW-3D
Section II

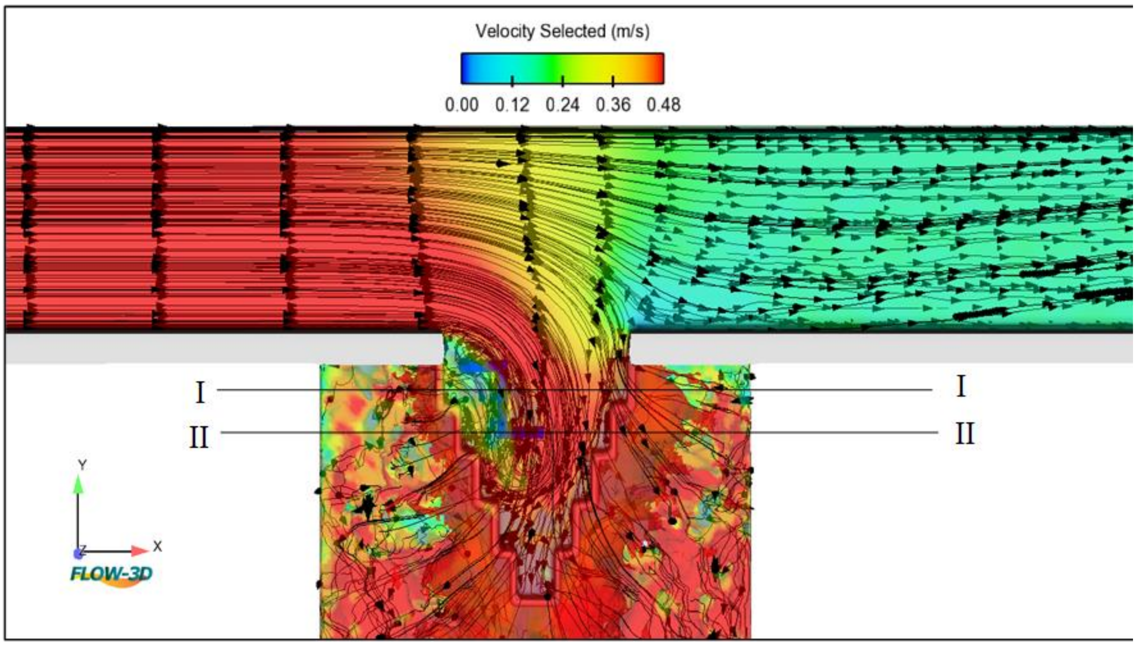
Velocity Selected (m/s)
0.00
0.12
0.24
0.36
0.48
I
II
I
II
Y
Z
X
FLOW-3D

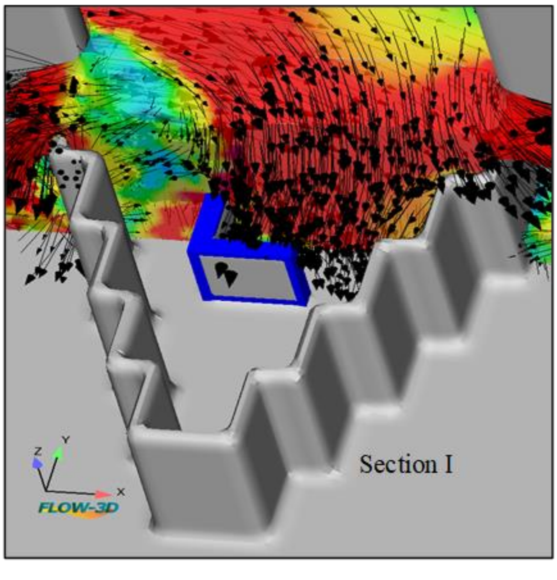
Z
Y
X
FLOW-3D
Section I

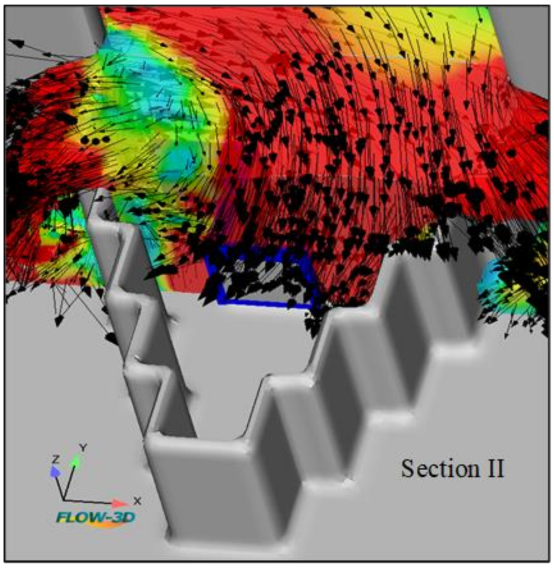
Z
Y
X
FLOW-3D
Section II

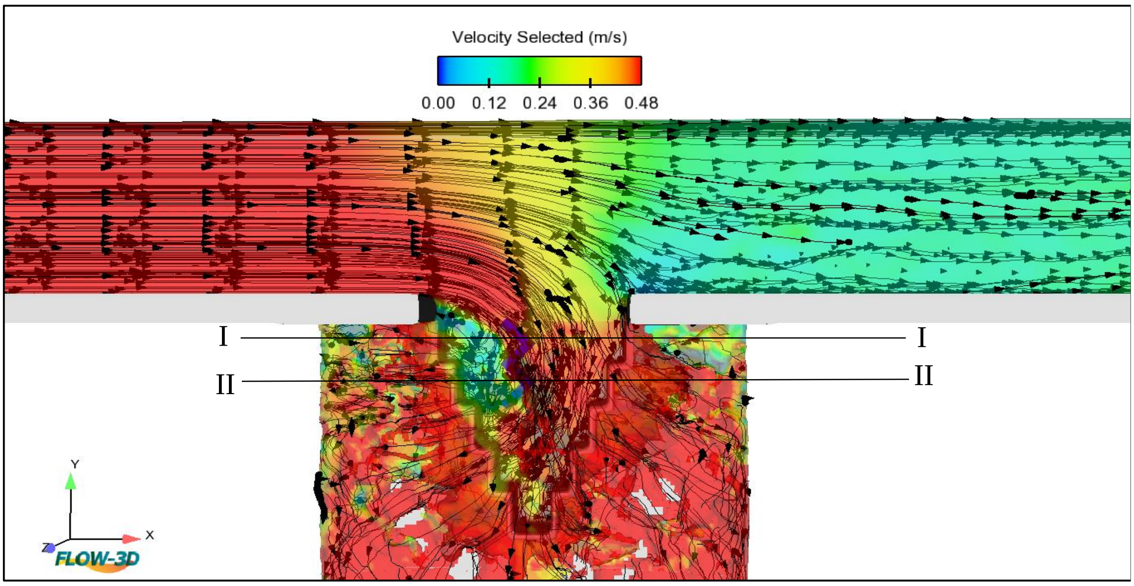
Velocity Selected (m/s)
0.00
0.12
0.24
0.36
0.48
I
I
II
II
Y
X
Z
FLOW-3D

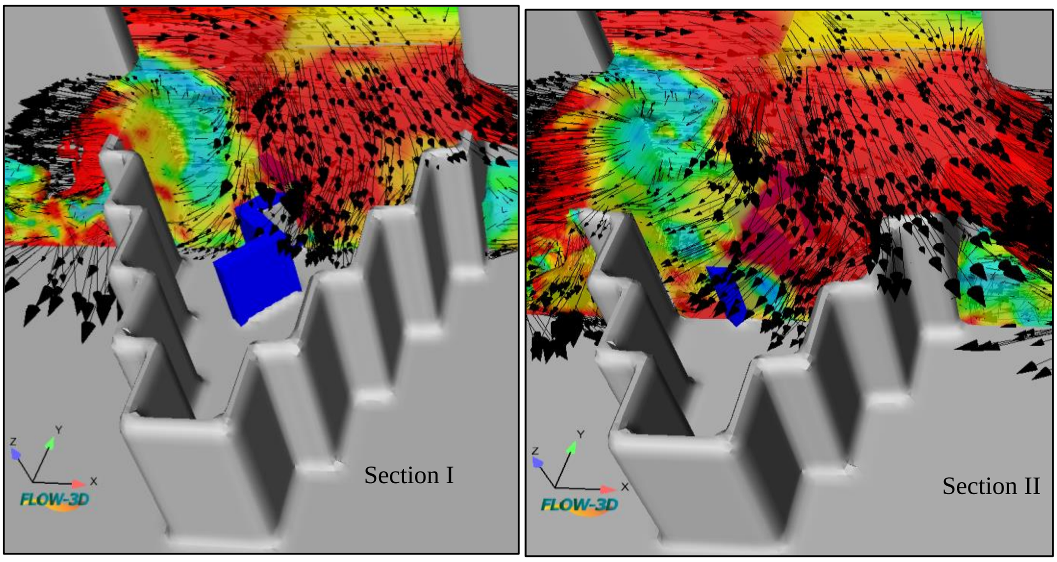
Z
Y
X
FLOW-3D
Section I
Z
Y
X
FLOW-3D
Section II

الخلاصة

هدار المتاهه الجانبي هو منشأ هيدروليكي مهم للتحكم في مستويات المياه في الانهارو القنوات. فان الهدار الجانبي يمكن ان يستخدم في زيادة كمية عندما يكون عرض الفتحة الجانبية محدودا الماء المتدفق من القناة ، هدار المتاهة الجانبي يفضل بدلا عن الهدار الاعتيادي لنفس عرض الفتحة الجانبية. مع ذلك تشكل الدوامة في الهدارات الجانبية عادة ما يعرقل تدفق التيار.

اقترحت الدراسة الحالية اربعة انواع من المنشات المضادة للدوامات المثبتة في هدار المتاهة الجانبي المدرج بمختلف الخواص الهيدروليكية. تبحث الدراسة الحالية تكون الدوامات عند مقدم القناة الرئيسية عمليا وعدديا. وكذلك تأثير تثبيت مضاد الدوامة في هذه الهدارات على كفاءة التصريف وتقييم اداء الموديلات المقترحة. باستخدام بيانات من 168 تجربة بدون تثبيت مضاد الدوامة للمقارنة و 672 تجربة للحصول على افضل اداء من مضاد الدوامة لتحسين كفاءة التصريف و 528 تجربة من قياسات السرعة لبحث شدة التيارات الثانوية المتولدة من خلال التيار الجانبي وغيرها من الظروف الهيدروليكية . اجريت التجارب على عرضين لفتحة الهدار الجانبي المتدرج (0.45،0.30) م ، وارتفاعات مختلفة من الهدار (0.14،0.08) م ، وثلاثة مجاميع من الدرجات كل مجموعة تحتوي على (10،8،4) درجة ، ولزوايا (45°،60°) . تم محاكاة النماذج الفيزيائية عدديا للبحث في تكون الدوامة لمختلف ارتفاعات الماء وتوسيع نطاق البرنامج ليشمل الحالات التي لم تتم دراستها تجريبيا. تقنية ، الاضطراب ، جريان المائع تمت محاكاتها عدديا . بالبداية تم فحص تكون الدوامات بالنماذج وموقعها المضبوط ولاحقا تم فحص تثبيت المنشات التي تمنع تكون هذه الدوامات في الهدارات الجانبية المدرجة.

اظهرت النتائج تحسن أداء الهدار الجانبي حيث ازدادت قيم التصريف بزيادة عدد الدرجات ، وقلت كل من الزاوية وفتحة الهدار الجانبي .الموديلات التي تحتوي على عشر درجات ، زاوية ($45°=\theta$) ، وفتحة هدار جانبي (0.30) م اظهرت اعلى قيمة تصريف . لذلك ، تثبيت مضاد الدوامات يتحكم بالجريان ويزيد كفاءة الهدار الجانبي المدرج ويقلل من شدة التيارات الثانوية التي تنتج من تداخل التيارات الجانبية. بعد تحليل افضل نوع من مضاد الدوامة بالاخذ بنظر الاعتبار الشكل والارتفاع ،فأن هذا النوع قد تفوق على بقية الانواع بزيادة التصريف بنسبة 18% وتقليل التيارات الثانويه بنسبة 9%.

النتائج العددية اظهرت ان نسبة الخطأ بين البيانات العملية والعددية كان 3.07% مما يؤكد ان النموذج يؤدي الغرض بالتنبؤ بخصائص الجريان المتدفق فوق الهدار الجانبي المتدرج. تمت المحاكاة العددية لايجاد ابعاد المنشات المضادة للدوامة بتثبيت هذه المنشات في مكان الدوامة وتغيير المكان والابعاد لهذه المنشات لمختلف ارتفاعات الهدار وطول فتحة الهدار الجانبي وعدد الدرجات وكذلك يحسب البرنامج الخواص الهيدروليكية مثل مستويات الماء ، عدد فرود ، السرعة ،وتكون الدوامة في الهدار الجانبي المدرج.

جمهورية العراق
وزارة التعليم العالي والبحث العلمي
جامعة بابل/ كلية الهندسة
قسم الهندسة المدنية

تاثير مضاد الدوامة على هيدروليكية الهدار الجانبي المثلث المدرج

رسالة مقدمة إلى قسم الهندسة المدنية، كلية الهندسة، جامعةِ بابل وهي جزء مِنْ
متطلبات الحصول على درجة الماجستيرعلوم في الهندسة/ الهندسة المدنية / الموارد
المائية

من قبل:
ريام ضياء محمد حسن

اشراف:
أ.د ثائر جبار مزهر الفتلاوي

تشرين الثاني ,1444

November, 2022